The Dissertation Committee for Sheng-Heng Chung certifies that this is the approved version of the following dissertation:

CUSTOM-CELL-COMPONENT DESIGN AND DEVELOPMENT FOR RECHARGEABLE LITHIUM-SULFUR BATTERIES

Committee:

Arumugam Manthiram, Supervisor

John B. Goodenough

Paulo J. Ferreira

Guihua Yu

Gyeong S. Hwang

CUSTOM-CELL-COMPONENT DESIGN AND DEVELOPMENT FOR RECHARGEABLE LITHIUM-SULFUR BATTERIES

by

Sheng-Heng Chung, B.S., M.S.

Dissertation

Presented to the Faculty of the Graduate School of

The University of Texas at Austin

in Partial Fulfillment

of the Requirements

for the Degree of

Doctor of Philosophy

The University of Texas at Austin

May 2015

Acknowledgements

First of all, I would like to express my deep gratitude to my supervisor, Professor Arumugam Manthiram, for his inspiring guidance and continuous support during my years at the University of Texas at Austin. Without his valuable guidance, I could not have developed my research work successfully. I also want to express my gratitude to all my committee members, Professors John B. Goodenough, Paulo Ferreira, Guihua Yu, and Gyeong S. Hwang. They all agreed to serve as my committee without hesitation and gave me useful suggestions on my dissertation.

I would like to express my deep gratitude towards the former and current members in Prof. Manthiram's group, specifically, Dr. Yu-Sheng Su, Dr. Yongzhu Fu, Dr. Katharine Chemelewski, Dr. Veronica Augustyn, Dr. Il Tae Kim, Dr. Chih-Liang Wang, Dr. Chih-Chieh Wang, Zach Moorhead-Rosenberg, Pauline Han, Ke-Yu Lai, and Chi-Hao Chang for their kind help and inspiring discussions in my study on various aspects. I would like to thank Uzumaki Naruto for the continuous encouragement that always gives me the strength and freedom to pursue my goal. I also appreciate the financial support by the U. S. Department of Energy and Seven One Limited.

Last but not least, I am deeply indebted to my family for providing boundless love and unconditional support. I owe them many thanks. I would like to thank them for their love and support.

CUSTOM-CELL-COMPONENT DESIGN AND DEVELOPMENT FOR RECHARGEABLE LITHIUM-SULFUR BATTERIES

Sheng-Heng Chung, Ph.D.

The University of Texas at Austin, 2014

Supervisor: Arumugam Manthiram

Development of alternative cathodes that have high capacity and long cycle life at an affordable cost is critical for next generation rechargeable batteries to meet the ever-increasing requirements of global energy storage market. Lithium-sulfur batteries, employing sulfur cathodes, are increasingly being investigated due to their high theoretical capacity, low cost, and environmental friendliness. However, the practicality of lithium-sulfur technology is hindered by technical obstacles, such as short shelf and cycle life, arising from the shuttling of polysulfide intermediates between the cathode and the anode as well as the poor electronic conductivity of sulfur and the discharge product Li_2S. This dissertation focuses on overcoming some of these problems.

The sulfur cathode involves an electrochemical conversion reaction compared to the conventional insertion-reaction cathodes. Therefore, modifications in cell-component configurations/structures are needed to realize the full potential of lithium-sulfur cells. This dissertation explores various custom and functionalized cell components that can be adapted with pure sulfur cathodes, *e.g.*, porous current collectors in Chapter 3, interlayers in Chapter 4, sandwiched electrodes in Chapter 5, and surface-coated separators in Chapter 6. Each chapter introduces the new concept and design, followed by necessary modifications and development.

The porous current collectors embedded with pure sulfur cathodes are able to contain the active material in their porous space and ensure close contact between the insulating active material and the conductive matrix. Hence, a stable and reversible electrochemical-conversion reaction is facilitated. In addition, the use of highly porous substrates allows the resulting cell to accommodate high sulfur loading.

The interlayers inserted between the pure sulfur cathode and the separator effectively intercept the diffusing polysulfides, suppress polysulfide migration, localize the active material within the cathode region, and boost cell cycle stability.

The combination of porous current collectors and interlayers offers sandwiched electrode structure for the lithium/dissolved polysulfide cells. By way of integrating the advantages from the porous current collector and the interlayer, the sandwiched electrodes stabilize the dissolved polysulfide catholyte within the cathode region, resulting in a high discharge capacity, long-term cycle stability, and high sulfur loading.

The novel surface-coated separators have a polysulfide trap or filter coated onto one side of a commercial polymeric separator. The functional coatings possess physical and/or chemical polysulfide-trapping capabilities to intercept, absorb, and trap the dissolved polysulfides during cell discharge. The functional coatings also have high electrical conductivity and porous channels to facilitate electron, lithium-ion, and electrolyte mobility for reactivating the trapped active material. As a result, effective reutilization of the trapped active material leads to improved long-term cycle stability.

The investigation of the key electrochemical and engineering parameters of these novel cell components has allowed us to make progress on (i) understanding the materials chemistry of the applied functionalized cell components and (ii) the electrochemical performance of the resulting lithium-sulfur batteries.

Table of Contents

List of Tables

List of Figures

Chapter 1: Introduction*

1.1 RECHARGEABLE LITHIUM-SULFUR BATTERIES

The portable electronics market has been dominated by Lithium-ion (Li-ion) batteries for more than 20 years after Sony Inc. released the first commercial product in 1991.[1-3] The key factor that Li-ion batteries are successful in commercial application for years is their highest energy density among the known practical rechargeable battery systems. Following their impact in portables, the Li-ion technology is now beginning to enter into electric vehicles and grid storage of renewable energies (*e.g.*, solar and wind energy). However, the current Li-ion technology that is based on insertion-compound chemistry has reached the limitations of their charge-storage capacity and energy density. The practical capacities of the transition-metal oxide and phosphate cathodes that are currently used in lithium-ion technology have a limit of ~ 170 mA h g^{-1}.[1, 4-6] On the other hand, the theoretical capacity of the graphite anode is limited to ~ 370 mA h g^{-1}.[1, 4, 7] Therefore, alternative cathode and anode materials that offer higher capacities need to be developed. As a result, materials that undergo conversion reactions while accommodating more ions and electrons are becoming promising options to overcome the charge-storage limitations of current insertion-compound electrodes.[6-10] Moreover, cost, cycle life, safety, energy, power, and environmental impact are some of the criteria in choosing the appropriate battery chemistry for various applications.[6, 10, 11]

---

* A. Manthiram, Y. Fu, S.-H. Chung, C. Zu, and Y.-S. Su, "Rechargeable Lithium–Sulfur Batteries," *Chem. Rev.* 2014, **114**, 11751-11787.

* A. Manthiram, S.-H. Chung, and C. Zu, "Lithium–Sulfur Batteries: Progress and Prospects," *Adv. Mater.* 2015, **27**, 1980-2006.

S.-H. Chung carried out the preparation of the sulfur-cathode and the cell-configuration sections. C. Zu carried out the preparation of the Li_2S-cathode and the lithium-metal sections. Y. Fu carried out the preparation of the historical-development and the composite-cathode sections. Y.-S. Su carried out the preparation of the technical-challenge section. A. Manthiram led and supervised the project. All participated in the preparation of the manuscript.

In this regard, the lithium-sulfur (Li-S) battery is an attractive candidate to emerge as the next-generation energy-storage system at an affordable cost and with minimal environment impacts. The sulfur cathode offers a high theoretical capacity of 1672 mA h g^{-1} (calculated based on $S^0 \leftrightarrow S^{2-}$), which is an order of magnitude higher than those of the transition-metal oxide cathodes. On the other hand, the theoretical capacity of a lithium-metal anode is 3862 mA h g^{-1} (calculated based on $Li^+ \leftrightarrow Li^0$). The discharge-charge reaction of a lithium-sulfur cell has an average operating voltage of 2.15 V *v.s.* Li^+/Li^0. As a result, a lithium-sulfur cell attains a high energy density of ~ 2500 W h kg^{-1}, which is 3- 5 times higher than that of traditional Li-ion batteries.[11-14]

1.2 PRINCIPLE OF OPERATION

The common lithium-sulfur battery architecture is composed of a pure sulfur cathode and a lithium-metal anode separated by a polymeric separator immersed with liquid electrolyte. The schematic illustration of a typical lithium-sulfur cell is shown in Figure 1.1.

During cell discharge (Figure 1.1a), lithium metal (anode) is oxidized at the negative electrode to produce lithium ions and electrons. The lithium ions that are stripped from the lithium metal move to the positive electrode through the electrolyte internally and react with sulfur at the cathode along with the electrons flowing through the external circuit to form Li-polysulfides (Li_2S_x, x = 4 – 8). Subsequently, the polysulfide intermediates (Li_2S_x, x = 4 – 8) convert to the end-discharge product lithium sulfide (Li_2S) with a shortening of the sulfur chain length.

During cell charge (Figure 1.1b), the lithium ions migrate from the cathode to the lithium-metal anode through the electrolyte internally while the electrons travel back from the cathode to the anode through the external circuit, resulting in a plating of lithium onto the lithium-metal anode while the Li_2S converts reversibly toward S_8.

The overall electrochemical reaction ($16Li + S_8 = 8Li_2S$) involves two electrons per sulfur, translating into a large charge-storage capacity with sulfur.

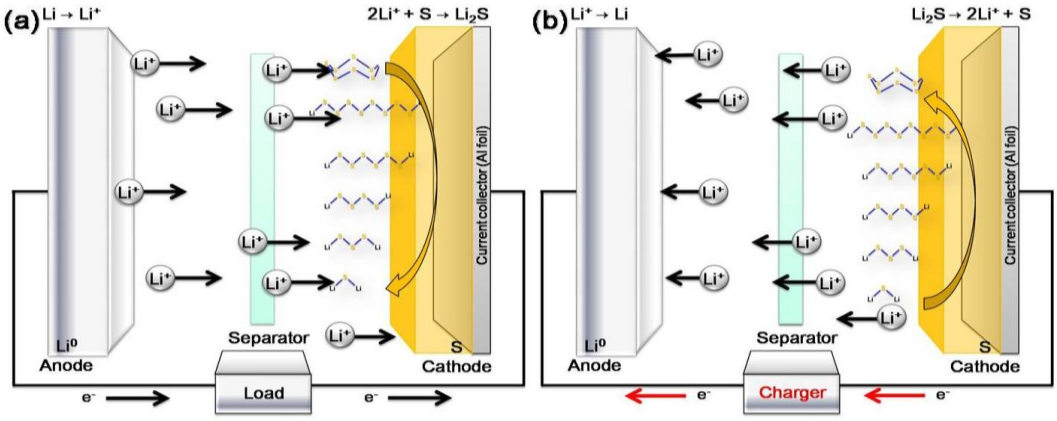

Figure 1.1: Schematic illustration of an ideal lithium-sulfur battery during (a) discharge and (b) charge

Figure 1.2 shows the typical discharge and charge processes of an ideal lithium-sulfur cell.[15] At the initial state, a fresh lithium-sulfur cell has an open-circuit voltage (OCV) that is attributed to the difference between the electrochemical potentials of the lithium-metal anode and the sulfur cathode.[16] The discharge curve of a lithium-sulfur cell has three electrochemical (reduction) conversion steps: (i) the upper plateau region, (ii) the sloping region, and (iii) the lower plateau region.[17, 18]

In the upper plateau region at ~ 2.3 V, the cyclo-sulfur is reduced to high-order lithium polysulfides Li_2S_x ($6 < x \leq 8$) by reacting with lithium ions.[17] The reduced polysulfide species easily dissolve into the liquid electrolyte, which increases the viscosity of the electrolyte and slows down lithium-ion transport. As a result, the diffusion overpotential and the corresponding impedance raise cause a concentration polarization. This leads to a voltage drop between 2.3 and 2.1 V.[19] In the sloping region, high-order polysulfides convert to Li_2S_4. The upper plateau and sloping regions belong to a solid-liquid phase reaction.[15, 17, 19] In the lower plateau region at ~ 2.1 V, polysulfide intermediates convert to the end-discharge product Li_2S with the incorporation of additional lithium, which is ascribed to be a slow solid-state reaction. Two discharge plateaus at 2.3 V and 2.1 V are usually observed in lithium-sulfur cells with ether-based liquid electrolytes, which represent the conversion of S_8 to Li_2S_4 and Li_2S_4 to Li_2S.[17]

The reversible conversion reaction shows a continuous flat lower plateau and upper plateau during charge. The two charge plateaus correspond to the oxidization reactions from Li_2S to S_8 via the formation of various polysulfide intermediates.[15] At the end of charge, crystalline sulfur has been detected via an *in operando* X-ray diffraction analysis.[20]

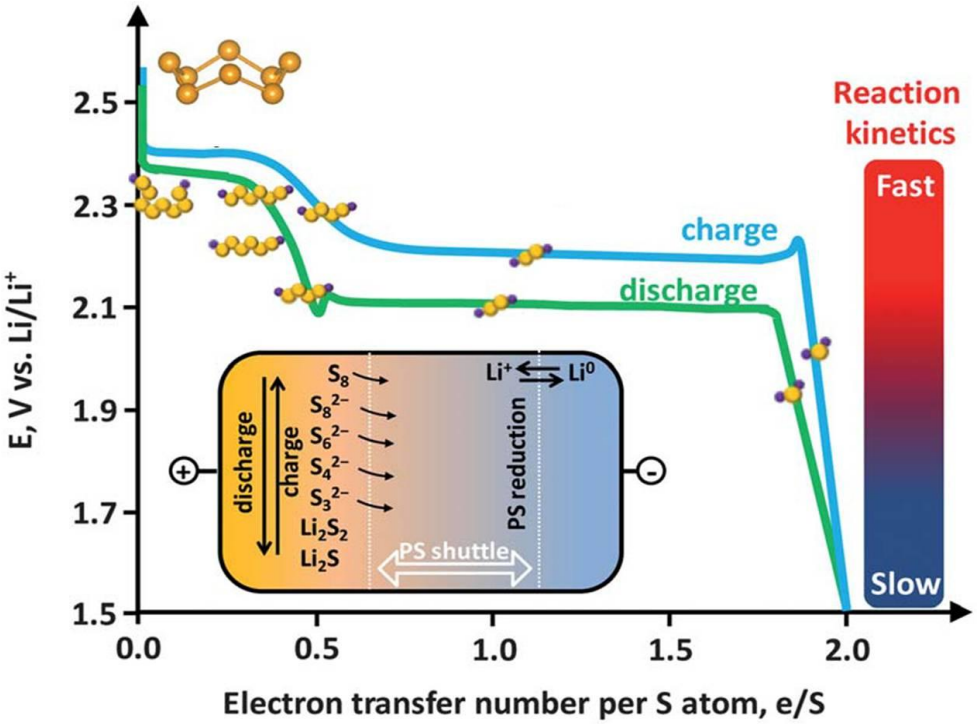

Figure 1.2: Typical discharge and charge processes of an ideal lithium-sulfur cell. Reprinted from ref. 15.

1.3 CHALLENGES OF LITHIUM-SULFUR BATTERIES

However, in the real cell, it is hard for the common lithium-sulfur cells to effectively and reversibly go through the above electrochemical conversion reactions. There are many scientific and technological challenges facing the lithium-sulfur technology, either with the materials or with the system.[11, 21, 22] First of all, the insulating nature of the active material limits the electrochemical utilization. Second, the soluble

polysulfide intermediates easily dissolve into the liquid electrolyte, resulting in polysulfide diffusion and a shuttle behavior. Third, the diffusing polysulfides are plated onto electrodes and convert to nonconductive agglomeration, passivating the electrodes. Forth, the chemical conversion reactions involve a huge volume change of the active material along with structural and morphological changes of the sulfur cathode, resulting in unstable electrochemical contact within the sulfur electrodes.[21, 23, 24] Thus, the conventional lithium-sulfur cell electrodes shown in Figure 1.3 illustrate these serious side reactions. These challenges are described in details in the following sections.

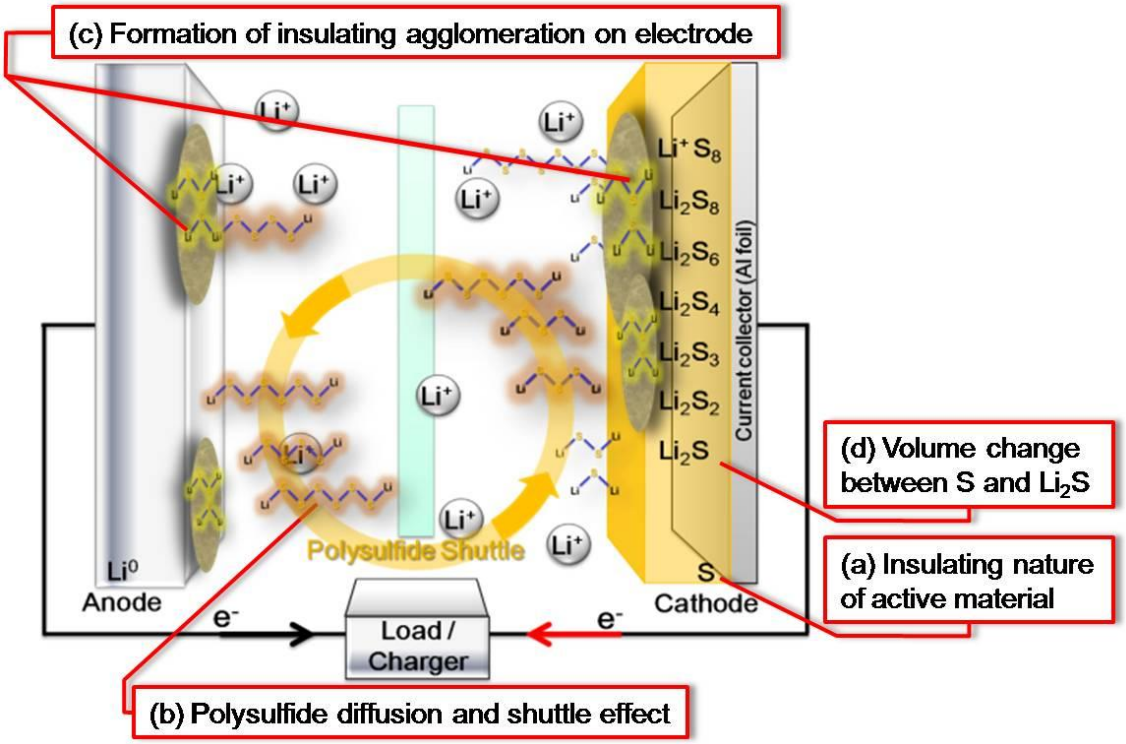

Figure 1.3: Schematic illustration of the challenges of lithium-sulfur batteries (clockwise): (a) insulating nature of the active material, (b) polysulfide diffusion and shuttle effect, (c) nonconductive agglomeration on the electrodes, and (d) huge volume change.

1.3.1 Insulating nature

Sulfur (electronic resistivity: 2×10^{29} ohm cm) and its end-discharge product Li_2S (electronic resistivity: 10^{14} ohm cm) have poor ionic and electronic conductivities, which make them hard to accept lithium ions from the electrolyte and electrons from the current collector.[23, 24] The high cathode resistance leads to a large polarization, which limits the electrochemical utilization and causes low specific capacity (less than 800 mA h g^{-1}; for a pure sulfur cathode with sulfur content of 70 wt. % and sulfur loading of 1.0 mg cm^{-2}). This intrinsic deficiency has been almost conquered by the incorporation of conductive additives to form a sulfur-based nanocomposite. This ensures smooth electron transport between the interfaces of conductor/active material.[11, 15]

1.3.2 Dissolved polysulfide diffusion

Lithium polysulfides (Li_2S_x, $x = 4 - 8$) are intermediate redox species derived from the reduction of cyclo-sulfur, which are highly soluble in the organic electrolyte.[25, 26] The polysulfide dissolution is beneficial to enhance active-material utilization. First, as polysulfides continuously dissolve into the electrolyte, the inner core of the bulk sulfur will get exposed to the electrolyte, resulting in an enhancement in the active-material utilization. Second, the dissolved polysulfides freely rearrange to electrochemically favorable positions in the cathode region of the cell.[27] The development of Li-polysulfide catholyte cells with a custom cathode configuration is the model that makes the best of the materials chemistry of polysulfide dissolution.[28, 29]

However, the dissolution behavior brings numerous drawbacks to lithium-sulfur cells with a conventional cell configuration.[26, 27] According to the materials chemistry principle, during cell discharge, the dissolved polysulfide anions will diffuse out from the cathode side of the cell, penetrate through the separator, and migrate toward the anode side of the cell. The polysulfide migration is driven by (i) chemical potential and (ii) polysulfide concentration differences between the cathode and the anode.[12, 23] The diffusion of the dissolved polysulfide anions causes dynamic instability during cell cycling. The unfavorable migration of the dissolved polysulfides leads to irreversible loss

of the active material from the sulfur cathode and even the collapse of the cathode structure, which causes capacity fade during cycling.[30, 31]

1.3.3 Shuttle effect

The shuttle effect is derived from the free migration of the dissolved polysulfides between the cathode and the anode. Higher-order polysulfides (Li_2S_x, $6 < x \leq 8$) are generated during the upper-charge-plateau region at the sulfur cathode side. The higher-order polysulfides diffuse to the anode side and react with the lithium metal to create lower-order polysulfides (Li_2S_x, $2 < x \leq 6$). Then, the lower-order polysulfides diffuse back to the cathode side and react with sulfur to form higher-order polysulfides. This repeated redox reactions create the polysulfide shuttle effect, which results in low Coulombic efficiency and anode corrosion. Severe shuttle behavior leads to poor charge efficiency and an irreversible oxidation of the active material.[32-34] Recently, the addition of $LiNO_3$ as a co-slat into the blank electrolyte has been shown to effectively protect the lithium-metal anode by forming a protective passivation layer, suppressing the shuttle effect.[35-37]

1.3.4 Self-discharge

The diffusion of the dissolved polysulfide anions also causes static instability during cell resting, which is the self-discharge.[33, 38] When the battery is resting, the self-discharge occurs because the active sulfur in the cathode reacts with the lithium ions in the electrolyte and produces soluble lithium polysulfides. As the cell storage time increases, dissolved polysulfides gradually migrate to the anode due to the concentration gradient and then react with lithium metal, followed by conversion into Li_2S. These result in a decrease in the OCV and discharge capacity.[38-40]

1.3.5 Nonconductive agglomeration

The nonconductive agglomeration easily forms thick and insulating layers onto the electrodes after cycling. The electrochemically inactive layer mainly consists of Li_2S_2 and Li_2S mixtures when cells are discharged or rested. This inactive region plated on the

electrode surface deteriorates the cyclability and electrochemical performance during cell cycling. On the other hand, the nonconductive agglomeration results in OCV drop from 2.4 to 2.1 V and irreversible capacity fade during cell resting. In addition, as the cell cycle number or storage time increases, the nonconductive agglomeration blocks the electron and ion transport in the electrode, causing cell failure.[41, 42]

1.3.6 Volume change

The hung volume expansion during discharge is another inevitable problem for lithium-sulfur cells. On account of the different densities of sulfur (α phase, 2.07 g cm^{-3}) and Li_2S (1.66 g cm^{-3}), sulfur cathode experiences a volume change of 80 %.[43-45] Severe volume expansion of the active material during the electrochemical conversion reaction may pulverize the solid-state Li_2S, cause huge crack formation, and break the electrical contact between the insulating active material and the conductive substrate or the current collector. This creates isolated sulfur in the cathode during cycling, resulting in inactive regions in the cell.

1.3.7 Morphology reconstruction

The electrochemical conversion reaction of lithium-sulfur cells involves a solid-liquid-solid phase transition, polysulfide diffusion, and huge volume changes. This indicates that the morphology of sulfur cathode may also change during cycling. The uneven redistribution of the active material in the cathode may break the link between the active material and the conductive additive that are bonded by binders. The isolated active material and collapsed cathode cause inactive regions in cathode and further deteriorate the cathode architecture.

1.4 DESIGN CONSIDERATION

The lithium-sulfur battery, fabricated with a high-capacity sulfur cathode, is the most promising high-energy-density system. However, several scientific and technological challenges result from the sulfur cathode. The conventional cathode configuration that is borrowed from Li-ion cells contains the active material (pristine

sulfur) mixed with conductive carbon and binder.[46, 47] However, with a pure sulfur cathode prepared with sulfur-carbon-binder mixtures, it is difficult to effectively utilize and stabilize the active material. Clusters or agglomerates of insulating sulfur particles form inactive cores within the sulfur-carbon-binder mixtures, which limits the redox reaction. In addition, given the fact that lithium-sulfur batteries involve conversion reactions, unlike the insertion reactions in the conventional Li-ion batteries, innovations in cell configurations should be considered and could become attractive solutions to store the active material and confine the migrating polysulfides, as shown in Figure 1.4. Moreover, these novel cell configurations can be coupled with a pure sulfur cathode with high sulfur loading and high sulfur content. However, caution should be exercised that the weight/volume of these alternative or novel cell components does not sacrifice the overall energy density.

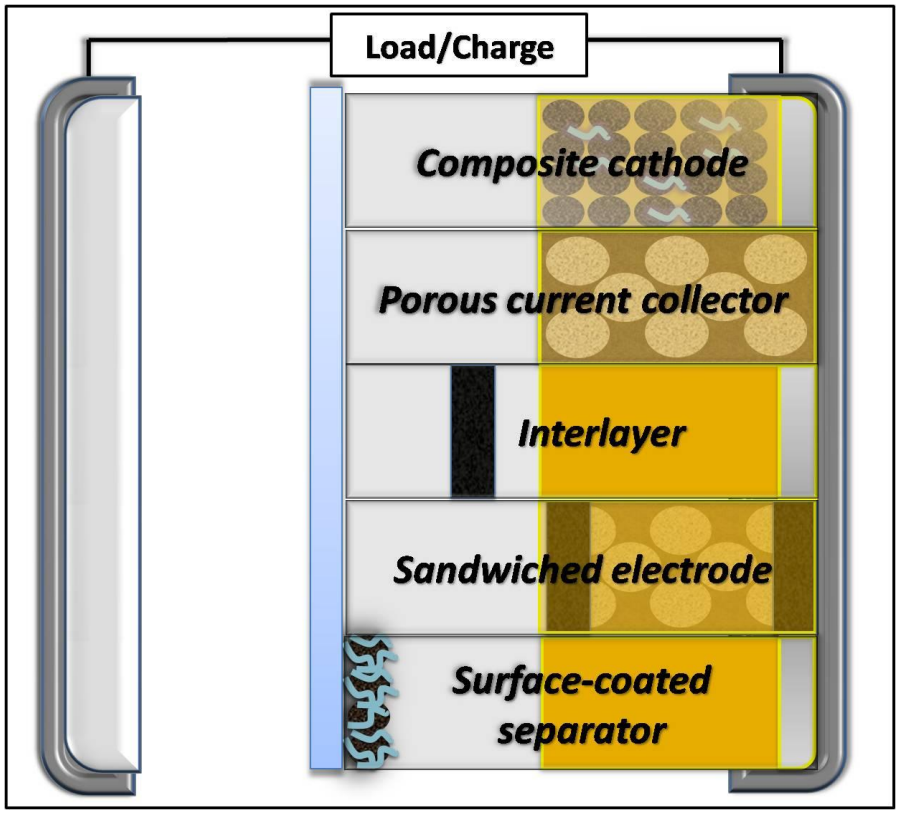

Figure 1.4: Schematic illustration of custom cathode configurations designed for high-performance lithium-sulfur cell development.

1.5 CATHODE MATERIALS

To solve the scientific challenges that have plagued the commercial development of lithium-sulfur batteries, modification of the physical/chemical properties and the morphology of sulfur was the first step in the development of lithium-sulfur technology. Pristine sulfur in the cathode mixtures (the sulfur-carbon-binder mixtures) is, first, replaced by various sulfur-porous-carbon nanocomposites or sulfur-conductive-polymer nanocomposites to increase the cathode conductivity and suppress polysulfide migration.[48-51] However, the addition of extra conductive additives limits the sulfur content in the nanocomposite, which reduces the sulfur content in the composite cathode. The nanocomposite preparation also increases the complexity for widespread use. Therefore, a balance between sulfur loading and battery performance is required.

A high-performance lithium-sulfur cell relies heavily on the optimization within the cathode configuration. A practical cathode design should include high cathode conductivity, outstanding polysulfide-trapping capability, and a robust electrode structure. The most promising approach is the encapsulation of sulfur within conductive additives to form a sulfur-based composite cathode. Porous carbon substrates and conductive polymers are essential to enhance the redox accessibility of the insulating sulfur (conductivity of 5×10^{-30} S cm^{-1}). The high surface area and porosity of porous carbon materials, as well as the chemical gradient created by polymer coatings, could satisfy the critical requirements of good electronic and ionic conductivities and retention of polysulfides within sulfur-based composite cathodes. Moreover, a porous carbon substrate or a soft polymer can buffer the huge volume changes of the sequestered active material.[21, 52] Surface functionalization techniques further modify the morphologies of the nanocomposites to limit the diffusion of polysulfide out of the nanocomposites or block the migrating polysulfides.[12, 15]

1.5.1 Sulfur-carbon nanocomposites

Conductive carbon acts well as an effective electronic conductor to enhance the utilization of the insulating sulfur in sulfur-carbon-binder mixtures. Its loose clusters serve as a porous framework to contain the redox products.[46] However, poor links between the active material and the carbon matrix, as well as the unstable architecture of the carbon clusters, results in rapid capacity fade and low efficiency during the initial several cycles. This results in unstable and poor cyclability with a cycle life of less than 50 cycles. Recent progress on sulfur-carbon composite cathodes has minimized these problems. Sulfur-carbon nanocomposites benefit from their hierarchical micro-/meso-porous structural design, satisfying the criteria for encapsulating sulfur into porous substrates.[15, 23, 53, 54]

1.5.1.1 Sulfur-carbon nanocomposite preparation: heat-treatment methods

The most efficient heat-treatment method was presented by Nazar's group in 2009, which lighted up a life for sulfur-carbon composite cathodes. Ji *et al.* first presented sulfur-mesoporous-carbon nanocomposites synthesized by a melt-diffusion process, as shown in Figure 1.5.[55] The melt-diffusion process heated the sulfur to 155 ℃. At this temperature, the liquid sulfur has the lowest viscosity. The CMK-3 ordered mesoporous carbon, synthesized by using the SBA-15 silica template, has a high conductivity, uniform and narrow mesopores (pore size: 3 nm), a large pore volume (2.1 $cm^3\ g^{-1}$), and an interconnected porous structure. The high porosity and continuous porous structure allow the liquid sulfur to achieve excellent active material encapsulation in the mesoporous space and hence, for the first time, exhibited a high initial discharge capacity of 1320 mA h g^{-1} with a good efficiency of 99.94 % in lithium-sulfur batteries.[52, 55]

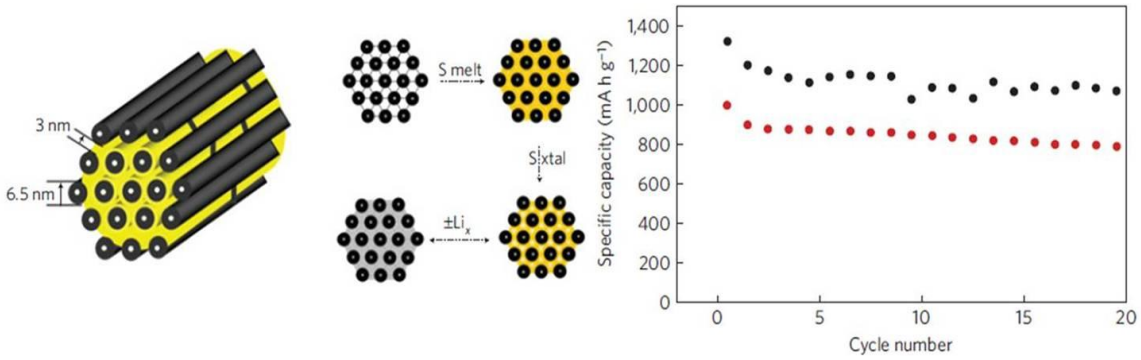

Figure 1.5: Schematic model and cell performance of the sulfur-mesoporous-carbon nanocomposite. Reprinted from ref. 55.

On the other hand, Archer's group introduced carbon capsules for sealing the active material by way of a sulfur-vaporization method, which improved both cyclability and electrochemical utilization. Jayaprakash *et al.* utilized the sulfur-vaporization route to infuse gaseous sulfur into porous hollow carbon with a mesoporous shell, as shown in Figure 1.6.[56] The utilization of sulfur vapor leads to molecular-level contact between the insulating active material and the conductive carbon shell. The use of mesoporous hollow carbon capsules as the active-material host encapsulates and sequesters up to 70 wt. % active material in their interior and porous shell. As a reference, this sulfur content refers to the content of active material in the nanocomposite. The carbon protection shell minimizes the polysulfide dissolution and the shuttle effect. Moreover, the mesoporous shell allows access of electrolyte and preserves fast lithium-ion transport. Therefore, this scalable procedure produces efficient uptake of elemental sulfur with effective ion and electron transport for achieving outstanding cyclability. These porous hollow carbon@sulfur nanocomposites provided a long cycle life of 100 cycles and a high reversible capacity approaching 1000 mA h g^{-1} at a high cycling rate.[23, 56]

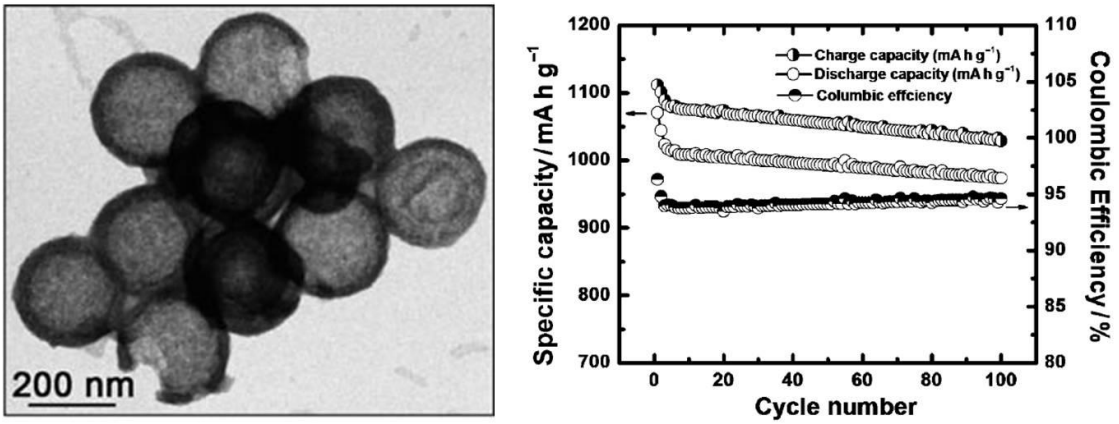

Figure 1.6: SEM inspection and cell performance of the porous hollow carbon@sulfur nanocomposite. Reprinted from ref. 56.

To sum up, the merit of the heat-treatment method (melt-diffusion or sulfur-vaporization processes) aims at impregnating porous carbon matrices with the active material during heat treatment. These processes encapsulate the melting or vaporizing sulfur into the narrow porous spaces of the carbon host, resulting in a molecular-level contact among the encapsulated active material and the conductive carbon host, which ensures the resulting nanocomposites to have a high initial discharge capacity and stable cyclability. So, the heat treatment route has dominated the preparation processes for synthesizing sulfur-carbon nanocomposites. The progress has developed lots of derived synthesis routes including the two-step heat treatment (sulfur melting and then vaporizing),[57-59] sulfur melting diffusion method,[13, 55, 60-68] sulfur vaporizing method,[56, 69, 70] and chemical-deposition/thermal-treatment process.[71]

1.5.1.2 Sulfur-carbon nanocomposite preparation: chemical-synthesis methods

In addition to the heat-treatment procedures, chemical-synthesis approach is another favorable process for synthesizing sulfur-carbon nanocomposites and creating a strong binding between sulfur and the carbon substrate. By going through a heterogeneous nucleation, the precipitated sulfur is strongly held by or absorbed into the

carbon substrate. Currently, the attractive solution-based synthesis routes are supported by CS_2, Na_2S, and water-based solutions.

First, CS_2 can be utilized as the matrix solution to channel the dissolved sulfur into the hierarchical micro-/meso-pores of the porous carbon substrate (*e.g.*, activated microporous carbon (MPC)[72] and carbon nanotubes (CNTs)[73]) and to fill the micro-/meso-pores with the sulfur-containing solution, resulting in an excellent sulfur encapsulation within the porous carbon and thereby achieving a high initial discharge capacity. The improved electrochemical performance indicates that the CS_2-based solution may be an attractive method for preparing the sulfur-carbon nanocomposites.[72, 73] However, the application of the toxic CS_2 may cancel the advantage from the environmentally friendly sulfur. On the other hand, the Na_2S solution method starts by adding Na_2S to distilled water and then follows the chemical deposition reaction ($S_x^{2-} + 2H^+ \rightarrow (x-1)S\downarrow + H_2S$) in an aqueous solution. The sulfur nucleates on the dispersed carbon substrates and accomplishes a strong incorporation into the porous carbon host. The molecular sulfur incorporated into the conductive carbon eliminates the high cathode resistance and provides a high active material utilization of above 70 %. However, the toxicity concern still exists with the byproduct H_2S.[60, 74]

In comparison with the two methods described above, a water-based solution synthesis route was reported as a facile and nontoxic manufacturing process for synthesizing core-shell structured nanocomposites at room temperature.[75-77] The strong chemical bonding between the sulfur nucleates and the dispersed carbon allowed this approach to be applicable to any carbon substrates. Most importantly, the water-based synthesis route avoids use of toxic raw materials and generation of toxic products. However, the formation of the sulfur core in the core-shell-structured sulfur-carbon nanocomposites may cause a nonconductive core in the agglomerates of the active material.[75] On the other hand, the formation of nonconductive sulfur shells on the core-shell-structured carbon-sulfur nanocomposites may limit the rate capability and the electrochemical utilization.[76] To prevent sulfur aggregation, Ji *et al.* reported an

method by using graphene oxide as a sulfur immobilizer.[71] Graphene oxide has strong reactive functional groups on its surface to bond the nanosized sulfur particles (tens of nanometers).[78] The nanocomposites were prepared by a two-step chemical deposition and thermal treatment process. The resulting graphene oxide-sulfur nanocomposites had a thin and uniform sulfur coating on the conductive graphene oxide sheet to avoid the aggregation of large sulfur particles. The nanocomposite exhibited good electrochemical reversibility and capacity stability.

1.5.1.3 Sulfur-carbon nanocomposite preparation: porous carbon hosts

With the understanding of the synthesis process of sulfur-carbon composites, it is instructive to look at how various carbon substrates influence cell performance.[15] From the very beginning, carbon black that has high electrical conductivity was used for preparing the sulfur-carbon-binder mixtures to decrease the cathode resistance.[47] Soon after, the active carbon that has a high surface area and abundant micropores was used to absorb the active material and to limit polysulfide dissolution.[49, 50] Now, porous and conductive carbons have been widely applied in sulfur-carbon nanocomposites due to their porous structure and electrical conductivity. These are essential criteria for simultaneously immobilizing the active material and enhancing the cathode conductivity. The cathode conductivity is increased by two morphological routes: (i) formation of a conductive carbon network, *e.g.*, carbon nanoparticle clusters,[47, 49, 50, 75, 76] and (ii) intimate connection between the conductive framework and the insulating sulfur.[55-57, 66, 72] The engineered porous carbon and macroporous network not only promote retention of sulfur but also enhance lithium-ion and electrolyte transport in the composites.[15, 23]

The categories of porous carbon can be divided into three major types by their nanopore size (D, diameter). Each type of porous carbon possesses unique morphological advantages.

(i) Microporous carbon (micropores with D < 2 nm): Microporous carbon has been demonstrated as the ideal container for accommodating and immobilizing the active material.[23, 57, 72]

(ii) Mesoporous carbon (mesopores with 2 nm < D < 50 nm): Mesoporous carbon can enhance sulfur encapsulation as the designed pore size is small or can improve lithium ion and electrolyte transport as well as raise the tolerance toward high sulfur loading as the pore size is large.[55, 61, 72, 79]

(iii) Macroporous carbon (macropores with D > 50 nm): Macroporous carbon is usually derived from an interwoven network of CNTs or carbon nanofibers (CNFs) and is able to ensure excellent electrolyte immersion or suppress polysulfide migration due to its high electrolyte absorbability.[48, 51] In addition, the application of a sp^2 carbon framework greatly improves the mechanical strength and electrical conductivity.[23, 80, 81]

To develop high-capacity sulfur-carbon composite cathodes, the combination of a highly conductive carbon network with a porous carbon nanostructure is a novel method for a composited conductive/porous carbon host to effectively utilize the immobilized sulfur for lithium-sulfur batteries. In a composite conductive/porous carbon host, the conductive carbon materials (CNFs, CNTs, and graphene) effectively raise the redox capability of the encapsulated active material that is protected by the nanoporous carbon substrate.[70, 82-85] On the other hand, heteroatom doping chemically improves the reactivity and facilitate chemical sulfur-adsorption to the chemically stable carbon host.[80, 86-90] To achieve practical applications, an increase in total accessible pore volume will be essential to enhance sulfur loading and sulfur content.[24, 61] After impregnating sulfur into open pores, voids are necessary to ensure good electrolyte impregnation and fast lithium-ion transport to achieve a high-rate cell performance. These extra voids can also buffer volume changes of the active material. The graphitization level and the mechanical strength of the carbon hosts dominate the improvements in, respectively, cathode conductivity and the integrity of the nanocomposite structure.[23, 60, 61, 72]

1.5.2. Sulfur-polymer nanocomposites

Polymers are another type of frequently used additive in rechargeable lithium-sulfur batteries, especially the conductive polymer coating on sulfur particles.

Conductive polymers can be tailored or used to modify the surface of cathodes to facilitate ion and charge transport.[12, 23] The corresponding synthesis strategies aim at confining sulfur and its redox products in nanocomposites with controlled morphology. Core-shell structures, in which the insulating sulfur is the core and the conductive polymer is the shell, facilitate ion and electron transport and provide more freedom for compositional changes.

Wang *et al*. introduced the first sulfur-conductive polymer nanocomposites synthesized with polyacrylonitrile (PAN) and sublimed sulfur at ~ 300 ℃, as shown in Figure 1.7.[91] Following this, extensive efforts have targeted the synthesis of sulfur-conductive-polymer nanocomposites with various conductive polymers and optimized core-shell structures.[23, 54] For example, various core-shell structured sulfur-polypyrrole nanocomposites with unique microstructure and morphologies have been used in composite cathodes.[92-94] The conductive-polymer coating functions as a stable interface between the liquid electrolyte and polysulfide species, allowing the accessibility of ions and charge, but sequestering the diffusion of the active material. In addition to the core-shell structure, conductive polymers have recently been used to mimic the structure of CNTs and CNFs or been modified with additional functionalities. Electropositive groups on the sulfur-polymer nanocomposites attract polysulfides through electrostatic forces, reducing the loss of active material during cell cycling and proving long-term cyclability.[95, 96] Accordingly, sulfur-conductive-polymer nanocomposites containing dispersed sulfur and conductive nanoparticles could become a viable approach to chemically overcome some of the persistent problems associated with rechargeable lithium-sulfur batteries. [23, 93]

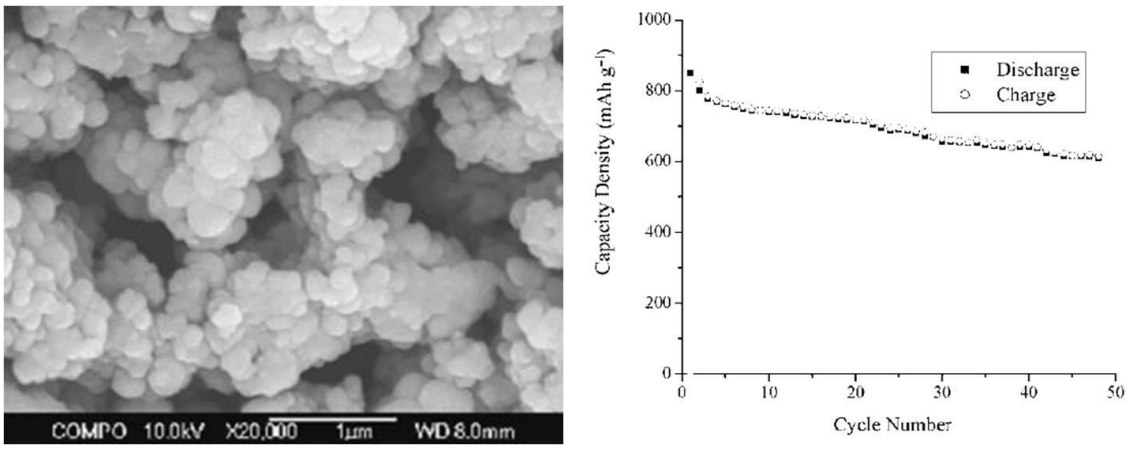

Figure 1.7: SEM inspection and cell performance of the conductive polymer-sulfur nanocomposite. Reprinted from ref. 91.

1.5.3. Polymer-supported sulfur-carbon nanocomposites

Recent advancements in nanoscience and nanotechnology have offered exciting opportunities for the development of a mixed soft-polymer coating with conductive/porous carbon substrate for sulfur-based nanocomposites. Various polymer-coated sulfur-carbon nanocomposites that can effectively encapsulate the redox products and maintain a robust but porous electrode structure have been reported. These advantages are essential for improving the electrochemical performance.[15, 52]

As a pioneer in high-performance composite cathodes, Ji *et al.* first demonstrated enhanced discharge capacity and stability of a polyethylene glycol (PEG)-coated sulfur-CMK-3 nanocomposite.[55] These PEG-coated sulfur-carbon nanocomposites physically contain the active material in their ordered CMK-3 mesoporous carbon substrates and further chemically retard polysulfide diffusion by creating a chemical gradient in the nanocomposites. In addition to improving the electrochemical reversibility, the soft-polymer coating can tolerate huge volume changes from the trapped active material.

Follow-up studies have extended to various polymer-supported sulfur-carbon composites with unique chemical functions and porous carbon structures. For example,

Wang *et al.* reported PEG-wrapped graphene-sulfur nanocomposites. The synthesized sub-micrometer sulfur particles are coated with PEG surfactants and graphene sheets, which function as a chemical and physical protection coating for trapping polysulfides. The soft PEG coating accommodates the volume change of the wrapped sulfur particles during cell cycling. The conductive graphene coating offers the encapsulated sulfur particles a robust and electrically conductive shell.[97] Wu *et al.* presented polyaniline-coated sulfur-multiwall carbon nanotube (MWCNT) nanocomposites. The nanocomposites possess a conductive MWCNT network to improve the cathode conductivity. The porous polyaniline shell reduces the lithium-ion transfer pathway and prevents the dissolution of the active material.[98] In view of the results of the intensive research in this area, the integration of conductive and porous substrates with functional surface coatings shows even better electrochemical performance than the use of these individual approaches.[97-104] Based on the physical adsorption/absorption or chemical anchoring/trapping capability, these nanocomposites in different contexts suppress the polysulfide dissolution and diffusion issue.[103]

1.5.4. Smaller sulfur molecules

The developments regarding microporous carbon synthesis and sulfur-encapsulation techniques have opened another useful research direction to limit the rapid capacity fading by avoiding the formation of soluble polysulfide intermediates (Li_2S_x, $x = 4 – 8$). The concept is different from the conventional methods that depend on chemical sulfur-carbon/polymer bonding or physical polysulfide-absorption/adsorption capacity of the porous hosts. By using smaller sulfur molecules ($S_{2–4}$), the aim is to confine them in the narrow space of a conductive microporous carbon matrix as the starting active material. As a result, this approach may theoretically eliminate the formation of soluble polysulfides and improve the close contact between $S_{2–4}$ and the conductive carbon host.[13, 23]

Zhang *et al*. prepared sulfur-carbon spherical composites and encapsulated sulfur into the carbon micropores. An electrochemical stability up to 500 cycles and a superior

high-rate performance were obtained, as shown in Figure 1.8.[57] Xin *et al.* encapsulated smaller sulfur molecules into a core/porous-sheath matrix. The encapsulated metastable small sulfur molecules were tightly held in the confined nanospace of the conductive MPC matrix (pore size of 0.5 nm). This limited the formation of cyclo-S_8 molecules with the dimensions of 0.7 nm, which avoids the unfavorable transformation between cyclo-S_8 and S_4^{2-}. Electrochemical analyses provide convincing evidence that the small sulfur molecules show a single discharge plateau at 1.9 V (the lower-discharge plateau) and a single reduction peak in the cyclic voltammetry curves. This provides electrochemical evidence that the discharge/charge process effectively avoids polysulfide formation and hence limits the loss of active material.[63] On the other hand, by way of tuning the pore structure of a hierarchical micro-/mesoporous carbon, the enhanced polysulfide retention and fast electrochemical kinetics show a long lifespan of 800 cycles with a reversible capacity of 600 mA h g^{-1} at a 1C rate.[62]

A series of research concludes that the concept of using chain-like small sulfur molecules is a promising approach to improve cell performance. The small sulfur molecules are confined within the limited nanospace of the carbon micropores. The limited nanospace and the strong interaction between the active material and carbon substrate avoid the formation of unfavorable soluble polysulfides and subsequent polysulfide dissolution and diffusion. Close contact with the conductive carbon host further improves the electrochemical activity of the active material. Thus, an effective cooperation between the smaller sulfur molecule and the MPC may overcome the severe polysulfide diffusion problem in lithium-sulfur cells. The use of micro-/mesoporous carbon has been shown to facilitate electron and lithium-ion transference, as well as increase the loading of smaller sulfur molecules to above 50 wt. %. As a reference, this sulfur content refers to the content of active material in the nanocomposite.[13, 23]

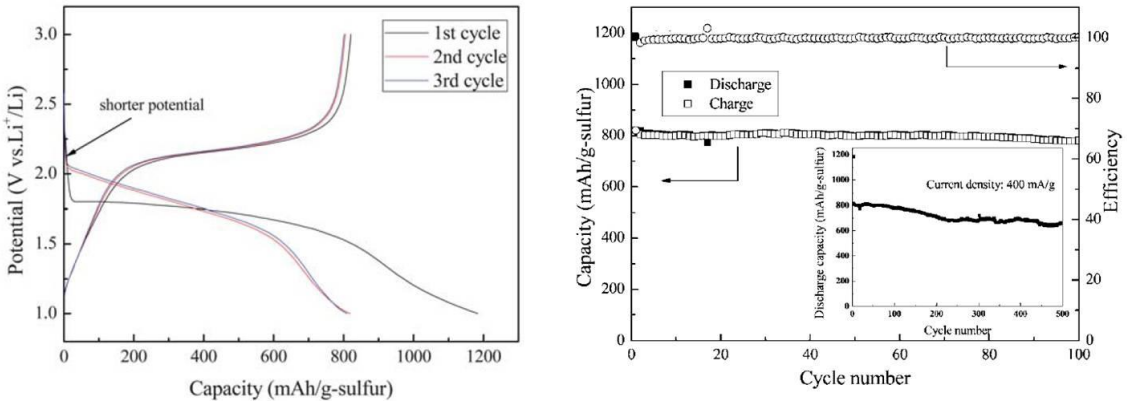

Figure 1.8. Electrochemical characteristic and cell performance of the low-molecular elemental sulfur/microporous carbon nanocomposite. Reprinted from ref. 57.

1.5.5. Li_2S cathodes

Lithium sulfide (Li_2S), the final discharge product of sulfur, is another promising cathode material for high-energy lithium-sulfur battery systems because of its high theoretical capacity of 1166 mA h g^{-1}.[105-108] Moreover, Li_2S is a prelithiated active material. As a result, the lithium-metal anode can be replaced by a high-capacity tin or silicon anode. The use of Sn- or Si-Li_2S cells mitigates safety concerns resulting from lithium metal and its dendrites.[7, 106, 109, 110] However, the poor electronic and ionic conductivities of Li_2S cause the slow oxidation of solid-state bulk Li_2S, which leads to large energy barrier (overpotential) when charging the Li_2S cathode, as shown in Figure 1.9.[111] Also, Li_2S cathodes still suffer from polysulfide diffusion. As a result, Li_2S-carbon nanocomposites with a uniform Li_2S distribution in the carbon host were utilized in the cathode to increase the conductivity and retard polysulfide diffusion.[107-109, 112-114] On the other hand, surface functional groups,[115-117] an ionic conductive material,[118] and redox mediators[111, 119] were applied to modify the chemical/physical properties of the cathode and the electrolyte. The progress on Li_2S cathode development may attract more efforts to develop the practical non-Li anode/Li_2S battery.

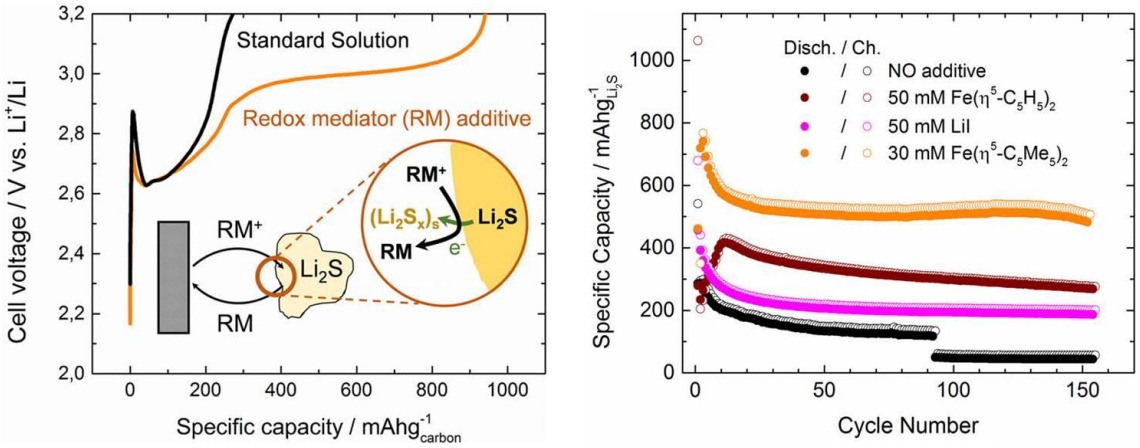

Figure 1.9: Electrochemical characteristic and cell performance of the Li_2S cathode with redox mediators. Reprinted from ref. 111.

1.5.6. Selenium cathodes

Selenium (Se), an element in the same group in the periodic table as sulfur, is another prospective candidate for the active material. Se has a high theoretical capacity of 675 mA h g^{-1} and a high theoretical volumetric capacity density of 3253 mA h cm^{-3}, which is comparable to that of S (3467 mA h cm^{-3}).[120] Se containing a d-electron possesses much lower electronic resistivity of 1×10^5 ohm cm in compared with that of sulfur. This indicates that Se cathodes could theoretically have higher electrochemical utilization and faster redox kinetics.[120-122]

Abouimrane *et al.* were the pioneers to use Se and Se_xS_y-based cathodes in both lithium and sodium cells. Se cathodes exhibit better electrochemical activity and limited shuttle effect compared with sulfur cathodes. In addition, Li-Se cells deliver a high output voltage of up to 4.6 V, demonstrating an attractive high volumetric energy density, as shown in Figure 1.10.[121] Follow-up studies reported that Se-carbon nanocomposites greatly enhance the discharge capacity by avoiding the formation of bulk Se particles and restrain the polyselenides by applying porous carbon substrates.[122] A Se@microporous carbon polyhedral extended the lifespan to 3000 cycles.[123] In short-term studies, Se-based nanocomposites have already achieved many advances and breakthroughs.[124-126]

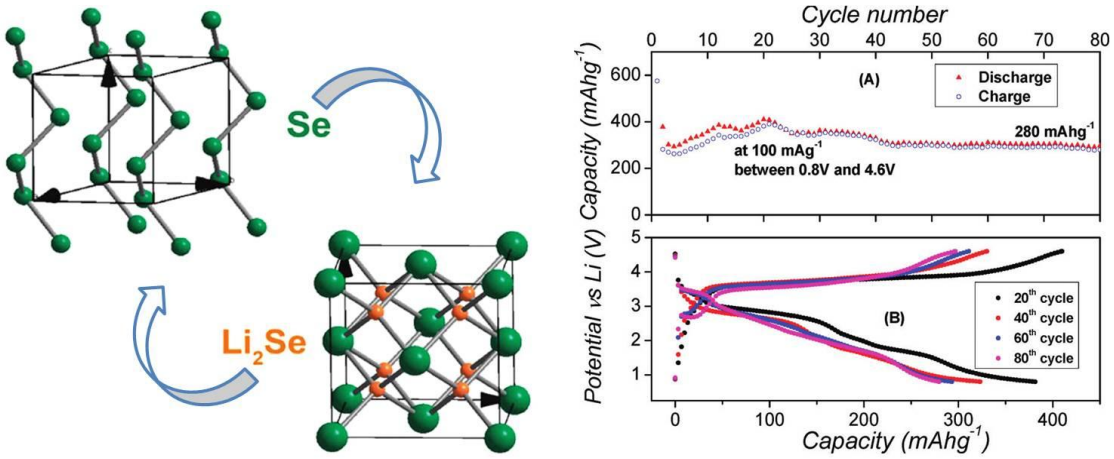

Figure 1.10: Schematic model and cell performance of the Li-Se cell. Reprinted from ref. 121.

1.5.7. Polysulfide catholyte

Polysulfides were the first active material that was used in lithium-sulfur batteries. In 1979, Rauh *et al.* did the pioneer research on the first lithium-dissolved polysulfide cell. The cell utilized Li_2S_n polysulfide catholyte with organic THF electrolyte and $LiAsF_6$ as the supporting electrolyte. The polysulfide catholyte provided a high utilization of sulfur in the initial discharge. This is because the soluble polysulfides have higher reactivity compared to solid sulfur particles, resulting in a high capacity of up to 1.83 electrons per sulfur. At 50 ℃, the electrochemical utilization almost reaches 100 %.[26] The cyclability of the lithium-dissolved polysulfide cells was further enhanced by adding co-salt additives,[127] applying alternative electrolyte systems,[127, 128] or employing with novel cell configurations, as shown in Figure 1.11.[18, 28, 29] According to its physical characteristics, the dissolved polysulfide catholyte could be utilized in redox flow batteries. By way of controlling the cutoff voltages, a half-flow-mode lithium-sulfur battery allows soluble polysulfides to be present in the catholyte, which could lead to long cycle life.[129]

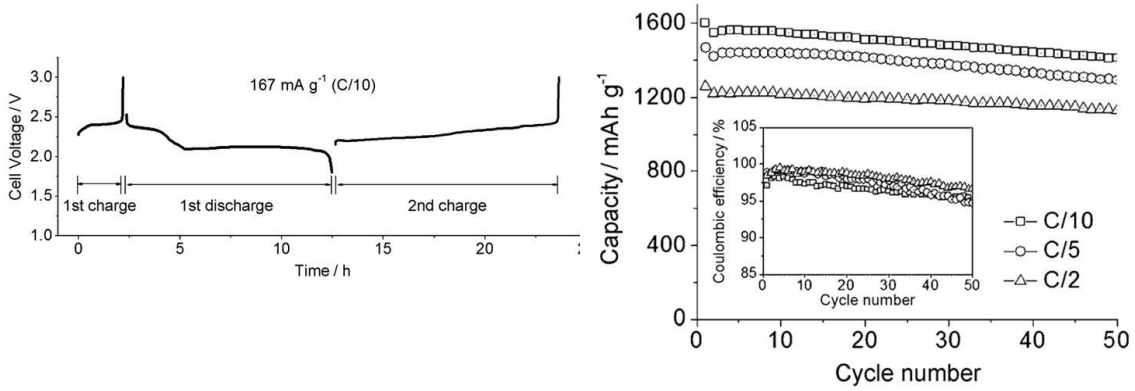

Figure 1.11: Electrochemical characteristic and cell performance of the lithium-dissolved polysulfide cell. Reprinted from ref. 29.

1.6 CURRENT COLLECTORS

The conventional current collector used in lithium-sulfur battery research is a 2 dimensional (2D) aluminum foil, which is just a flat supporter in the cathode. Moreover, the aluminum foil may encounter oxidation and corrosion during cycling, causing the sulfur to lose electrical contact with the current collector and increasing the internal resistance of the battery.[11, 22, 130] Therefore, appropriate, alternative current collectors are of great interest for long-term cycle stability and high energy density. New cell configuration designs that uses a 3D conductive/porous-metal current collector or a free-standing composite electrodes have demonstrated improvements with regard to cell cyclability for various rechargeable battery systems (*e.g.*, nickel/metal hydride batteries,[131] $LiFePO_4$ cathodes, [132, 133] solar-charged textile batteries,[134] and lithium-sulfur batteries[81, 135]).

1.6.1 Porous current collectors

In the lithium-sulfur battery, the conductive/porous matrix of the porous current collector not only works as an inner conductive framework to guarantee fast electron transport, but also as an active material container to stabilize the active material mixtures in its conductive skeleton. This design enables superior electrochemical stability of the

sulfur cathodes with a capacity retention rate of 92 % after 50 cycles.[135] Ballauff and co-workers conducted quantitative analysis on the capacity fading of lithium-sulfur batteries with different cell configurations.[136] According to the capacity-fading model, they concluded that porous-metal current collectors have positive effects on the long-term cycle stability of batteries. The improved cycle stability may result from the stronger interaction between the metal substrates and sulfur species.[136, 137]

1.6.2 Current-collector free electrodes

In addition to modifying the conventional 2D current collector, another new approach is to employ a sulfur-based nanocomposite as a current-collector free electrode, such as an activated carbon-fiber cloth,[138] a vertically aligned CNT electrode,[64, 139, 140] a free-standing graphene,[141-144] and a self-weaving MWCNT.[81, 144] The direct application of the composite electrode not only eliminates the bulk resistance from the added binder but also decreases the net weight of the electrode.[81, 138, 139] As a reference, the weight of the conventional aluminum foil current collector accounts for about 15 – 20 wt. % of a battery.[11, 22] Progress on free-standing composite cathode is focused on the development of highly conductive substrates with a light weight and a high porosity. The most essential requirement is that the applied conductive and porous substrate must have either a free-standing shape or a self-weaving characteristic, which is important to guarantee its normal function as an electrode. Moreover, the flexible and robust substrate should retain its complete structure after impregnating the active material and during cell cycling.

1.7 BINDERS

In addition to the current collector, it may be necessary to customize other cell components for lithium-sulfur batteries. Conventional polytetrafluoroethylene (PTFE) or polyvinylidene difluoride (PVdF) binders are used to link sulfur particles or sulfur-based nanocomposites with the conductive carbon and the current collector. Although they are chemically stable during cycling, conventional binders can neither effectively tolerate the huge volume changes occurring during cycling nor suppress the polysulfide dissolution

and migration. Thus, alternative binders that can create robust electrode architecture and possess polysulfide-retention capability have been considered for lithium-sulfur batteries.[11, 12, 47]

Shim *et al.* first investigated sulfur cathodes with a poly(ethylene oxide) (PEO) binder with different mixing processes, ball milling, and mechanical stirring methods.[47] The study indicated that the preparation methods affect the morphology of the PEO binder and the porosity in the sulfur cathodes, which influences the cycle performance. A cationic polyelectrolyte binder, poly (acrylamide- *co*-diallyldimethylammonium chloride) (AMAC), was used with high-loading sulfur electrodes (sulfur content of 80 wt. %), as reported by Zhang.[145] Sun *et al.* used a natural gelatin polymer as the binder in cathode preparation.[146] The gelatin binder has high adhesion ability, ensuring the structure stability of the sulfur cathode, as well as good dispersion ability, mitigating the aggregation of the active material during cathode preparation and cell cycling. Other alternative binders that can enhance the adhesion among cathode mixtures, or suppress the agglomeration of cathode material mixtures, have also been reported.[45, 147-149]

1.8 SEPARATORS

The polymeric separators that are widely used in commercial Li-ion batteries work as the lithium-ion transporting medium and the electronic insulator. In addition, the commercial separators possess excellent mechanical strength and flexibility to protect it from being pierced and losing functions.[11, 12, 38] However, the commercial separators cannot block the migrating polysulfides that shuttle between the anode and the cathode.

Thus, the custom separators with chemical and physical polysulfide-blocking capability have been successfully applied in lithium-sulfur batteries. In the first case, lithiated Nafion ionomer film [150] and Nafion-coated separator[151, 152] have been investigated as custom separators to improve the cycle performance. The Nafion functional layer has excellent stability and good cationic conductivity, which allows lithium cations to pass through but rejects polysulfide anions. However, the cation-exchange process and the application of polymer coating may decrease the ionic

and electronic conductivity of the cathode. As a result, the Nafion modified separators attain good cycle stability but have limited enhancement in electrochemical utilization.[150-153] In the second case, Chung and Manthiram first conceived an idea of a custom separator with a carbon coating on one side of the commercial separator, as shown in Figure 1.12.[38] The carbon coating facing the sulfur cathode functions as a polysulfide trap and as an upper-current collector to intercept the migrating active material, achieving an efficient reutilization of the trapped active material during long-term cycling. The conventional separator serves as an electrically insulating membrane to facilitate the flow of electrolyte and lithium ions but blocks electron transport. Furthermore, it functions as a highly robust substrate to support the coating layer, providing the carbon-coated separator with flexibility and outstanding mechanical strength. By way of using a functional carbon coating, the carbon-coated separators achieve both stable cyclability and high electrochemical utilization.[38, 99, 154]

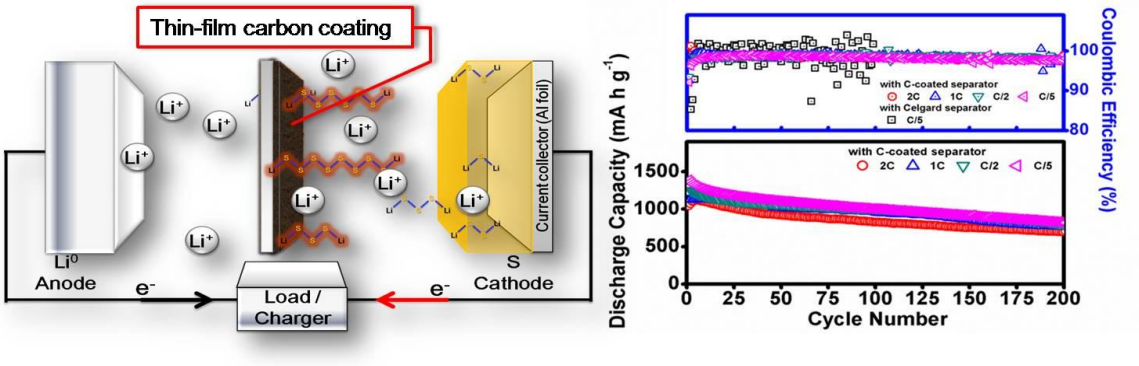

Figure 1.12: Schematic model and electrochemical performance of the cell employing the Super P carbon-coated separator. Reprinted from ref. 38.

1.9 ELECTROLYTE

Electrolyte acts as the ion transport media between the anode and cathode. Liquid electrolyte is widely used in batteries because of its high ionic conductivity. In

lithium-sulfur batteries, electrolyte is critical because the polysulfide intermediates could dissolve in the liquid electrolyte and shuttle between the cathode and anode.[11, 155]

Thus, in addition to addressing the polysulfide-dissolution issue by the sulfur-cathode development, the electrolyte optimization in lithium-sulfur cells is another supporting strategy to enhance the electrochemical utilization and the capacity retention rate. The electrolyte development including co-slat additives[119, 156-158] and mixed electrolyte[158-161] aims at suppressing the dissolution of active material into the liquid electrolyte and at stopping the polysulfide shuttle effect, which attains high electrochemical efficiency.[119, 155, 158] However, a comprehensive electrolyte review paper reported by Zhang indicates that the dissolution of active material into the organic liquid electrolyte is inevitable or even essential because it is a necessary operation step in lithium-sulfur cells. On the other hand, the gel polymer and solid-state electrolytes may show progress by achieving new material chemistry. It is considered that the gel polymer and the solid-state electrolyte may function as a separator in a cell, theoretically isolating the negative and positive electrodes from each other, preventing the redox intermediate from diffusing to the anode side.[11, 23, 155, 162, 163]

1.10 ANODES

Lithium metal is the primarily used anode in lithium-sulfur cells due to its low potential, high capacity, and high gravimetric energy density. However, lithium metal is unstable in the organic electrolyte currently used in lithium-sulfur cells. The redox reactions between lithium metal and organics/polysulfides form a passivation layer on metallic lithium anode and cause the shuttle phenomenon.[164, 165] Furthermore, lithium dendrites can form and penetrate through the separator, shorting the cell and causing thermal runaway and fire.[166]

Thus, Lee *et al.* first introduced a protection layer on the surface of the lithium-metal anode by the UV curing method in order to enhance the cycle efficiency and mitigate the safety issue.[167] Hassoun *et al.* presented a pioneering study on lithiated silicon anode. The lithiated metal-free anode coupled with sulfur-mesoporous-carbon

composite cathode exhibits a long cycle life with an expected low cost and high safety.[110] The development on lithiated anode shows a great potential to operate with a sulfur cathode and therefore to form a high-safety lithium-sulfur battery.[110, 168] On the other hand, alternative metal-free anode is widely coupled with Li_2S cathodes that have been introduced in section 1.5.5, which is possible to attain a theoretical specific energy of 1550 W h kg^{-1} at a more controllable fabrication process as compared to lithiated anodes.[11, 23, 106, 109, 110]

1.11 OBJECTIVES

The primary objective of my dissertation is to demonstrate that custom cell configurations are essential for improving the performance of lithium-sulfur batteries at an affordable cost and with a low environmental impact. These custom cell configurations presented in my dissertation aim at stabilizing, reactivating, and reutilizing the active material, which are very different from traditional methods that focus on isolating the active material within nanocomposites by an electrochemically stable shell (*e.g.*, conductive polymer and carbon) and thereby limiting the polysulfide dissolution. In addition, custom cell configurations attain enhanced cell performance by employing pure sulfur cathodes with high sulfur content. Moreover, the fabrication processes are designed to be facile and easily adaptable for large-scale applications as describing in Chapter 2, the general experimental methods. From Chapter 3 to Chapter 6, each chapter systematically introduces each specific custom cell component consisting of a series of relative studies, as shown in Figure 1.13.

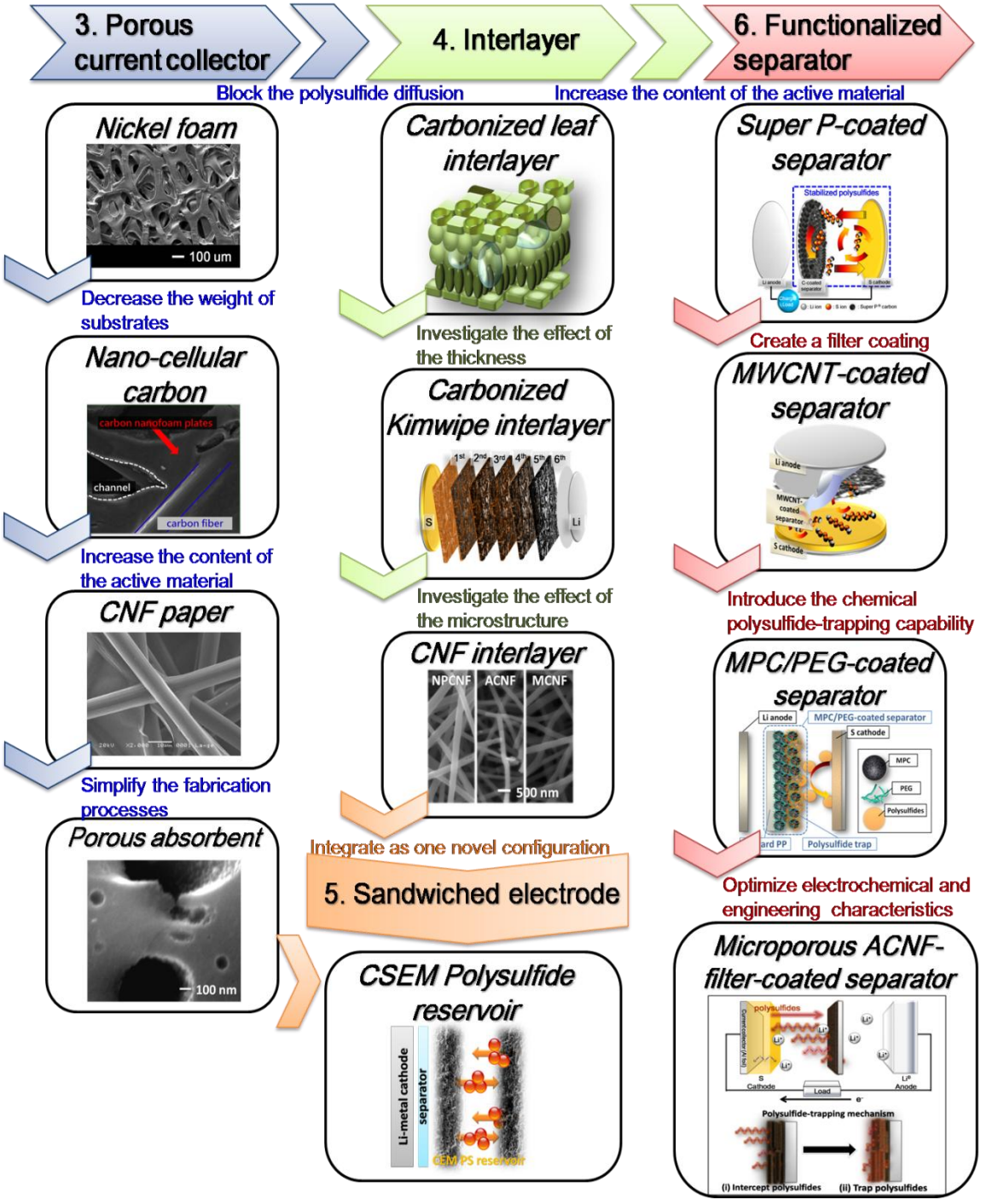

Figure. 1.13: A sketch of the dissertation.

Chapter 3 introduces a series of porous current collectors (*e.g.*, metal foams, nano-cellular carbons, CNF papers, and porous CEM absorbents) that are embedded with pure sulfur cathodes for holding the active material and confining soluble polysulfides. In the first case, nickel foam matrices provide the porous sulfur cathodes with high capacity retention. In the second case, nano-cellular carbon current collectors exclude the weight concern encountered by the metal foam current collectors and further extend the cycle life of the cells. In the third case, highly porous CNF papers allow the sulfur content and loading to attain, respectively, 2.3 mg cm^{-2} and 80 wt. %, yet displaying excellent electrochemical utilization and efficiency. In the fourth case, a small amount of porous polysulfide absorbents are added into pure sulfur cathodes for storing the dissolved polysulfides and hence providing the cells with low capacity fade and long lifespan of 150 cycles.

Chapter 4 presents the analysis on the morphology and microstructure of the interlayer toward the cell performance. Thus, three optimized carbon interlayers that are inserted between the separator and cathode function as polysulfide-diffusion inhibitors, localizing the polysulfides within the cathode region of the cell. In the first case, carbonized-leaf interlayers indicate that the surface microstructure and morphology of interlayers control their polysulfide-intercepting capability. In the second case, carbonized-Kimwipe-paper interlayers demonstrate the importance of the thickness of interlayers for enhancing the cycle stability. With an optimized thickness, in the third case, three CNF interlayers with tunable micro-/meso-/macro-pores conclude that the pore size, surface area, and electrical conductivity influence the rate performance of the cells.

Chapter 5 introduces the first sandwiched electrode in Li-dissolved polysulfide cells. The carbonized sucrose-coated eggshell membranes (CSEM) sandwiched electrode that functions as a polysulfide reservoir has a bottom CSEM as the porous current collector and a top CSEM as the polysulfide-diffusion inhibitor, and the dissolved polysulfide catholyte is stabilized in between. The CSEM current collector reduces the

cathode resistance and enhances the active material utilization. The CSEM inhibitor intercepts the migrating polysulfides and suppresses the loss of active material.

Chapter 6 introduces the first carbon-coated separators in lithium-sulfur cells. In the first case, Super P carbon-coated separators are the prototypical carbon-coated separators that integrate two necessary components already used inside the cell, the carbon black and the separator, to form custom separators. This work focuses on introducing a new concept that high-performance lithium-sulfur batteries could be realized by a facile and practical technique. In the second case, MWCNT-coated separators that are prepared by a vacuum filtration process successfully attach a fibrous filter onto the polypropylene sheet, which further extends the application of the carbon-coated separator and its performance. In the third case, first, MPC-coated separators prove that the carbon-coated-separator configuration exhibit better physical polysulfide-trapping capability than the composite-cathode configuration. Second, PEG/MPC-coated separators investigate the chemical polysulfide-trapping capability by utilizing PEG binder for not only bonding the MPC particles but also immobilizing the migrating polysulfides. In the fourth case, the functionalized separators with a microporous ACNF filter attain outstanding mechanical strength and flexibility by modifying the fabrication processes. Also, the investigation on the ACNF-filter coatings demonstrates that the key parameters for enhancing the polysulfide-trapping capability are the high microporosity and small micropores less than 1.2 nm.

Finally, Chapter 7 gives the summary of these approaches and recommendations for follow-up modifications.

Chapter 2: General experimental procedures

2.1 MATERIALS SYNTHESIS

Pristine sulfur used in my dissertation was synthesized by a precipitation method at room temperature. The sulfur deposition process was carried out by mixing 0.02 mole of sodium thiosulfate ($Na_2S_2O_3$; Fisher scientific) and 2 mL of hydrochloric acid (HCl; Fisher Scientific) in 750 mL of deionized water for 24 h. The precipitated sulfur was filtered and washed with 100 mL of deionized water, ethanol, and acetone three times, and was then dried for 24 h at 50 ℃ in an air oven.

The detailed synthesis and fabrication procedures of the custom-cell components are described in the respective chapters.

2.2 MATERIALS CHARACTERIZATION

The general physical and chemical properties of the materials employed in the experiments were characterized by the following techniques. The specific characterization procedures will be described in the respective chapters.

2.2.1 Porous structure analysis

Surface area measurements were carried out by the Multi-point Brunauer-Emmett-Teller (BET) method with a volumetric sorption analyzer (NOVA 2000, Quantachrome Instruments) and an automated gas sorption analyzer (AutoSorb iQ2, Quantachrome Instruments). The BET data were based on the 7-point BET model with a correlation coefficient of > 0.999. The nitrogen adsorption-desorption isotherms were measured at -196 ℃ with the above gas sorption analyzers. The pore-size distributions were determined by the Barrett-Joyner-Halenda (BJH) model for general distributions, the Horvath-Kawazoe (HK) model for micropores, and the density functional theory (DFT) model for micro-/mesopores. Micropore surface area, micropore volume, and micropore size were estimated by the t-plot method calculated with the

active carbon model and Dubinin-Astakhov (DA) method supported with the Dubinin-Radushkevich (DR) method.

2.2.2 Scanning electron microscopy (SEM)

The morphology and microstructure of samples was inspected with a scanning electron microscope (SEM) (JSM 5610, JEOL) and a field emission scanning electron microscope (FE-SEM) (Quanta 650, FEI). SEM samples were dried for 1 h at 50 ℃ in a vacuum oven before inspection. The cycled samples were retrieved inside an argon-filled glove box, rinsed with blank electrolyte for 3 minutes, and transported in an argon-filled sealed vessel. The blank electrolyte that used for rinsing the cycle samples contained only the 1:1 volume ratio of DME/DOL.

2.2.3 Transmission and scanning transmission electron microscopy (TEM/STEM)

The morphology and microstructure of the samples were investigated with a high-resolution transmission electron microscope (TEM) (2010F, JEOL) equipped with a scanning transmission electron microscope (STEM).

2.2.4 Energy dispersive X-ray spectroscopy (EDS / EDX)

Both SEMs and TEM described in sections 2.2.2 and 2.2.3 are equipped with energy dispersive X-ray spectrometers (EDS / EDX) for collecting the elemental signals and conducting the elemental mapping.

2.2.5 Raman spectroscopy

The Raman analysis of the chemical state of the carbonaceous material was conducted with a Raman microscope (Renishaw inVia Raman microscope) with 532-nm laser and a 2400 lines mm^{-1} grating stage at a 50X objective lens.

2.2.6 Fourier transform infrared spectroscopy (FTIR)

Fourier transform infrared (FTIR) spectroscopy data were obtained with KBr pellets with a PerkinElmer IR spectrometer.

2.3 ELECTROCHEMICAL CHARACTERIZATION

2.3.1 Cathode preparation

Pure sulfur cathodes were fabricated by coating the active material slurry onto an aluminum foil current collector by the tape casting method, followed by evaporation of the N-methyl-2-pyrrolidone (NMP; Aldrich) solvent for 24 h at 50 ℃ in an air oven. The tape casting method used an automatic film applicator (1132N, Sheen) with a standard number 6 blade at a traverse speed of 50 mm s^{-1}. For the pure sulfur cathode, the active material slurry was prepared by mixing precipitated sulfur, Super P carbon (TIMCAL), and polyvinylidene fluoride (PVDF L#1120; solution viscosity: 550 mPa s; Kureha) in NMP for 2 days. The pure sulfur cathode refers to the readily-prepared cathode containing only the necessary components: active sulfur, conductive carbon additive, and binder.[38, 47, 99, 169] The sulfur content was at least above 60 wt. %.

2.3.2 Cell assembly

The CR2032-type coin cells were assembled with the pure sulfur cathode, separator (Celgard 2500), lithium anode (Aldrich), and nickel foam spacers. Cell components were dried in a vacuum oven for one hour at 50 ℃ prior to cell assembly. All cells were assembled in an argon-filled glove box. The electrolyte was prepared by dissolving 1.85 M $LiCF_3SO_3$ salt (Acros Organics) and 0.1 M $LiNO_3$ co-salt (Acros Organics) in a 1:1 volume ratio of 1, 2-dimethoxyethane (DME; Acros Organics) and 1, 3-dioxolane (DOL; Acros Organics). The assembled cells were allowed to rest for 30 minutes at 25 ℃ before the electrochemical measurements. The cell-assembly process with the custom-cell components will be described in the respective chapters. The liquid electrolyte that was used in each study focusing on different custom-cell components was controlled to have the same ingredients in order to have consistency with the various investigations in this dissertation.

2.3.3 Electrochemical impedance spectroscopy (EIS)

The electrochemical impedance spectroscopy (EIS) data were recorded with a computer-interfaced impedance analyzer in the frequency range of 1 MHz to 100 mHz with an applied voltage of 5 mV. The impedance analysis system has a potentiostat (SI 1287, Solartron) as the electrochemical interface coupled with an impedance analyzer (SI 1260, Solartron). The SI 1287 is a wide bandwidth potentiostat with a full range of direct current (DC) capabilities, which works as an electrochemical interface. The SI 1260 is a flexible frequency response analyzer for battery research. The integration of SI 1260 and 1287 is for investigating the impedance spectroscopy over the frequency range of 10 μHz to 1 MHz. EIS data were obtained at the open-circuit voltage of the cells with the Li metal foil as both auxiliary and reference electrodes.

2.3.4 Cyclic voltammograms (CV)

The cyclic voltammetry (CV) data were performed with a universal potentiostat (VoltaLab PGZ 402, Radiometer Analytical) between 1.8 and 2.8 V at an adjustable scan rate (mV s^{-1}).

2.3.5 Discharge/charge profiles and cyclability data

The discharge/charge voltage profiles and cyclability data were collected with a programmable battery cycler (Arbin Instruments). The cells were first discharged to 1.8 V and then charged to 2.8 V for a full cycle. The complete electrochemical cycling performance was investigated at a C/5 rate, based on the mass and theoretical capacity of sulfur (C = 1672 mA g^{-1}). The rate capability of the cells was assessed with adjustable cycling rates.

Chapter 3: Development of porous current collectors*

3.1 INTRODUCTION

In the pursuit of applying rechargeable batteries in electric vehicles and integrating energy storage devices with green power plants, lithium-sulfur batteries have received considerable attention in recent years as sulfur offers a high theoretical capacity of 1672 mA h g^{-1} compared to the currently used insertion-compound cathodes.[24, 52] Also, sulfur is abundant and inexpensive. However, the commercialization of lithium-sulfur batteries is hampered by low electrochemical utilization, poor capacity retention, and short cycle life. First, the low practical capacity of sulfur cathodes is related to the insulating nature of sulfur and its discharge products (Li_2S/Li_2S_2 mixtures).[52, 170] Second, the low capacity retention and short cycle life are related to the diffusion of the polysulfide intermediates.[52] In the beginning, the sulfur in the cathode reacts with lithium ions and converts into polysulfide intermediates (Li_2S_x, $x = 4 - 8$).[33] Then, the highly soluble polysulfides freely diffuse through the separator and shuttle between the anode and the cathode upon charging, thereby corroding the Li anode and triggering the active material loss.[171] The active material loss resulting from the polysulfide diffusion causes severe capacity fade during cycling.[32, 33, 171]

---

* S.-H. Chung and A. Manthiram, "Lithium-sulfur batteries with superior cycle stability by employing porous current collectors," *Electrochim. Acta* 2013, **107**, 569-576.

*S.-H. Chung and A. Manthiram, "Nano-cellular carbon current collectors with stable cyclability for Li-S batteries," *J. Mater. Chem. A* 2013, **1**, 9590-9596.

*S.-H. Chung and A. Manthiram, "Low-cost, porous carbon current collector with high sulfur loading for lithium-sulfur batteries," *Electrochem. Commun.* 2013, **38**, 91-95.

*S.-H. Chung and A. Manthiram, "Eggshell membrane-derived polysulfide absorbents for highly stable and reversible lithium-sulfur cells," *ACS Sustainable Chem. Eng.* 2014, **2**, 2248-2252.

S.-H. Chung carried out the cell design and the experimental work. A. Manthiram supervised the project. All participated in the preparation of the manuscript.

To overcome the above scientific and technological challenges, recent research has focused on retaining the polysulfides with the cathode structure by employing sulfur-carbon nanocomposites,[24, 55, 58, 172] bifunctional carbon interlayers,[173, 174] or a polymer electrolyte membrane.[162] However, very limited work has been carried out on modifying the configuration of a necessary component already present inside the cell: the current collector. Thus far, only a few researchers have applied novel porous matrices as alternative current collectors, including carbon cloths,[138] carbon-coated aluminum foil electrodes,[127] carbon foam matrices,[175] non-woven carbon papers,[175] and carbon nanotubes. [140, 175] Among these successful work, the porous current collectors are designed to contain the dissolved polysulfide intermediates and to channel the electrolyte into the sulfur cathode region. The architectural design of current collectors has the potential to become a viable approach for successfully developing lithium-sulfur batteries.

Here, we present a series of porous-current-collector design for improving the electrochemical performance of lithium-sulfur cells that use pure sulfur cathodes. Figure 3.1 illustrates four optimized porous current collectors with three on the macroscale (nickel foam, nano-cellular carbon, and CNF paper) and one on the microscale (carbonized eggshell membranes (CEM) derived polysulfide absorbent).

First, we present the concept of 3D sulfur-nickel foam (SNF) cathodes by applying nickel foam matrix as a bifunctional current collector in lithium-sulfur batteries. In the SNF cathodes, the nickel foam matrix works as an electron transport network to improve the electrical conductivity of the cathode, as a container to accommodate the active material, and as a cage to retain the polysulfides in the cathode region during the charge/discharge process. The SNF cathodes are prepared by a facile paste-absorption method to optimize the porous structure of the cathode by improving the contact between the active material and the foam matrix. We find that lithium-sulfur batteries employing SNF cathodes exhibit superior cycle stability, high discharge capacity, excellent capacity retention, and low self-discharge behavior.[135]

Second, in order to decrease the weight of the applied porous current collector, we present a nano-cellular carbon current collector (NC current collector, MarkeTech). The porous carbon framework of the NC current collectors is composed of interwoven carbon fibers with the carbon nanofoam firmly attached to each other. This unique micro-/meso-/macro-porous architecture offers large surface area, high absorption capability, and light weight. These characteristics make the NC current collector an appealing lightweight, porous current collector.[176]

Third, we present the feasibility of applying a porous CNF current collector (PCCC: Toray carbon paper H-030, Fuel Cell Earth), which is a low-cost electrode support and is used in fuel cells. This multi-functional PCCC has high electrical conductivity for decreasing the cathode resistance, high porosity for accommodating the active material, and superior absorptivity for holding the electrolyte containing the dissolved polysulfides. Stabilizing the electrolyte containing the dissolved polysulfides within the PCCC by its unique physical properties is the core of this work. By localizing/stabilizing the electrochemical reaction within the cathode region, the PCCC facilitates a high sulfur content of 70 – 80 % (equivalent to high sulfur loading of 2.1 – 2.3 mg cm^{-2}) as well as a high active material utilization with stable cyclability. A key factor for preparing the high-performance cathodes is the uniform sulfur coating. The excellent active material coating on the PCCC is achieved by the one-step paste-absorption method.[177]

Fourth, we present the use of carbonized eggshell membranes (CEMs) in sulfur cathodes as a polysulfide absorbent. After carbonizing at 800 ℃ in an inert argon atmosphere, the CEM absorbent has abundant micropores for absorbing the migrating PSs, which effectively mitigates the severe polysulfide diffusion. After absorbing the polysulfides, the conductive CEM provides fast electron transport, ensuring the continuous reactivation and reutilization of the trapped active material. Therefore, the cathode with 10 wt. % CEM absorbent offers a high reversible capacity of 860 mA h g^{-1}

with an excellent capacity retention rate of 85 % and a low capacity fade rate of 0.10 % per cycle for 150 cycles.[178]

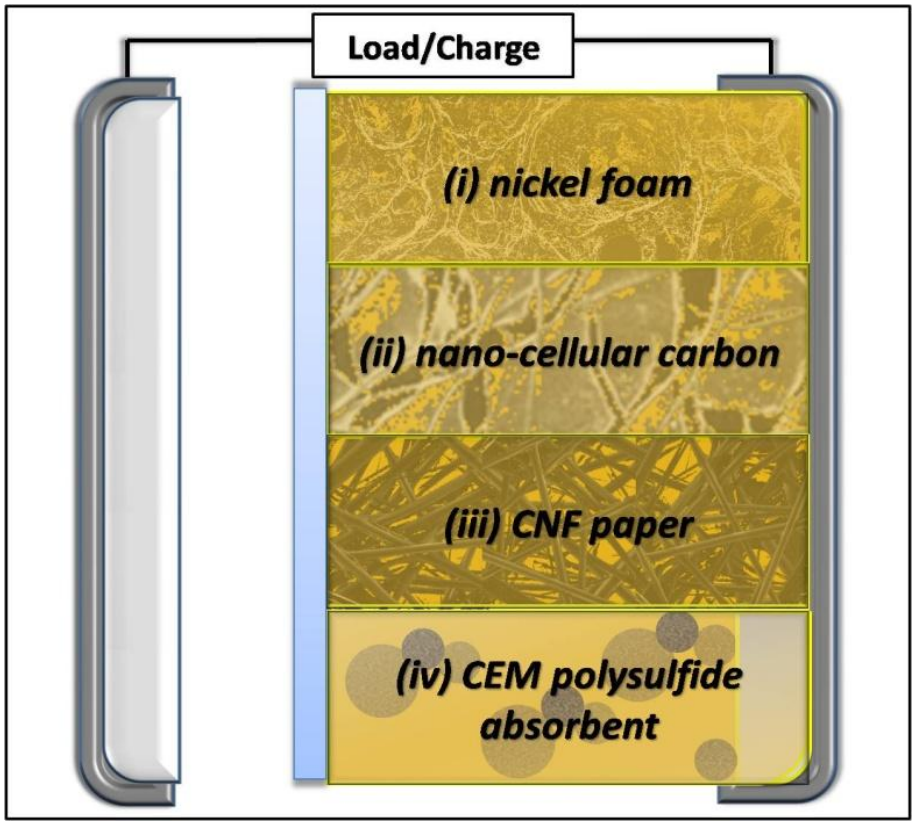

Figure 3.1: Schematic of the porous current collectors: (i) nickel foam, (ii) nano-cellular carbon, (iii) CNF paper, and (iv) CEM polysulfide absorbent.

3.2 EXPERIMENTAL

3.2.1 Paste-absorption method for porous current collector application

A paste-absorption method was used to fabricate porous cathodes with porous current collectors. First, the well-mixed paste was dropped onto a petri dish. Each paste drop was covered by a porous-current-collector disk and allowed to absorb for 2 min by the capillary force. Second, the porous current collectors were pressed to channel the

absorbed paste into the inner pore spaces of the porous current collector, and to ensure a uniform sulfur coating on the skeleton of the porous current collector. Then, the porous cathodes loaded with the active-material paste were dried in a convection oven at 50 ℃ for 24 h. The dried porous cathodes were uniformly loaded with the same amount of active material and had a close connection between the active material and the porous substrate.

In the first case, the porous cathodes employing nickel-foam current collectors were roll-pressed from the thickness of 0.14 to 0.1 mm. The resultant 3D SNF cathodes have a sulfur loading of 2.0 mg cm^{-2} and a sulfur content of 60 wt. % and 70 wt. %, as shown in Figure 3.2a. In the second case, the porous cathodes employing the nano-cellular carbon current collectors (thickness: 0.3 mm; density: 0.4 g cm^{-3}) have a high sulfur loading of 2.2 mg cm^{-2} and a sulfur content of 70 wt. %, as shown in Figure 3.2b. In the third case, the porous cathodes employing the porous carbon current collectors (thickness: 0.1 mm; density: 0.4 g cm^{-3}; porosity: 80 %) further increase the loading up to 2.3 mg cm^{-2} and sulfur content to above 80 wt. %. As a reference, the control cells have a sulfur content of 60 to 70 wt. % with the corresponding sulfur loading of 0.8 to 1.2 mg cm^{-2} due to the 2D flat morphology of the aluminum foil.

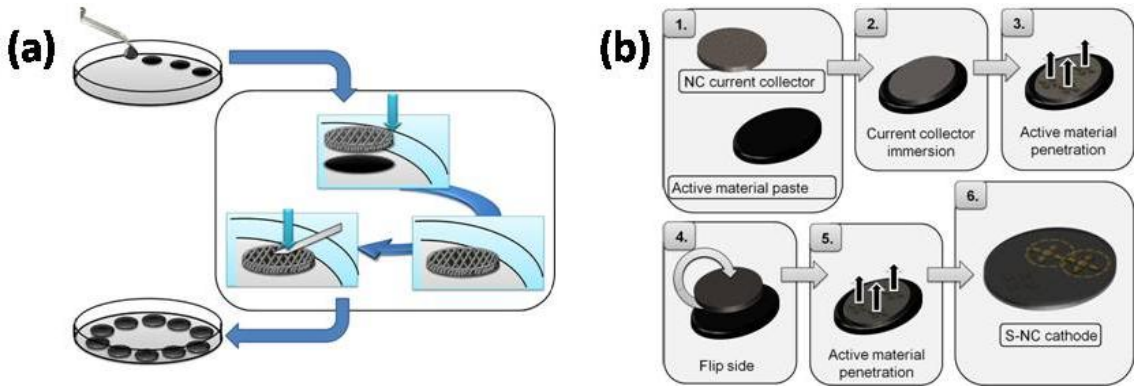

Figure 3.2: Illustration of the paste-absorption method for (a) the 3D SNF cathode fabrication and (b) the S-NC cathode fabrication.

3.2.2 CEM and CEM-S cathode preparation

Commercial eggs purchased from a supermarket were broken and the egg white and egg yolk were removed. The recyclable eggshell was washed with deionized water and the hard shell ($CaCO_3$) was etched away with 1 M HCl for 2 h. The remaining organic eggshell membrane was rinsed again with deionized water and immersed into 500 mL of 40 wt. % sucrose solution (sucrose; Fisher Scientific) at room temperature, followed by pre-carbonizing in an oven at 180 ℃ for 12 h via the hydrothermal method. The pre-carbonized CEM was subsequently carbonized in a tube furnace in argon atmosphere at 800 ℃ for 12 h with a heating rate of 1 ℃ min^{-1}. To be a suitable PS absorbent, after carbonization, the CEM sheets were ground in an agate mortar to form micron-sized CEM powder (CEMs) and were not required to be in a free-standing, thin-film shape or nanoparticles, which greatly simplifies the cathode preparation.

The CEM-S cathode was prepared by mixing 60 wt. % precipitated sulfur, 10 wt. % CEM, 15 wt. % Super P carbon (TIMCAL), and 15 wt. % polyvinylidene fluoride (PVDF; Kureha) binder in N-methyl-2-pyrolidone (NMP; Aldrich) under continuous stirring for 2 days. The active material paste was coated onto an aluminum foil current collector by a slurry casting method and dried in a vacuum oven overnight at 50 ℃, followed by pressing with a roller machine and cutting into circular electrodes with a diameter of 12 mm. For the sake of comparison, the conventional S cathode contained 60 wt. % precipitated sulfur, 25 wt. % Super P carbon, and 15 wt. % PVDF. Both cathodes were controlled with the same sulfur content of 60 wt. % and sulfur loading of ~ 1.3 mg cm^{-2}.

3.2.3 Cell assembly

The CR2032-type coin cells were assembled with the porous cathode, separator (Celgard 2500), lithium anode (Aldrich), and nickel foam spacers. The porous cathode included the pure sulfur cathodes that employed the nickel foam, nano-cellular carbon, CNF paper, or CEM absorbent. The assembled cells were allowed to rest for 30 min at 25

℃ before the electrochemical measurements. The electrochemical and microstructural analyses have been described in Chapter 2.

3.3 RESULTS AND DISCUSSION

3.3.1 Nickel foam current collector: a porous metal current collector

Conventional lithium-sulfur batteries suffer from severe capacity fade and self-discharge attributed to the loss of the active material and polysulfide diffusion. Here, we present a porous cathode architecture, which suppresses the loss of active material and self-discharge behavior in lithium-sulfur systems. 3D sulfur-nickel foam cathodes (SNF cathodes) have porous, electrically conductive nickel foam substrates as bifunctional current collectors. It was found that these cathodes have a stable cycle life with a high discharge capacity retention rate of 92 % after 50 cycles. Moreover, SNF cathodes reduce the self-discharge and retain 85 % of their original capacities after resting for two months. The porous architecture of nickel foam accommodates the active material and traps polysulfides in the cathode region during cycling and battery storage, effectively reducing the loss of active material and capacity. In addition, it provides an excellent internal electron transport network by ensuring intimate contact between the active material and nickel foam, resulting in low cell impedance and improved capacities. The study demonstrates that the 3D nickel foam is an attractive bifunctional current collector for lithium-sulfur batteries.

3.3.1.1 Microstructure

The cross-sectional and surface SEM images shown in Figure 3.3a and 3.3b indicate that the nickel foam matrices have a ductile strip-type framework and an uneven surface. Their interwoven strip-type structure provides abundant porous spaces, which could serve as sites to absorb the active material. The 3D multilayer contact surfaces can enlarge the accessible reaction area. Furthermore, the nickel foam has a highly flexible structure, which could cushion the mechanical strain from the volume change of the active material during cycling.[175, 179]

The paste-absorption method applied can accurately impregnate the nickel foam disks with equivalent masses of active material. The cross-section and surface of the SNF cathodes show that the porous spaces and surface of the nickel foam can be uniformly filled and covered by the active material as shown in Figure 3.3c and 3.3d. The dark porous background in the images is the active material and the bright features are the framework of the nickel foam, demonstrating the high retention of active material. The porous spaces of the ductile nickel foam hold sulfur and absorb polysulfides in the cathode region, thereby avoiding severe active material loss during cell storage and cycling. Overall, the facile procedure, the superior active material coverage, and the controllable approach for precisely loading the active material make the paste absorption method an attractive procedure for manufacturing porous cathodes.

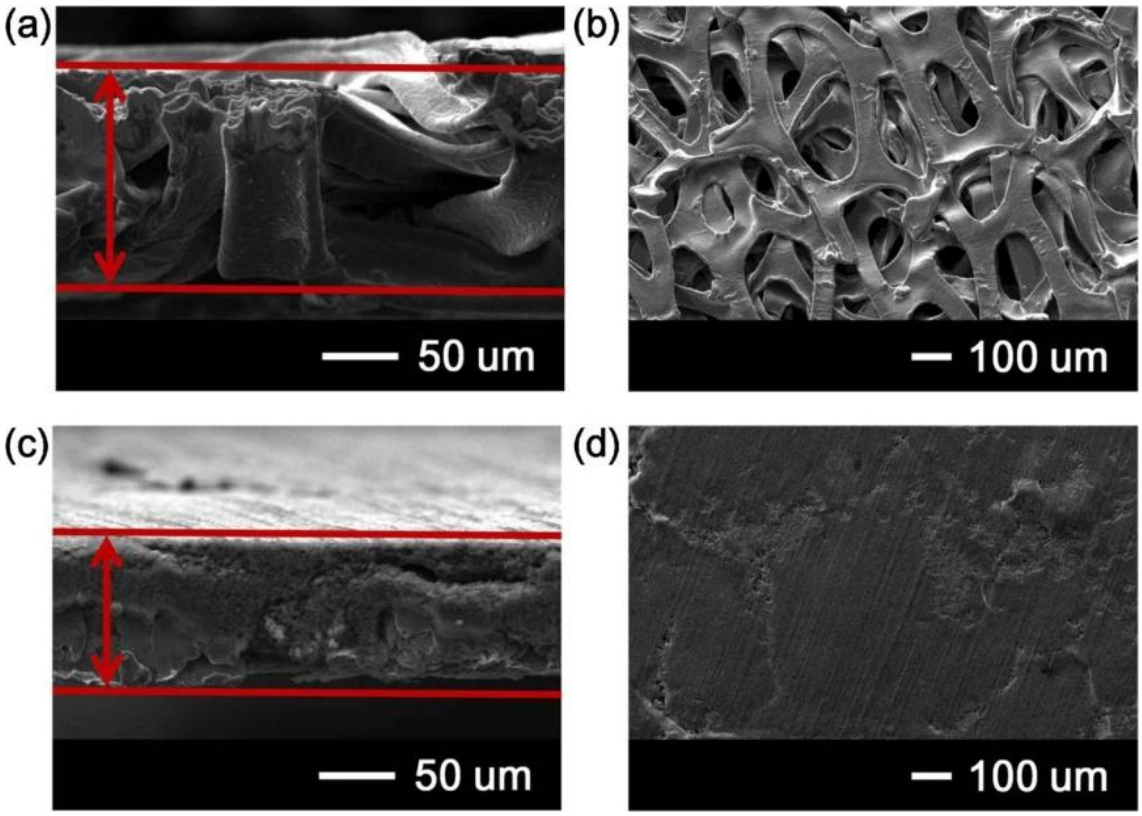

Figure 3.3: SEM morphology of the (a) cross section and (b) surface of the 3D nickel foam matrices and the (c) cross section and (d) surface of the SNF cathodes.

3.3.1.2 Cyclic voltammetry and charge/discharge profiles

To investigate the enhanced charge/discharge behavior of the SNF cathodes, cyclic voltammetry (CV) measurements were conducted on the cells with the SNF cathodes and the conventional cathodes. In Figure 3.4a, the CV curves of the SNF cathodes show two cathodic peaks starting at 2.4 and 2.1 V, which are consistent with the two-step reduction of sulfur.[10, 17] The first peak at 2.4 V involves the reduction reaction from sulfur (S_8) to soluble lithium polysulfides (Li_2S_x, $x = 4 – 8$).[17, 33] The second peak at 2.1 V corresponds to the reduction reaction of polysulfides to insoluble Li_2S_2/Li_2S.[17, 33] The two overlapped anodic peaks at 2.3 V indicate the reversible oxidation reaction from Li_2S_2/Li_2S to elemental sulfur or long-chain polysulfides.[56] The sharp cathodic and anodic peaks imply an electrochemically stable environment within the cathodes leading to complete reduction/oxidation reactions during cycling. Notably, there are no apparent current or potential changes in these overlapped peaks with repeated scans, attesting to the superior reversibility and cycling stability. In contrast, the conventional cathodes show a series of typically unstable and diminished CV patterns in the successive cycles as shown in Figure 3.4b. First, the broad cathodic and anodic peaks continuously shrink, indicating the irreversible loss of capacity.[49, 75] Second, the cathodic peaks shift to lower potential, and the anodic peaks shift to higher potential, evidencing polarization and deteriorated cyclability.[48, 75]

The stable cycling processes of SNF cathodes can be further explained by the charge/discharge profiles in Figure 3.4c. In different cycles, the two discharge plateaus in the voltage ranges of 2.3 and 2.0 V exactly match the two cathodic peaks shown in the CV curves in Figure 3.4a. In the discharge process, the long lower discharge plateau represents the major discharge capacity of lithium-sulfur batteries, in which polysulfides are reduced to sulfides.[17, 180] In the charge process, the two charge plateaus resemble the two oxidation peaks shown in the CV curves. As the cell voltage approaches 2.8 V, the vertical voltage rise suggests that cells employing SNF cathodes are completely charged without much shuttling effect.[180, 181] After the first cycle, the overlapped charge/discharge plateaus display no obvious capacity fade or voltage changes, showing superior

electrochemical reversibility with good capacity retention. In comparison with the stable cyclability of SNF cathodes, the typical capacity loss and the shrinkage of the plateaus are observed in the charge/discharge profiles of conventional cathodes with increasing cycle number, as shown in Figure 3.4d.[42, 75] In the conventional cathode configuration, the soluble polysulfides easily diffuse into the liquid electrolyte from the conventional 2D current collectors, and the Li_2S_2/Li_2S can also readily precipitate and accumulate on the flat surface of the conventional cathode, leading to capacity fade and poor cyclability.

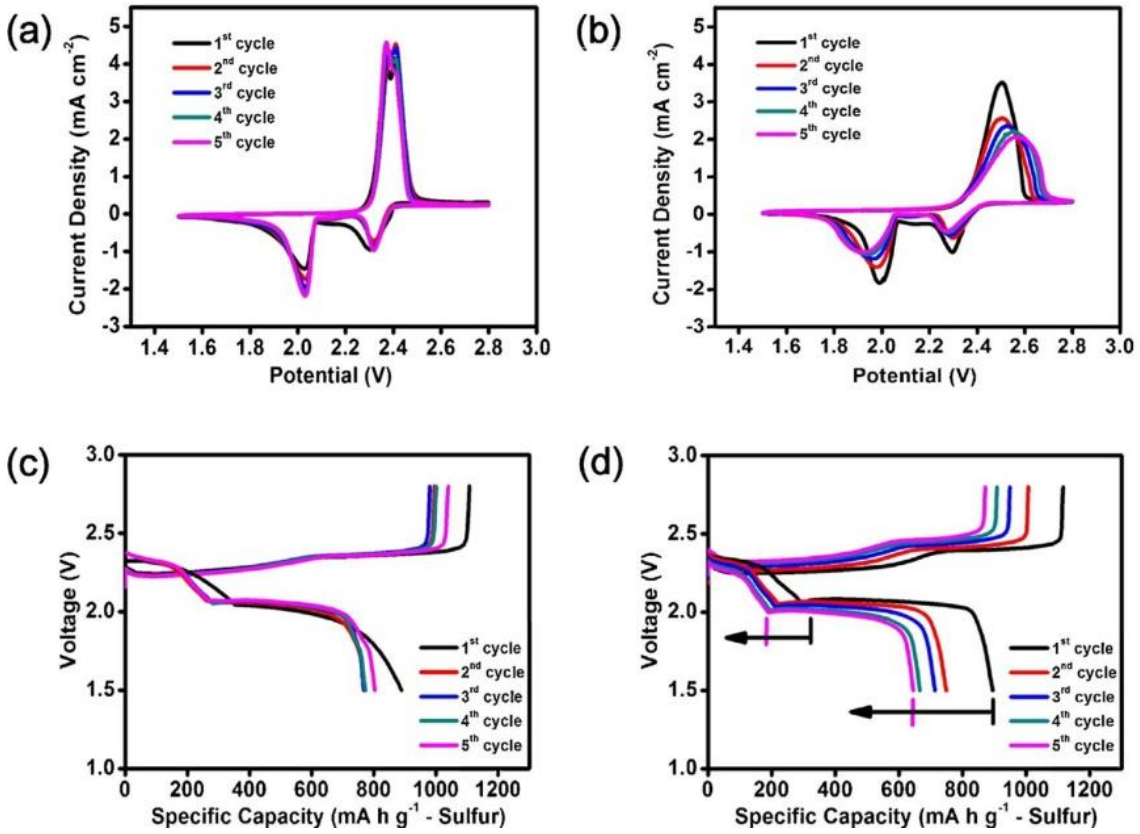

Figure 3.4: Cyclic voltammetry plots of (a) the SNF cathodes and (b) the conventional cathodes at a scan rate of 0.1 mV s^{-1} in the voltage window of 1.5 – 2.8 V. Charge/discharge profiles of (c) the SNF cathodes and (d) the conventional cathodes at a C/5 rate.

3.3.1.3 Electrochemical cycling

The cycling profiles of the cells employing the SNF cathodes show superior cycling stability. An average discharge capacity of > 810 mA h g^{-1} for 50 cycles with a sulfur content of 60 wt. % is shown in Figure 3.5. After increasing the sulfur content in the paste to 70 wt. %, the cells maintain a stable discharge capacity of 720 mA h g^{-1}. After 50 cycles, the capacity retention rates of the cells with 60 wt. % or 70 wt. % of sulfur in the pastes are > 92 %. In contrast, cells with the conventional cathodes show severe capacity fade of 21 % after the first cycle. After 50 cycles, the conventional cathodes maintain a discharge capacity of only 420 mA h g^{-1}. The good cycling performance of the SNF cathodes may result from the excellent active material retention by the ductile, porous nickel substrates, which suppress the loss of the active material and prevent polysulfides from diffusing into the organic electrolyte.[133, 175] In the SNF cathode fabrication, the capillary force channels the paste to penetrate into the substrate and uniformly keeps it at stable absorption positions, which could also allow active material to reach the most electrochemically stable position during cycling. Besides, the electrically conductive skeleton of the nickel foam works as the electron transport network in the cathodes and improves the electrical conductivity of the cathodes, resulting in high discharge capacity and improved cycle life.

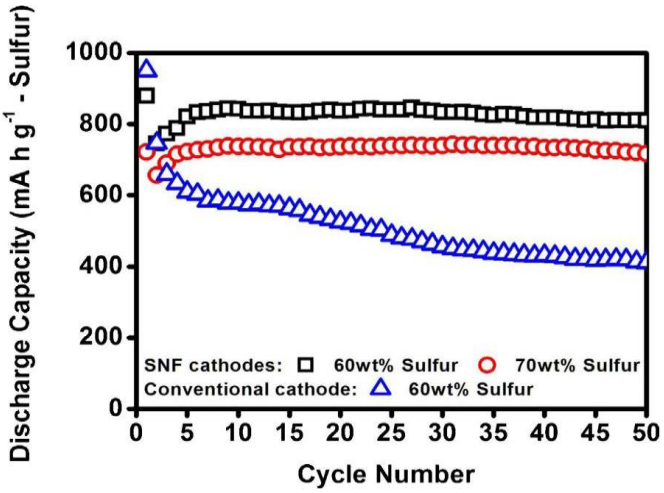

Figure 3.5: Cycling profiles of lithium-sulfur cells with the SNF cathodes and conventional cathodes at a C/5 rate.

3.3.1.4 Self-discharge behavior

Another improvement associated with the SNF cathodes is the decrease in the self-discharge behavior of the cells over a long-term storage time as shown in Figure 3.6. In Figure 3.6a, cells employing SNF cathodes retain 86 % of their original discharge capacity after three weeks of resting, which almost stop fading over the following resting times. After two months of resting, the cells maintain 85 % of their original capacity. In Figure 3.6b, the OCV of SNF cathodes remains at a constant value of around 2.4 V over the same period of time. The excellent capacity retention and the stable OCV over long-term storage indicate that applying the SNF cathodes could significantly suppress the self-discharge problems of current lithium-sulfur batteries. Some groups have also found that the self-discharge of lithium-sulfur batteries is related to the physical properties of the current collectors and their ability to protect the sulfur cathodes.[39, 40] In our study, we found that cells applying the conventional cathodes with flat aluminum foil current collectors still suffer severe self-discharge as reported in the literature.[33] After only one week of storage time, conventional batteries lose 59 % of their original discharge capacity in addition to a continuously decreasing OCV from 2.4 to lower than 2.2 V as shown in Figure 3.6.

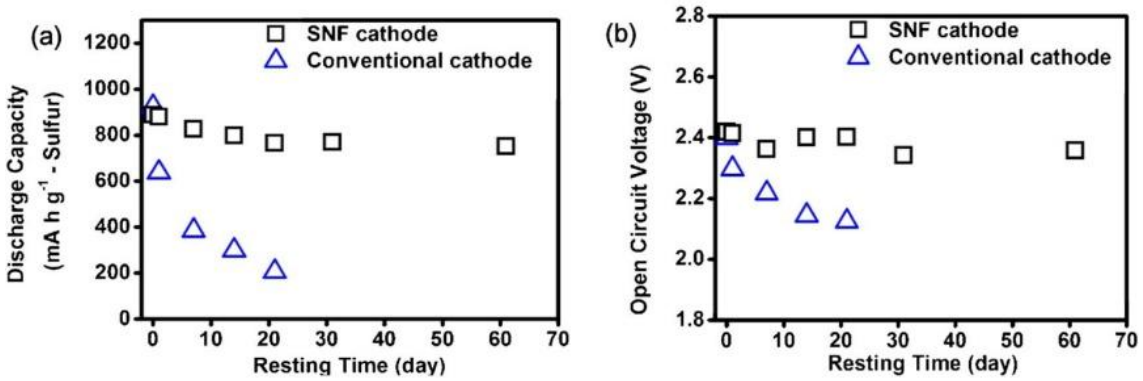

Figure 3.6: (a) Self-discharge analysis and (b) open-circuit voltage of the SNF cathodes and the conventional cathodes with different resting times.

The discharge curves after different storage times seen in Figure 3.7 show the superior storage capability of the SNF cathodes in comparison to the conventional cathodes. In Figure 3.7a, the discharge curves of the SNF cathodes show a slight fade from 888 to 766 mA h g^{-1} in the initial three weeks, then stabilize after that point. The discharge curves also maintain separate and complete upper and lower plateaus after two months of storage time. The overlapped discharge curves further indicate that the active material and accessible reaction surface are well maintained by the porous structure of the SNF cathodes. In contrast, the discharge curves of the cells with conventional cathodes show an obvious capacity fade as seen in Figure 3.7b. A severe reduction of the upper plateau appears after the cells have rested for only one day, corresponding to a capacity fade of 250 mA h g^{-1}. When the resting time increases, the lower discharge plateau starts to shrink, corresponding to the continuous capacity fade. The disappearance and shrinking of the discharge plateaus may result from the dissolution of sulfur and the formation of Li_2S_2/Li_2S from polysulfides during long-term storage.[39, 40]

In the mathematical model reported by Mikhaylik and Akridge,[33] the low self-discharge of the SNF cathodes can be assessed by their low estimated self-discharge constant (K_S), which can be evaluated by comparing the remaining upper plateau discharge capacity (Q_H) and original upper plateau discharge capacity (Q^0_H) with the resting time (T_R) via a self-discharge constant equation: $\ln (Q_H / Q^0_H) = - K_s T_R$.[33] The experimental calculation evidences that SNF cathodes offer a low rate of self-discharge with a low self-discharge constant value of 7.2×10^{-3} per day, which is less than 1/20 of the value of the conventional cathodes (1.6×10^{-1} per day) as shown in Figure 3.7c. The low self-discharge constant and the linear fitting tendency conclude that the nickel foam matrices are important containers, which can avoid the active material continuously and slowly dissolving into the electrolyte during long-term storage. This eliminates the severe loss of active material and the irreversible capacity fading problem facing slurry-cast sulfur electrodes.[33, 40]

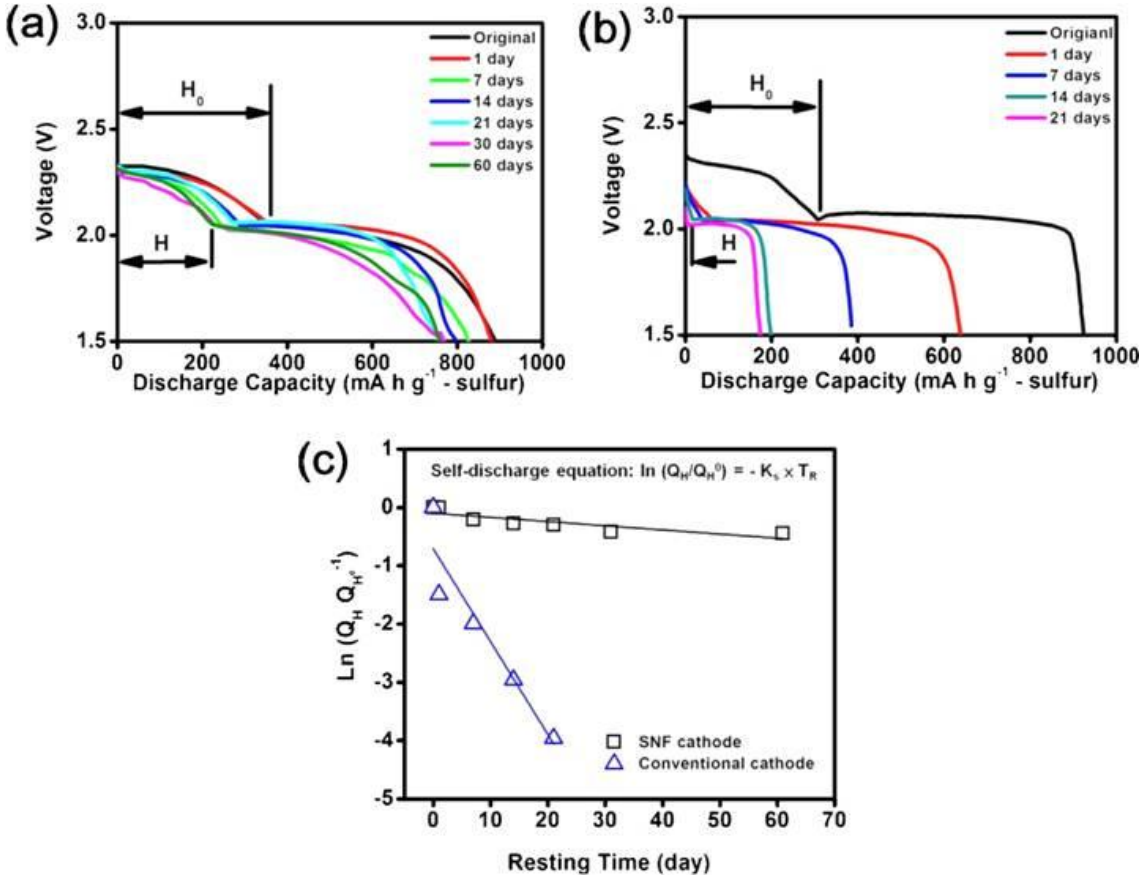

Figure 3.7: Self-discharge analysis: (a) initial discharge curves of the SNF cathodes, (b) initial discharge curves of the conventional cathodes after different resting times, and (c) natural logarithm of upper plateau discharge capacity (Q_H) divided by the original upper plateau discharge capacity (Q^0_H) as a function of resting time (T_R).

3.3.1.5 Morphological analysis of cycled cathodes

After 50 cycles, the SNF cathodes were retrieved from the coin cells. The cross-section, surface, and broken surface morphological changes were investigated by SEM, as shown in Figure 3.8. In comparison to the fresh SNF cathodes seen in Figure 3.3c and 3.3d, the filled active material maintains a constant porous morphology after 50 cycles. The dark porous background is the active material and the bright interwoven parts are the framework of the nickel foam. In Figure 3.8a, the active material remains well

distributed in the pore spaces and is tightly trapped by the 3D skeleton of the nickel foam after cycling. These microstructures indicate that the pore spaces serve as adsorption sites and cages to accommodate the active material and limit the diffusion of lithium polysulfides during cycling. In Figure 3.8b, the surface morphology of the cycled SNF cathodes maintains a constant porous surface architecture, suggesting that the accessible reaction surface is remained. Figure 3.8c shows the broken surface morphology of the 3D SNF cathodes after 50 cycles. The broken surface samples are useful to investigate the inner structure and morphological changes in the SNF cathodes. The inner active material uniformly coats and wraps around the surface of the nickel foam conductive framework, even after 50 cycles. This close connection creates optimized electron pathways in the SNF cathodes, resulting in improved discharge capacity and excellent cyclability.

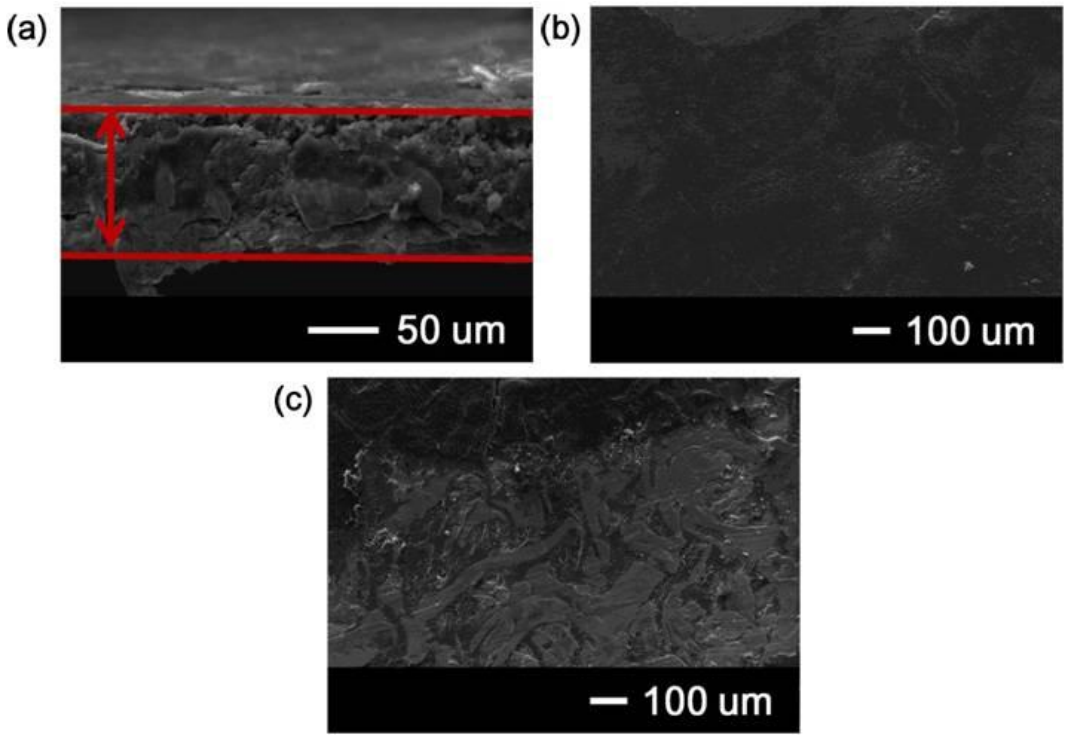

Figure 3.8: SEM morphology of the (a) cross section, (b) surface, and (c) broken surface of the SNF cathodes after 50 cycles at a C/5 rate.

3.3.1.6 Electrochemical impedance spectroscopy

To further demonstrate the superior electrochemical performance of SNF cathodes, AC impedance measurements were performed on cells with the fresh SNF cathodes and conventional cathodes, as shown in Figure 3.9a. The impedance of the cells decreases with the SNF cathodes. Generally, the AC impedance spectrum of Li-ion battery system has three major parts based on the various frequency regions.[59, 131] In the high-frequency region, the real part of the impedance (the intercept on the x-axis) corresponds to the Ohmic resistance. In the middle-frequency region, the semicircles arise from the charge-transfer impedance. In the low-frequency region, an inclined line denotes the Warburg impedance. In our study, the decrease of impedance is mainly due to the reduction of the charge-transfer resistance because of the use of the high electrically conductive framework of the nickel foam as the current collector. Moreover, the 3D porous electrode architecture of SNF cathodes further reduces the impedance through enlarging the contact area between the active material and the current collector. Figure 3.9b and 3.9c compare the impedance of the cells with SNF cathodes and conventional cathodes after different cycles. After the first cycle, the impedance of SNF cathodes first decreases, then remains at a constant low impedance value, as shown in Figure 3.9b. The decrease in the impedance may be attributed to the rearrangement of the physically stable active material occupying amore electrochemically favorable position, implying a closer con-tact and better coverage between the active material and nickel foam after the first cycle. The constant impedance spectra after the first cycle confirm that SNF cathodes undergo stable and reversible electrochemical cycling processes. However, in contrast, the cells using conventional cathodes exhibit continuously increasing impedance after the first cycle, indicating poor cyclability and severe capacity fade.

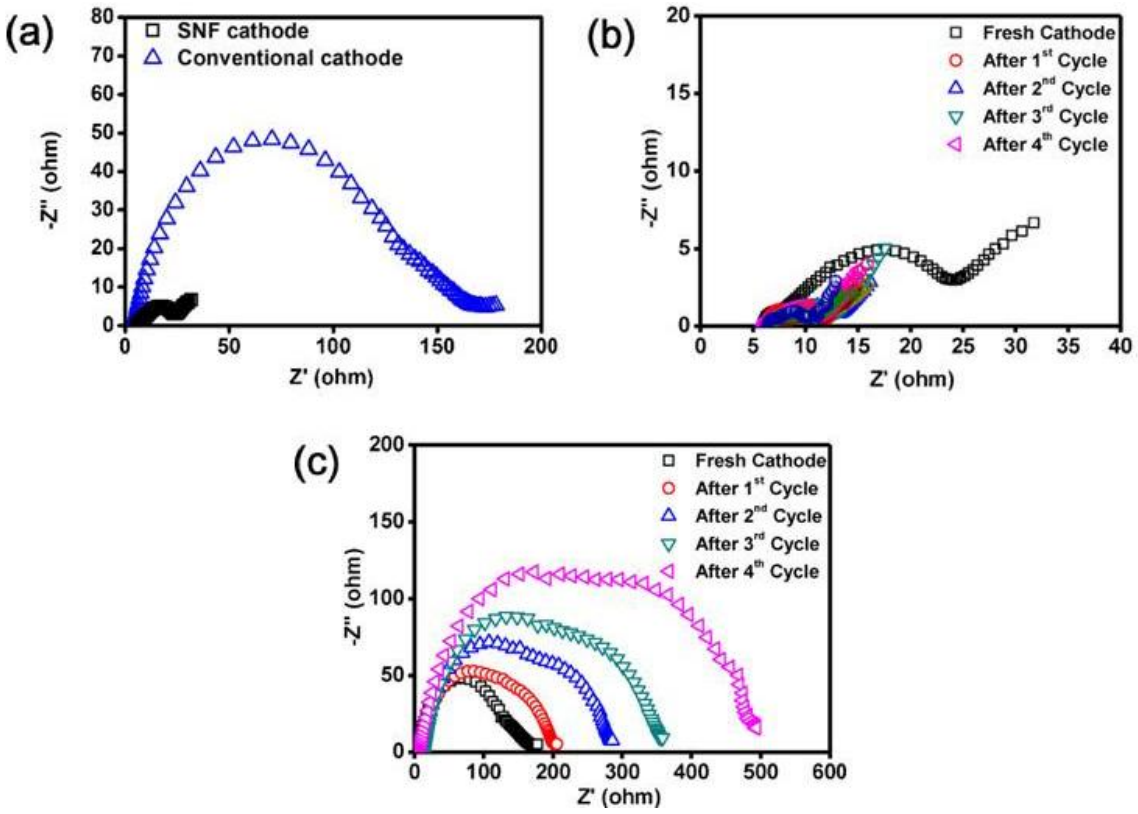

Figure 3.9: (a) Impedance of the cell employing the SNF cathodes compared with that employing the conventional cathodes, (b) impedance of the cell with the SNF cathodes after different cycles, and (c) impedance of the cell with conventional cathodes after different cycles.

3.3.1.7 Summary

3D sulfur-nickel foam (SNF) cathodes based on porous and conductive nickel foam have been fabricated by a facile and precise paste-absorption method, which can enhance the contact between the active material and the conductive skeleton of the nickel foam. The microstructure shows that the active material fills and is tightly absorbed by the abundant pore spaces of the nickel foam. The inner pore spaces serve as ductile containers to accommodate the active material and retain polysulfides in the cathode region during battery storage and cycling processes. Meanwhile, the uneven multilayer

surface of the SNF cathodes enlarges the accessible reaction surface areas by a rugged 3D framework. These properties allow for decreased impedance and excellent cycle stability. Cells with the SNF cathodes achieved an average discharge capacity of > 810 mA h g^{-1} for 50 cycles, and maintained 85% of their initial capacity after two months of resting time. The superior cycle stability, high capacity retention, and low self-discharge indicate that SNF cathodes are a viable approach to improve the cycle performance of lithium-sulfur batteries.

3.3.2 Nano-cellular carbon current collector: a lightweight, porous carbon current collector

Lithium-sulfur batteries have been investigated with a simple modification of the electrode configuration by applying a nano-cellular carbon current collector (NC current collector). This micro-/meso-/macro-porous electrode is composed of interwoven carbon fibers with the carbon nanofoam firmly attached to them. The nanofoam plate functions as a reservoir to store the active material and localize the dissolved polysulfides, stabilizing the electrochemical reaction within the cathode region. As a result, the NC current collector offers a considerably high discharge capacity and superior cycle stability.

3.3.2.1 Structure and microstructure analysis of the active-material container

To examine the advantages of micro-/meso-/macro-/porous current collectors, nitrogen adsorption-desorption isotherms and pore-size distribution curves were analyzed by BET measurements of the NC current collectors, the fresh S-NC cathodes, and the cycled cathodes. The NC current collector has a specific surface area of 194 m^2 g^{-1} and a pore volume of 0.58 cm^3 g^{-1}. In Figure 3.10a, isotherms of the NC current collectors can be identified as mixed IUPAC types I & IV for a micro- and meso-porous structure.[182] Below the relative pressure of $P/P_0 < 0.1$, the nitrogen adsorption in this low-pressure region matches the IUPAC type I isotherms for microporosity.[174, 182] At $P/P_0 = 0.1 – 1.0$, the typical hysteresis loop results from the capillary condensation phenomenon of the

mesoporous structure, matching the IUPAC type IV classification for mesoporosity. In Figure 3.10b, the essential micro- and meso-porous absorption sites have diameters, respectively, of 1.4 – 2.0 nm and 6.5 – 50 nm. The mesopores with large diameters further facilitate high active material loading.[61]

The surface area and pore volume of the S-NC cathodes are, respectively, 66 m^2 g^{-1} and 0.51 cm^3 g^{-1}. First, the comparatively smaller surface area and pore volume demonstrate that the active material takes the micro- and meso-pores as absorption sites. Moreover, the decrease of the pore volume contributed by micropores matches with the disappearance of the type I adsorption characteristic shown in Figure 3.10a. Additionally, the mesopores with a diameter of 2 – 6 nm appear after active material loading, as shown in Figure 3.10b. After the active material slurry penetrates into the large mesopores and macroporous channels, these pores, which are partially filled up with the active material, turn into mesopores later.[58] The newly formed and retained mesopores conform well to the hysteresis loop shown in Figure 3.10a. After cycling, the surface area of the S-NC cathodes decreases to 20 m^2 g^{-1}, corresponding with the decrease in pore volume to 0.20 cm^3 g^{-1}. In Figure 3.10a, the retention of the mesopore hysteresis loop in the cycled cathodes evidences that the configuration of cathodes maintains the porous structure after cycling. Also, as seen in Figure 3.10b, the absence of micropores and the decrease in mesopores after cycling indicate that these pores fully play the role of absorption sites and help contain the rearranged sulfur particles or long-chain lithium polysulfides.

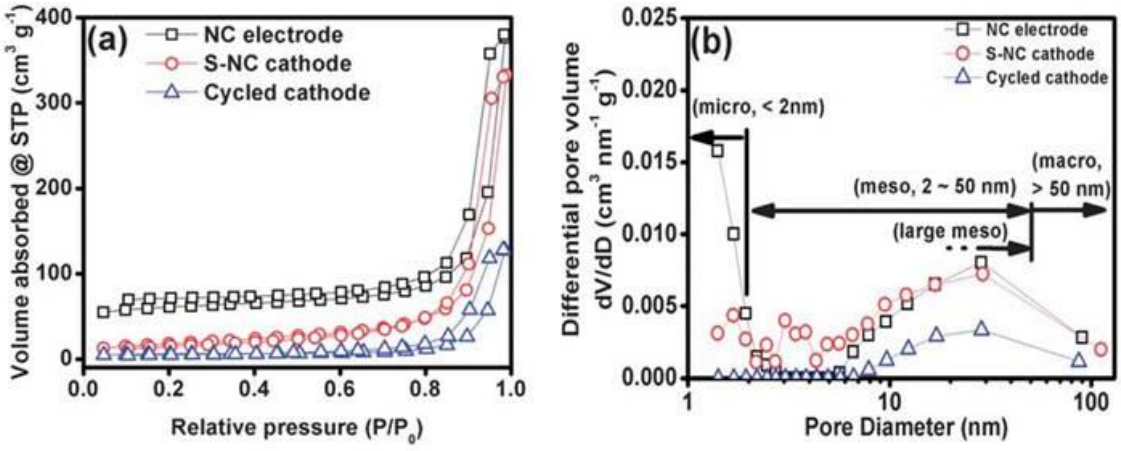

Figure 3.10: Surface area analysis: (a) isotherms and (b) pore size distributions of the NC current collectors, fresh S-NC cathodes, and cycled S-NC cathodes.

The architectural advantages of the micro-/meso-/macro-porous current collectors were further investigated by microstructural analyses. In Figure 3.11a and 3.11b, the surface and cross-sectional scanning electron microscopy (SEM) images of the NC current collectors show the open cell and the continuous porous framework. The porous framework includes interspersed macroporous channels, interwoven carbon fibers, and carbon nanofoam plates. The apertures between the plates form macroporous channels, which are important for our porous cathode preparation process[135] and have been reported to be a necessary conduit for electrolyte permeation.[58, 173] The interwoven carbon fiber serves as an inner electron pathway to offset the resistance from the insulating sulfur and strengthens the mechanical properties of the current collector. The strong mechanical properties and structural integrity allow NC current collectors to endure the volume change of the active material during cycling. Figure 3.11a and 3.11c evidence that the carbon nanofoam plates are firmly attached onto the carbon fibers. The attached nanofoam (Figure 3.11d) possesses ordered meso- and micro-porosity simultaneously as evident by the BET and SEM data.

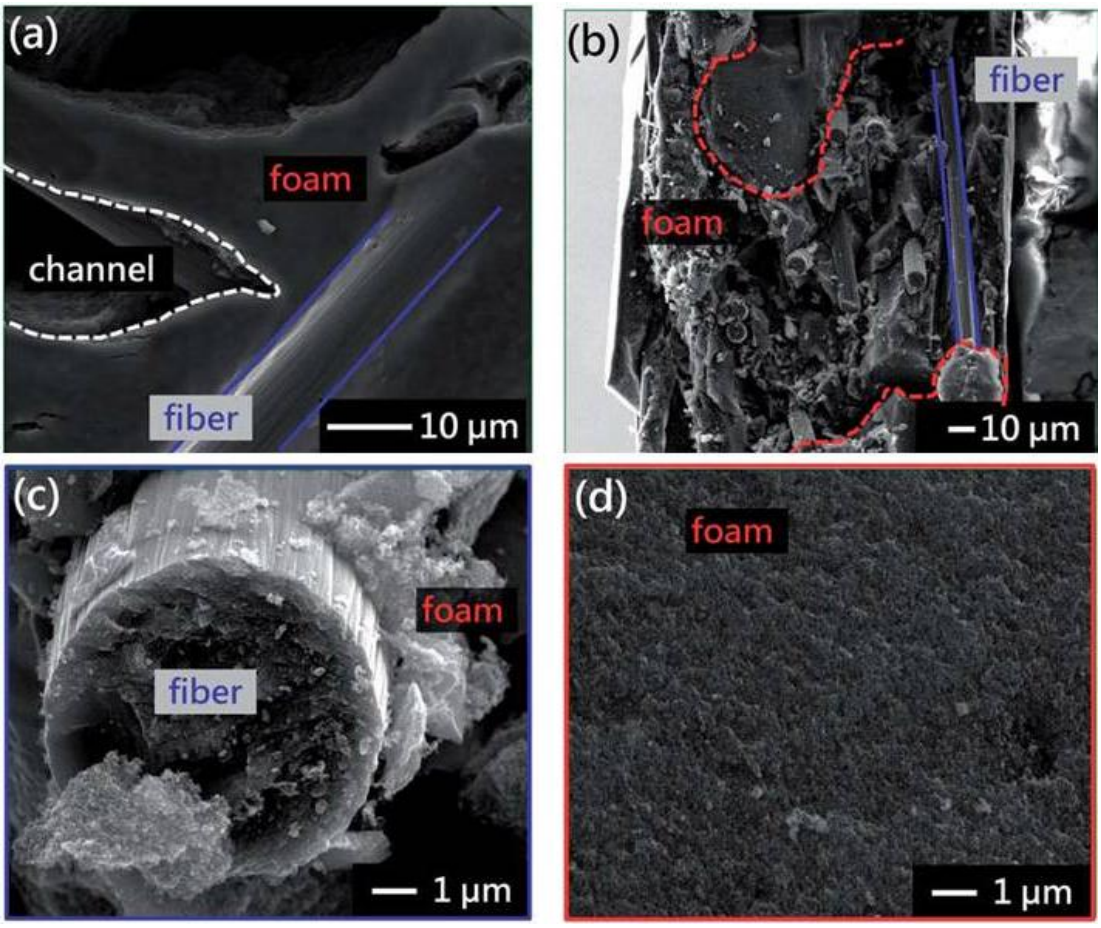

Figure 3.11: Microstructure and morphology of the NC current collectors: (a) surface SEM image, (b) cross-sectional SEM image, (c) cross-sectional image of the carbon fiber, and (d) cross-sectional image of the carbon nanofoam plate.

3.3.2.2 Structure and microstructure analysis of the carbon nanofoam

Scanning transmission electron microscopy (STEM) with element mapping of the S-NC cathodes before and after cycles shows the uniform and undiminished sulfur distribution (Figure 3.12). Therefore, the nanofoam plates are essential absorption sites and effective containers for the active material.

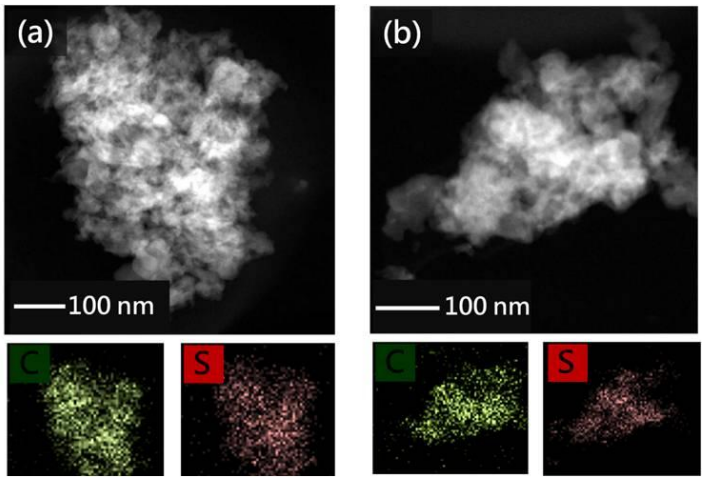

Figure 3.12: STEM and EDS microanalysis of (a) the fresh S-NC cathodes and (b) the cycled S-NC cathodes.

To confirm the importance of the nanofoam reservoir, high-magnification SEM/EDS with elemental mapping was carried out on the cross-sectional carbon nanofoam before and after sulfur impregnation and after cycling as presented in Figure 3.13. In Figure 3.13a, the nanofoam plates of NC current collectors show uniform micro- and meso-porous architecture. When the NC current collectors were impregnated with the active material, the macroporous channel network allowed the active material to penetrate inside the carbon framework. Thus, the active material was able to tightly coat the surface of the carbon framework and fill the inner pores (Figure 3.13b). The porous morphology shows no obvious changes after sulfur impregnation. However, the EDS spectra and elemental mapping detected from the interior part of the cross-section of the carbon nanofoam prove that sulfur was absorbed inside the carbon micropores. In Figure 3.13c, the cycled cathodes still exhibit strong sulfur EDS signal and a uniform sulfur mapping image, which demonstrates that the embedded sulfur is maintained in the porous spaces and the dissolved polysulfides may infiltrate later into the micro- and mesopores. The BET, SEM, TEM and EDS analytical data all confirm that the porous network of NC current collectors stores the active material successfully. Importantly, the nanofoam plates are the major reservoirs to suppress the severe active material loss.

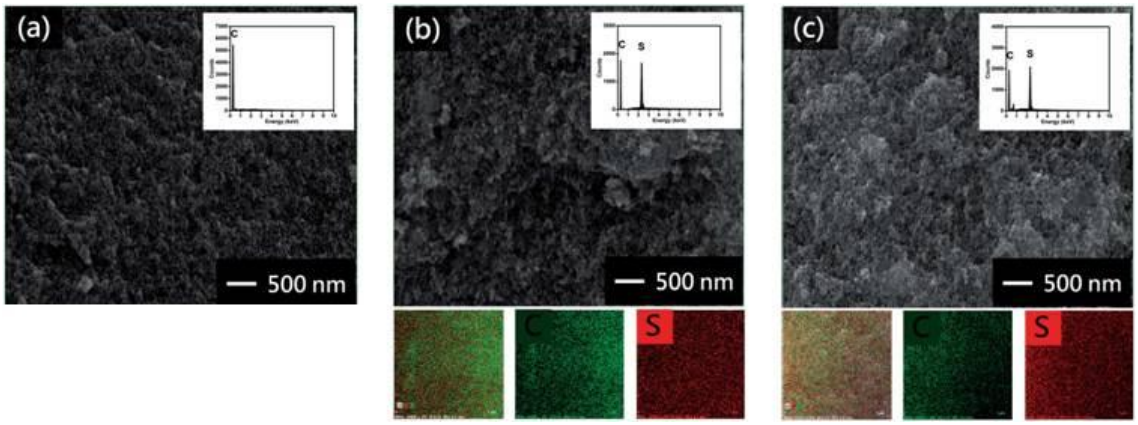

Figure 3.13: Cross-section SEM images and EDS microanalysis of the carbon nanofoam plates from the (a) NC current collectors, (b) fresh S-NC cathodes with elemental mapping, and (c) cycled S-NC cathodes with elemental mapping.

After cycling, the encapsulated active material and newly trapped Li_2S_8/S_8 mixtures exhibit a homogeneous distribution and close contact with NC current collectors as presented in Figure 3.14a. Furthermore, the cycled cathodes maintain complete sulfur coverage, as evidenced by the undiminished sulfur EDS signal and the uniform sulfur element mapping data. The active material encapsulated in the cycled cathodes shows a rough appearance with only slight agglomeration, which may be the trapped Li_2S_8/S_8 mixtures after cycling.[55, 180] Although the rearranged or trapped active material agglomeration may cause local insulating zones in S-NC cathodes, the conductive carbon skeleton can transport electrons to break through the inactive region and continually reactivate the absorbed active material. In addition, there is no obvious insulating Li_2S/Li_2S_2 precipitation on the fully discharged S-NC cathodes (Figure 3.14b and 3.14c). This indicates that the accessible reaction area is protected from the deposition of the inactive precipitates, which is usually covered on the surface of the conventional sulfur cathodes (Figure 3.14d to 3.14f). Moreover, electrolyte absorption tests were conducted with the fresh S-NC cathodes and conventional cathodes to identify the necessity of the electrolyte conduit in the S-NC cathodes. The average amount of electrolyte absorbed by the S-NC cathodes (20.3 μL cm^{-2}) was considerably higher than that superficially

adsorbed by the conventional flat cathodes (9.0 μL cm^{-2}). The high electrolyte absorption capability ensures that the electrolyte easily penetrates inside the cathodes, which localizes the discharge/charge reactions occurring in the cathode region.

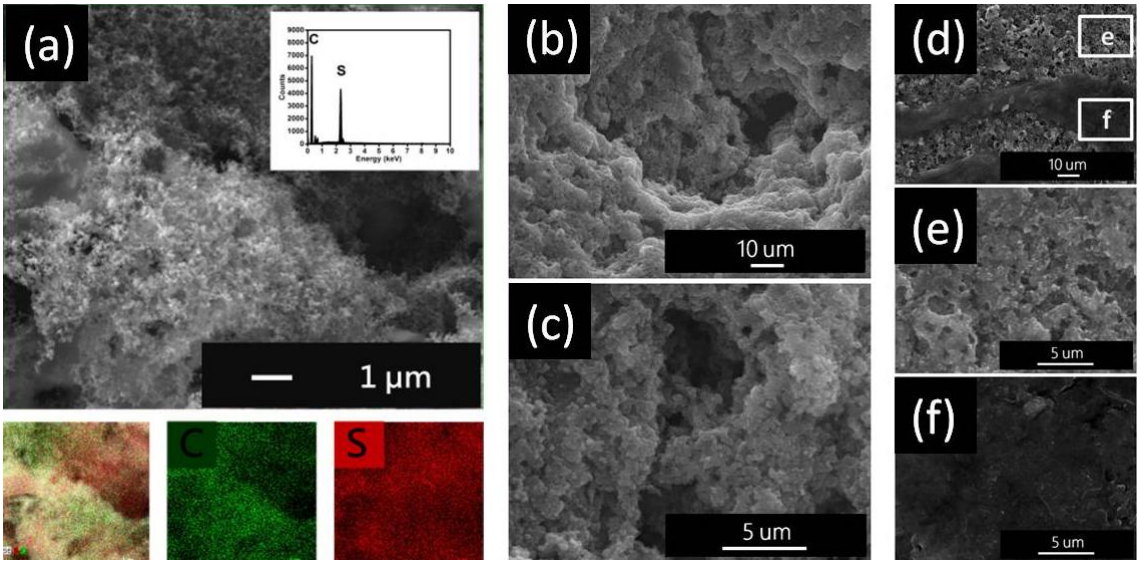

Figure 3.14: Surface SEM images and EDS microanalysis: (a) cycled S-NC cathodes with elemental mapping, (b) S-NC cathodes after the initial discharge process, (c) high-magnification SEM images of (b) and (d) conventional 2D cathodes after the initial discharge process, (e) high-magnification SEM image of the light area in (d), and (f) high-magnification SEM image of the dark area in (d).

3.3.2.3 Electrochemical performance

The stabilized cycling mechanism of the S-NC cathodes was investigated by cyclic voltammetry (CV) measurements and charge/discharge voltage profiles. Figure 3.15a shows the CV curves of S-NC cathodes in the initial five cycles. The charge and discharge reactions are in accordance with the typical sulfur oxidation/reduction reactions.[181] The two cathodic peaks, starting at 2.4 and 2.1 V, correspond to the two-step reduction reaction from elemental sulfur (cyclic S_8) to soluble lithium polysulfides (Li_2S_x, x = 4 – 8) to insoluble Li_2S_2/Li_2S mixtures.[26] At 2.3 – 2.4 V during charging, the two

overlapped anodic peaks are attributed to the reversible oxidation reaction from Li_2S_2/Li_2S to elemental sulfur or long-chain polysulfides.[32] More importantly, the overlapped sharp cathodic and anodic peaks display no obvious peak intensity and potential changes, which indicates an electrochemically stable environment within the S-NC cathodes. This results in good reversibility of the reduction/oxidation reactions during repeated cycling processes.

Typical charge/discharge voltage profiles of the S-NC cathodes at different cycling rates (C/2, C/5, and C/10) are presented in Figure 3.15b – 3.15d. The charge/discharge curves nearly overlap and correlate with the anodic/cathodic peaks in the CV curves as shown in Figure 3.15a. These overlapped upper and lower discharge plateaus at different cycling rates demonstrate the superior cyclability of the S-NC cathodes. At C/5 and C/10 rates, the fully utilized upper discharge plateau (theoretical value is 419 mA h g^{-1}) solidly evidences that no active material loss has occurred in this system.[17, 33] As the cell voltage approaches 2.8 V, the vertical voltage rises which suggests that batteries employing S-NC cathodes can be completely charged.[26, 75, 180] At a C/10 rate, the reduction reaction of the $LiNO_3$ additives occurs, causing an additional discharge plateau beginning at 1.8 V.[36]

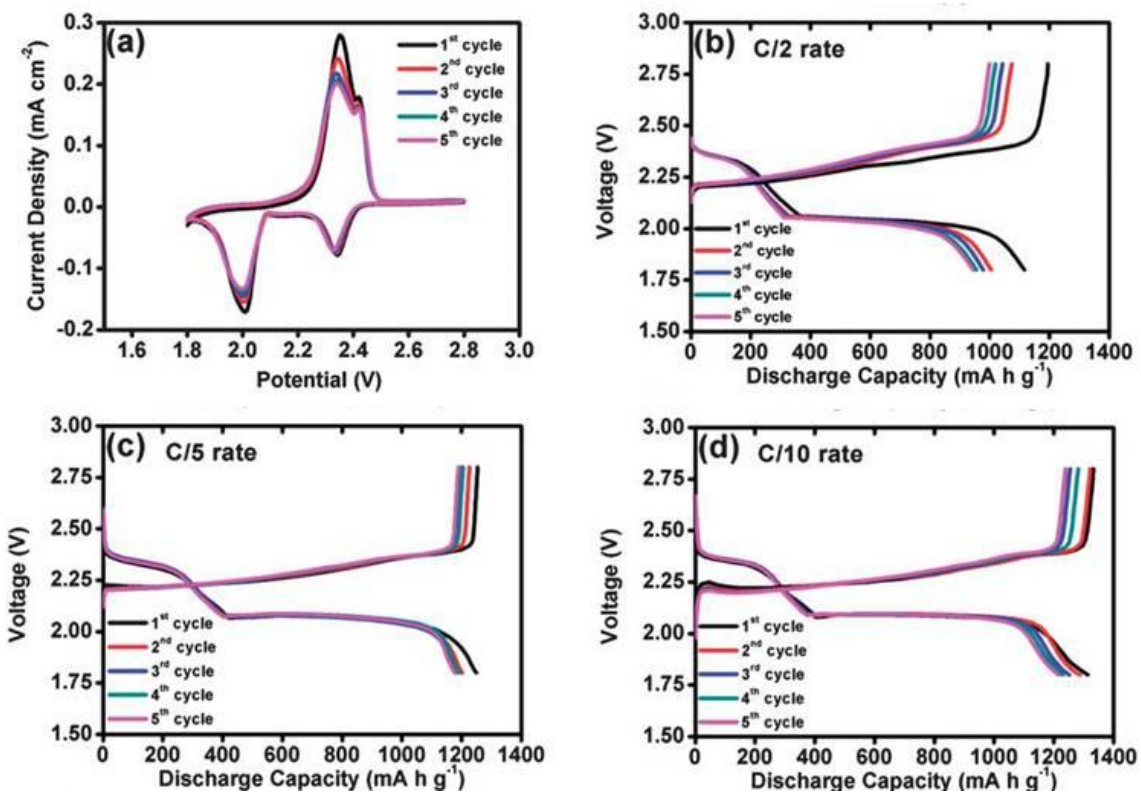

Figure 3.15: Electrochemical cyclability analysis: (a) cyclic voltammetry plots at a scan rate of 0.1 mV s^{-1} at 1.8 – 2.8 V and charge/discharge profiles of the S-NC cathodes at (b) C/2 rate, (c) C/5 rate, and (d) C/10 rate.

3.3.2.4 Cycling performance

Figure 3.16a reveals that the S-NC cathodes have high discharge capacity, superior cycling performance, and high capacity retention. Application of the S-NC cathodes in lithium-sulfur cells raises the initial discharge capacity of pure sulfur cathodes from 871 mA h g^{-1} to 1249 mA h g^{-1}, which approaches 75 % of the theoretical capacity of sulfur (1672 mA h g^{-1}). The simple structural improvement of the current collector offers considerable improvement in the discharge capacity and cycle stability in subsequent cycling processes. The electrochemical behavior of the modified lithium-sulfur cells was investigated by electrochemical impedance spectroscopy (EIS) as

shown in Figure 3.16b. The substantial shrinkage in the charge transfer resistance (R_{ct}) after applying the S-NC cathodes indicates that the highly conductive NC current collectors successfully reduce the resistance from the insulating sulfur.[19] Therefore, the embedded carbon skeleton functions effectively as an inner electron pathway to enhance the active material utilization and electrochemical kinetics.

The S-NC cathodes exhibit both high discharge capacities and superior cycle stability at different cycling rates as shown in Figure 3.16c. The initial discharge capacities of the S-NC cathodes approach 1314, 1249, and 1116 mA h g^{-1} at, respectively, C/10, C/5, and C/2 rates. After 50 cycles, the discharge capacities are 1107, 994, and 838 mA h g^{-1}, which represent capacity retentions of 84 %, 80 %, and 79 %. Also, this configuration modification further extends the cycle life of the sulfur cathodes to over 100 cycles as shown in Figure 3.16d. At the C/10 rate, the cell maintains a high capacity of 955 mA h g^{-1}, with a capacity retention of 73 % after 100 cycles. The stable cyclability and the high capacity retention result from the same factors: the micro-/meso-/macro-porous structure of the NC current collectors. First, the macropores directly channel the electrolyte into the surrounding micro- and mesoporous absorption sites. This phenomenon maintains an intimate contact between the electrolyte, active material, and carbon matrix, thereby improving the sulfur utilization and limiting the shuttle effect.[18, 58] Second, the porous electrodes tightly hold the active material in their absorption sites.[173] Thus, the micro-/meso-.macro-pores may localize the electrochemical processes inside the S-NC cathode region, avoiding severe active material loss and alleviating the shuttle effect.

The merit of this investigation is the feasibility. Therefore, it is important to raise the sulfur loading while still maintaining improved cycling performance. Accordingly, the sulfur loading in the S-NC cathodes was increased from 1.8 to 2.2 mg cm^{-2}. However, the cycling performance of the cells remains excellent as seen in Figure 3.17. The high tolerance of the S-NC cathodes for sulfur loading can be attributed to the large mesopore size in the NC current collectors.[61]

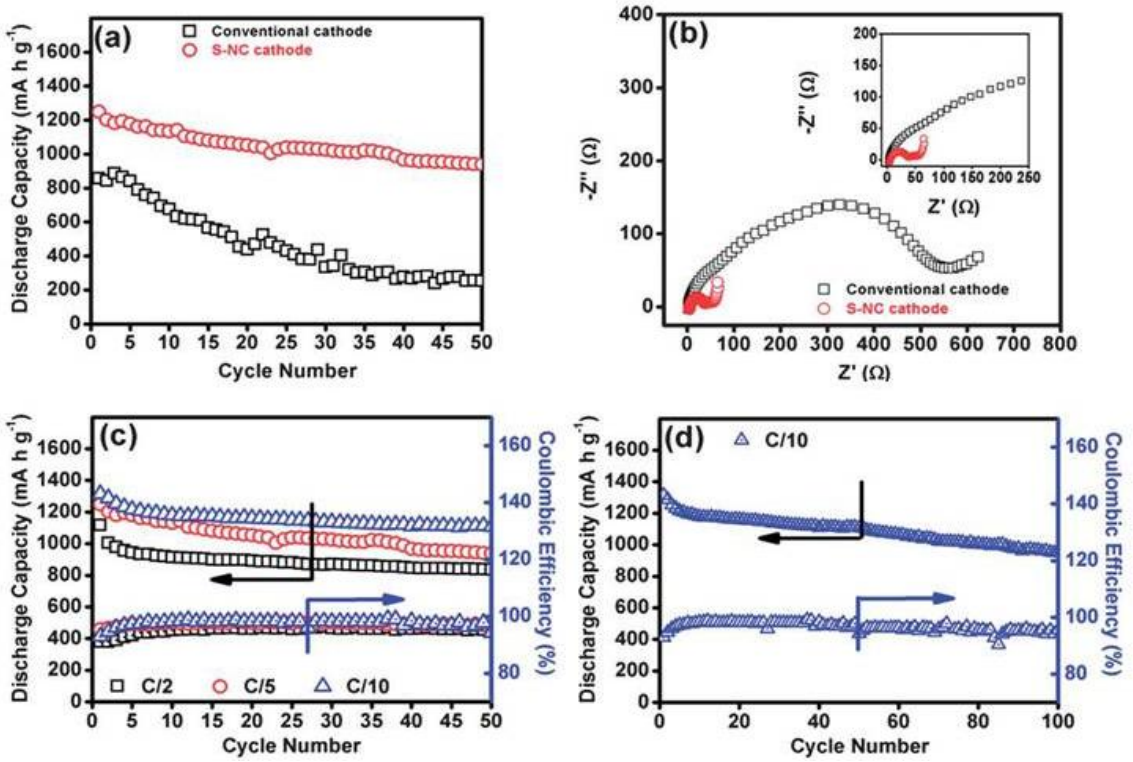

Figure 3.16: Electrochemical properties of S-NC cathodes with 70 wt. % sulfur: (a) cyclability of the cells at a C/5 rate, (b) Nyquist plots of the cells measured with fresh cathodes, (c) cyclability of the cells with the S-NC cathodes at different cycling rates, and (d) long-term cyclability of the S-NC cathodes at a C/10 rate.

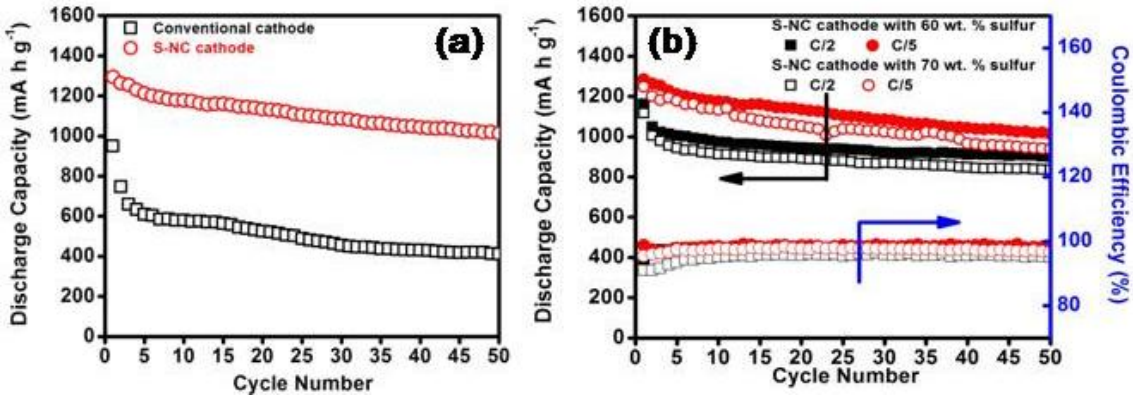

Figure 3.17: Cyclability of the lithium-sulfur cells: (a) comparison of the S-NC cathodes and the conventional cathodes with 70 wt. % sulfur at C/5 rate and (b) S-NC cathodes with 60 and 70 wt. % sulfur cycled at different cycling rates.

3.3.2.5 Summary

A simple architecture improvement of the cathodes provides a high discharge capacity of 1314 mA h g^{-1} with a good capacity retention of 84 % after 50 cycles. Furthermore, the high sulfur loading and facile cathode preparation attest that this bifunctional electrode is an attractive current collector for lithium-sulfur cell development. These improvements are associated with the micro-meso-macro-porous carbon framework. The inner electrically conductive skeleton is the key aspect, which increases the discharge capacity and active material utilization. The NC current collector further inhibits active material loss and the polysulfide shuttle effect via its micro-/meso-/macro- porosity to accommodate the active material, retain polysulfides, and channel the electrolyte. Combining the high absorption capability with intimate active material coating, the S-NC cathodes effectively constrain the electrochemical reactions within the cathode region, thereby providing superior cycling stability. In conclusion, application of alternative current collectors with a unique 3D structure is an attractive strategy to overcome the technical limitations of lithium-sulfur batteries.

3.3.3 Porous carbon current collector: a lightweight, porous CNF current collector

Lithium-sulfur batteries with a porous carbon current collector (PCCC), high sulfur loading (2.3 mg cm^{-2}, equal to 80 wt. % sulfur content), high capacity, and long cycle life have been fabricated with a simple one-step paste absorption method. The intimate contact between the insulating sulfur and the embedded conductive matrix allows high active material loading. The high absorptivity of electrolyte by the PCCC facilitates efficient retention of soluble polysulfides within the PCCC, so the 3D cathode architecture stabilizes the electrochemical reaction within the porous space.

3.3.3.1 Microstructure

In Figure 3.18a and 3.18b, the coalescing carbon fiber matrix of the PCCC shows abundant porous spaces for storing the active material and absorbing the electrolyte,

implying that the 3D PCCC can stabilize the electrochemical reaction within its porous architecture.

First, during cathode preparation, the highly porous network channels the active material paste to penetrate into the PCCC, achieving good sulfur coverage on the interwoven fibers, as evidenced in the SEM images/scheme of the fresh cathodes (Figure 3.18c and 3.18d). The sulfur particles with diameters of 2 – 4 μm were first wrapped by the conductive carbon black with a diameter of 30 – 60 nm and then were tightly coated onto the carbon fibers. The elemental mapping data reconfirm intimate sulfur coating on the carbon substrate. Second, during cell assembling and cycling, the porous network turns to channel the electrolyte to wet the coated active material, accomplishing excellent electrolyte immersion and thereby localizing the active material and the electrolyte within the porous cathode.[135, 173] The SEM images/scheme of the cycled cathodes (Figure 3.18e and 3.18f) reveal the absence of large-size sulfur agglomerations. In addition, the more uniform sulfur signals detected in the elemental mapping indicates that the active material migrates to the electrochemically favorable positions. The rearranging active material results in a conversion of large sulfur particles/agglomeration into uniform, small particle dispersion and then is stored within the porous network and absorbed in the nano-size conductive carbon black clusters. Therefore, the cycled cathodes retain the unblocked electrolyte channel for electrolyte immersion/penetration. As a result, the rearranging active material and the absorbed electrolyte closely contact with the conductive carbon network and are localized within the porous matrix. The SEM image of the broken surface of the sulfur-PCCC cathode (Figure 3.18g) prepared by removing the surface active material with a razor blade shows excellent active material coverage/encapsulation.

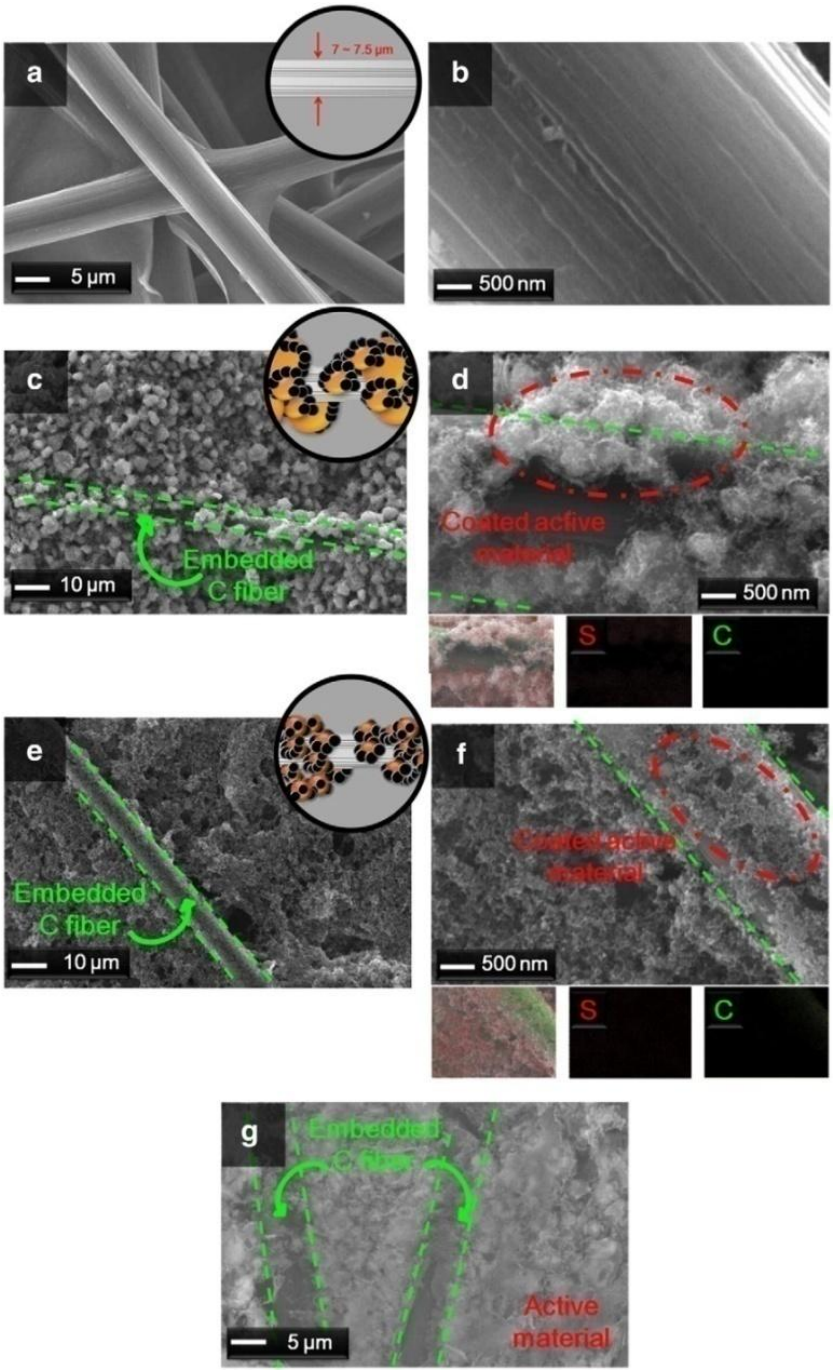

Figure 3.18: SEM images: (a) PCCC, (b) PCCC under high magnification, (c) fresh cathode, (d) fresh cathode under high magnification, (e) cycled cathode, (f) cycled cathode under high magnification, and (g) cathode configuration of the porous cathode.

3.3.3.2 Electrochemical analysis

The EIS of the fresh cathodes (Figure 3.19a) shows that the PCCC significantly decreases the charge-transfer resistance from 595 to 59 Ω because the embedded conductive substrate effectively reduces the resistance of the coated active material. Figure 3.19b to 3.19d show the discharge/charge curves of the sulfur-PCCC cathodes at various rates. Those overlapped curves show no obvious decline in capacity during cycling, demonstrating the high reversibility. The upper discharge plateau at 2.35 V and lower discharge plateau at 2.0 V represent the reduction from sulfur to long-chain polysulfides and from polysulfides to Li_2S_2/Li_2S. The overlapped charge plateaus represent the backward reaction from Li_2S_2/Li_2S to Li_2S_8/S.[10, 181] The long lower discharge plateaus at various rates suggest improved active material utilization, as indicated by an enhancement in the initial discharge capacity from 845 mA h g^{-1} (AFCC; only 50% of the theoretical value) to 1205 mA h g^{-1} (PCCC; 72% of the theoretical value). Moreover, the upper discharge capacities at various rates approach the theoretical value (419 mA h g^{-1}).[183] In the subsequent cycles, the upper plateau discharge capacities remain nearly the same, implying limited active material loss.[33] The inhibited polysulfide dissolution further limits the polysulfide shuttling, as evidenced by the vertical voltage rise at 2.8 V (the end of charge).[33, 135] The CV curves of the cells with PCCC for the initial five cycles (Figure 3.19e), displaying the two separated cathodic peaks and the two overlapped anodic peaks, are consistent with the discharge/charge profiles (at a C/10 rate).[33, 180, 181] The overpotential of the cathodic peak at 2.35 V disappears after the initial cycle because the rearranging active material occupies the electrochemically favorable sites. Therefore, in the subsequently scanning, the overlapped CV curves show no peak intensity and potential changes.

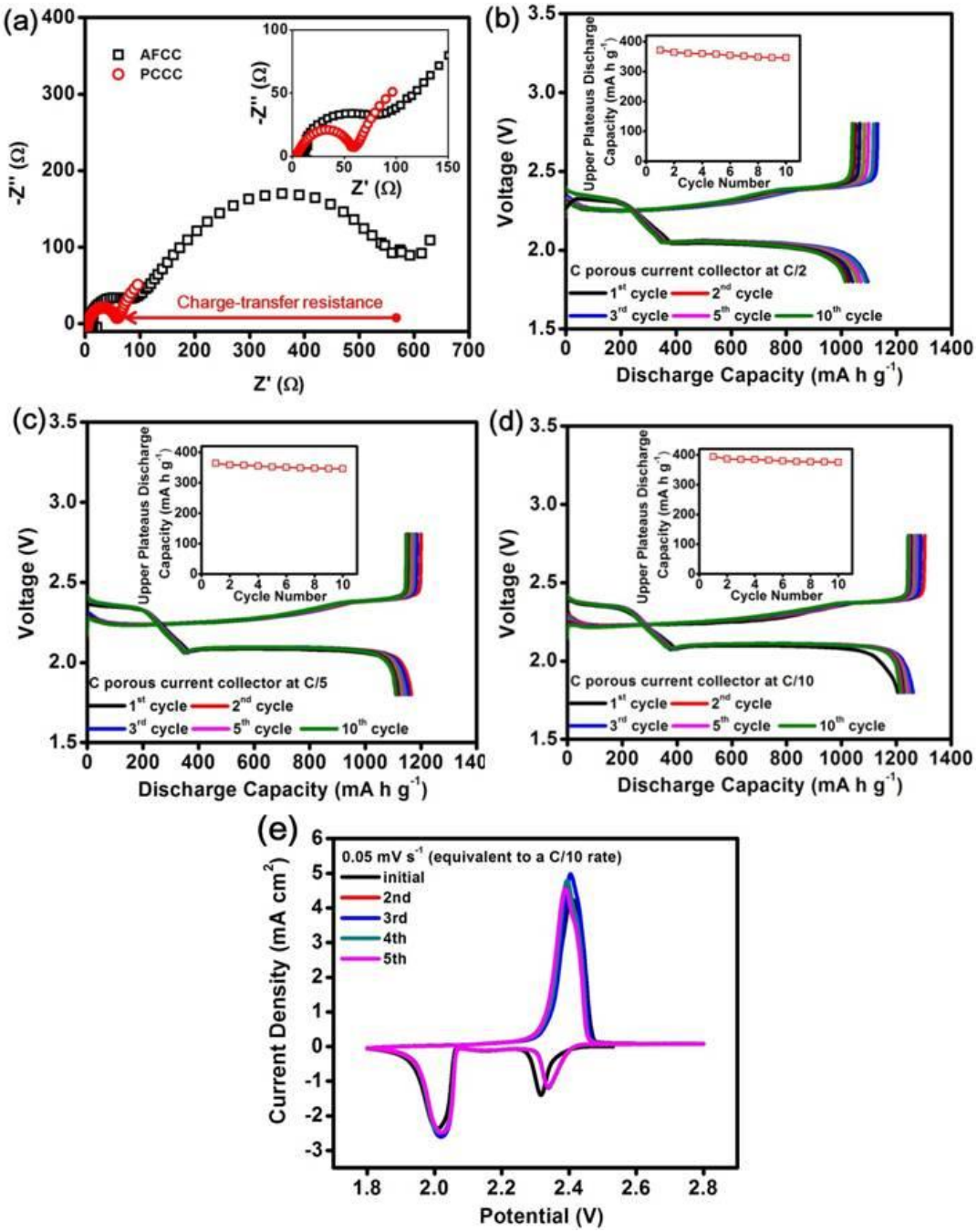

Figure 3.19: Electrochemical properties of the porous cathode (PCCC): (a) EIS of fresh cathodes, discharge/charge curves at (b) C/2, (c) C/5, and (d) C/10 rates (the insert displays the variation of the capacity in the upper plateau with cycling), and (e) CV curves at a 0.05 mV s^{-1} scanning rate.

3.3.3.3 Cycling performance

Figure 3.20a shows the cycling performances of the cells with 70 wt. % sulfur content at various cycling rates. The cells with sulfur-PCCC cathodes exhibit high discharge capacity with stable cyclability. The discharge capacities of the cells are 1080, 961, and 767 mA h g^{-1} at, respectively, C/10, C/5, and C/2 rates for over 50 cycles. The corresponding capacity retentions are 90, 85, and 74% and the Coulombic efficiencies are 98, 96, and 95 %. The high cycling stability of the cells at slow rates of discharge could result from the following: (i) the soluble polysulfides have sufficient time to be absorbed by the porous substrate and (ii) the Li_2S formed may be converted easily during subsequent charge.[135, 171]

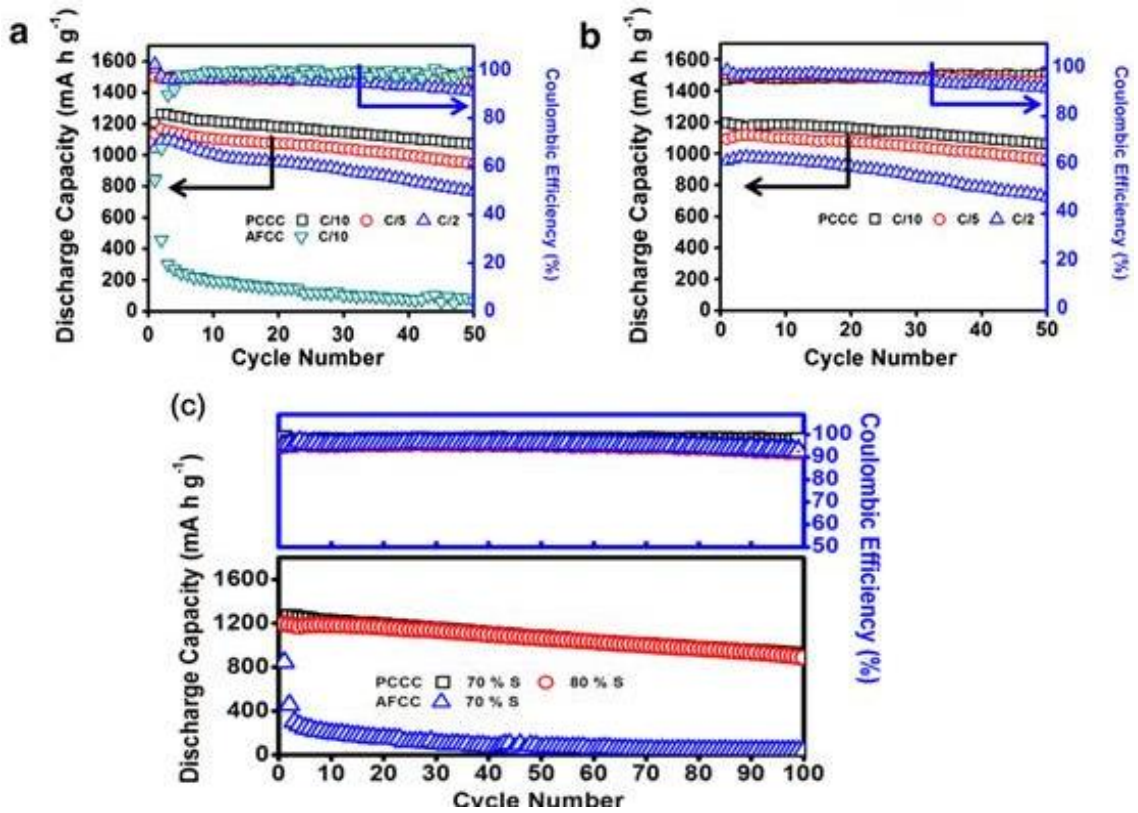

Figure 3.20: Cycling performances: (a) cathodes with 70 wt. % sulfur content at various cycling rates, (b) cathodes with 80 wt. % sulfur content at various cycling rates, and (c) cycle life of various cathodes at a C/10 rate.

The cells applying the sulfur-PCCC cathodes further allow a higher sulfur content of 80 wt. % compared to our previous porous cathode systems[135, 176] and exhibit high discharge capacity and excellent cycle stability (Figure 3.20b). The outstanding cell performance even at such high sulfur loading of 2.3 mg cm^{-2} is due to the following: (i) intimate contact of the insulating sulfur with the wrapping carbon nano-particles and the coalescing carbon fiber framework and (ii) excellent electrolyte absorptivity. The amount of electrolyte absorbed in the porous cathodes is 26.0 μL cm^{-2} (70 wt. % sulfur) or 23.0 μL cm^{-2} (80 wt. % sulfur), which is much higher than that adsorbed on a flat cathode (9.0 μL cm^{-2}). The PCCC system thus suppresses the loss of active material by absorbing efficiently the electrolyte that contains the dissolved polysulfides.[174, 176, 184] Therefore, the PCCC system with sulfur contents of 70 and 80 wt. % displays longer cycle life with a higher discharge capacity (900 mA h g^{-1}) and Coulombic efficiency (above 94 %) compared to the AFCC system that suffers from severe capacity fade (Figure 3.20c).

3.3.3.4 Summary

In summary, sulfur cathodes with a uniform active material distribution within a porous carbon current collector have been prepared by a facile, low-cost paste-absorption method. The high porosity of the carbon substrate allows high sulfur loadings (up to 2.3 mg cm^{-2}) and provides remarkable electrolyte absorption. The intimate contact between the coalescing carbon fibers and the active material that is also wrapped by the nano-carbon particles results in high discharge capacity. The high electrolyte absorptivity retains the dissolved polysulfide within the cathode structure, achieving superior cycle stability.

3.3.4 Porous polysulfide absorbents

The carbonized eggshell membrane (CEM) powder with abundant micropores and high porosity is embedded within conventional sulfur cathodes (CEM-S cathodes) as a

CEM-polysulfide absorbent for lithium-sulfur batteries. The CEM-polysulfide absorbent effectively limits the irreversible active-material loss from CEM-S cathodes and prevents the formation of severe inactive agglomerations on the surface of the cathode during cycling. In addition to trapping the migrating polysulfides, the conductive and porous CEM facilitates efficient electron transport and electrolyte immersion, which ensures successive reactivation and reutilization of the trapped active material. As a result, the CEM-S cathodes with a reasonable sulfur content of 60 wt. % exhibit a high capacity retention rate of 85 % and a low capacity fade rate of 0.10 % per cycle for 150 cycles. Such superior cycle stability suggests that natural starting materials with unique porous structures can be utilized to manufacture high-performance cell components for lithium-sulfur cells.

3.3.4.1 Morphology and Microstructure analysis

Porous CEMs are expected to absorb the soluble polysulfides within the cathode region via their natural micropores and high porosity,[185-187] as illustrated in Figure 3.21a and 3.21b. During cell discharge, the polysulfides produced are absorbed by the porous CEMs, suppressing the severe polysulfide diffusion. At full discharge, the absorbed polysulfides reduce to Li_2S_2/Li_2S, which are tightly held and surrounded by the conductive CEM and Super P carbon. This avoids the formation of nonconductive precipitation on the exterior surface of the electrodes and improves the connection between the active material and conductive additives.[138, 177] As a reference, the Super P is a commercial conductive carbon commonly used in cathode preparation in lithium-sulfur and Li-ion batteries. During cell charge, the conductive and porous CEM provides efficient electron/charge transport and electrolyte immersion, ensuring the reversible conversion reaction from Li_2S_2/Li_2S to Li_2S_8/S_8.[177, 186]

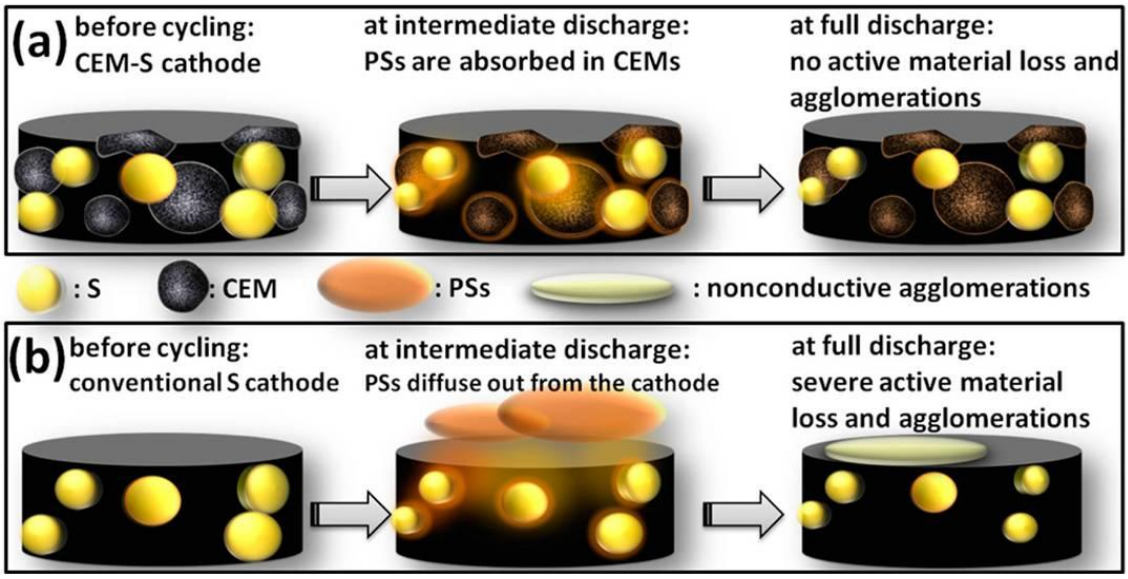

Figure 3.21: Schematics of (a) CEM-S cathode and (b) conventional S cathode.

After carbonization, the organic eggshell membrane converts into a carbon thin film with a uniform fibrous network structure, as shown in the scanning electron microscopy (SEM) images and the corresponding elemental mapping results (Figure 3.22a). Figure 3.22b indicates that the ground CEM powder mainly consists of carbon. The Raman spectrum of CEMs (Figure 3.22c) shows two carbon peaks at ~1349 cm^{-1} (disorder-induced D band) and ~1590 cm^{-1} (graphitic G band). The intensity of the G band to the D band indicates that the CEM is a partially graphitized carbonaceous material, which is known as an appealing electrode material because of its high conductivity.[188]

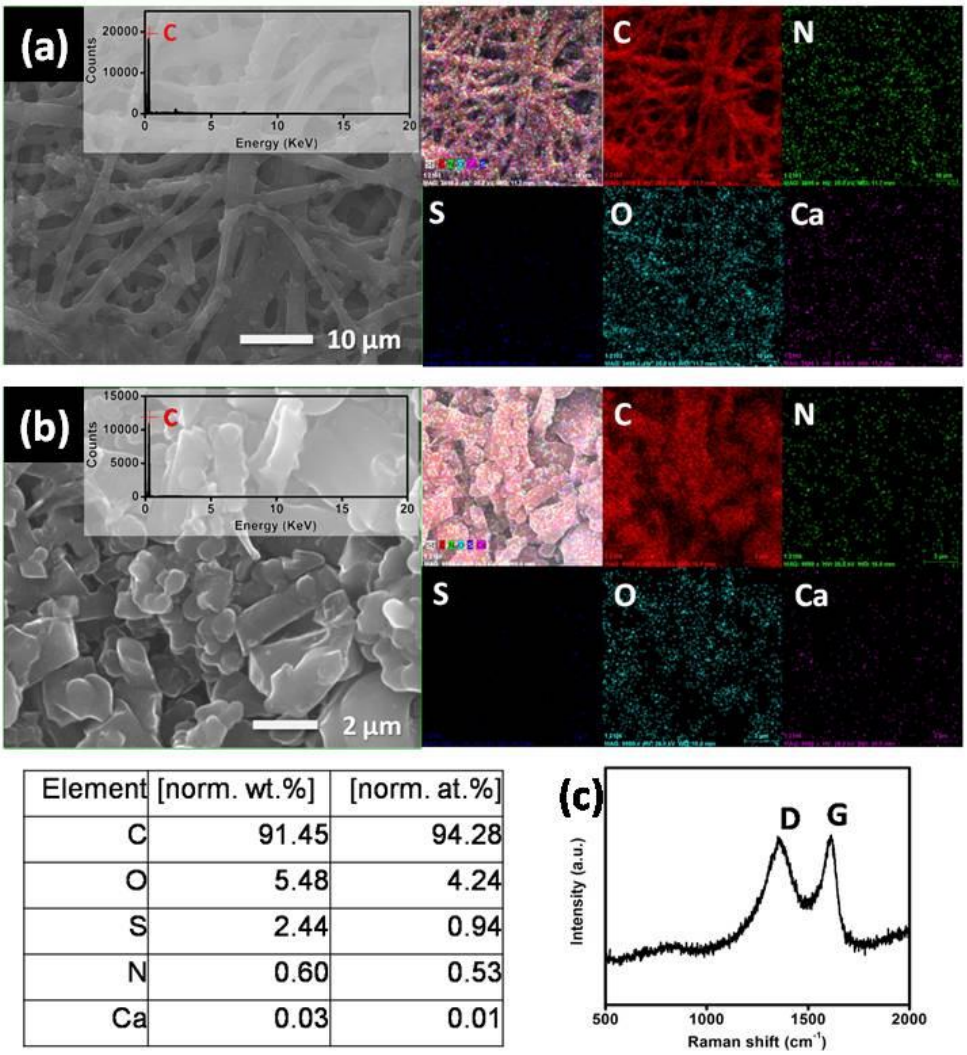

Element	[norm. wt.%]	[norm. at.%]
C	91.45	94.28
O	5.48	4.24
S	2.44	0.94
N	0.60	0.53
Ca	0.03	0.01

Figure 3.22: SEM observation and elemental mapping of (a) the CEM sheet and (b) the CEM powder. (c) Raman spectrum of the CEM powder.

In Figure 3.23a and 3.23b, the high-magnification SEM and high-resolution transmission electron microscopy (TEM) images depict that the CEMs possess abundant micropores intrinsically composited throughout their meso-/macroporous structure. The micropore is the major factor for absorbing the PSs before they escape out of the cathode region.[28, 57, 189] The meso-/macropore functions are the electrolyte pathways for (i) channeling the liquid electrolyte containing the dissolved polysulfides to the micropores

and (ii) transporting charges and electrolyte for reactivating the absorbed active material.[177, 185-187, 189] After immobilizing the diffusing polysulfides, the porous CEM tolerates the volume changes from the trapped active material during repeated cycling, ensuring intimate connection between the active material and conductive carbon. The natural micropores and high porosity of CEMs are assessed by nitrogen adsorption-desorption isotherms (Figure 3.23c) and pore-size distribution curves (Figure 3.23d). The CEM has a high surface area of 487 m^2 g^{-1} with a micropore area of 315 m^2 g^{-1} and a total pore volume of 0.31 cm^3 g^{-1} with a micropore volume of 0.25 cm^3 g^{-1}. The IUPAC type I isotherms[182] and a high fraction of micropores in the pore-size distribution curves demonstrate high microporosity in CEMs. On the other hand, the Super P conductive carbon shows a relatively low surface area (63 m^2 g^{-1}) with no micropores.

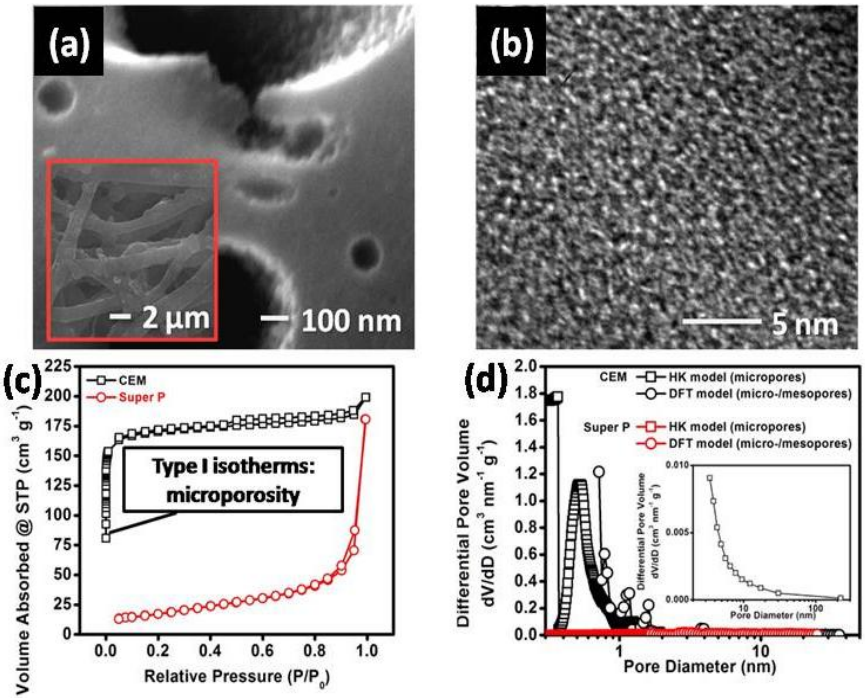

Figure 3.23: Microstructural analysis of CEMs: (a) SEM observation (inset is CEM sheet), (b) TEM observation, (c) Brunauer-Emmett-Teller (BET) isotherms, and (d) pore-size distributions with Horvath-Kawazoe (HK) and density functional theory (DFT) models (inset is Barrett-Joyner-Halenda (BJH) model).

3.3.4.2 Electrochemical characterization

Figure 3.24a shows the cyclic voltammetry (CV) curves of the CEM-S cathode at a scan rate of 0.05 mV s^{-1} during the initial 20 cycles. During cell discharge, the CV curves display the typical two-step reduction reactions. The cathodic peak I starting at ~ 2.4 V indicates the reduction reaction from S_8 to soluble polysulfides. The cathodic peak II starting at ~2.1 V corresponds to subsequent reduction reaction from soluble polysulfides to the end-discharge products (Li_2S_2/Li_2S).[17, 154, 180, 181] During cell charge, the two overlapping anodic peaks III and IV represent the continuous oxidization reactions from Li_2S_2/Li_2S to polysulfides and from polysulfides to Li_2S_8/S_8.[13, 52, 56] The overlapping anodic peaks depict that the S_8^{2-} intermediate with a facile oxidation kinetic may be one of the end-charge products.[52] During repeated cycling, the CV curves exhibit overlapping cathodic and anodic peaks, indicating good electrochemical stabilization of the CEM-S cathode. Figure 3.24b presents the discharge/charge profiles of the cell utilizing the CEM-S cathode at a C/10 rate for 150 cycles. The cycling rate (C/10) is based on the mass and theoretical capacity of sulfur (C = 1672 mA g^{-1}). During long-term cycling (150 cycles), the well-retained upper-discharge plateaus (signified as I) demonstrate that the migrating polysulfides are absorbed into the CEM absorbent, and severe active material loss has not occurred.[17, 154] The almost complete lower-discharge plateaus (signified as II) attest to the excellent reversibility of the CEM-S cathode. During cell charge, the vertical voltage rise from 2.4 to 2.8 V indicates a complete charge reaction.[154, 190] These improvements were not observed with the conventional sulfur cathode (sulfur cathodes without CEMs), as shown in Figure 3.24c.

The electrochemical impedance spectroscopy (EIS) data of the CEM-S cathode (Figure 3.25) exhibit a stable cathode resistance of as low as 40 − 50 Ohm for 30 cycles, which is not seen with the conventional sulfur cathode. The increase in resistance observed in the conventional sulfur cathode may result from the redeposition of the diffusing polysulfides that forms nonconductive agglomerations on the surface of conventional sulfur cathodes during cycling (Figure 3.26).[185-187] The nonconductive agglomeration is believed to be Li_2S/Li_2S_2 mixtures, as reported in the lithium-sulfur

literature.[52, 171] On the other hand, a comparison of the CEM-S cathode before and after cycling shows no obvious morphological changes (Figure 3.27). The cycled CEM-S cathode displays the elemental sulfur signals uniformly distributed in the carbon matrix. These indicate no apparent active material loss from the cathode and no inactive agglomerates on the cathode.

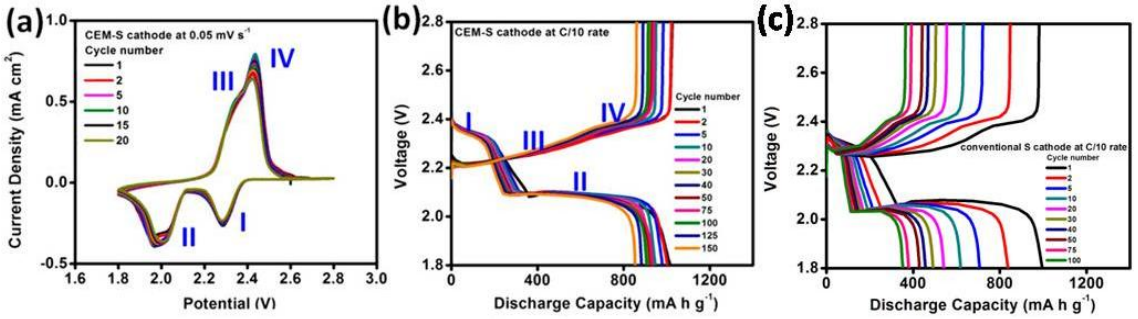

Figure 3.24: Electrochemical measurements of lithium-sulfur cells employing the CEM-S cathode: (a) cyclic voltammograms at a 0.05 mV s^{-1} scanning rate and (b) discharge/charge curves at a C/10 rate. (c) Electrochemical discharge/charge curves of the cell with the conventional S cathode at a C/10 rate.

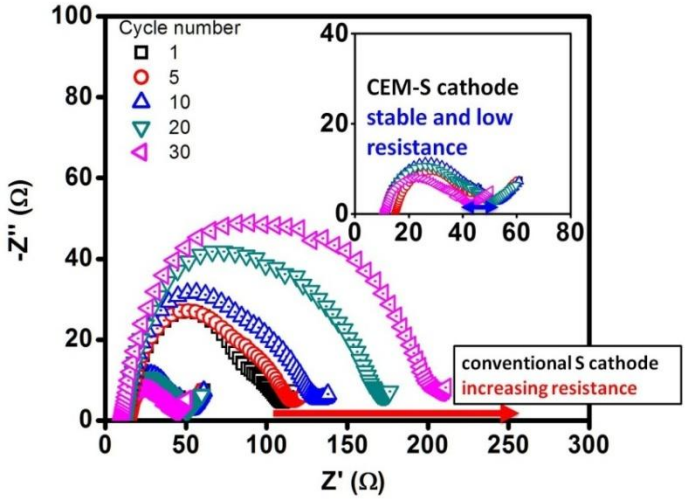

Figure 3.25: Electrochemical impedance spectroscopy (EIS) of the cells with different cathodes. (Inset is the EIS of the cell with the CEM-S cathode).

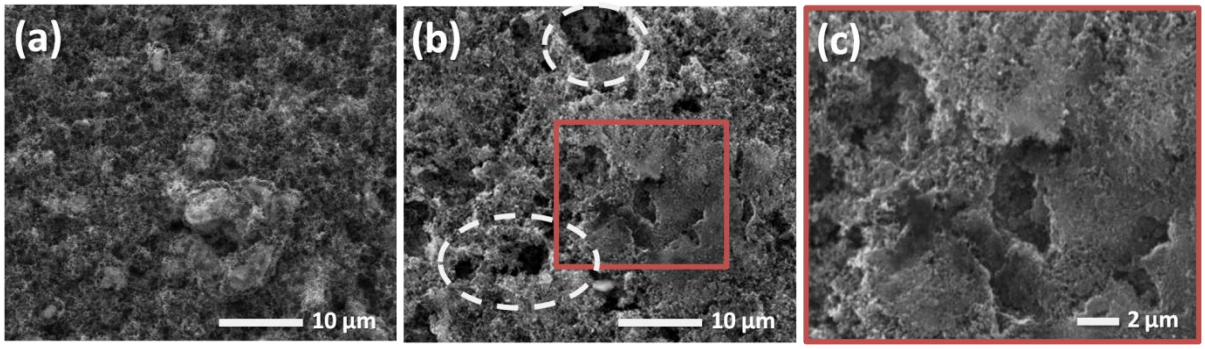

Figure 3.26: SEM observation of the conventional sulfur cathodes (a) before and (b, c) after 100 cycles.

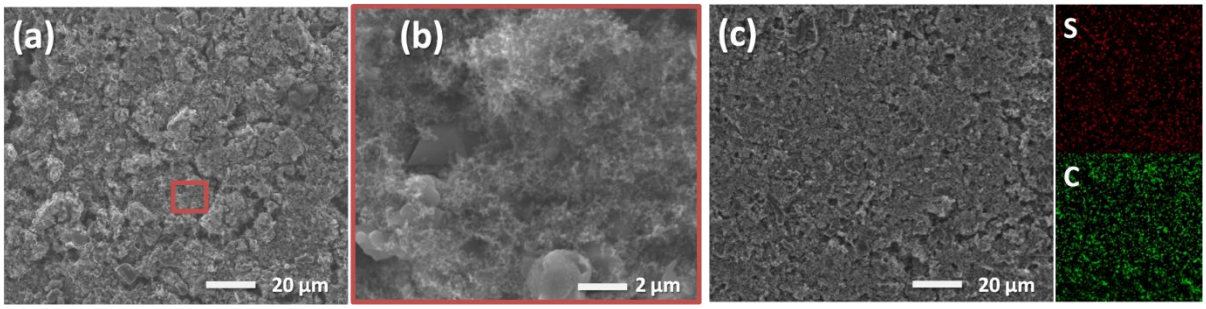

Figure 3.27: SEM observation and elemental mapping of the CEM-S cathodes (a, b) before and (c) after 150 cycles.

3.3.4.3 Cycling performance

Figure 3.28a shows the comparison of the cyclability between the CEM-S cathodes and the conventional sulfur cathode. The initial discharge capacities (Q_1) of the CEM-S cathode and the conventional S cathode are, respectively, 1016 and 1000 mA h g^{-1}. After the first cycle, the CEM-S cathode exhibits a high reversible capacity of 1002 mA h g^{-1} in the second cycle (Q_2) with excellent capacity retention (Q_2/Q_1) of 99%. However, the conventional sulfur cathode shows severe capacity fade from 1000 to 837 mA h g^{-1} (Q_2/Q_1 = 84 %) after one cycle. The high reversibility of the CEM-S cathode indicates that the polysulfides are absorbed by CEMs. Thus, the cycled CEM absorbents

display distinguishable elemental sulfur signals in CEM absorbents, as shown in Figure 3.28b. This confirms that the active material is stabilized within the CEM-S cathode. As a result, the CEM absorbent ensures cells to accomplish stable cyclability over 150 cycles with a reversible capacity of 860 mA h g^{-1} and an average Coulombic efficiency above 98 %, indicating high reversibility and minimal shuttle effect. The corresponding capacity retention (Q_{150}/Q_1) after 150 cycles is 85%, and the capacity fade rate is only 0.10 % per cycle. Such superior cycle stability results from the use of CEM absorbents within the cathode for efficiently absorbing the migrating polysulfides. A comparative analysis with other polysulfide adsorbent/absorbent derived from engineering raw materials indicates that the CEM absorbent offers excellent long-term cyclability for lithium-sulfur batteries (Table 3.1).[185-187, 191-194]

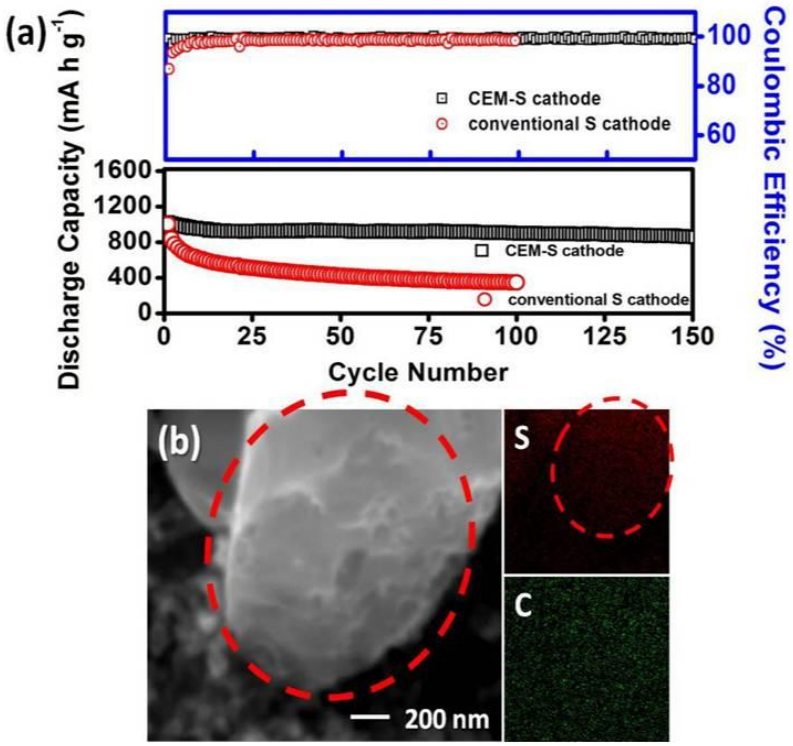

Figure 3.28: (a) Long-term cyclability of the lithium-sulfur cells employing the CEM-S cathode and conventional sulfur cathode. (b) SEM observation and elemental mapping of the cycled CEM absorbent.

Table 3.1: Summary of the performance data of the lithium-sulfur batteries with adsorbents/absorbents.

oxide nanoparticles					
Adsorbent /absorbent	**Content**	**Initial discharge capacity (mA h g^{-1})**	**Reversible capacity (mA h g^{-1}) (cycle life)**	**Capacity retention (capacity fade rate)**	**Cycling parameters**
$Mg_{06}Ni_{0.4}O$ (in pure S cathode)[192]	20 wt % S, 55 wt % C, 15 wt % $Mg_{0.6}Ni_{0.4}O$, and 10 wt % binder	1185	1008 (50 cycles)	85 % (0.3 % per cycle)	0.1C rate at 1.5-3.5 V
γ-Al_2O_3 (in pure S cathode)[194]	50 wt % S, 20 wt % C, 10 wt % γ-Al_2O_3, and 20 wt % binder	750	660 (25 cycles)	88 % (0.48 % per cycle)	0.06C rate at 1.5-3.0 V
$Mg_{06}Ni_{0.4}O$ (in S/ PAN/$Mg_{0.6}Ni_{0.4}O$ composite cathode)[191]	30.8 wt % S, 49.2 wt % PAN/$Mg_{0.6}Ni_{0.4}O$, 10 wt % C, and 10 wt % binder	1545	1223 (100 cycles)	79 % (0.21 % per cycle)	0.1C rate at 1.0 - 3.0 V
engineering porous absorbents					
Adsorbent /absorbent	**Content**	**Initial discharge capacity (mA h g^{-1})**	**Reversible capacity (mA h g^{-1}) (cycle life)**	**Capacity retention (capacity fade rate)**	**Cycling parameters**
SBA-15: silica (in SBA-15-SCM/S composite cathode)[186]	59.85 wt % S, 25.65 wt % C, 9.5 wt % SBA-15, and 5 wt % binder	960	650 (40 cycles)	68 % (0.81 % per cycle)	0.2C rate at 1.5 - 3.0 V
BHPC: pig bone based hierarchical porous carbon (in pure S cathode)[185]	63 wt % S, 6 wt % BHPC, 24 wt % C, and 7 wt % binder	1265	643 (50 cycles)	51 % (0.98 % per cycle)	0.3C rate at 1.5 - 2.8 V
TiO_2 (in SCM/S-TiO_2 composite cathode)[187]	48 wt % S, 28.4 wt % C, 3.6 wt % TiO_2, 10 wt % C, and 10 wt % binder	1201	750 (200 cycles)	62 % (0.19 % per cycle)	1 C rate at 1.5 - 3.0 V
Our approach					
Adsorbent /absorbent	**Content**	**Initial discharge capacity (mA h g^{-1})**	**Reversible capacity (mA h g^{-1}) (cycle life)**	**Capacity retention (capacity fade rate)**	**Cycling parameters**
CEM (in pure S cathode)[178]	60 wt % S, 10 wt % CEM, 15 wt % C, and 15 wt % binder	1016	860 (150cycles)	85 % (0.10 % per cycle)	0.1 C rate at 1.8 - 2.8 V

3.3.4.4 Summary

In summary, the CEM derived from a sustainable natural eggshell membrane with a unique porous structure has been evidenced as polysulfide absorbents for improving the cycle stability of lithium-sulfur cells. The CEM absorbent with inherent microporous absorption sites prevents severe active material loss and redeposition of nonconductive agglomerations on the surface of CEM-S cathodes during cycling. Therefore, the CEM-S cathode with a reasonable sulfur content of 60 wt. % provides cells with a high reversible capacity of 860 mA h g^{-1} and a low capacity fade rate of 0.10 % per cycle for 150 cycles.

3.4 CONCLUSIONS

In conclusion, porous current collectors embedded with pure sulfur cathodes have shown that they can stabilize the active material within the resulting cathode. On the macroscale, the application of porous metal and carbon substrates as the active material container ensures close contact among the insulating active material, charges, and electrolyte with the conductive matrix. The porous current collector inherently has a high mechanical strength to ensure the complete electrode structure is retained during cycling. As such, a stable and fast electrochemical redox reaction is guaranteed. However, the volumetric energy density of the lithium-sulfur cell is strongly related to the thickness of the porous carbon current collector, which should be optimized in future developments. Our solution is to embed porous, conductive polysulfide absorbents within sulfur cathodes to immobilize the migrating polysulfides, facilitate electron transport, and assist electrolyte immersion on the microscale. These holistic mechanisms ensure a successful reutilization of the trapped active material for long cycle lifespan. More importantly, the improved cycle stability results from a small amount of polysulfide absorbents (less than 10 wt. %), which guarantees the sulfur cathode to remain high content of active material. Therefore, the use of porous, conductive substrate enhances the electrochemical reversibility of the resulting cathode and allows further increase in sulfur loading and content in the porous carbon current collector on both macroscale and microscale, which implies a promising gravimetric energy density.

Chapter 4: Development of interlayers*

4.1 INTRODUCTION

To usher the green energy revolution, high-energy rechargeable batteries must utilize cost-effective green materials to achieve commercial viability and global sustainability. The lithium-sulfur battery fulfills the above requirements as the inexpensive and environmentally benign sulfur cathode offers an order-of-magnitude higher capacity (1672 mA h g^{-1}) than the cathodes currently used for lithium-ion batteries.[4, 10, 195] Consequently, lithium-sulfur batteries have received considerable attention and much progress has been made during the past few years. To achieve large-scale commercialization of lithium-sulfur batteries, the following challenges must be solved: (i) poor electrochemical utilization of sulfur, and (ii) low discharge/charge efficiency and short cycle life.[33, 52, 55, 158] First, full utilization of the capacity of a pure sulfur cathode is difficult owing to the insulating nature of sulfur and its discharge products (Li_2S_2/Li_2S).[52, 55] A pure sulfur cathode contains only pure sulfur, a conductive carbon, and a binder. Second, the low Coulombic efficiency and severe capacity fading arise from the shuttle effect of the dissolved polysulfides. The polysulfide intermediates (Li_2S_x, x = 4 – 8) that form during the discharge/charge processes are highly soluble in the liquid electrolyte.[33, 52] The dissolved polysulfides freely diffuse through the separator

---

* S.-H. Chung and A. Manthiram, "A natural carbonized leaf as a polysulfide inhibitor for high-performance lithium-sulfur cells," *ChemSusChem.* 2014, **7**, 1655-1661.

*S.-H. Chung and A. Manthiram, "A hierarchical carbonized paper with controllable thickness as a modulable interlayer system for high performance Li-S batteries, *Chem. Commun.* 2014, **50**, 4184-4187.

S.-H. Chung carried out the cell design and the experimental work. A. Manthiram supervised the project. All participated in the preparation of the manuscript.

* R. Singhal, S-H. Chung, A. Manthiram, and V. Kalra, "A free-standing carbon nanofiber interlayer for high performance lithium-sulfur batteries," *J. Mater. Chem. A* 2015, **3**, 4530-4538.

S.-H. Chung carried out the electrochemical measurements and was supervised by A. Manthiram. R. Singhal carried out the CNF preparation and was supervised by V. Kalra at Drexel University. All participated in the preparation of the manuscript.

and shuttle between the anode and the cathode, resulting in low electrochemical efficiency and severe capacity fading. These shuttling polysulfides further corrode the Li anode and cause loss of active material, shortening the cycle life.[11, 33, 158]

To overcome these challenges, synthesizing sulfur-carbon composites[11, 57, 63, 186, 196-204] and applying surface coatings of conductive polymers[11, 95, 100, 205, 206] are promising ways to improve the discharge capacity and the cycle life of lithium-sulfur cells. Many carbon materials have been engineered to have micro-/meso-porous absorption sites or form a conductive network for storing the active material, trapping the dissolved polysulfides, or absorbing the electrolyte.[11, 58, 62, 64, 138, 189, 201, 207] These advanced cathode nanocomposites and novel composite electrodes utilize conductive and porous substrates in different ways to increase active-material utilization and suppress loss of the active material. However, theoretically, dissolved polysulfide anions will inevitably move toward the anode, driven by the chemical potential and concentration differences between the cathode and the anode during cell discharge. Accordingly, a polysulfide trap in between the sulfur cathode and the separator may be a suitable and an essential cell component for advanced lithium-sulfur cells to localize the polysulfide species at the cathode side of the cell. This concept was first developed by Manthiram group as an "interlayer."[11, 23]

The free-standing interlayer has to be flexible in order to provide smooth contact with the top surface of the cathode. In addition, the interlayer needs to possess a porous structure or a large amount of accessible nanospace to store the shuttling polysulfides. As a result, the interlayer is enabled to work bifunctionally in the cell. First, the inserted interlayer functions as an upper-current collector, which can improve the efficient electron conduction by its high electrical conductivity and fast ion transport through its abundant nanospace. Second, its nanospace further plays a more significant role as the polysulfide-trapping site, which can effectively suppress the migration of dissolved polysulfides. A series of novel interlayer developments and relative analyses demonstrates that using an interlayer is a facile approach to provide lithium-sulfur cells

with high electrochemical utilization and excellent cycle stability. In addition, the interlayer further allows the use of the readily prepared pure sulfur cathodes that contain high sulfur loading.[23, 173, 174]

Here, we focus on the configuration-microstructure-performance relationship of various interlayers, which is the key parameter for the interlayer development. In order to build the fundamental understanding, three differently optimized interlayers (Figure 4.1) were designed: (i) carbonized leaf (CL) interlayer for the surface microstructure and morphology study, (ii) carbonized Kimwipes (CK) interlayer for the thickness study, and (iii) porous CNF interlayer for the pore size, surface area, pore volume, and electrical conductivity study.

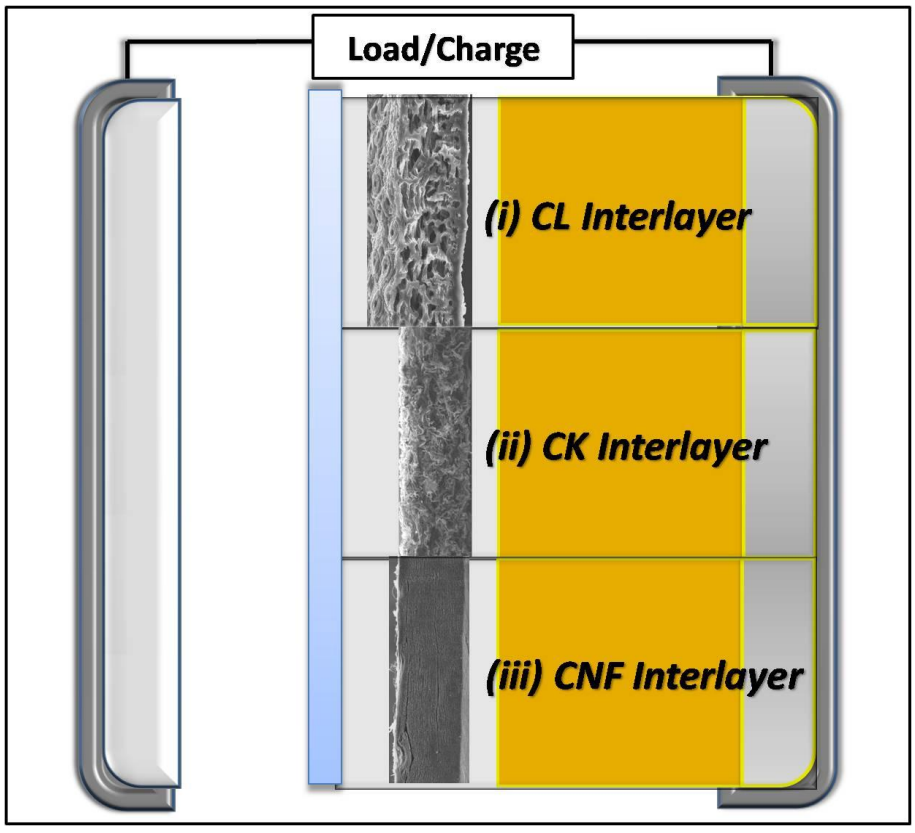

Figure 4.1: Schematic of the cells employing various bifunctional interlayers: (i) CL interlayer, (ii) CK interlayer, and (iii) CNF interlayers.

First, a natural carbonized leaf (CL) interlayer covering on the pure sulfur cathode utilizes a polysulfide locking-film on one side to suppress polysulfide diffusion and an electrolyte reservoir on the other side to absorb the electrolyte containing dissolved polysulfides. The CL interlayer turns a critical organ of higher plants into a key component of highly reversible lithium-sulfur cells. In addition, the CL interlayer that remains its unique architecture and morphology allows us to understand the impact of the surface microstructure and morphology of interlayers on the electrochemical performance.[208]

Second, a carbonized Kimwipes (CK) paper is an effective, low-cost hierarchical interlayer for lithium-sulfur cells. To the best of our knowledge, the CK interlayer with various layer modules is the most inexpensive interlayer substrate and also has a light weight. Moreover, this new interlayer has controllable thickness for analyzing the polysulfide interception mechanism of the interlayer architecture. The layered structure effectively intercepts and traps the migrating polysulfides from one CK interlayer to another, pointing out the importance of interlayer thickness on cycling performance.[209]

Third, a series of free-standing porous CNF interlayers with tunable surface area, porous structure, and electrical conductivity have been studied to enhance the lithium-sulfur battery capacity and cycle life. It was found that the optimized thickness of the interlayer is a critical factor to achieve good cell performance, which is possibly more important than other materials characteristics (*e.g.*, surface area, pore size, pore volume, and conductivity). [210]

4.2 EXPERIMENTAL

4.2.1 Carbonized leaf (CL) interlayer fabrication

The natural leaves were first picked from trees and washed with deionized water. Then, the leaves were supported by a 2.0 cm × 4.0 cm carbon paper (Toray carbon paper H-030, Fuel Cell Earth) to keep a flat film shape and were carbonized for 2 h at 800 ℃ with a heating rate of 2 ℃ min^{-1} in a tube furnace under flowing argon. After carbonization, the carbonized leaves (CLs) formed free-standing carbon thin film, and the

Toray carbon papers could be easily separated from the CLs, indicating that the carbon shape supporter did not influence the electrochemical properties of CLs.[211] The CLs were rinsed again with deionized water for 5 min without any acid/alkali treatments that may alter the natural microstructure [185, 188, 211-213] and were then dried in a convection oven at 100 ℃ before use. A simple schematic fabrication process of the CLs is shown in Figure 4.2. Moreover, the cycled CLs remain in complete thin film shape (Figure 4.2c), evidencing that they have enough mechanical strength for ensuring successful cell assembly and cell cycling. The Toray carbon papers were reused for the next batch of the CL carbonization process.

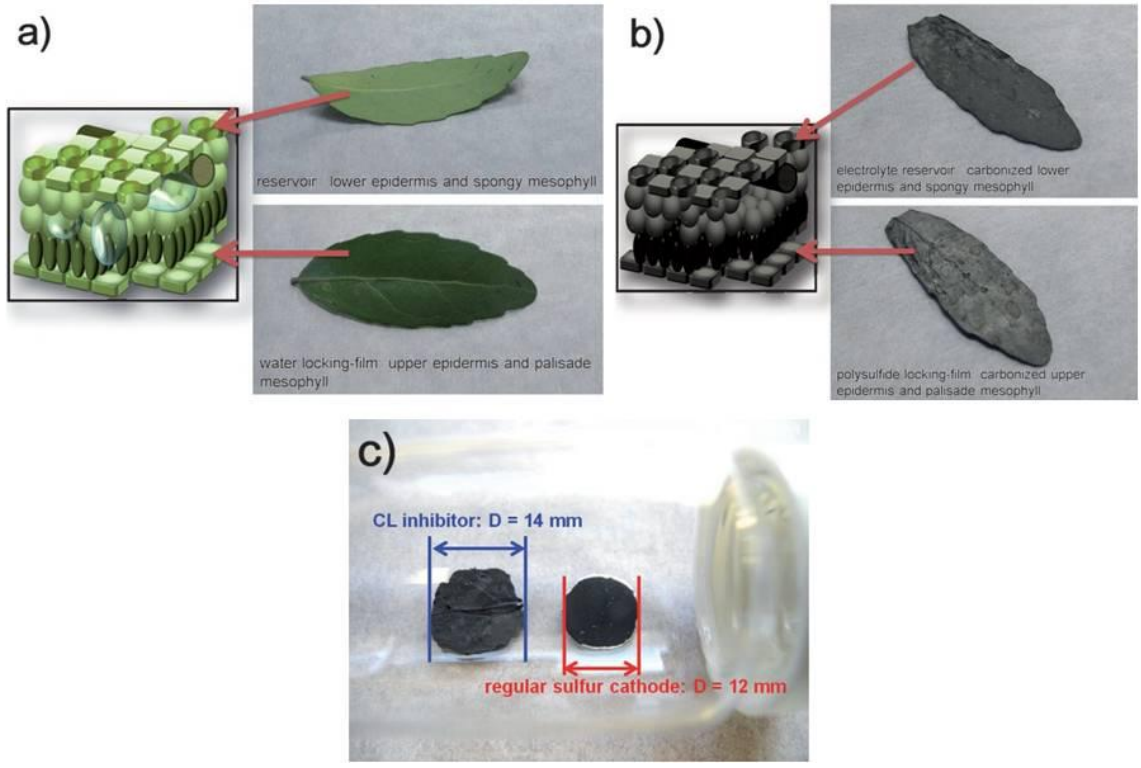

Figure 4.2: Schematic fabrication process of the CLs: (a) natural leaf, (b) carbonized natural leaf, and (c) cycled CL polysulfide diffusion inhibitor.

4.2.2 Carbonized Kimwipes paper (CK) interlayer fabrication

The cost-effective carbonized Kimwipes (CK) papers were prepared by a carbonization route. The Kimwipes paper was folded into layers and directly carbonized for 2 h at 800 ℃ with a heating rate of 2 ℃ min^{-1} in a tube furnace under flowing argon. After carbonization, the multilayer CK paper formed a free-standing carbon thin film with a size of around 2.0 cm × 6.0 cm. The size was limited by the diameter of the tube furnace. The CK paper was cut into circular discs (12 mm in diameter) with various thicknesses as the interlayer. The CK paper offers two major advantages. First, the CK paper was prepared by a facile and low-cost production method, avoiding any kind of complex multistep processes, acid/alkali treatments, hard template processes, and extra chemical additives. Second, it is noteworthy to emphasize that the CK paper has a light weight of as low as 0.23 mg cm^{-2} and can be easily prepared from single layer to multilayer. The light weight and controllable modular manufacture are not so easy to be fulfilled by other carbon interlayers. Most importantly, this layered structure provides benefits for us, for the first time, to investigate the thickness effect and analyze the interception mechanism of each layer in the interlayer.

4.2.3 Carbon nanofiber (CNF) interlayer fabrication

The carbon nanofiber (CNF) interlayers were prepared by Professor Kalra's group at Drexel University and provided to us. 10 wt. % polyacrylonitrile (PAN, MW = 15000; Sigma Aldrich) was dissolved in *N*,*N*-dimethylformamide (DMF, Sigma Aldrich) at room temperature and stirred for 4 – 5 h. The nanofibers were electrospun at room temperature with relative humidity below 20 % using a 22 gauge stainless steel needle (Hamilton Co.). The distance between the needle tip and the grounded collector (aluminum foil) was kept at 15 cm, and an applied voltage of 13 – 14 kV was used to obtain a stable Taylor cone. The electrospun nanofibers were stabilized in air by heating to 280 ℃ at a rate of 5 ℃ min^{-1} for 5 h. The stabilized nanofibers were then pyrolyzed (carbonized) under steady nitrogen flow in a horizontal tube furnace at a heating rate of 2 ℃ min^{-1} to the temperature of 1000 ℃ and held for 1 h. The thus fabricated carbon nanofibers are

denoted as NPCNFs (nonporous carbon nanofibers). To fabricate activated carbon nanofibers (ACNFs), the stabilized PAN nanofibers were activated at 900 ℃ at a ramping rate of 5 ℃ min^{-1}. When the activation temperature was reached during nitrogen pyrolysis as described above, the nitrogen flow was replaced by carbon dioxide (CO_2), held for 1 h at 900 ℃, and then allowed to cool down to room temperature in a nitrogen atmosphere. As shown in the Results section, ACNFs consist largely of micropores (< 2 nm). The meso-microporous carbon nanofibers (MCNFs) were fabricated by the selective decomposition of a sacrificial polymer previously reported by the Kalra group.[214] Briefly, the electrospinning solution consisting of 40 wt. % PAN and 60 wt. % Nafion with a total solid concentration of 17 wt. % in DMF was electrospun. The electrospun nanofibers were then heat treated (stabilized in air and pyrolyzed in nitrogen) under the same conditions as those used for NPCNFs. During this heat treatment, PAN converted to carbon and Nafion decomposed out forming pores (micro/meso) within the nanofibers.

4.2.3 Cell assembly

The cell employing the interlayer configuration has an interlayer inserted between the pure sulfur cathode and the commercial separator, as shown in Figure 4.1.

First, the CL interlayer was placed with the polysulfide locking-film (upper epidermis) pointing toward the cathode and the electrolyte reservoir (lower epidermis) toward the separator as the original configuration. The cell utilizing the CL-interlayer configuration used pure sulfur cathodes with a sulfur loading of 1.3 mg cm^{-2} and a sulfur content of 70 wt. %. The control cells with the CL interlayer inserted with the electrolyte reservoir pointing toward the cathode are named as the reverse direction configuration. These two opposite CL-interlayer configurations were utilized to investigate the effect of surface microstructure and morphology of the interlayer toward the cell performance. Second, in order to explore the relationship between the thickness of the interlayer and cell performance, the CK interlayer with various layers was placed between the separator and the sulfur cathode as the interlayer. The cell utilizing the CK-interlayer configuration used pure sulfur cathodes with a sulfur loading of 1.1 mg cm^{-2} and a sulfur content of 60

wt. %. Third, according to the analytical data from the CK interlayer, NPCNF, ACNF, and MCNF interlayers were designed to have an optimized thickness. Subsequently, various CNF interlayers with tunable pore size, surface area, and electrical conductivity were used to identify other design parameters for interlayer development. The cells utilizing the CNF-interlayer configuration used pure sulfur cathodes with (i) a sulfur loading of 1.2 mg cm^{-2} and a sulfur content of 60 wt. % and (ii) a sulfur loading of 1.4 mg cm^{-2} and a sulfur content of 70 wt. %.

4.3 RESULTS AND DISCUSSION

4.3.1 Carbonized leaf (CL) interlayer: the effect of surface microstructure and morphology on electrochemical performance

Attracted by the unique tissue and functions of leaves, a natural carbonized leaf (CL) is presented as a polysulfide diffusion inhibitor in lithium-sulfur batteries. The CL that is covered on the pure sulfur cathode effectively suppresses the polysulfide shuttling mechanism and enables the use of pure sulfur as the cathode. A low charge resistance and a high discharge capacity of 1320 mA h g^{-1} arise from the improved cell conductivity due to the innately integral conductive carbon network of the CL. The unique microstructure of CL leads to a high discharge/charge efficiency of > 98 %, low capacity fade of 0.18 % per cycle, and good long-term cyclability over 150 cycles. The structural gradient and the micro/mesoporous adsorption sites of CL effectively intercept/trap the migrating polysulfides and facilitate their reutilization. The green CL polysulfide diffusion inhibitor thus offers a viable approach for developing high-performance lithium-sulfur batteries.

4.3.1.1 Cell configuration design

The leaf is a critical organ of higher plants. Its anatomy comprises the upper epidermis, the palisade mesophyll, the spongy mesophyll (containing veins and air space), and the lower epidermis (containing many stomata), as shown in Figure 4.3a. The hierarchically arranged epidermis and parenchyma cells create an anatomically layered structure within the leaf, which acts as both a water-locking film and as a reservoir. The

upper epidermis and the closely arranging palisade mesophyll mitigate the loss of moisture and serve as the water-locking film while the spongy mesophyll and the lower epidermis store and transport water within their pores, functioning as a reservoir. The natural functional structures in leaves share characteristics with engineered materials designed specifically for preventing polysulfide migration in lithium-sulfur cells. This makes them an ideal candidate as polysulfide diffusion inhibitor layers as shown in Figure 4.3b. The carbonized water-locking film faces the cathode in order to intercept the dissolved polysulfides while the porous reservoir faces the separator to ensure proper wetting of the inhibitor layer by the electrolyte. Figure 4.3c – 4.3e show the integral carbon framework, the continuous porous network, and the perfectly retained natural leaf structure of the CLs. The hierarchical structure consists of two sides: one side (the carbonized reservoir) more porous than the other (the carbonized water-locking film), creating a pore-size gradient. This allows us to investigate the effect of (i) surface microstructure and (ii) morphology of the interlayer on the electrochemical performance. Figure 4.3c shows that the pores and stomata of the lower epidermis, which served as water reservoirs and exchange openings in the plant, now provide the same function for the electrolyte. The widely distributed stomata provide major electrolyte pathways (Figure 4.4a and 4.4b) while the cracks/pores formed during the carbonization process provide minor ones. These electrolyte channels enable the CL to absorb a significant volume of electrolyte (as high as 30 μL cm^{-2}). For a comparison, the amount of electrolyte adsorbed on the surface of the sulfur cathode is less than 10 μL cm^{-2}. A cross-sectional scanning electron microscopy (SEM) image of CLs (Figure 4.3d) displays the pore-size gradient (marked in white) from loosely arranged spongy mesophyll tissues at the lower epidermis to closely arranged palisade mesophyll tissues at the upper epidermis, which makes CL interlayer as an ideal sample for understanding the influence of morphology of the interlayer. The carbonized upper epidermis (Figure 4.3e and Figure 4.4c and 4.4d), which used to trap water in the leaf, now serves to trap the migrating polysulfides as the polysulfide locking-film.

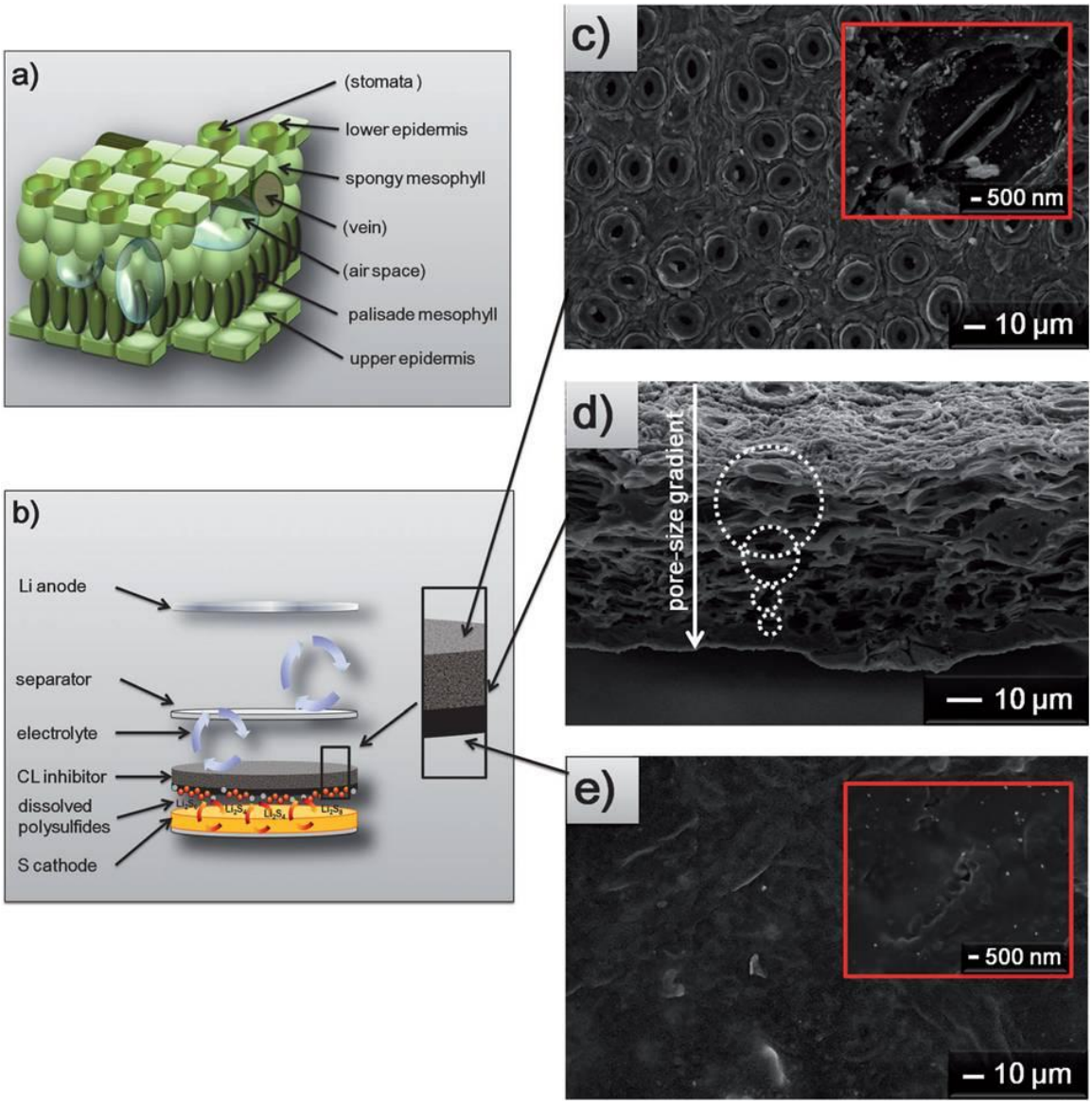

Figure 4.3: Schematics of (a) the leaf, and (b) the CL polysulfide diffusion inhibitor; and SEM microanalysis of the (c) surface of the electrolyte reservoir, (d) cross-section of the CL, and (e) surface of the polysulfide locking-film.

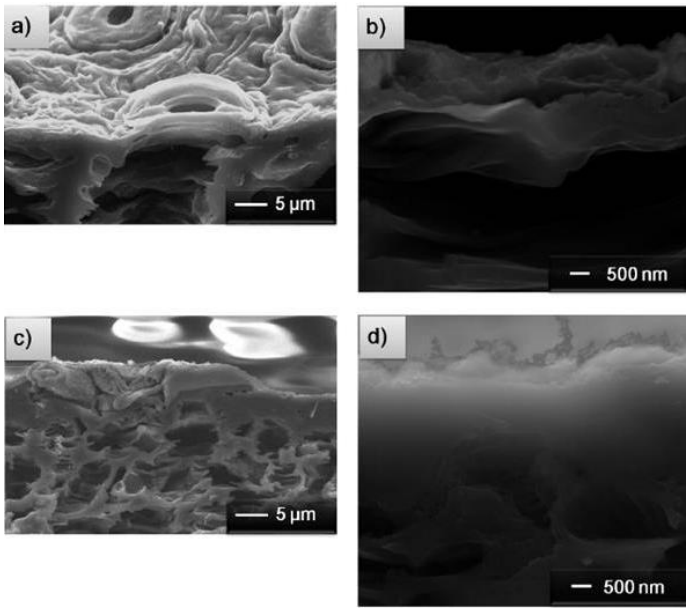

Figure 4.4: Cross-sectional microanalysis of CLs: (a) the electrolyte reservoir, (b) high-magnification images of the stomata on the electrolyte reservoir, (c) the polysulfide locking-film, and (d) high-magnification images of (c).

4.3.1.2 Microstructure and morphology analysis

After cycling, the morphological changes of the CL inhibitors were analyzed by elemental mapping with SEM. In Figure 4.5a, the lower epidermis shows no obvious polysulfide agglomerations and the stomata remain unblocked. The corresponding elemental mapping data show weak sulfur signals, which may come from the $LiCF_3SO_3$ salt that was added into the electrolyte but not from the escaping polysulfides that dissolve from the cathode. Therefore, we believe that the dissolved polysulfides may be blocked and trapped within the hierarchical structure of the CL polysulfide diffusion inhibitor. This argument is confirmed by the morphological analyses in the cross-sectional SEM image, as shown in Figure 4.5b. From the lower epidermis to the upper epidermis, the sulfur elemental mapping data displays an increasing concentration gradient that matches the carbon elemental mapping data, corresponding to the hierarchical pore-size structure gradient. The sulfur concentration gradient demonstrates

that the major polysulfide trapping layers are the upper epidermis and the closely arranged palisade mesophyll. The trapped polysulfides are then absorbed by the micropores and distributed on the carbonized mesophyll tissue (Figure 4.5d).[63, 174, 176, 215] Therefore, polysulfide agglomerations are difficult to identify in Figure 4.5a. However, the comparison between Figure 4.3e and Figure 4.5c shows that the surface of the cycled upper epidermis is covered by the trapped polysulfides. The trapped active material forms a layer of fluffy precipitates (marked in white), as shown in Figure 4.5c. Moreover, the strong sulfur signal in the elemental mapping results confirms this microstructural observation. On the other hand, the carbon signals are still strong, implying that the trapped sulfur/sulfides do not severely cover the conductive carbon network.

To identify the existence of the intrinsic micro-/meso-pores and their ability to absorb the active material, nitrogen adsorption-desorption isotherms and pore-size distribution curves were obtained for the CL polysulfide diffusion inhibitors before and after cycling. The CLs naturally have a high specific surface area of 390 $m^2 g^{-1}$ (36 % contributed by micropores) and a pore volume of 0.34 $cm^3 g^{-1}$ (0.22 $cm^3 g^{-1}$ from micropores), providing the essential micro-/meso-porous absorption sites and abundant porous spaces for active material accumulation and electrolyte penetration.[62, 173, 174, 176, 215] After cycling, the CLs possess a lower specific surface area and pore volume of, respectively, 21 $m^2 g^{-1}$ and 0.02 $cm^3 g^{-1}$ (0.01 $cm^3 g^{-1}$ from micropores), implying that the micro-/meso-porous absorption sites are almost fully utilized for absorbing the migrating polysulfides and the electrolyte.

In Figure 4.5e, the CLs display the mixed IUPAC type I and type IV isotherms for the typical micro-/meso-porous structure.[182] The type I isotherms show a certain nitrogen adsorption in the low-pressure region (relative pressure of $P/P_0 < 0.1$), demonstrating the existence of microporosity. The type IV isotherms display the typical hysteresis loop at $P/P_0 = 0.4 – 1.0$ resulting from the capillary condensation phenomenon of the carbon mesopores, confirming the existence of mesoporosity. Thus, the pore-size distribution curves (Figure 4.5f) illustrate that the microporous absorption sites and the mesoporous

absorption sites have diameters of, respectively, 1.4 – 2.0 nm and 2.0 – 15 nm. After trapping the polysulfides, the cycled CLs show the disappearance of the type I and type IV isotherms as well as the obvious decrease of the pore volume contributed by the micro-/meso-pores. This demonstrates that most of the micro-/meso-porous absorption sites were used to trap or absorb the polysulfides. The remaining empty micro-/meso-pores may belong to the porous side of the CLs since most of the dissolved polysulfides were trapped in the polysulfide locking-film.

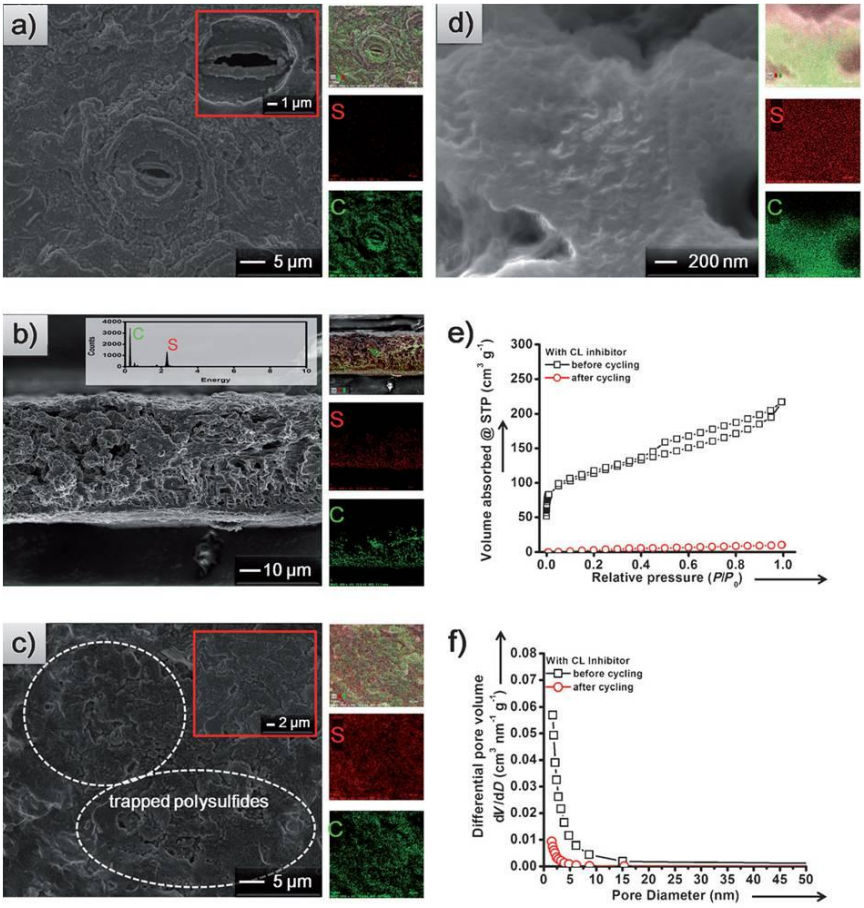

Figure 4.5: SEM/energy dispersive spectroscopy (EDS) microanalysis of the cycled CL polysulfide diffusion inhibitors: (a) surface image of the electrolyte reservoir, (b) cross-sectional image of the cycled CL, (c) surface image of the polysulfide locking-film, and (d) micro/mesoporous structure of CL, and (e) isotherms and (f) pore size distributions of the CLs and the cycled CL polysulfide diffusion inhibitors.

4.3.1.3 Electrochemical analysis

The discharge/charge voltage profiles of the cells employing the CLs at various cycling rates during the initial 20 cycles are presented in Figure 4.6a – 4.6c. During cell discharge, the two separate and continuous plateaus indicate complete two-step reduction reactions: (i) from elemental sulfur (S_8) to long-chain polysulfides (Li_2S_x, x = 4 – 8) corresponding to the upper plateau at ~ 2.4 V, and (ii) from polysulfides to Li_2S_2/Li_2S corresponding to the lower plateau at ~ 2.1 V.[17, 135, 177] There is almost no change in the upper and lower discharge voltage plateaus during continuous cycling and at various discharge rates, demonstrating that the cells possess high reversibility and good rate performance when the CL inhibitor is used. The same phenomena are observed in the cells with the CL inhibitor but without the addition of 0.1m $LiNO_3$ co-salt (Figure 4.7a – 4.7c). The nitrate anion has been evidenced to form a passivation layer on the Li-metal anode, effectively mitigating the Li corrosion issue and enhancing the discharge/charge efficiency.[35, 36] Therefore, it is reasonable to expect that the addition of $LiNO_3$ aims to further raise the average Coulombic efficiencies of the cells from 91 % (without $LiNO_3$) to above 97 % (with 0.1M $LiNO_3$).

The loss of the active material and capacity fade behavior caused by the polysulfide diffusion can be analyzed by investigating the capacities of the upper discharge voltage plateaus.[17, 33, 135, 177] This is because the highly soluble polysulfides are formed and freely diffuse through the separator in this upper plateau region. In Figure 4.6 (cells using the electrolyte with $LiNO_3$) and Figure 4.7 (cells using the electrolyte without $LiNO_3$), the upper discharge voltage plateaus with the CL inhibitors show no decrease in capacity or voltage changes. This can be visualized in Figure 4.6d and 4.7d where the upper plateau capacities remain mostly unchanged with cycling and approach 91.4 % (89.2 %: cells using the electrolyte without $LiNO_3$) and 94.5 % (94.1 %: cells using the electrolyte without $LiNO_3$) of the theoretical value (419 mA h g^{-1})[17] at, respectively, C/5 and C/10 rates. This demonstrates that the CL inhibitor effectively suppresses the diffusion of polysulfides and eliminates the severe loss of active material and capacity fade. As a result, the cycled cathode retains a uniform sulfur distribution, as shown in

Figure 4.8a. In addition, the extended lower discharge voltage plateaus in Figure 4.6a indicate that the trapped polysulfides were easily reactivated because the CL has a conductive carbon network for transferring electrons into the inactive area.[173, 216, 217] For the sake of comparison, the discharge/charge curves of the cells without the CL show the typical capacity fade and poor cyclability, as shown in Figure 4.9a and 4.9b. On the surface of the cycled cathodes, obvious traces of the active material loss can be observed (Figure 4.8b).

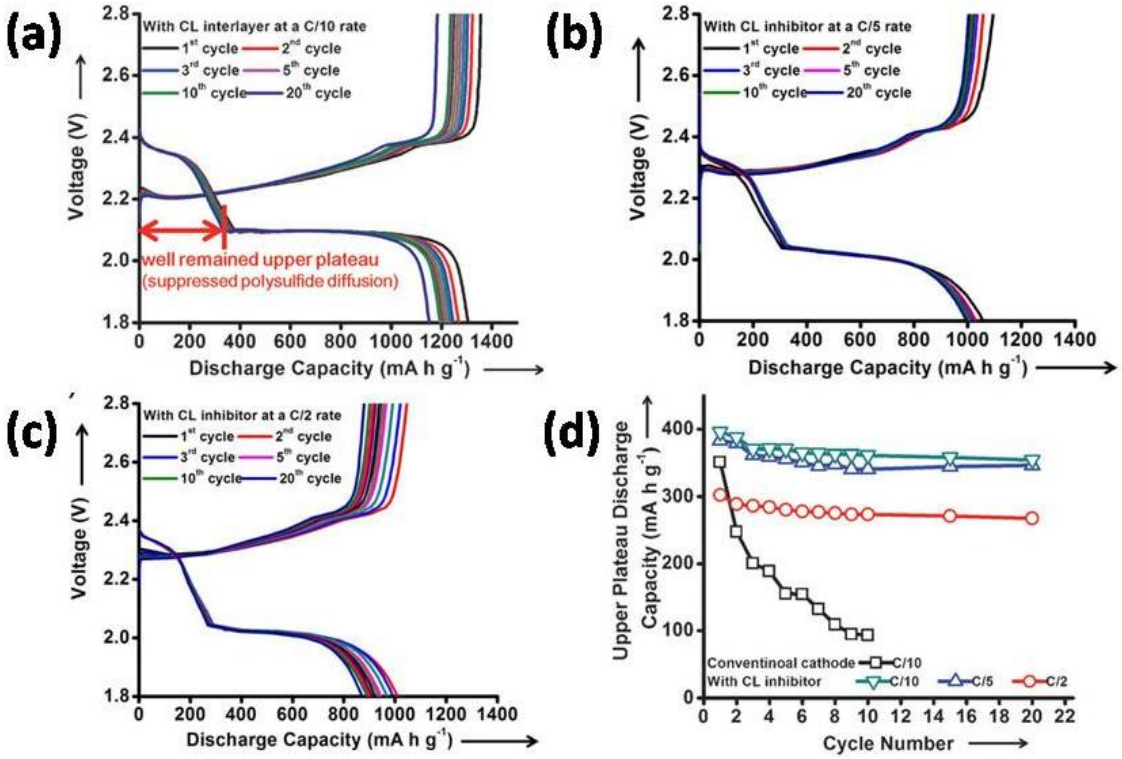

Figure 4.6: Electrochemical properties: the discharge/charge profiles of the CL inhibitor at (a) C/10 rate, (b) C/5 rate, and (c) C/2 rate. (d) Upper plateau discharge capacities of the cells with and without the CL polysulfide diffusion inhibitor.

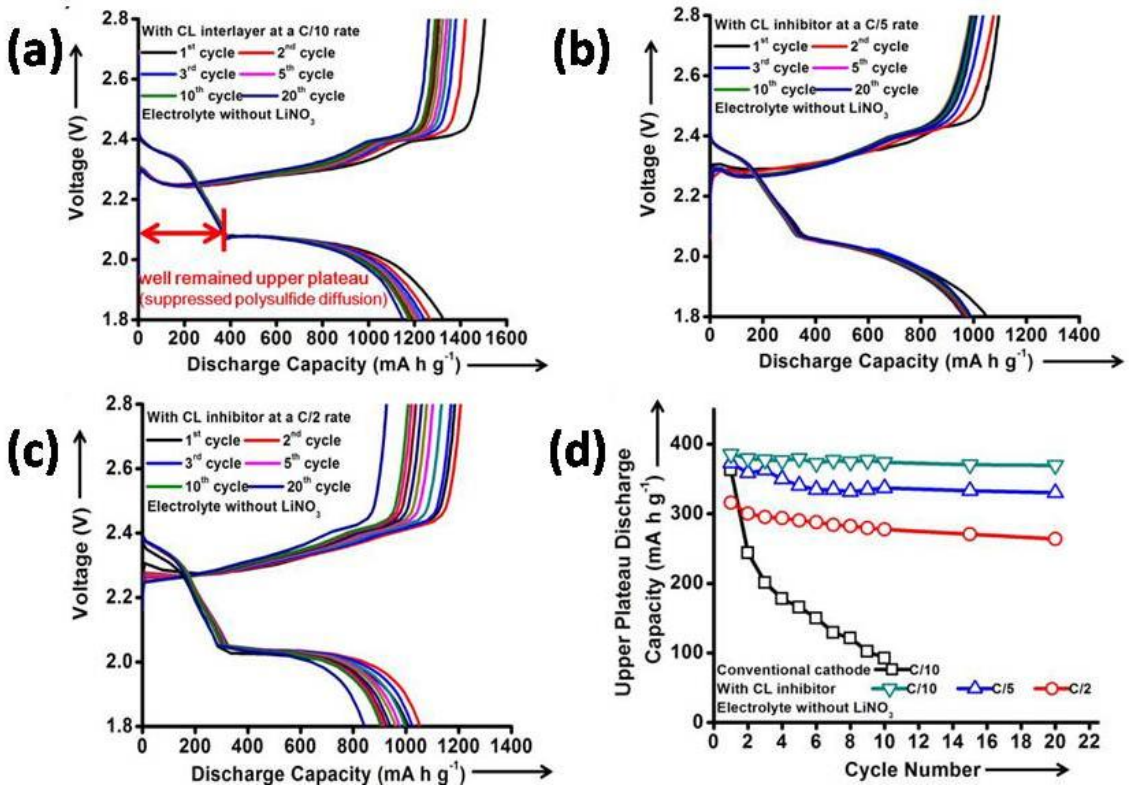

Figure 4.7: Electrochemical properties: the discharge/charge profiles of the CL inhibitor without the addition of $LiNO_3$ in the electrolyte at (a) C/10 rate, (b) C/5 rate, and (c) C/2 rate. (d) Upper plateau discharge capacities of the cells with and without the CL polysulfide diffusion inhibitor.

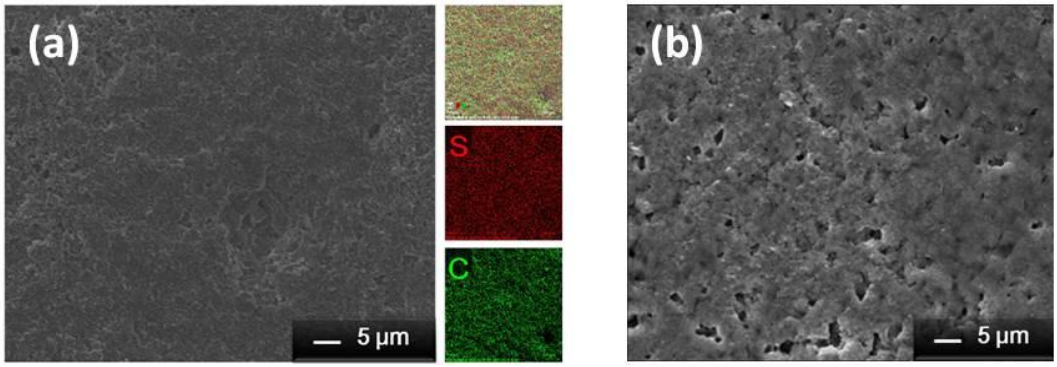

Figure 4.8: SEM/EDS microanalysis and elemental mapping of the cycled sulfur cathodes (a) with and (b) without the CL polysulfide diffusion inhibitor system.

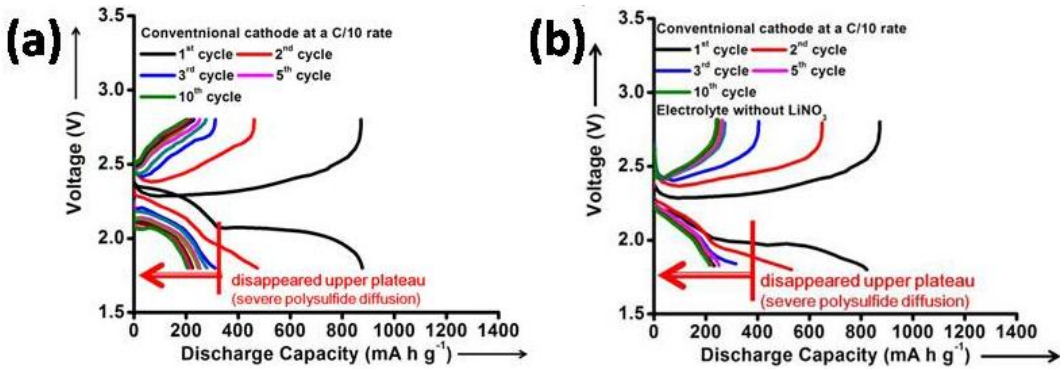

Figure 4.9: Electrochemical properties of the cells using conventional cell configuration with and without the $LiNO_3$ in electrolyte: Discharge/charge profiles of the cell (a) with $LiNO_3$ and (b) without $LiNO_3$.

The stable cycling mechanism of the CL inhibitor system was further investigated by cyclic voltammetry (CV) for the initial 20 cycles at a scanning rate of 0.05 mV s^{-1} (equivalent to a C/10 rate), as shown in Figure 4.10a. The two cathodic peaks and overlapping anodic peaks are in agreement with the discharge/charge curves, displaying the typical sulfur reduction/oxidation reactions.[180, 181] The disappearance of the overpotential of the initial cathodic peak implies that the rearranging active material migrates to electrochemically favorable positions. Therefore, in subsequent scans, the sharp overlapping cathodic and anodic peaks display no obvious peak intensity and potential changes, confirming the excellent reversibility of the system with the CL. The same phenomenon is observed in cells that employ the CL inhibitors at 0.1 mV s^{-1} and 0.25 mV s^{-1} (equivalent to C/5 and C/2 rates) as shown in Figure 4.10b and 4.10c. The improved electrochemical utilization with the CL inhibitor is also characterized by electrochemical impedance spectroscopy. In Figure 4.10d, the internal resistance of the lithium-sulfur cell upon incorporation of the conductive CL inhibitor decreases from 500 to 40 Ohms. The decrease in the charge-transfer resistance (R_{ct}) results from the conductive carbon network of the CLs. These electron pathways increase the conductivity of the sulfur cathodes, resulting in high active material utilization approaching 80 % and high discharge capacity of 1320 mA h g^{-1}.

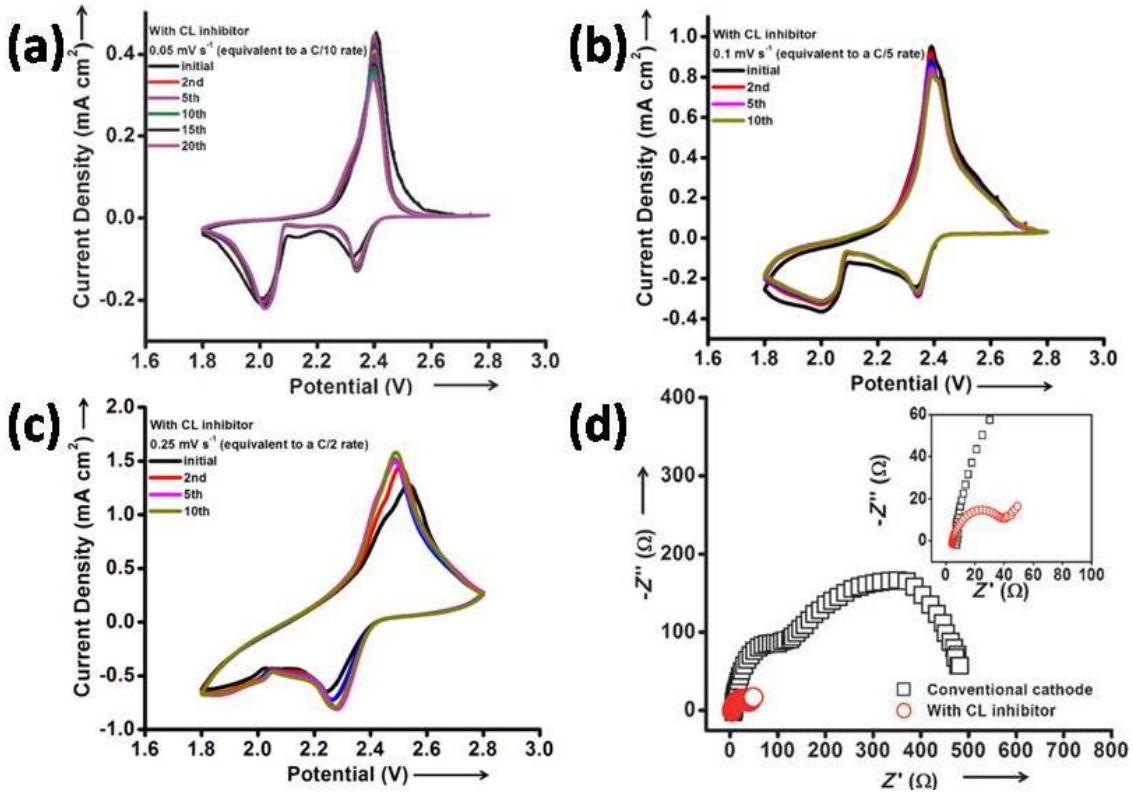

Figure 4.10: Electrochemical properties of the cells with and without the CL polysulfide diffusion inhibitor: CV plots at a scanning rate of (a) 0.05 mV s^{-1}, (b) 0.1 mV s^{-1}, and (c) 0.25 mV s^{-1}. (d) EIS plots.

4.3.1.4 Cell performance

The cycling performance of the CL inhibitors (Figure 4.11a) reveals significant improvements over conventional cells: higher discharge capacity, superior cyclability, and higher Coulombic efficiency. The cells containing CL inhibitors show an enhanced initial discharge capacity from 845 to 1320 mA h g^{-1} compared to pure sulfur cathodes containing an active material content of 70 wt. %. After 100 cycles, the discharge capacities of the cells with CL inhibitors are 1013, 850, and 829 mA h g^{-1} at, respectively, C/10, C/5, and C/2 rates. At various cycling rates, the corresponding capacity retentions approach 80 % and the average Coulombic efficiencies of cells are above 97 %,

indicating high reversibility with minimal shuttle effect with the CL system. Because the highly soluble polysulfides have more time to migrate when the cells are cycled at a low cycling rate than at a high cycling rate, it is noteworthy to emphasize that the cells that cycle at a C/10 rate also display high capacity retention and high Coulombic efficiency. This demonstrates that the polysulfide-diffusion problem is effectively suppressed in this system, extending the cycle life. The reversible capacity stabilizes around 800 mA h g^{-1} with high Coulombic efficiency (98.3 %) and low capacity fade (0.18 % per cycle) after 150 cycles at C/2 and C/5 rates (Figure 4.11b). For a comparison, the sulfur cathodes without the CL inhibitors suffer low capacity, severe capacity fade, and short cycle life.

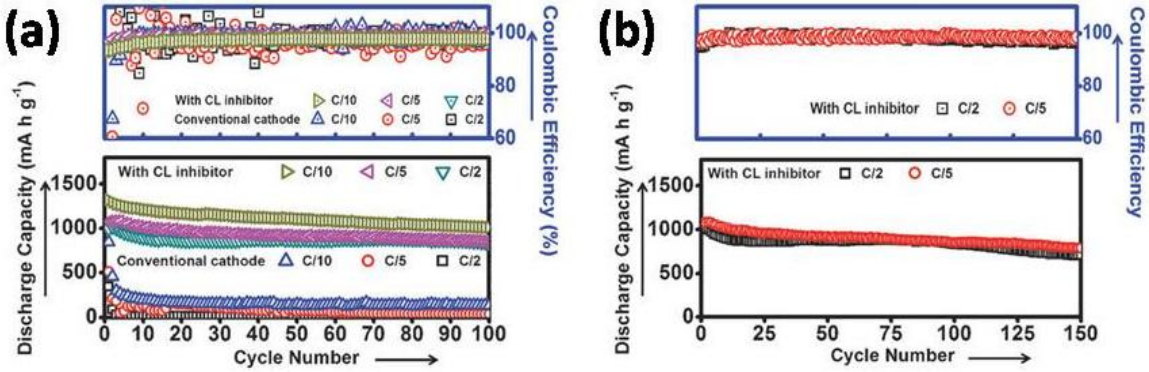

Figure 4.11: Performances of the cells with and without the CL polysulfide diffusion inhibitor: (a) cyclability and (b) cycle life.

4.3.1.5 Effect of the surface microstructure and morphology of the interlayer

After identifying the significant enhancements contributed by the polysulfide diffusion inhibitor on cycling performance, it is instructive to discuss why the CL inhibitor is designed to be inserted into the cell with the polysulfide locking-film pointing toward the cathode. In this original configuration, the polysulfide locking-film closely covers the pure sulfur cathode. Clearly, this intimate contact allows the polysulfide locking-film to immediately and effectively localize the dissolved polysulfides in the cathode before they diffuse out, as shown in Figure 4.12a.

However, the CL inhibitor that has a reverse direction position (electrolyte reservoir pointing toward the cathode) does not have the polysulfide locking-film closely contacting with the cathode, as shown in Figure 4.12b. In this situation, the dissolved polysulfide may freely diffuse out from the cathode. After escaping from the cathode, the diffusing polysulfides may not be stabilized in the cathode but subsequently immobilized in the reservoir architecture of the CLs. Therefore, the reverse CL inhibitor shows a slightly lower capacity but still accomplishes stable cycling performance compared to that of the original direction position, as shown in Figure 4.12c. In general, according to the enhanced capacity and cycle stability, the CL polysulfide diffusion inhibitor rescues the pure sulfur cathode from low sulfur utilization and poor cyclability.

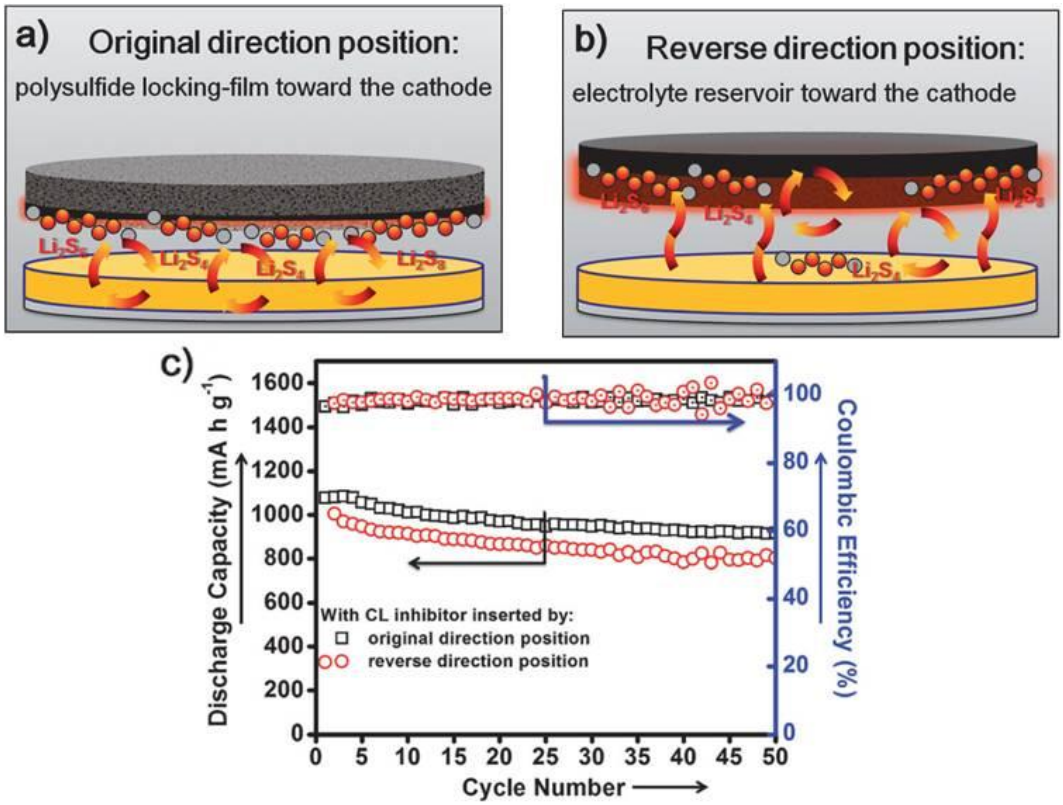

Figure 4.12: Schematics of the function of the CL polysulfide diffusion inhibitor with (a) original direction position and (b) reverse direction position. (c) Cyclability of the cells with the CL inhibitor inserted with two opposite direction positions at a C/5 rate.

4.3.1.6 Summary

We successfully employ the inherent moisture retention properties of natural leaves to suppress the polysulfide shuttling mechanism in lithium–sulfur batteries. The incorporation of a carbonized leaf (CL) polysulfide diffusion inhibitor offers several advantages over conventional cells without a CL. A high discharge capacity of 1320 mA h g^{-1} arises from improved cell conductivity due to the inherent conductive carbon network of the CL. A high Coulombic efficiency (98 %), low capacity fade (0.18% per cycle), and long-term cycling stability result from the micro/mesoporous adsorption sites and the hierarchical pore-size gradient that help trap the dissolved polysulfides. This demonstrates the importance of the surface microstructure and the morphology of the CL interlayers.

4.3.2 Carbonized Kimwipes (CK) interlayer: effect of thickness on electrochemical performance

The Kimwipes paper composed of long fiber pulp is well-known for its mechanical strength and high liquid absorption ability. In an effort to adapt these characteristics for use in a lithium-sulfur cell, we carbonized the Kimwipes for 2 h at 800 ℃ under an argon atmosphere. The carbonized Kimwipes paper (CK) retains the interlocking fiber network, serving as the interlayer for intercepting the migrating polysulfide species and then reutilizing the trapped active material.[28, 173, 218] The CK interlayer has been found to be a modulable, low-cost hierarchical interlayer for lithium-sulfur cells, leading to a high discharge capacity with superior cycling stability and rate performance. Moreover, this modulable interlayer offers a way to control the thickness by simply adjusting the number of folded layers in each CK interlayer. Thus, we were able to examine the relationship between the thickness of the interlayer and the cell performance. In addition, after separating the CK paper layers from a cycled interlayer, we thoroughly inspect the interception mechanism in each layer.

4.3.2.1 Morphology and microstructure analysis

Figure 4.13a shows the scanning electron microscopy (SEM) image of the CK paper. The CK paper retains the interweaving long-fiber architecture and possesses a layered porous network. The Brunauer-Emmett-Teller (BET) measurements show that the CK paper has a high surface area of 310 m^2 g^{-1} and a pore volume of 0.27 cm^3 g^{-1}. The inserted high-magnification SEM image shows many micro-cracks on the surface of the CK paper. The porous network and the surface micro-cracks may aid in trapping the diffusing polysulfides.[28, 173, 218] Figure 4.13b shows the cross-sectional SEM of the CK interlayer (with various layers). As the number of included layers increases from 1 to 6, the corresponding thickness of the CK paper module increases from 35 to 240 μm. Figure 4.14 shows the excellent mechanical strength of the CK paper, which indicates that the CK paper can form a free-standing interlayer with adjustable thickness. The high water absorptivity of the Kimwipes provides the CK paper with a similar electrolyte absorptivity of as high as 74 μL cm^{-2} (Figure 4.13c). As a result, the CK interlayer may provide three critical advantages for the sulfur cathode: (i) the interwoven fiber assists electron transport and enhances cathode conductivity;[209, 218] (ii) the controllable layered architecture can suppress the migration of polysulfides;[173, 218] and (iii) the highly porous morphology ensures an excellent electrolyte immersion/penetration upon cell cycling.[28, 176, 218, 219]

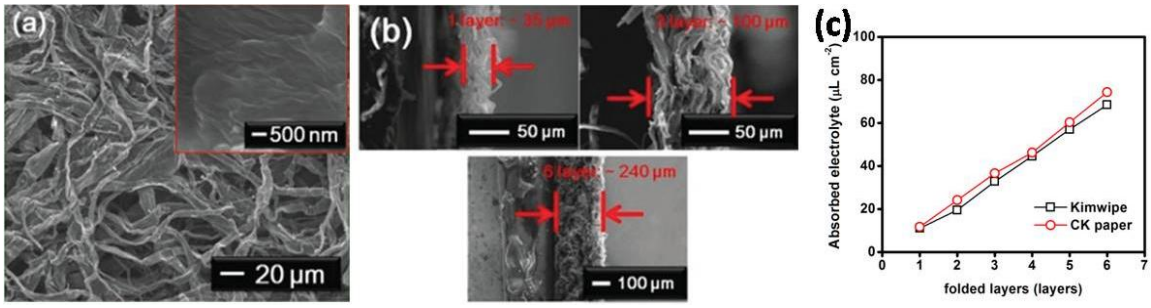

Figure 4.13: (a) Surface SEM image of the CK paper. Characterization of the CK interlayer with various multilayer modules: (b) cross-sectional SEM microanalyses and (c) electrolyte absorption tests.

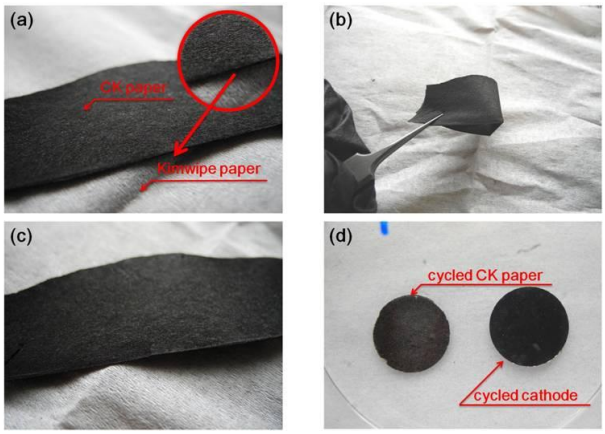

Figure 4.14: Morphology of the CK paper: (a) comparison between the Kimwipes paper and the CK paper, (b) excellent flexibility of the CK paper, (c) CK paper after bending, and (d) cycled CK paper.

4.3.2.2 Effect of thickness

The second advantage, the controllable layered architecture, prompts an investigation of the relationship between the thickness of the interlayer and cell performance. The CK interlayer with 1, 3, or 6 layers was placed between the separator and the sulfur cathode as a polysulfide inhibitor. In Figure 4.15a, electrochemical impedance spectroscopy (EIS) shows the cell resistance/impedance of the cells with different numbers of CK paper layers. The charge transfer resistance (R_{ct}) significantly decreased when the CK interlayer was used.[173, 218] The low resistance arises from the conductive CK paper, providing additional electron pathways to the insulating sulfur, enhancing the active material utilization.[173] Accordingly, in Figure 4.15b, the cell with a single-layer CK interlayer shows an improvement in the initial discharge capacity from 945 to 1094 mA h g^{-1}. The initial discharge capacities further increase to 1235 mA h g^{-1} when a CK interlayer with the 6-layer module was used. The increase in active material utilization from 65 % (1 layer) to 74 % (6 layers) is a result of the additional conductive pathways in the cathode. Furthermore, the cycling stability of the cells with the 6-layer module shows significant enhancement in capacity retention to as high as 92 % after 50

cycles. The enhanced cyclability is due to the polysulfide locking-films and absorption sites in the layered module, effectively confining the electrochemical reaction within the cathode region. Based on the structural and electrochemical analyses as well as the concerns over the mechanical properties and weight of the interlayers, the CK interlayer with the 6-layer module was utilized for the following investigation.

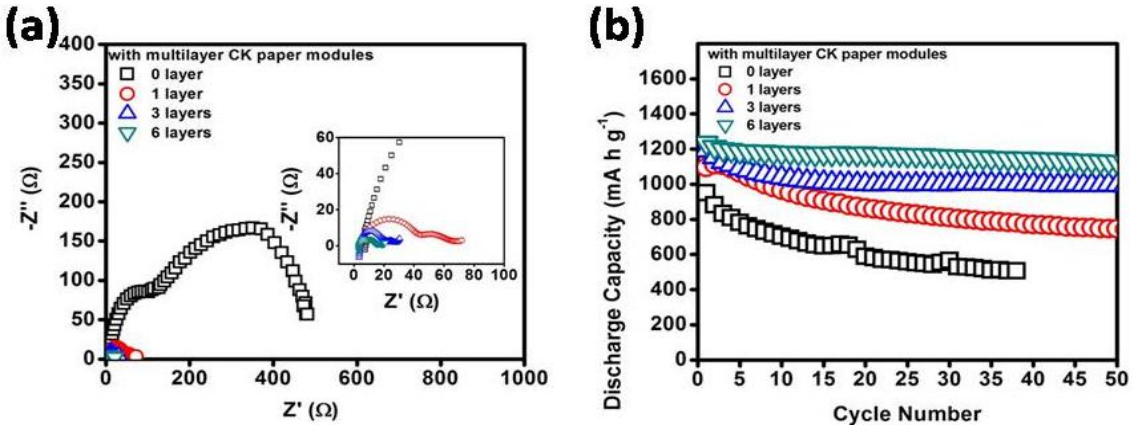

Figure 4.15: Electrochemical analysis of the cells applying CK interlayers with various multilayer modules: (a) EIS of fresh cells and (b) cyclability of the cells at a C/5 rate.

4.3.2.3 Electrochemical analysis of the cells with optimized CK interlayer

Figure 4.16a shows the cyclic voltammetry (CV) curves of the cell utilizing the CK interlayer during the initial 20 cycles. In the cathodic sweep, the CV curves display the typical two-step reduction reactions: (i) from sulfur to long-chain polysulfides signified as the cathodic peak I starting at 2.43 V and (ii) the subsequent transformation of the long-chain polysulfides to Li_2S_2/Li_2S signified as the cathodic peak II starting at 2.07 V.[17, 181] In the anodic sweep, the oxidation of Li_2S_2/Li_2S to Li_2S_8/S_8 shows two overlapping anodic peaks between 2.24 and 2.48 V.[181] The absence of any decrease in peak intensity and potential shifts in subsequent CV scans indicates high reversibility. The reversible discharge-charge curves (Figure 4.16b) reconfirm stable cyclability and show complete upper and lower discharge plateaus.[17] The severe capacity fade and plateau shrinkages commonly associated with conventional lithium-sulfur cell

configurations (Figure 4.16c) have been mitigated.[24, 181] The complete upper discharge plateaus in the CK paper system indicate that the limited loss of the active material is due to the entrapment, reutilization, and stabilization of the migrating polysulfides within the cathode region of the cell. Therefore, the cells employing the CK interlayer display more stable upper plateaus than those with conventional cell configuration (Figure 4.16d) and approach high upper plateau discharge capacities of 393 mA h g^{-1} at a C/5 rate (the theoretical value is 419 mA h g^{-1}). The stable upper discharge plateaus suggest superior cyclability while the extended lower discharge plateaus indicate enhanced active material utilization.

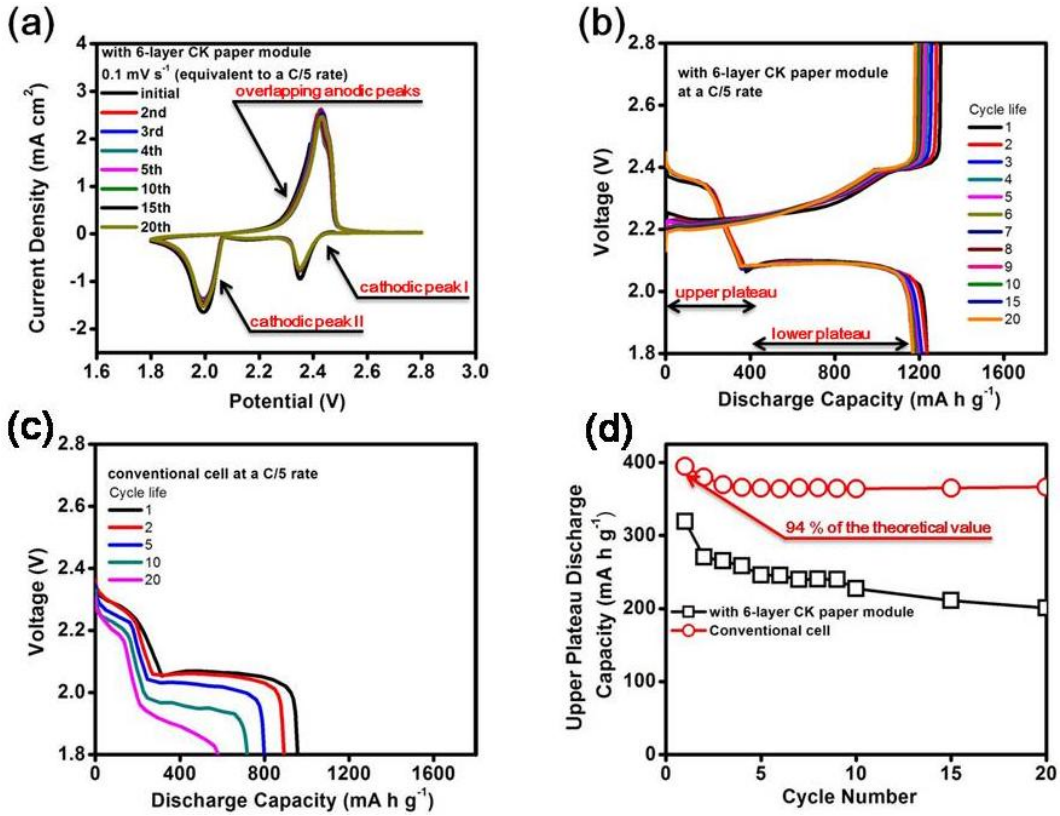

Figure 4.16: Electrochemical properties of the cells with and without a CK interlayer with 6-layer modules: (a) CV plots, (b) discharge-charge curves of the cell with the CK interlayer, (c) discharge-charge curves of the conventional cell, and (d) variation of the capacity in the upper plateau of both cell configurations with cycling.

4.3.2.4 Cell performance

The cycling performance shown in Figure 4.17a reveals that the cells covered with the CK interlayer exhibit stable cyclability and high Coulombic efficiency at various cycling rates. After being covered with the CK interlayer, sulfur cathodes achieve discharge capacities of 1311, 1235, 1192, 1174, and 1165 mA h g^{-1} at, respectively, C/10, C/5, C/2, 1C, and 2C rates. The excellent rate capability allows the cells to remain stable in a wide range of cycling rates from C/10 to 2C. After 100 cycles, the discharge capacities of the CK interlayer cells are 1086, 1044, 974, 890, and 824 mA h g^{-1} at, respectively, C/10, C/5, C/2, 1C, and 2C rates. The corresponding capacity retentions are 83, 85, 82, 76, and 71%. The excellent cycle stability arises from two mechanisms: (i) the soluble polysulfides are well absorbed/stabilized within the cathode region and (ii) the polysulfides that are localized in the cathode region assist conversion and reutilization of the precipitated Li_2S_2/Li_2S during cycling. As a reference, the stable cycling performance of the cells employing the CK interlayer with the 3-layer module is shown in Figure 4.18.

At higher cycling rates (2C – C/2), the cells exhibit long cycle life (Figure 4.17b): after 200 cycles they retain discharge capacities of 847, 800, and 780 mA h g^{-1} at, respectively, C/2, 1C, and 2C rates. The corresponding capacity fade rates are only 0.14 – 0.17 % per cycle. Such long-term cyclability results from the reutilization of trapped polysulfides in the hierarchical porous network.[28, 173, 218] The CK interlayer was designed to intercept the migrating polysulfides, absorb the electrolyte containing the dissolved polysulfides, and concomitantly stabilize the electrochemical materials within the cathode region for successive reutilization, as shown in the cell configuration schematic (Figure 4.17c). The reactivation ability of the trapped active material in the CK interlayer is due to the excellent electrolyte immersion/penetration, efficient electron transport, and intimate three-phase boundary involving the electrolyte, conductive network, and the active material.

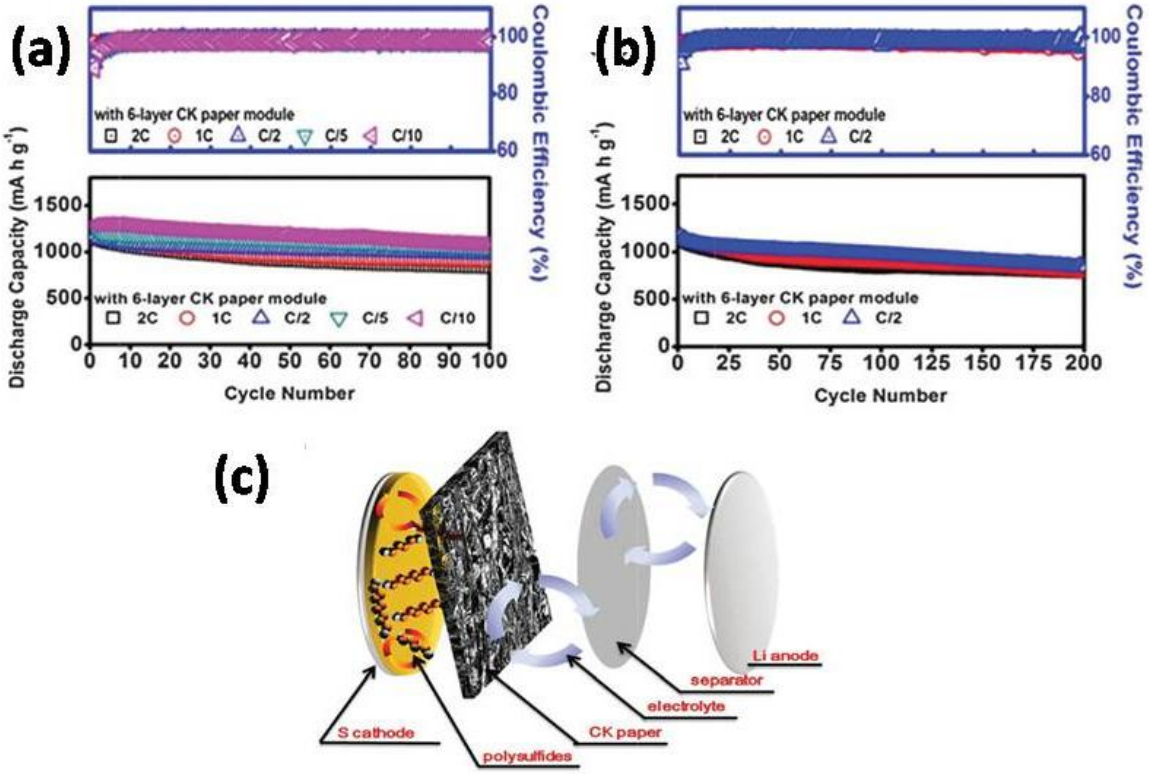

Figure 4.17: Cell performance of the CK interlayer with 6-layer modules: (a) cyclability and (b) long-term cycle life. (c) A schematic model of the cells.

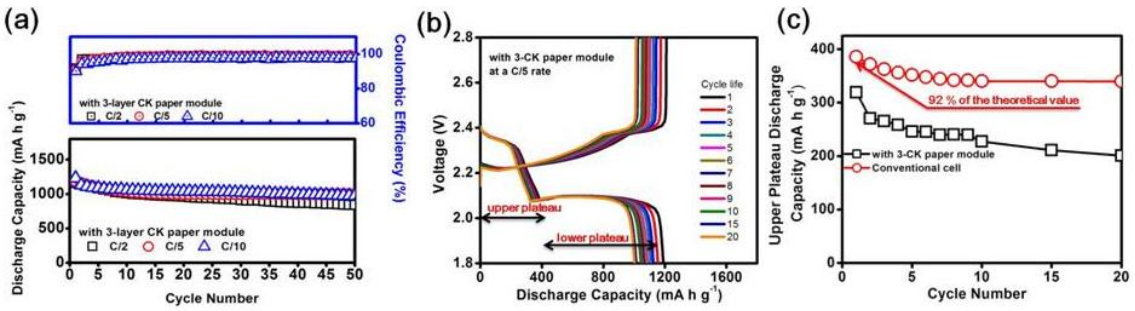

Figure 4.18: Electrochemical properties of the CK interlayer with the 3-layer module: (a) cyclability of the cells at various cycling rates, (b) discharge/charge curves, (c) variation of the capacity in the upper plateau region with cycling.

4.3.2.5 Polysulfide-intercepting mechanism

Detailed analyses of the hierarchical interlayer module by inspecting the surface SEM/EDS and elemental mapping results are summarized in Figure 4.19 (low-magnification inspection) and Figure 4.20 (high-magnification inspection of Figure 4.19). Figure 4.19 and 4.20 show the 1st through 6th layer of the CK paper from the cathode side to the separator side. A schematic model showing the sulfur concentration gradient is shown in Figure 4.19g. The 1st and 2nd layers from the sulfur cathode (Figure 4.19a and 4.19b as well as Figure 4.20a and 4.20b) show a large amount of trapped/intercepted active material in the SEM images and EDS.[28, 181, 218] According to the sulfur signal in the elemental mapping data, the diffusing polysulfides may first be suppressed by the 1st layer and then be continuously intercepted by the layered structure within each CK layer. This demonstrates the importance of the surface morphology and the thickness of the interlayer. The trapped species may sit within the 3D interwoven fibers or cover on the surface of the fibers. Therefore, the amount of trapped escaping polysulfides gradually decreases from one interlayer to another, as evidenced by the decrease in sulfur concentration from Figure 4.19c to 4.19e and also from Figure 4.20c to 4.20e. As a result, in Figure 4.19f and 4.20f, the 6th CK layer maintains the most porous structure and displays the weakest sulfur signal intensity in the EDS and in the elemental mapping results. The weak sulfur signal may result from the $LiCF_3SO_3$ salt in the electrolyte. In addition, the carbon signals in the elemental mapping results shown in Figure 4.19 are still discernible, suggesting that the trapped/absorbed active materials do not cause nonconductive agglomerations or block the porous electrolyte channels but continuously reactivate and contribute to the overall capacity. Morphological changes and sulfur concentration gradient in the CK interlayer with the 6-layer module can be found in the cross-sectional SEM in Figure 4.21, reconfirming the effective polysulfide interception effect.

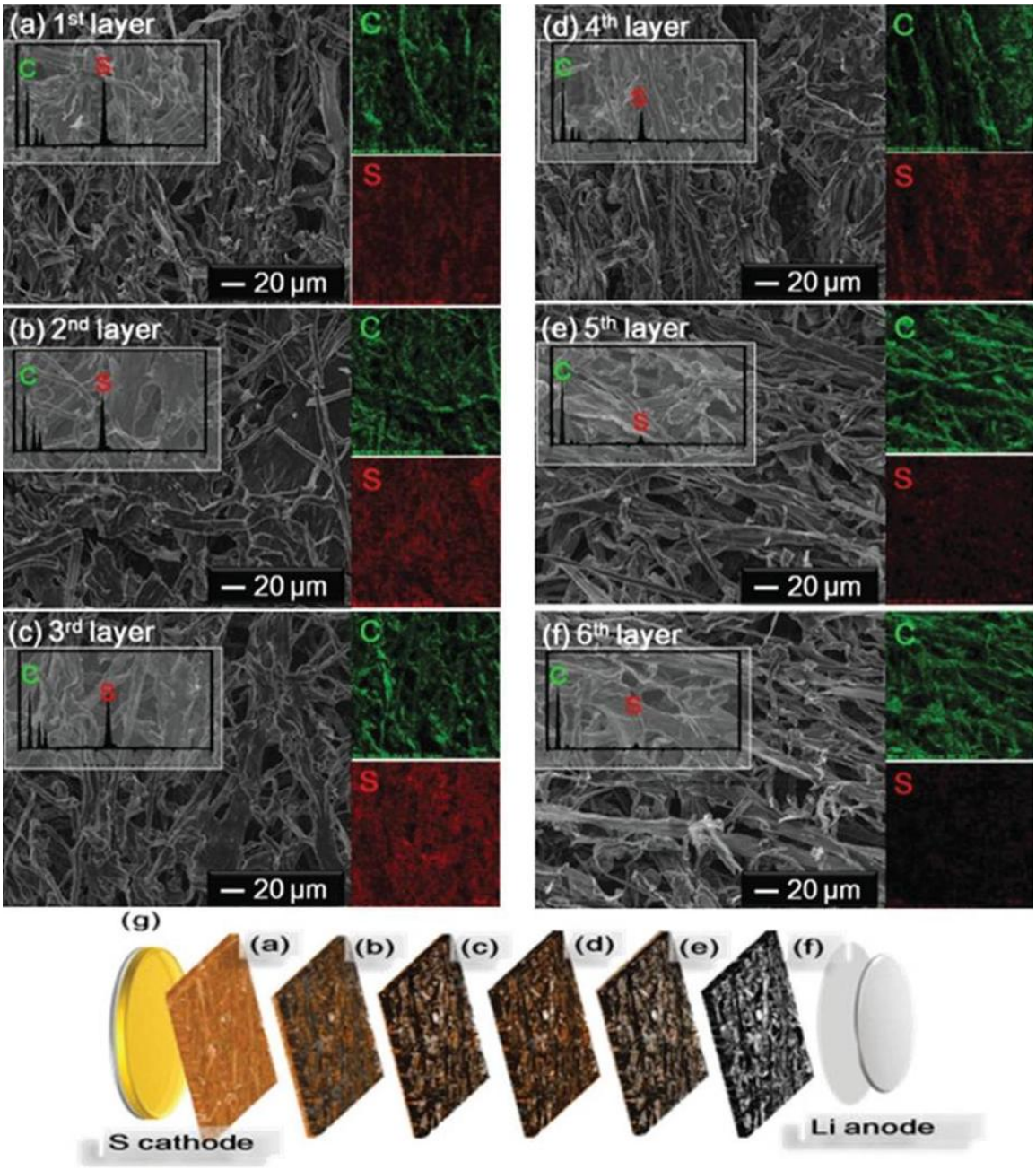

Figure 4.19: SEM/EDS microanalyses of the CK interlayer with a 6-layer module: (a) 1st layer, (b) 2nd layer, (c) 3rd layer, (d) 4th layer, (e) 5th layer, and (f) 6th layer. (g) A schematic of the cycled CK interlayer.

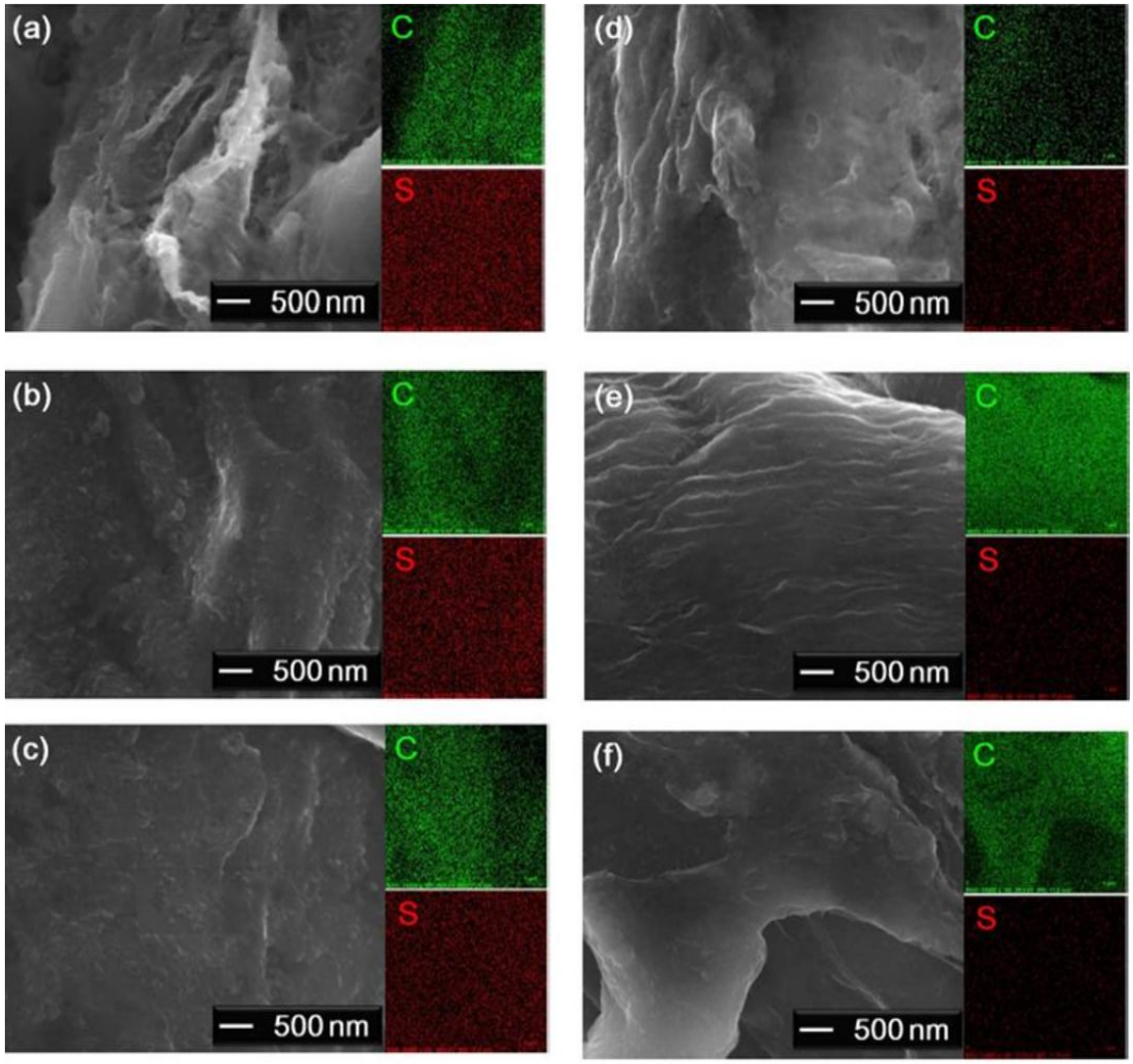

Figure 4.20: High-magnification SEM/EDS and elemental mapping microanalyses of the CK interlayer with 6-layer module: (a) 1st layer, (b) 2nd layer, (c) 3rd layer, (d) 4th layer, (e) 5th layer, and (f) 6th layer.

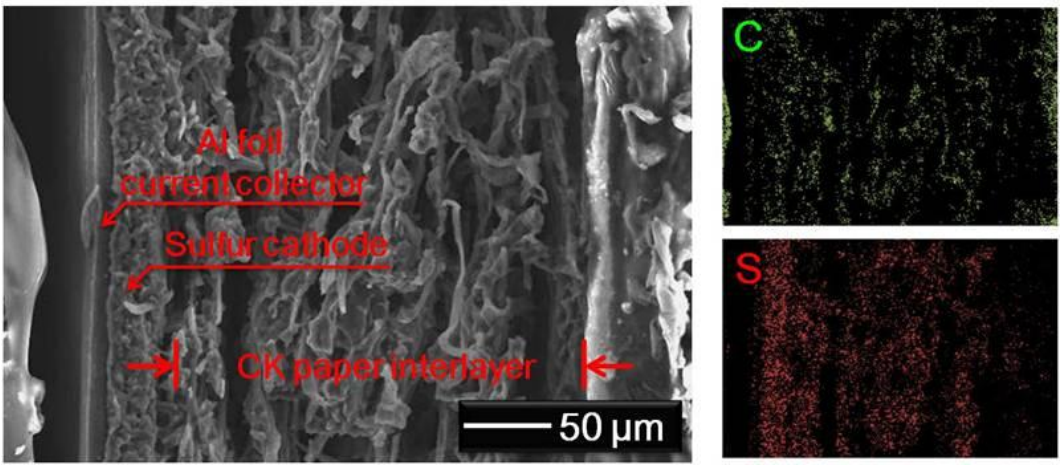

Figure 4.21: Low-magnification cross-sectional SEM and elemental mapping microanalysis of the CK interlayer.

4.3.2.6 Summary

In summary, the free-standing CK interlayer is a promising low-cost, effective carbon interlayer that leads to excellent cycling performance with the sulfur cathodes. The CK interlayer possesses a hierarchically porous structure and 3D interwoven fiber network for absorbing/trapping the active material, channeling the electrolyte, and transporting electrons. As a result, the sulfur cathode employing the CK interlayer displays a high initial discharge capacity (over 1300 mA h g^{-1}), long-term cycle stability (over 200 cycles), high Coulombic efficiency (above 98 %), and excellent rate performance (2C – C/10). The interception mechanism of the hierarchical CK paper is demonstrated by the decrease in the sulfur concentration gradient in the carbon interlayer, which reveals the importance of an optimized thickness for intercepting the migrating polysulfides. The trapped active materials are continuously reutilized and thereby provide high discharge capacity in subsequent cycles.

4.3.3 Carbon nanofiber (CNF) interlayer: effects of thickness, surface area, pore size, and electrical conductivity on electrochemical performance

Free-standing porous carbon nanofibers with tunable surface area and porous structure have been investigated as an interlayer between the pure sulfur cathode and the separator to inhibit the diffusion of polysulfides in lithium-sulfur batteries. Specifically, the effects of thickness, surface area, and pore size of carbon nanofiber (CNF) interlayers on the performance of lithium-sulfur batteries have been studied. The CNF interlayer not only reduces the cell resistance but also traps the migrating polysulfides and localizes them, thereby improving the discharge capacity as well as cyclability. It was found that the optimum thickness of the interlayer is a critical factor to achieve good cell performance, which is more important than surface area, pore structure, and electrical conductivity.

4.3.3.1 Microstructure, morphology, and characteristic analyses

CNF mats fabricated by electrospinning (by Drexel University) were directly used as an interlayer between the separator and the cathode to provide electron pathways and trap polysulfides. Three different techniques discussed in the Experimental section 4.2.3 were used to obtain CNF mats with different surface areas, porous structure, and electrical conductivity. The carbonized polyacrylonitrile (PAN) nanofibers are denoted as NPCNFs, CO_2 activated carbonized PAN nanofibers as ACNFs, and carbonized PAN-Nafion nanofibers as MCNFs. The SEM images depicting the non-woven nanofibrous morphologies[220, 221] of the NPCNF, ACNF, and MCNF are shown in Figure 4.22. Nitrogen adsorption-desorption was used to characterize the specific surface area and pore size distribution of the CNFs (Table 4.1 and Figure 4.23). The electrical conductivity values of the CNF interlayers are also listed in Table 4.1. The NPCNF with a surface area of only 54 m^2 g^{-1} has a low pore volume of 0.09 cm^3 g^{-1} and is mostly macropores. The macroporous structure is the inter-fiber spacing from the non-woven structure of the electrospun mat.[222] The ACNF has a surface area of 459 m^2 g^{-1} with 81.2

% micropore volume, indicating the high microporosity. The MCNF with a surface area of 680 m^2 g^{-1} has a micropore volume of 54 % and thus has both meso- and micro-pores.

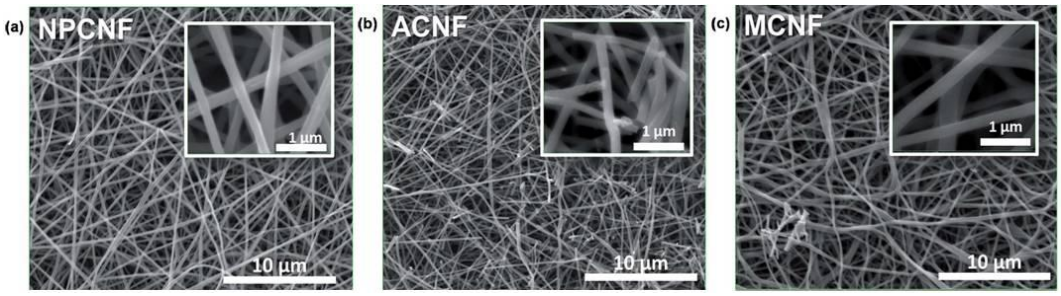

Figure 4.22: SEM images of (a) NPCNF, (b) ACNF, and (c) MCNF interlayers.

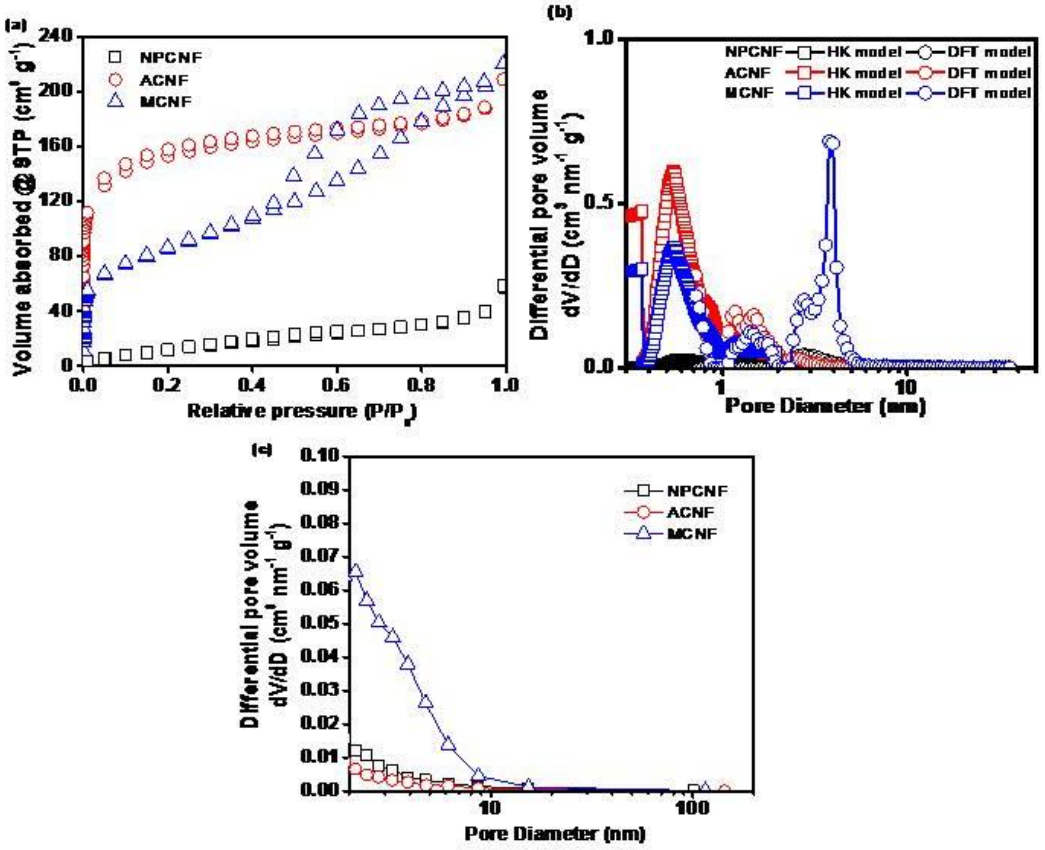

Figure 4.23: Porosity measurements of NPCNF, ACNF, and MCNF nanofibers: (a) nitrogen sorption isotherms, (b) pore size distribution with Horvath-Kawazoe (HK) and density functional theory (DFT) method, (c) pore size distribution with Barrett-Joyner-Halenda (BJH) method.

Table 4.1: Properties of the NPCNF, ACNF, and MCNF interlayers

Samples	Conductivity(S cm^{-1})	Surface Area ($m^2 g^{-1}$)	Total pore volume (cc g^{-1})	Micropore Surface Area ($m^2 g^{-1}$)	Micropore volume (cc g^{-1})
NPCNF	1.94	54.07	0.0886	-	0.0203
ACNF	0.63	459.38	0.3236	238.66	0.2651
MCNF	0.80	679.51	0.5857	98.26	0.3149

The surface chemistry of these materials was characterized by XPS to decouple the effect of surface area/pore size distribution (PSD) and surface functionalities (if any) on the battery performance. Figure 4.24a shows the nearly overlapping XPS survey scans of the NPCNF, ACNF, and MCNF. Table 4.2 lists the elemental composition and surface functional group distribution obtained by deconvolution of C1s and N1s peaks (Figure 4.24c and 4.24c) from XPS spectra. The elemental composition shows that all samples have 4 – 5% oxygen on the surface, which improves the wetting ability of the CNFs and decreases the hydrophobicity. The improved hydrophilicity has been reported in the literature to improve the polysulfide-trapping capability of carbon substrates.[55, 223, 224] The XPS data, however, do not show any significant difference in the surface elemental composition as well as the surface functionalities for the three CNFs. This establishes that the difference in the performance of these materials will not be influenced by the surface functional groups.

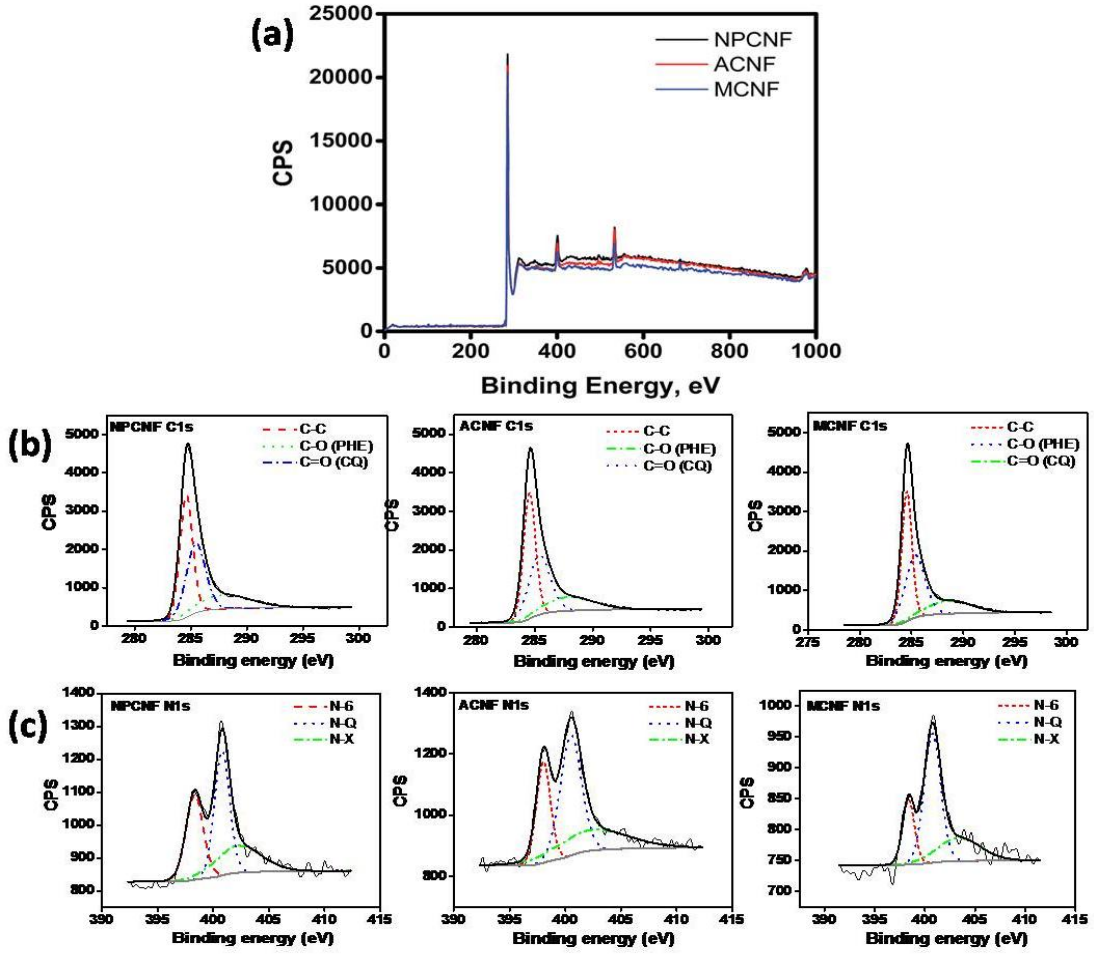

Figure 4.24: XPS analyses of various CNF interlayers: (a) survey scans, (b) deconvoluted C1s XPS peaks, and (c) deconvoluted N1s XPS peaks.

Table 4.2: Summary of elemental composition and surface functional group distribution obtained from XPS peak analysis.

Samples	C at.%	N at.%	O at.%	C1s peaks				N1s peaks		
				C-C[a]	C-O (PHE)[b]	C=O (CQ)[c]	COO[d]	N-6[e]	N-Q[f]	N-X[g]
NPCNF	89.4	7.05	3.55	42.72	36.88	20.4	-	31.98	41.11	26.92
ACNF	88.69	6.41	4.9	40.53	39.46	20.01	-	25.86	46.54	27.6
MCNF	91.55	4.38	3.58	41.94	39.42	-	18.63	19.54	54.88	25.58

[a] 284.6 eV; [b] 285.6 ±0.12 eV; [c] 287.7 ±0.1 eV; [d] 288.9 eV; [e] 398.1 ±0.2 eV; [f] 400.9 ±0.17 eV; [g] 402.5 ±1.64 eV

4.3.3.2 Comparative analysis of cells employing the conventional configuration and the interlayer configuration

In Figure 4.25, the cycling performance of lithium-sulfur cells with and without an ACNF interlayer demonstrates a significant improvement in the cell performance while using the interlayer. The initial discharge capacities of the cell using conventional sulfur cathodes (a sulfur content of 60 wt. %) increase from 1226 to 1519 mA h g^{-1} on incorporating the ACNF interlayer into the pure sulfur cathode cells. ACNF interlayer cells also show good cyclability with a capacity retention rate approaching 60 % (reversible capacity: 910 mA h g^{-1}) after 200 cycles. The ACNF interlayer further allows the use of conventional sulfur cathodes with a high sulfur loading of 70 wt. %, boosting the initial discharge capacity from 845 (without interlayer) to 1515 mA h g^{-1} (with interlayer) and achieves a high reversible capacity of 810 mA h g^{-1} after 200 cycles. Such an improvement in performance is attributed to the interlayer acting as a repository for polysulfide intermediates, thereby improving the initial discharge capacity and providing reactive sites to improve the reutilization of the active material.[208, 209]

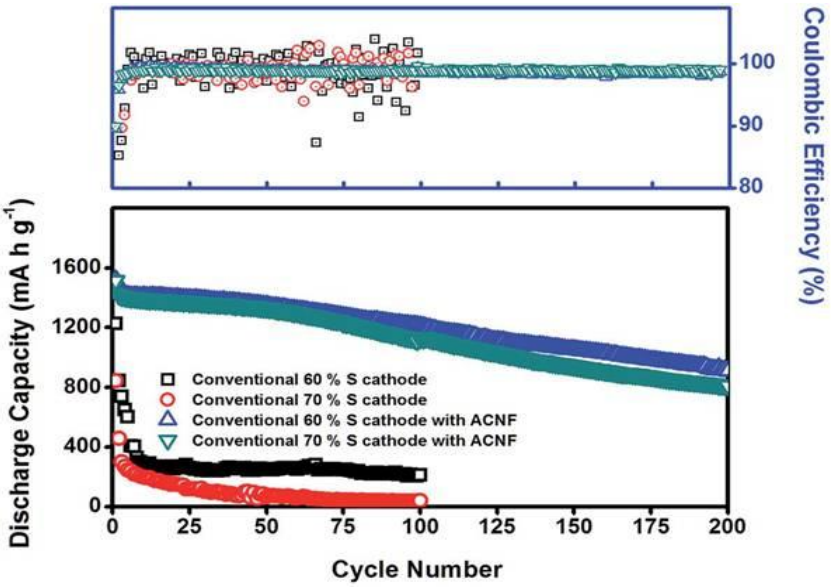

Figure 4.25: Cycling performance comparisons with and without ACNF interlayers in lithium-sulfur cells.

The SEM and elemental mapping of the in-plane and cross-section of the interlayer after cycling (Figure 4.26) confirm the entrapment of the active material. After 200 cycles, the ACNF interlayer shows uniform sulfur distribution in its microporous structure. The TEM image displaying the adsorption of polysulfides on the surface of the ACNF interlayer is shown in Figure 4.27.

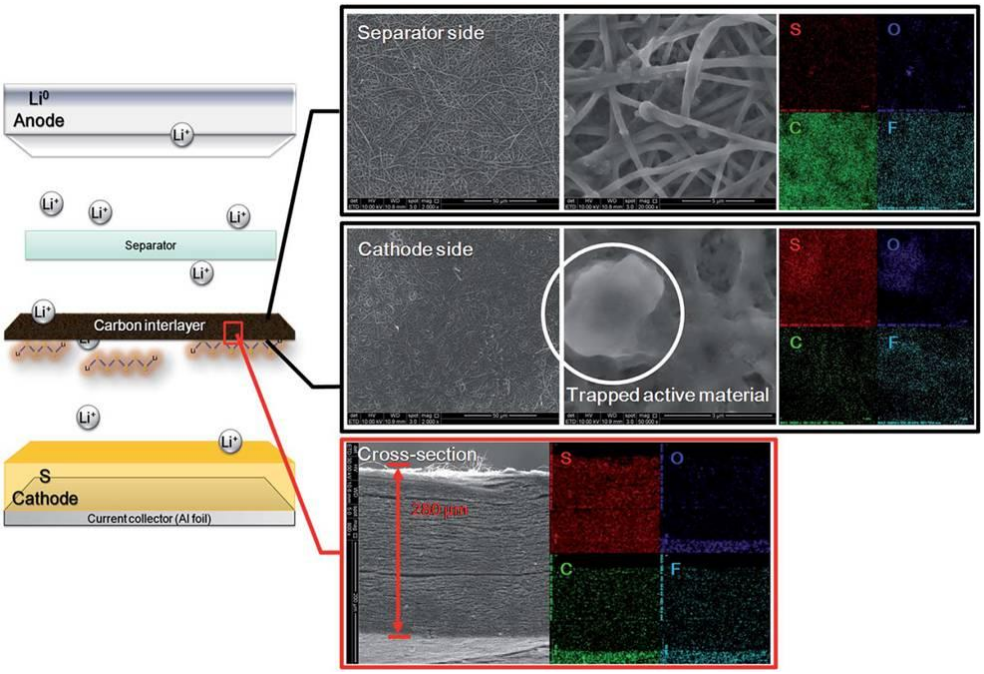

Figure 4.26: SEM and EDS images illustrating the capturing of polysulfides by the ACNF interlayer.

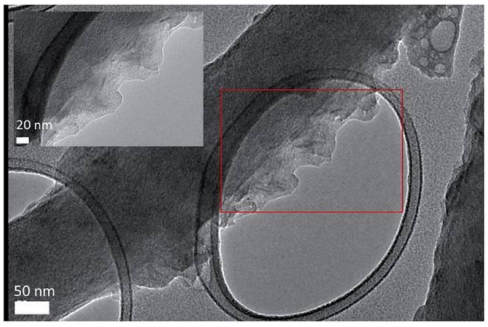

Figure 4.27: TEM image of the cycled ACNF interlayer after 100 cycles. The inset shows the magnified image of the highlighted rectangular portion showing the trapping of lithium polysulfides by the nanofibers.

4.3.3.3 Effect of optimization on the interlayer thickness

The effect of the CNF thickness on the cycling performance was then investigated. It was found that the discharge capacity is significantly affected by the thickness of the interlayer and an improvement in performance was observed with increasing thickness of the interlayer. A systematic study of the effect of thickness on cell performance was carried out by varying the weight of NPCNF and ACNF interlayers from 1.3 to 4.2 mg cm^{-2} at C/5 rate. Figure 4.28 shows an improvement in the initial discharge capacity as well as cyclability with increasing thickness of the interlayer. High initial discharge capacities of 1572 mA h g^{-1} and 1519 mA h g^{-1} were obtained, respectively, for 4.2 mg cm^{-2} NPCNF and ACNF interlayers at C/5 rate. As can be seen in the SEM image in Figure 4.26, the interlayer surface facing the cathode side shows more trapped polysulfides than the surface facing the separator. Thus, we believe that, with long-term cycling, the polysulfides gradually diffuse through the interlayer, thus an optimum thickness is essential to capture most of the migrating polysulfides.[209] Hence, 4.2 mg cm^{-2} weight interlayer that shows the best performance was selected as the optimum weight/thickness interlayer for further studies.

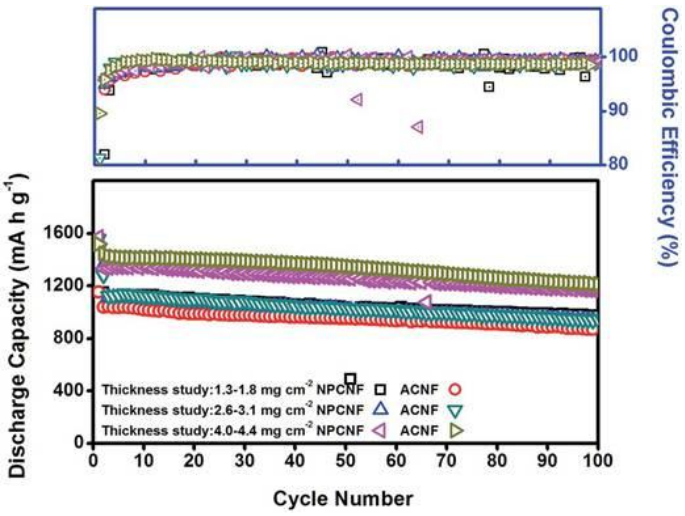

Figure 4.28: Battery cycling performance comparison with varying thicknesses of NPCNF and ACNF interlayers.

4.3.3.4 Electrochemical analysis

Figure 4.29 compares the Nyquist plots of the lithium-sulfur cells with and without the interlayer configuration. The charge-transfer resistance reduces significantly from 583 ohms without interlayer to 74 ohms with interlayer, indicating that the interlayer provides a conductive pathway.[173] The cyclic voltammetry (CV) curves (at 0.1 mV s^{-1} scanning rate) of the lithium-sulfur cells with the NPCNF, ACNF, and MCNF interlayers for the initial ten cycles are shown in Figure 4.30a – 4.30c. After the initial cycle, the active-sulfur particle rearranges itself to more energetically favorable sites[173] and hence the subsequent scans nearly overlap in interlayer cells, showing good electrochemical reversibility. A slight drop in the oxidation peak is observed in the subsequent CV curves of ACNF and MCNF interlayers. We believe that the polysulfides trapped in the micropores of ACNFs and MCNFs become inaccessible as more layers of polysulfides deposit on them and hence are not charged completely. The two reduction and oxidation peaks in the CV curves are consistent with the two discharge and charge plateaus shown in the discharge-charge profiles (Figure 4.30d – 4.30f). A similar two step electrochemical process in both discharge and charge steps has been observed previously for lithium-sulfur batteries.[13, 17] First, the reduction of S_8 to long chain polysulfides (Li_2S_x, x = 4 – 8) (Peak I) takes place, followed by subsequent reduction to solid Li_2S2/Li_2S (Peak II). Peak III corresponds to the oxidation of Li_2S_2/Li_2S to Li_2S_4 and Peak IV corresponds to the subsequent oxidation to Li_2S_8/S.[17, 181]

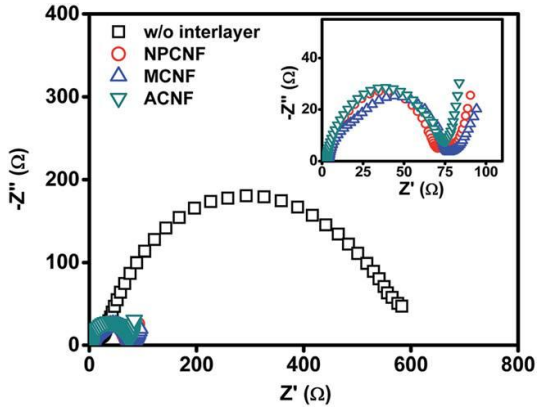

Figure 4.29: Nyquist plots for lithium-sulfur cells with and without interlayers.

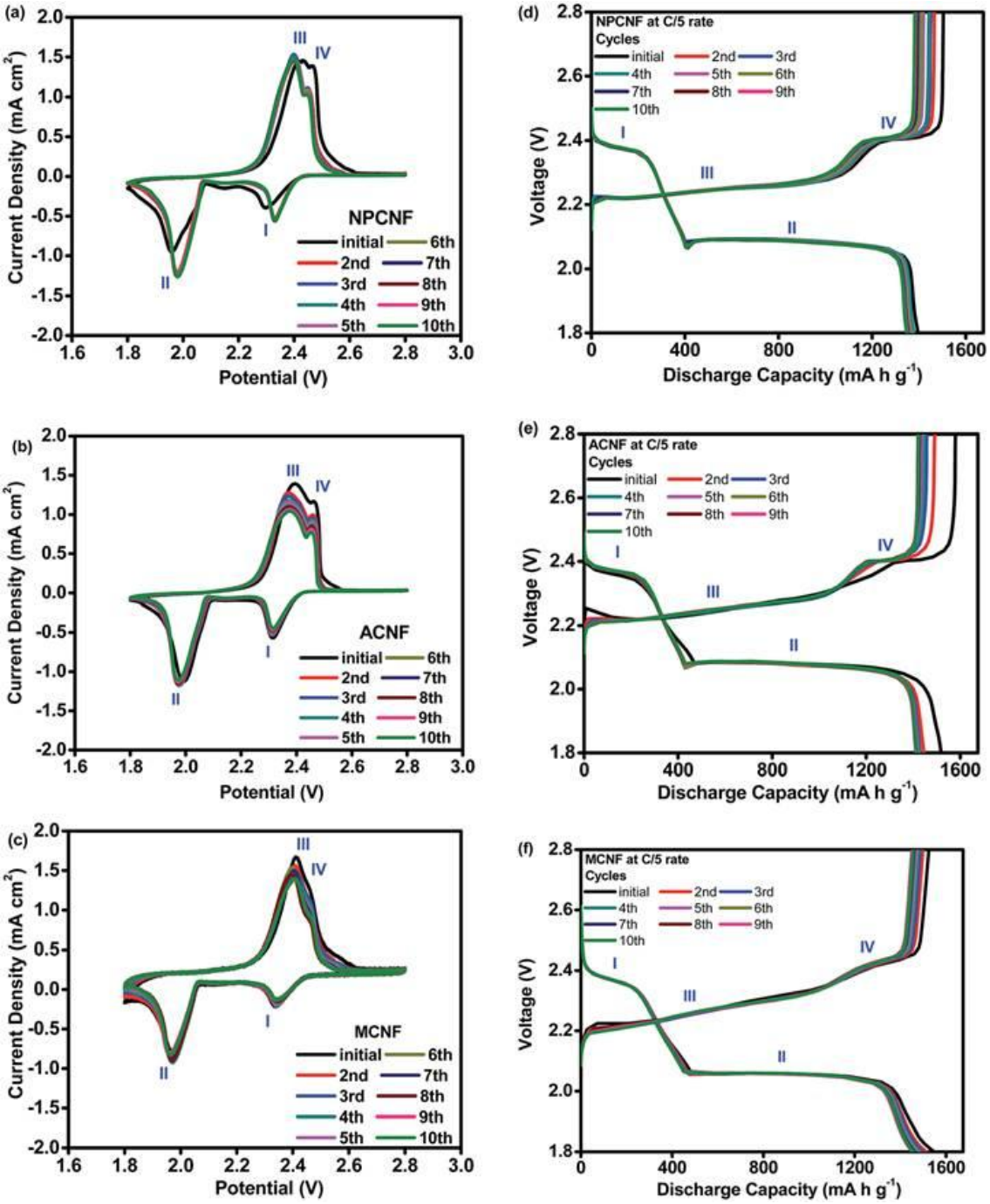

Figure 4.30: (a – c) Cyclic voltammetry plots and (d – f) discharge-charge plots of the first 10 cycles at C/5 rate for lithium-sulfur batteries with (a and d) NPCNF, (b and e) ACNF, and (c and f) MCNF interlayers.

4.3.3.5 Effect of the microstructure, porosity, and electrical conductivity of the interlayer on cell performance

Then, the NPCNF, ACNF, and MCNF interlayers were utilized as testing platform for investigating the effect of the microstructure, porosity, and electrical conductivity on the electrochemical performance of cells with the interlayer configuration.

The cycling performances of the NPCNF, ACNF, and MCNF interlayers are compared at different cycling rates (C/5 and 1C rates) in Figure 3.31 and summarized in Table 4.3. The initial discharge capacity of the cells at C/5 rate with any of these CNF interlayers is above 1510 mA h g^{-1} (> 90 % active material utilization), which is possibly due to the use of an optimized thickness of these carbon nanofiber interlayers. This reconfirms that the thickness of interlayers is the key factor on improving the cell performance. In addition, the similar fibrous network structure may also result in the similar cyclability. NPCNFs, despite less than one-twelfth of the surface area of MCNFs and one-ninth of the surface area of ACNFs, show comparable initial discharge capacity at C/5 rate. But it shows higher capacity fading (20 % loss in 50 cycles) - almost twice that of ACNF and MCNF interlayer cells at this discharge rate. At a fast cycling rate (1C rate), NPCNF interlayer cells deliver nearly 20 % lower initial discharge capacity compared to ACNFs and MCNFs, but show a much higher capacity retention on cycling, nearly 100 % after 50 cycles and 90% after 100 cycles, when calculated based on the 1st cycle discharge capacity.

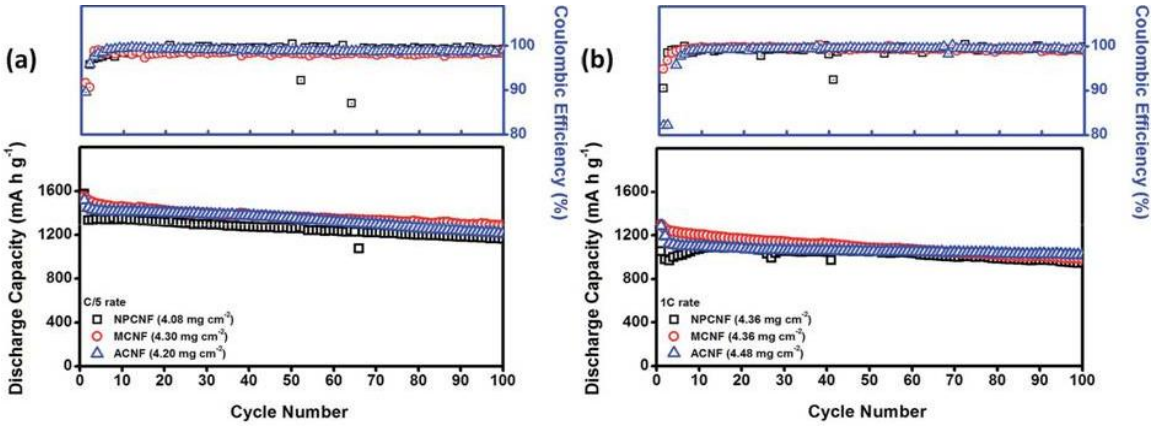

Figure 4.31: Comparison of the cycling performances of lithium-sulfur cells with various interlayers at (a) C/5 and (b) 1C rates.

We expect that the initial discharge performance depends on how well the interlayer traps the intermediate polysulfides for the complete reduction reaction to take place. Therefore, one would expect the discharge capacity to increase with increasing surface area - a trend seen at a high rate of 1C. However, the effect of surface area becomes less prominent at a slow rate of C/5, possibly due to the large amount of time available for the diffusion of polysulfides through the interlayer nullifying the effect of surface area during the initial discharge. Thus, at slow rates, the thickness of the interlayer plays a more important role in hindering the diffusion of polysulfides towards the anode. We believe that the reversible capacity (or cyclability), in contrast, not only depends on the polysulfide trapping efficiency of the interlayer, but is also influenced by the accessibility of the trapped active material in the interlayer, which in turn is affected by the pore size/structure and conductivity of the interlayer as well as the charging rate. At faster charge-discharge rates (1C), NPCNF seems to reach the highest capacity retention rate when calculated based on the initial discharge capacity (Table 4.3).

Table 4.3: Comparison of the cell performances with different CNF interlayers

	Cut-off potential, V	Rate	1st Discharge capacity, mAh g^{-1}	% Capacity retention	
				50 cycles	100 cycles
NPCNF interlayer	1.8-2.8	C/5	1571.69	80.01	73.91
	1.8-2.8	1C	1053.19	99.88	89.96
ACNF interlayer	1.8-2.8	C/5	1518.77	88.97	79.98
	1.8-2.8	1C	1285.08	82.00	79.25
MCNF interlayer	1.8-2.8	C/5	1548.71	87.95	83.06
	1.8-2.8	1C	1297.90	83.66	76.08
	Cut-off potential, V	**Rate**	**18th Discharge capacity, mAh g^{-1}**	**% Capacity retention**	
				50 cycles	**100 cycles**
NPCNF interlayer	1.8-2.8	1C	1093.03	96.24	86.68
ACNF interlayer	1.8-2.8	1C	1083.02	97.30	94.03
MCNF interlayer	1.8-2.8	1C	1171.29	92.70	84.30

However, the apparent highest capacity retention may result from the low active material utilization (due to the low surface area) and the stabilization process in the initial few cycles (from the 1^{st} cycle to the 18^{th} cycle). Thus, the capacity retention after 50^{th} and 100^{th} cycles based on the discharge capacity at the 18^{th} cycle is also presented for a fair comparison. The results show that, based on the 18^{th} cycle data, the capacity retention varies as ACNFs > NPCNFs > MCNFs. Interestingly, the ACNF samples attain the highest capacity retention of 94 % in comparison to NPCNFs with the highest electrical conductivity (capacity retention of 86 %) and MCNFs with the highest surface area (capacity retention of 84 %). This could be explained by the difference in the pore structure because of the differences in the fabrication procedures of the three interlayers.

The NPCNF is a nonporous nanofiber with a high conductivity but lacks abundant accessible reaction sites, which results in limited sulfur-carbon contact, resulting in a relatively low capacity retention rate. The pore structure of MCNFs arises from the decomposition of the sacrificial polymer, which leads to a through-connected meso-/microporous structure throughout the fiber.[214, 225] In ACNFs, the micropores are

largely formed on the nanofiber surface via CO_2 activation. Hence, the pores in MCNFs would be less accessible than those in ACNFs at high cycling rates, thus leading to lower capacity retention in the former. At the slow C/5 rate, however, there is sufficient time for the reactivation of the trapped active material, so as expected, the capacity retention increases with increasing surface area (MCNF > ACNF > NPCNF). The presence of larger mesopores in MCNFs may further facilitate the reactivation of the trapped active material by channeling the electrolyte *via* mesoporous pathways to the microporous trapping sites[226] and may also transport the electrolyte containing dissolved polysulfides to the microporous trapping sites.[28] This high performance of MCNFs is attributed to the synergistic effect of their high surface area micro-mesoporous structure preventing polysulfide diffusion and the inter-fiber macroporous structure providing electrolyte accessibility.

4.3.3.6 Summary

The performance of lithium-sulfur cells by inserting a free-standing CNF interlayer between the sulfur cathode and the separator has been investigated. The CNF interlayer not only reduces the electrochemical resistance but also localizes the migrating polysulfides and traps them, thereby improving the discharge capacity as well as cyclability. It was found that the optimum thickness of the interlayer is a significant factor to achieve good cell performance. The MCNF interlayer with optimum thickness, high surface area, meso–micro-porous structure delivered a high initial discharge capacity of 1549 mA h g^{-1} at C/5 rate, which is 92 % of the theoretical capacity of sulfur, with 98 % average Coulombic efficiency and 83 % capacity retention after 100 cycles.

4.4 CONCLUSIONS

In conclusion, the bifunctional interlayer has evidenced that it can effectively stabilize the migrating polysulfides within the cathode region of the cell, resulting in long-term cycle stability with high sulfur utilization. The polysulfide-intercepting

capability and the electrochemical performance of the cell with the interlayer configuration was investigated thoroughly by several designed interlayers.

In the CL interlayer study, the comparative analysis of the two opposite CL-interlayer configurations demonstrates that the surface architecture and morphology of the interlayer will dominate the cell electrochemical performance, especially the reversible discharge capacity. Hence, the inserted interlayers should have great capability to intercept the migrating polysulfides and to reactivate the trapped active material. Therefore, in the CK interlayer work, the capability to intercept the migrating polysulfides is investigated by studying the cycled modulable CK interlayer. The result evidences that the polysulfide-interception capability of interlayers can be greatly enhanced by optimizing the thickness of the interlayer. On the other hand, the reactivation capability toward the trapped active material in interlayers may result from the excellent electrolyte immersion/penetration, efficient electron transport, and intimate three-phase boundary involving the electrolyte, conductive network, and the active material. In the third work, various CNF interlayers (PNCNF, ACNF, and MCNF) with an optimum thickness reconfirm that the thickness of the fibrous interlayers is significant for cells to attain good electrochemical reversibility and stability, which is more important than other parameters (*e.g.*, surface area, pore size, and electrical conductivity).

Chapter 5: Development of a polysulfide reservoirs*

5.1 INTRODUCTION

The prospect of rechargeable batteries aims to power electric vehicles and to integrate energy storage systems with green energy power plants. To realize these practical applications, the most urgent issue in battery research is the development of a new cathode material to replace the current cathode materials, which suffer from capacity limitations.[6, 11, 24] Sulfur is one of the most promising cathode materials for next generation rechargeable batteries because of its high theoretical capacity (1672 mA h g^{-1}) and energy density (~ 2500 W h kg^{-1}).[10, 24, 52] In addition, sulfur offer other advantages, such as abundance, low cost, light weight, and environmental friendliness.[24, 52]

However, two main technical challenges impede the commercialization of the lithium-sulfur system. First, the specific discharge capacity of lithium-sulfur cells is limited by poor active material utilization caused by the insulating nature of sulfur and its discharge products (Li_2S).[33, 170] Second, the short cycle life and low Coulombic efficiency are related to a combination of polysulfide diffusion and its shuttling during cycling.[33, 227] The highly soluble polysulfides (Li_2S_x, $x = 4 - 8$) easily migrate through the separator, leading to the loss of active material and severe capacity fade. The diffused polysulfides further react with the Li-metal anode and corrode it, resulting in cell failure.[11, 228, 229]

The solutions to these problems are quite straightforward: improve the cathode conductivity and stabilize the active material within the cathode. However, achieving these objectives has proven difficult. One promising solution is to encapsulate sulfur in a sulfur-based nanocomposite. Sulfur-based nanocomposites not only improve the physical connection between the insulating sulfur and the conductive polymers/carbons, but also store the active material in their porous space.[22, 91, 95, 200, 201, 205-207] The prevalent sulfur

---

* S.-H. Chung and A. Manthiram, "Carbonized eggshell membrane as a natural polysulfide reservoir for highly reversible Li-S batteries," *Adv. Mater.* 2014, **26**, 1360-1365.
S.-H. Chung carried out the cell design and experimental work. A. Manthiram supervised the project. All participated in the preparation of the manuscript.

based nanocomposites have further inspired modifications of the cell configuration.[138, 173-176] The design principle on different cell configurations is to absorb the active material and the soluble polysulfides by diverse micro-/meso-/macro-porous carbon substrates that have high surface area and high electrical conductivity, which stabilizes the electrochemical reactions in the cathode. First, a porous carbon paper inserted between the sulfur cathode and the separator serves as a polysulfide barrier to limit polysulfide diffusion and localize the active material within the cathode side.[173, 174] Second, a 3D porous current collector with micro-/meso-/macro-porous structure that can store the active material, absorb the soluble polysulfides, and channel the electrolyte has the potential to substitute the conventional 2D flat current collectors.[66, 138, 175, 176] Recent developments in porous carbon substrates have made the dissolved sulfur cathodes and the dissolved polysulfide cathodes to have a new lease of life.[26, 29, 128] The feature of the liquid cathode system is their highly efficient electrochemical utilization.[26, 29, 128] After loading the porous substrates with the dissolved polysulfide catholyte, the encapsulated active material can be completely trapped by the porous framework, reducing the loss of active material. Therefore, the combination of cell configuration modifications with dissolved polysulfide catholyte can take a decisive path for developing high-performance lithium-sulfur cells with high specific capacity and long cycle life.

In this chapter, we present a natural material recycled from domestic waste as the electrode: an eggshell membrane. The eggshell membrane possesses a uniform microporous structure and an interwoven fiber network, making it an excellent nanomaterial synthesis template.[230, 231] To adopt the natural microporous architecture, we developed free-standing carbonized sucrose-coated eggshell membranes (CSEMs) and used them to form a reservoir for the dissolved Li_2S_6 polysulfide catholyte. The polysulfide catholyte contains 1.5 M sulfur in a regular 1:1 volume ratio 1,3-dioxolane (DOL)/1,2-dimethoxyethane (DME) electrolyte. In our study, the coalescing CSEM fibers that have high microporosity form a natural macro-/micro-porous framework. Therefore, the microscopic morphology of the CSEM reservoirs displays abundant

micropores for active material encapsulation and 3D accessible pathways for electrolyte penetration. Although the carbonized eggshell membrane (CEM) is not as conductive as a metal, the carbonized sucrose improves the electrical conductivity without reducing the microporosity. The macroscopic configuration of the CSEM reservoir has the bottom CSEM as a current collector, the top CSEM as an inhibitor, and the dissolved polysulfide catholyte stabilized in between. This configuration provides Li/dissolved polysulfide cells with high discharge capacity, excellent cycle stability, and high sulfur loading. Moreover, the free-standing CSEM itself has high electrical conductivity and a hierarchical macro-/micro-porous structure in contrast to the carbonized eggshell membrane reported by Li *et al.*[104] that required a conductive carbon disc bonded onto it. .

5.2 EXPERIMENTAL

5.2.1 Free-standing CSEM thin film fabrication

The eggs bought from a supermarket were broken, and the eggshells were washed with deionized water and immersed into 1 M HCl for 2 h to etch away the hard eggshell ($CaCO_3$). The remaining natural eggshell membrane was then rinsed thoroughly with deionized water and immersed into a 40 % sucrose solution (sucrose; Fisher Scientific) overnight to ensure complete sucrose coating on the eggshell membrane fibers. The sucrose-coated eggshell membranes were supported by a 1.5 cm × 4.0 cm Toray carbon paper (Fuel Cell Earth) to keep a flat film shape and were pre-carbonized by the hydrothermal method for 12 h at 180 ℃ in presence of 40 % sucrose solution. After pre-carbonizing, the coated sucrose became a carbon layer covered on the surface of the eggshell membrane. The pre-carbonized sucrose-coated eggshell membrane was subsequently carbonized for 12 h at 800 ℃ with a heating rate of 1 ℃ min^{-1} in a tube furnace under argon protection. After carbonization, the carbonized sucrose-coated eggshell membranes (CSEMs) converted into a light-weight carbon thin film. The free-standing CSEMs were easily removed from the Toray carbon paper. As a result, the Toray carbon paper does not influence the material and electrochemical analysis of the CSEMs. The resulting CSEMs were washed thoroughly with deionized water and dried

in a convection oven at 50 ℃ before use. An outstanding feature of the free-standing CSEM is its natural membrane shape in contrast to other artificial carbon electrode materials (*e.g.*, CNFs, CNTs, or spherical carbon powders) that require multistep processing, hard templating, acid-alkali treatments, or binder adjunction.

5.2.2 Li/dissolved polysulfide cell assembly

The dissolved polysulfide catholyte was prepared by mixing sublimed sulfur powder (Acros Organics) and Li_2S powder (Acros Organics) in the regular 1 M 1:1 volume ratio DME/DOL electrolyte. The precursor solution was heated for 18 h at 45 ℃ inside an argon-filled glove box to produce a reddish brown dissolved polysulfide solution (1.5 M sulfur in the solution). The regular DME/DOL electrolyte was prepared by dissolving 1 M $LiCF_3SO_3$ salt (Acros Organics) and 0.1 M $LiNO_3$ (Acros Organics) in a 1:1 volume ratio of DME (Acros Organics) and DOL (Acros Organics). The CSEM reservoir has a CSEM current collector loaded with the dissolved polysulfide catholyte and a CSEM inhibitor on the top. Then, in sequence, a polypropylene separator (Celgard), lithium foil, and a nickel foam spacer were placed into a CR2032 coin-type cell with the presence of the regular DME/DOL electrolyte. The cell was assembled in an argon-filled glove box. In each cell, the mass of active material in the CSEM reservoir was around 1.0 mg, representing a high sulfur loading of 3.0 – 3.2 mg cm^{-2}. However, for a comparison, the highest sulfur loading in conventional sulfur cathodes prepared by a slurry casting method on aluminum foil as current collector was only 1.4 mg cm^{-2} and is limited by the flat 2D morphology of the aluminum foil.

5.3 RESULTS AND DISCUSSION

5.3.1 Microstructure analysis and cell configuration design

The porous architecture and unique morphology of the natural micropores in the CSEM reservoirs were investigated by SEM microanalyses with elemental mapping. Figure 5.1 shows that the long-range porous network of the CEMs is composed of coalescing fibers. Different from the CEMs, the CSEM have the conductive carbon

coated onto the surface of the fibers as shown in Figure 5.2a. The carbonized sucrose reduces the resistivity from 1.36×10^{-3} to 5.57×10^{-4} ohm m. The carbonized sucrose and the high structural integrity of the fiber network provide high electrical conductivity.[104, 176] The interwoven fibers also form the macroporous channels for electrolyte penetration and immersion.[173, 176] Moreover, the microporous network facilitates polysulfide electrolyte impregnation and then effectively stores the active material in the CSEMs through its strong absorption.[138, 215] In addition, as has been reported in the literature, CEMs contain ~ 10 wt. % nitrogen and oxygen, which may benefit the specific capacity of carbon substrates.[87, 197, 211] However, nitrogen and oxygen elemental signals detected in CSEMs are much weaker than those in CEMs (Figure 5.3), possibly due to the coated carbon layer that decreases the nitrogen and oxygen signals. Therefore, the improvement of the CSEM reservoir may mainly result from its physical morphologies (macroporous networks and micropore arrays).

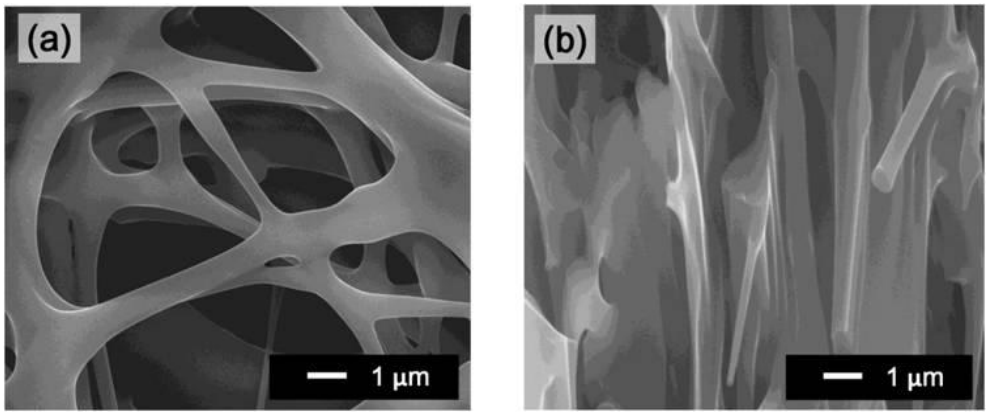

Figure 5.1: High-magnification SEM images of the CEMs: (a) surface image and (b) cross sectional image.

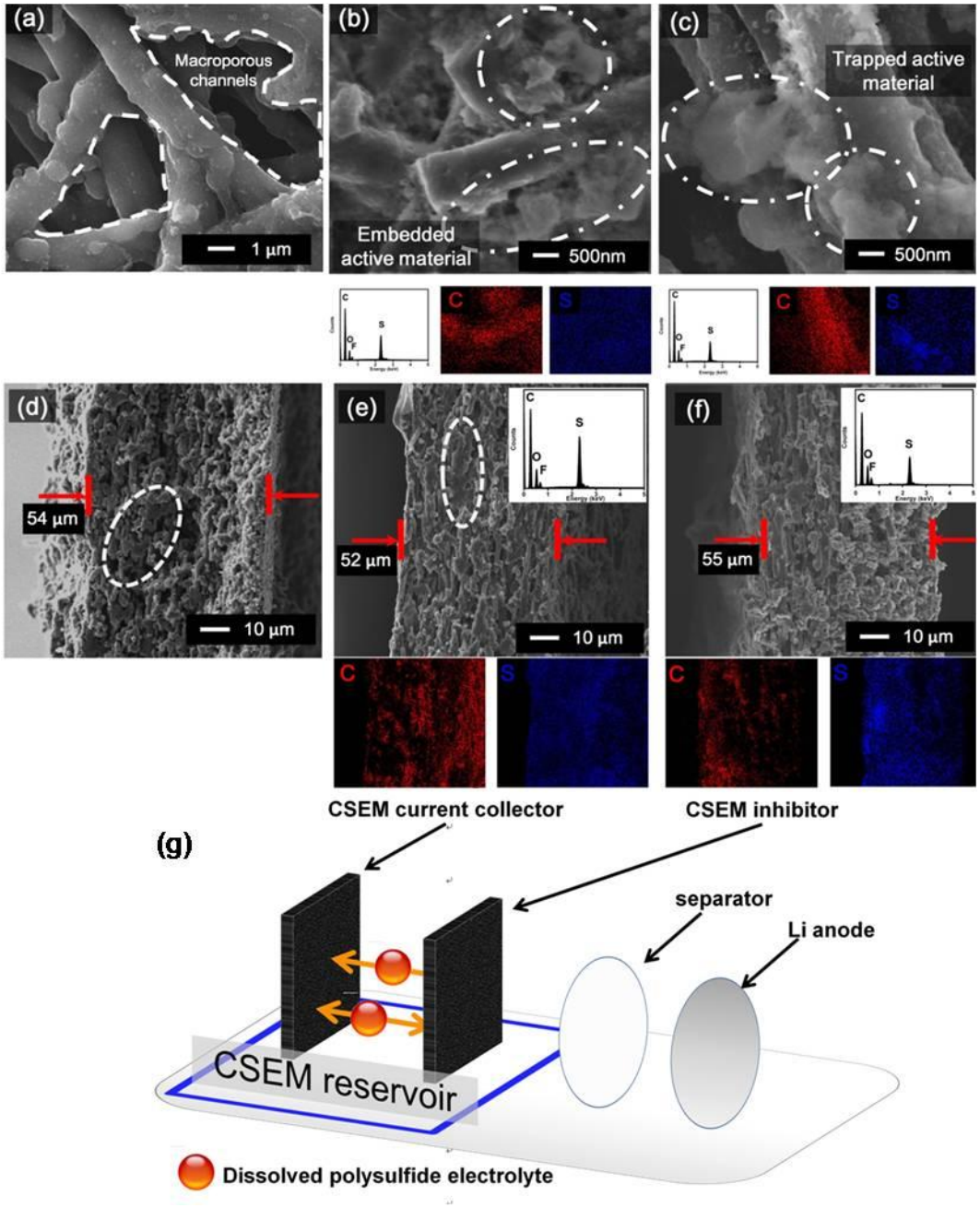

Figure 5.2: SEM/EDS and elemental mapping microanalysis: Surface microanalysis of (a) CSEMs, (b) cycled CSEM current collectors, and (c) cycled CSEM inhibitors. Cross-sectional microanalysis of (d) CSEMs, (e) cycled CSEM current collectors, and (f) cycled CSEM inhibitors. (g) Schematic model of the CSEM reservoir configuration.

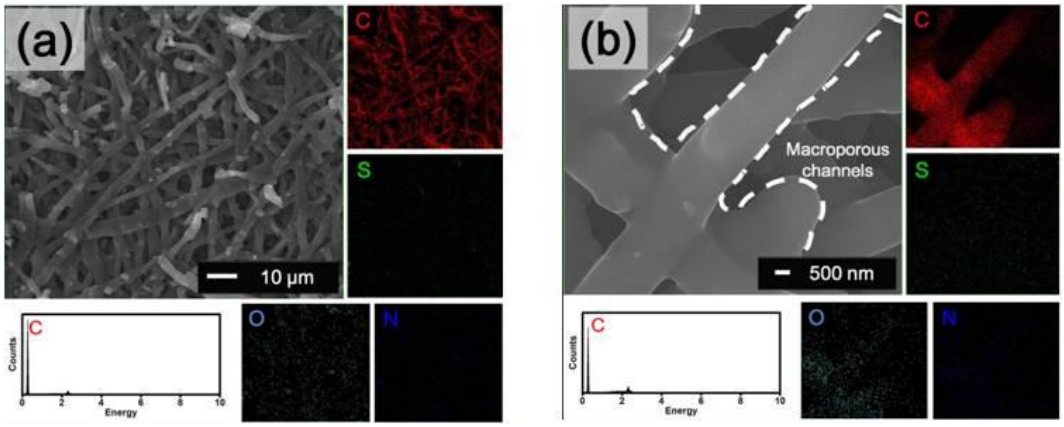

Figure 5.3: (a) Low- and (b) high-magnification surface SEM/EDS and elemental mapping results of the CSEMs.

The surface SEM image of the cycled CSEM current collectors (Figure 5.2b) reveals that the active material is excellently accommodated in the macro-/micro-porous network. The well-embedded active material is also observed in a uniformly distributed sulfur signal in the microporous matrix in the elemental mapping results. The corresponding low-magnification SEM and elemental mapping further indicates a wide range of the uniform active material encapsulation in the cycled CSEM current collectors (Figure 5.4a). Figure 5.2c exhibits the active-sulfur material trapped in the carbon matrix of the CSEMs inhibitors and unimpeded electrolyte channels in the inhibitors. The low-magnification SEM (Figure 5.4b) and elemental mapping of the CSEM inhibitor shows the porous surface with some dense parts and strong sulfur signal regions, which may be the captured active material. In Figure 5.2b and 5.2c, a comparison of the EDS spectra of the two CSEM components reveals a stronger sulfur signal in the current collector than in the inhibitor, which reconfirms that the CSEM current collector works as a container and the CSEM inhibitor functions as a dissolved polysulfide barrier.

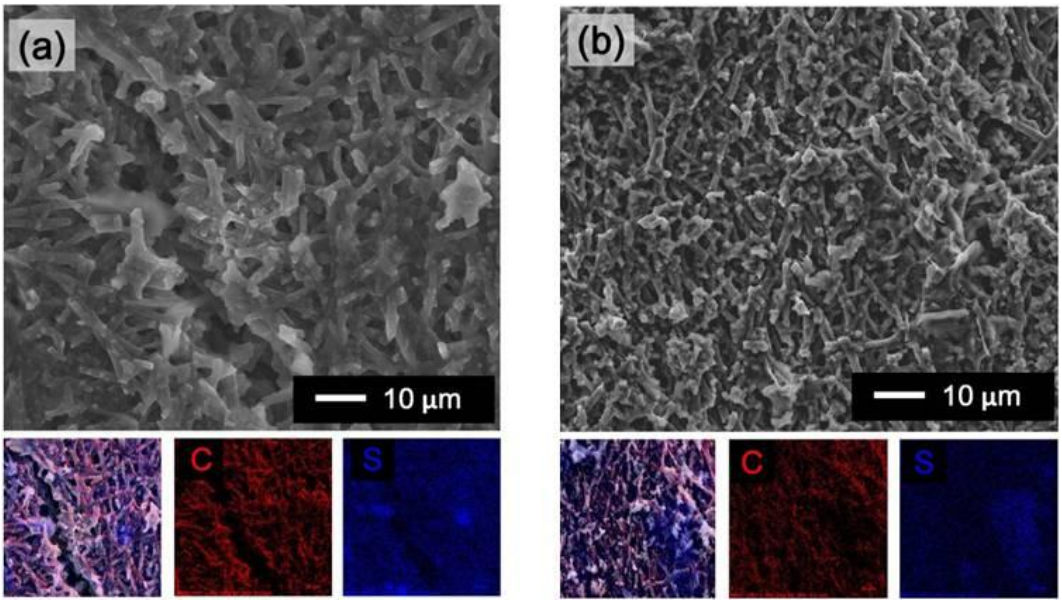

Figure 5.4: Low-magnification surface SEM images with elemental mapping results: (a) cycled CSEM current collector and (b) cycled CSEM inhibitor.

Cross sectional SEM of the CSEM (Figure 5.2d) displays its porous matrix and the coalescing fiber network (in the white mark). Figure 5.2e shows that the microstructure of the cycled CSEM current collector is similar to the pristine CSEMs and still has an unblocked macroporous network. However, the elemental mapping results depict a uniform sulfur encapsulation within the CSEM current collector, implying that the active material was excellently absorbed within the microporous network of the CSEM current collector and not precipitated on the surface. The excellent polysulfide electrolyte immersion and active material encapsulation also confirm the intimate connection between the insulating active material and the conductive matrix. The dense region enclosed within the white mark is the original coalescing fiber network. In Figure 5.2f, the SEM image of the CSEM inhibitor also reveals a well-maintained porous structure. However, the elemental mapping result indicates that the CSEM inhibitor trapped more active material in its micropores toward the cathode side than that toward the anode side. This demonstrates that the CSEM inhibitor can limit polysulfide diffusion

by intercepting the migrating polysulfides by its microporous absorption sites. As a result, the free-standing CSEM reservoir localizes well the active material and migrating polysulfides in the cathode region as shown in the Figure 5.2g. Moreover, the high-magnification cross-sectional SEM images and elemental mapping results of the cycled CSEM current collector and CSEM inhibitor (Figure 5.5) exhibit uniform sulfur signals in the micropore arrays and no active material agglomerates block the macro/microporous network, evidencing that the active material is encapsulated in the micropores.

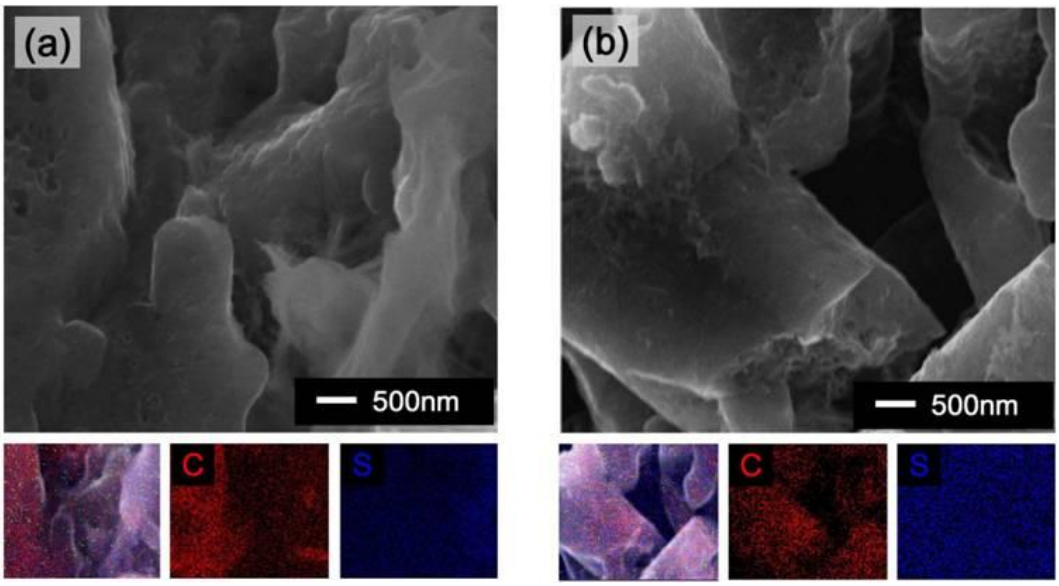

Figure 5.5: High-magnification cross-sectional SEM images with elemental mapping results of the microporous structure on the CSEM fibers: (a) cycled CSEM current collector and (b) cycled CSEM inhibitor.

Changes in surface area and porosity were investigated by the Brunauer-Emmett-Teller (BET) measurements on fresh and cycled CSEM reservoirs. The fresh CSEMs have a high surface area of 429 m^2 g^{-1} (35 % contributed by micropores) and pore volume of 0.36 cm^3 g^{-1} (the pore volume of CEMs is 0.27 cm^3 g^{-1}) with mixed IUPAC types I & IV isotherms.[180] For a comparison, the surface area of CEMs is 396 m^2

g^{-1} (30 % contributed by micropores). In Figure 5.6a and 5.6b, the IUPAC type I isotherms in the low-pressure region and a high fraction of micropores pore-size distribution curves demonstrate high microporosity in CSEMs. The hysteresis loop at $P/P_0 = 0.45 – 1.0$ represents the mesopores, which is provided by the carbonized sucrose. Interestingly, the type I isotherms at $P/P_0 \leq 0.1$ are identical to those in the CEMs (Figure 5.7a), which confirms that the high microporosity is preserved after sucrose coating. The pore size distribution curves (Figure 5.6b and 5.7b) and TEM images (Figure 5.6c and Figure 5.8) of the CSEMs and CEMs also exhibit identical micropore arrays with a micropore diameter of ≤ 1.45 nm in diameter. The well remained microporosity is also evidenced in pore volume analyses as shown in Figure 5.9. The pore volumes provided by the micropores in CEMs and CSEMs is, respectively, 0.23 and 0.26 $cm^3\ g^{-1}$. The pore volume analyses of fresh and cycled CSEMs shown in Figure 5.9 further demonstrate excellent active material encapsulation: the cycled CSEM reservoirs show minimal micropore volume (pore volume = 0.008 $cm^3\ g^{-1}$) and a low surface area of 0.3 $m^2\ g^{-1}$. In Figure 5.6a and 5.6b, the disappearance of the IUPAC type I isotherms and micropore volume suggest that the micropores serve as active material containers and that no severe loss of the active material is observed. In Figure 5.6d and 5.6e, the cycled CSEM current collector and the cycled CSEM inhibitor show smaller and fewer micropores, implying that micropores were fully or partially filled by the active material. Moreover, during TEM observation, the rearranging sulfur that fills in the micropores is limited by the microporous space; therefore, the particle size of sulfur in the microporous space is smaller than the size of the active material that is trapped by the porous network (Figure 5.2c). In addition, the absorbed/trapped active material in the micropores may further appear as randomly distributed black shadows in the TEM images.[176, 207] The BET analysis and SEM/TEM microanalyses reconfirm that the CSEM micropores are the major active material absorption sites.

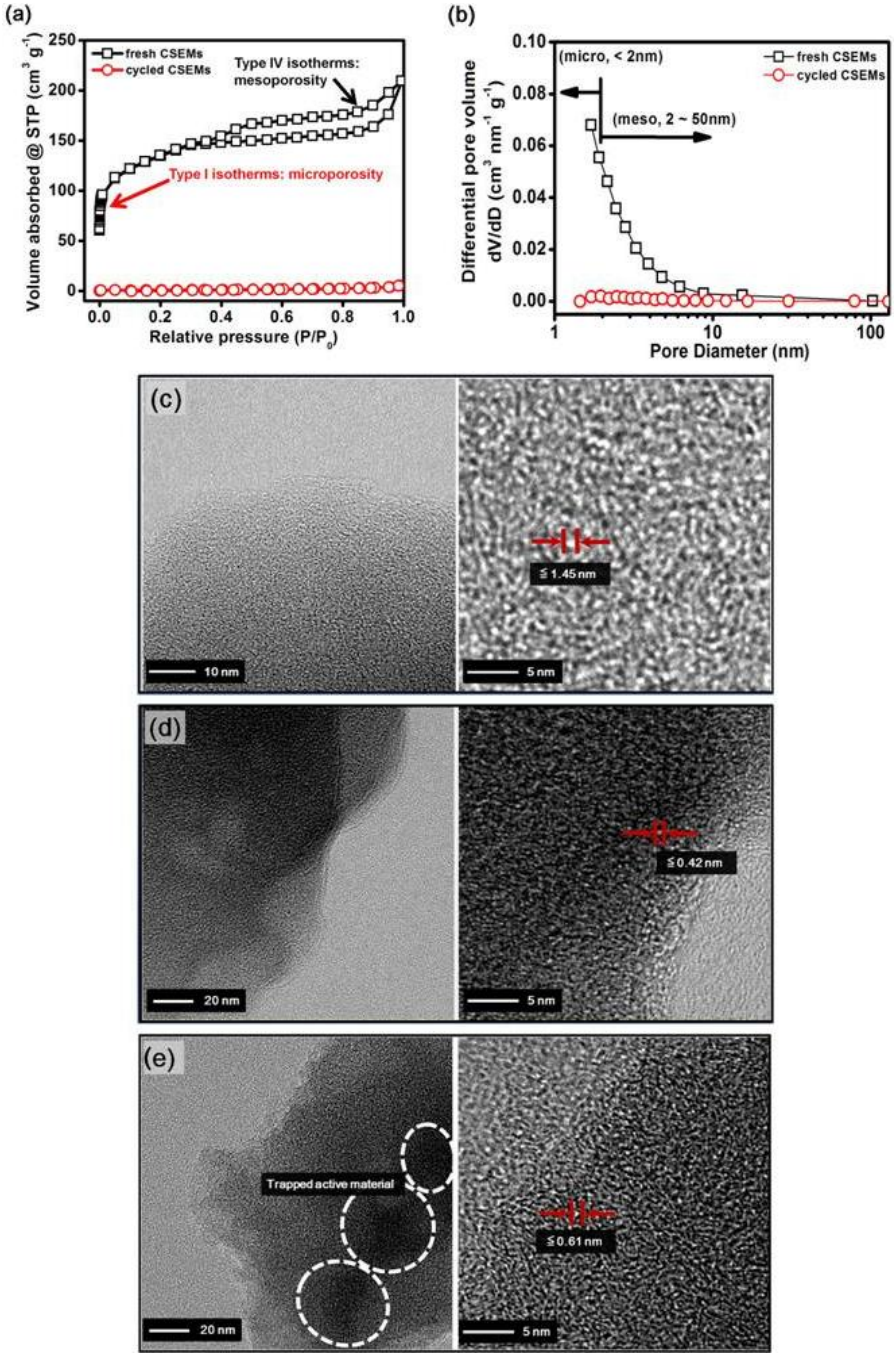

Figure 5.6: Surface area and microstructure analysis: (a) isotherms and (b) pore size distributions of the fresh and cycled CSEMs. TEM images with low and high magnification: (c) fresh CSEMs, (d) cycled CSEM current collectors, and (e) cycled CSEM inhibitors.

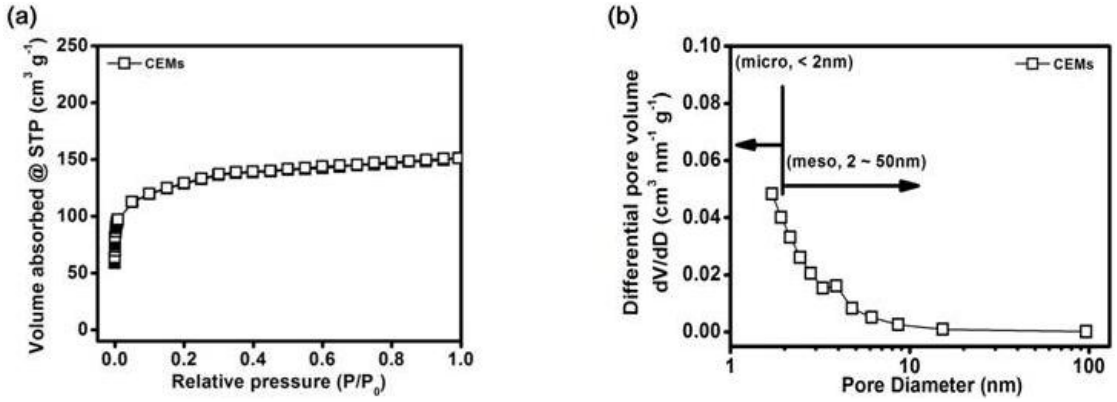

Figure 5.7: Surface area analysis: (a) isotherms and (b) pore size distributions of the CEMs.

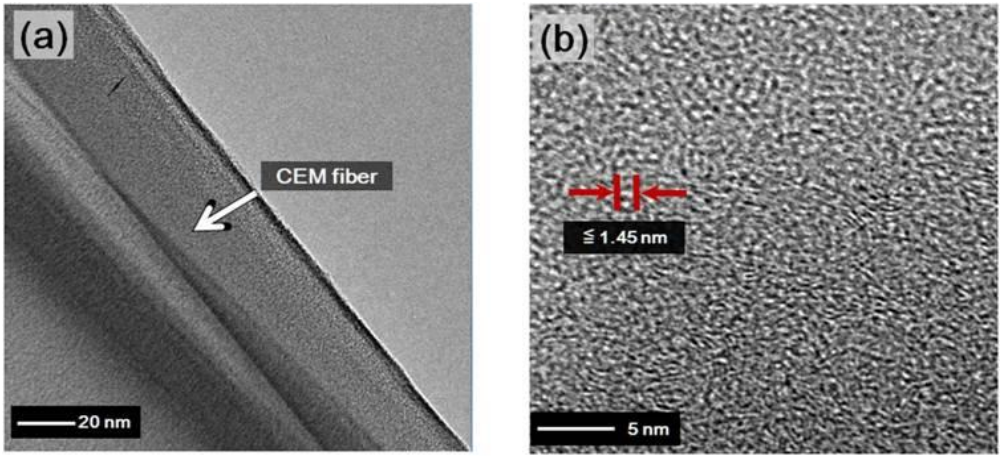

Figure 5.8: TEM images of the CEMs at (a) low and (b) high magnifications.

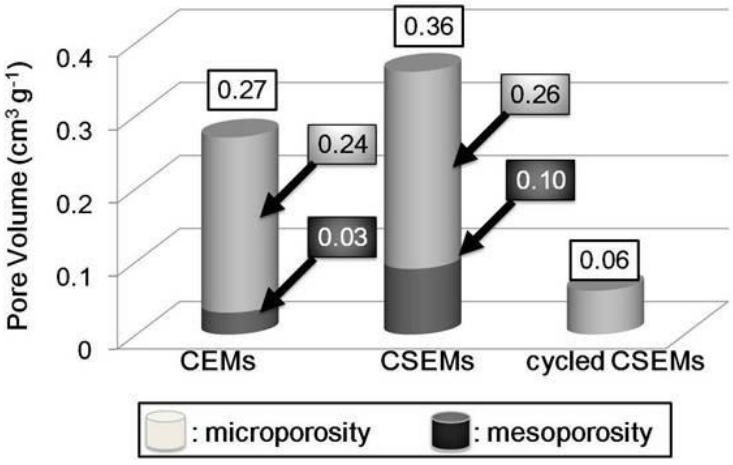

Figure 5.9: Pore volume analysis of the CEMs, CSEMs, and cycled CSEMs.

5.3.2 Electrochemical characterization and cell performance

Figure 5.10a shows the cyclic voltammetry plots (CV) of the CSEM reservoir for the initial twenty cycles. The cell was initially swept from the open-circuit voltage to 3.0 V, ensuring a complete Li_2S_6 to S/Li_2S_8 transformation.[20, 29, 55, 181] After the active material encapsulation via the *in situ* conversion of dissolved polysulfides, the CV curves show the typical two-step sulfur reduction process. The two cathodic peaks starting at 2.42 V and 2.08 V represent the conversion of, respectively, elemental sulfur to polysulfides and polysulfides to Li_2S_2/Li_2S.[29, 135] The two overlapped anodic peaks, between 2.2 and 2.5 V, are the oxidation reactions from Li_2S_2/Li_2S to Li_2S_8/S_8.[20, 29, 135] The absence of overpotential in the cathodic peak indicates decreased polarization because the active material migrates to electrochemically stable sites during the first cycle.[29, 173] In subsequent scans, the overlapping cathodic and anodic peaks maintain their sharp shape and display no obvious intensity changes and potential shifts, which suggests superior cycle stability and highly reversible redox reactions. Figure 5.10b, the stable and overlapping charge/discharge plateaus correlate well with the cathodic/anodic peaks in the CV (Figure 5.10a) and reconfirm the superior cyclability.[176, 207] The complete upper discharge plateaus suggest that the migrating polysulfides are localized in the cathode region and that severe active material loss has not occurred.[33] The appearance of the vertical voltage rise at 3.0 V indicates a complete charge process.[20, 181] The initial discharge capacity of the cell with CSEM reservoirs is 1327 mA h g^{-1}, which approaches 80 % of the theoretical capacity of sulfur (1672 mA h g^{-1}). The high active material utilization results from improved cathode conductivity achieved by encapsulating the active material in the conductive CSEM reservoir.

Impedance analysis (Figure 5.11a) confirms that the CSEM reservoir is more conductive than the conventional cathode. Although the CSEM reservoir has a higher sulfur loading than the conventional cathode, it still shows a substantial shrinkage in the charge transfer resistance (R_{ct}) from 560 Ohm to 59 Ohm. The low impedance confirms that the long-range continuity of the carbon-coated fiber network facilitates electron transfer and enhances electrochemical kinetics.[19, 60, 74, 232] The cycling performance in

Figure 5.10c reveals that the cells with CSEM reservoirs have high discharge capacity, stable cyclability, and high Columbic efficiency of > 97 % for over 100 cycles. After 100 cycles, the discharge capacity of cells approaches 1000 mA h g^{-1} with a capacity degradation rate of 0.25 % per cycle. The stable cyclability and the high capacity retention result from the synergistic effects of the natural micropores and the long-range porous network of the CSEMs (for a comparison, cells with CEM reservoirs also show a stable cycling performance in Figure 5.12), as well as the carbonized sucrose and the coalescing fiber framework of the CSEMs. First, the natural micropores throughout the CSEM are critical for accommodating the active material and absorbing the polysulfides during cycling, which have been thoroughly examined in the literatures.[62, 63, 72, 176] Therefore, the CSEM current collectors store active material and the CSEM inhibitors intercept the migrating polysulfides, as proved by the shrinkage/decrease of the micropores, suppressing the loss of the active material and offering excellent cycle stability. Second, the macroporous structure provides the essential electrolyte pathways to localize the catholyte within the cathode region and channel the electrolyte into the surrounding microporous absorption sites, forming an intimate contact among the electrolyte, active material, and carbon matrix.[138, 174] The intimate contact facilitates the electron transfer in the inactive area, as evidenced in the unchanged low resistances of CSEM reservoirs for over 20 cycles (Figure 5.11b). Third, the coated sucrose and coalescing fiber framework provides the CSEM reservoirs with a high electrical conductivity and continuous electron pathways, enhancing sulfur utilization.[77, 92, 176]

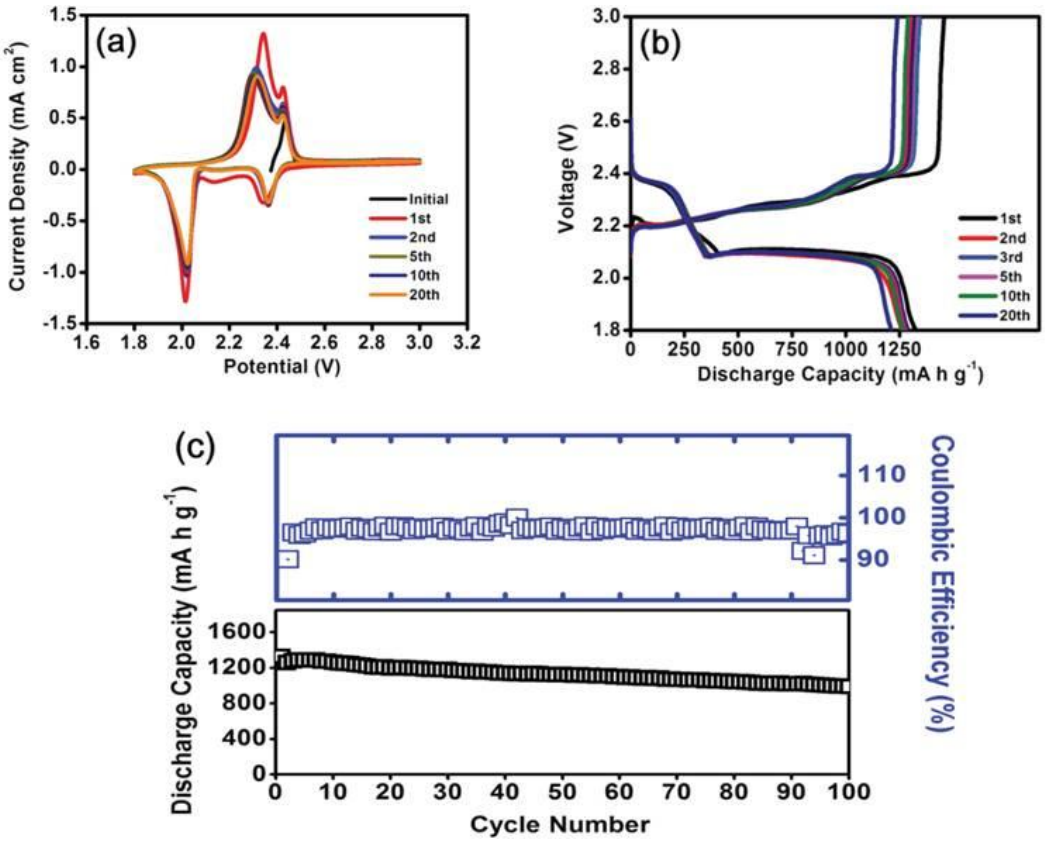

Figure 5.10: Electrochemical properties: (a) Cyclic voltammetry plots at a scan rate of 0.05 mV s^{-1} with 1.8 – 3.0 V voltage window, (b) charge/discharge profiles of the CSEM reservoir at C/10 rate, and (c) cyclability of the cells at a C/10 rate.

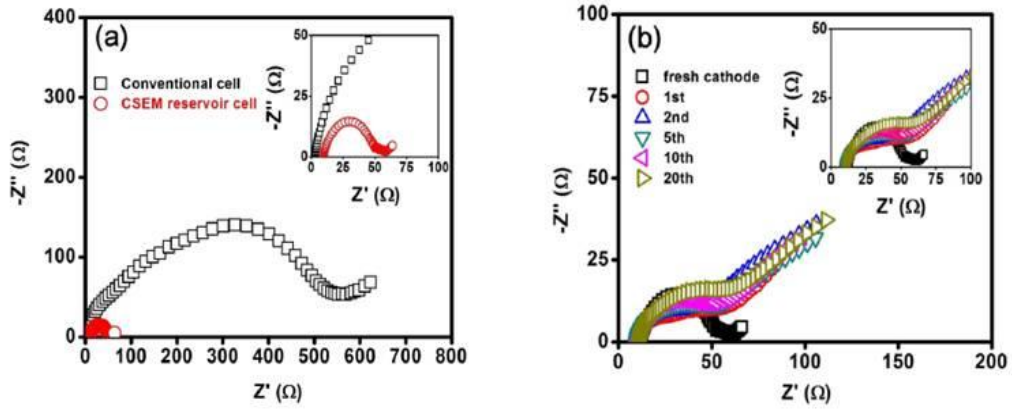

Figure 5.11: Electrochemical impedance spectroscopy plots: (a) cells with different cathode configuration and (b) cells with a CSEM reservoir cycled for 20 cycles.

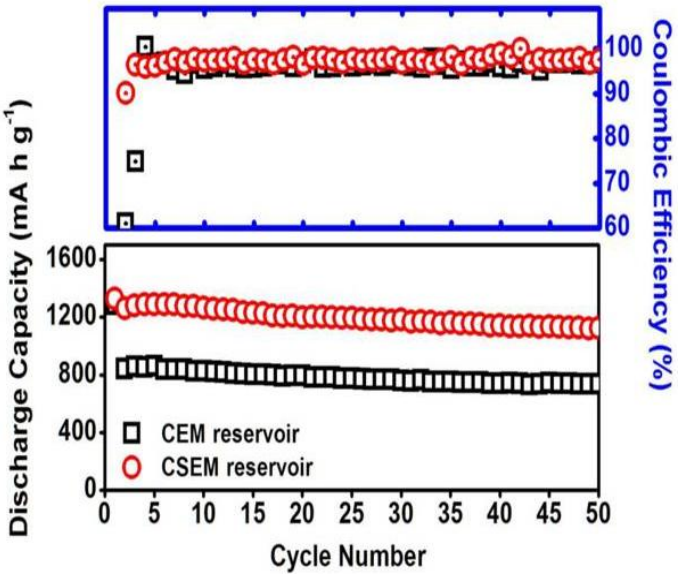

Figure 5.12: Electrochemical properties: cyclability of the cells with the CEMs at a C/10 rate.

5.4 CONCLUSIONS

In summary, the recycled natural eggshell membrane is a promising porous cathode substrate for improving the performance of lithium-sulfur batteries. The CSEMs possess the natural micropore arrays and macroporous network for storing/trapping the active material and channeling the electrolyte in the cathode. The configuration modification of applying the CSEM current collector significantly reduces the cathode resistance and enhances the active material utilization. The CSEM inhibitor effectively intercepts the migrating polysulfides and suppresses the loss of active material. Our biomaterial method localizes the dissolved polysulfides and stabilizes the electrochemical reaction within the cathode region, offering the Li/dissolved polysulfide cells with a high discharge capacity (1327 mA h g^{-1}), long-term cycle stability (over 100 cycles), and high sulfur loading (3.2 mg cm^{-2}).

Chapter 6: Development of surface-coated separators*

6.1 INTRODUCTION

Rechargeable batteries with a high capacity, acceptable cycle life, and low self-discharge are needed for meeting the ever increasing requirements of energy storage applications, from personal electronic devices to large-scale sustainable energy systems. Safe, cost-effective, and environmentally benign materials and manufacturing processes must also be pursued to meet the needs of manufacturing and global sustainability. Sulfur is abundant and environmentally benign and it offers higher theoretical capacity (1672 mA h g^{-1}) at a safer operating voltage (~ 2.1 V) compared to the conventional insertion-compound cathodes. Thus, the lithium-sulfur battery fulfills all of the above criteria and is considered to be a promising high-capacity system.[10, 52] However, the commercialization of lithium-sulfur cells is hampered by several technical challenges: (i) low electrochemical utilization, (ii) short cycle life, and (iii) severe self-discharge.[24, 27, 33, 227] Effective utilization of the high capacity is difficult with a pure sulfur cathode due to the insulating nature of both sulfur and its discharge end product (Li_2S_2/Li_2S).[24, 52, 227] Moreover, during the discharge/charge processes, sulfur converts to highly soluble

---

* S.-H. Chung and A. Manthiram, "Bifunctional separator with a light-weight carbon-coating for dynamically and statically stable lithium-sulfur batteries," *Adv. Funct. Mater.* 2014, **24**, 5299-5306.

*S.-H. Chung and A. Manthiram, "High-performance Li-S batteries with an ultra-lightweight MWCNT-coated separator," *J. Phys. Chem. Lett.* 2014, **5**, 1978-1983.

*S.-H. Chung and A. Manthiram, "A polyethylene glycol-wrapped microporous carbon coating as a polysulfide trap for utilizing pure sulfur cathodes in lithium-sulfur batteries," *Adv. Mater.* 2014, **26**, 7352-7357.

S.-H. Chung carried out the cell design and the experimental work. A. Manthiram supervised the project. All participated in the preparation of the manuscript.

*S-H. Chung, P. Han, R. Singhal, V. Kalra, and A. Manthiram, "Microporous Carbon Nanofiber Filter for Polysulfide towards Electrochemically Stable Rechargeable Lithium-Sulfur Batteries," 2015.

S.-H. Chung carried out the cell design and electrochemical measurements and was supervised by A. Manthiram. P. Han assisted S.-H. Chung with some cell preparation. R. Singhal prepared the ACNF by electrospinning and was supervised by V. Karla at Drexel University. All participated in the preparation of the manuscript.

polysulfides (Li_2S_x, $x = 4 – 8$). The polysulfides easily dissolve into the liquid electrolyte, diffuse through the separator, and shuttle between the anode and cathode. The loss of the active material and the shuttling species lead to "dynamic" capacity fade during cycling, resulting in low electrochemical efficiency and short cycle life.[27, 33, 227] Moreover, during cell resting, sulfur gradually reacts with the lithium ions in the electrolyte, transforms to polysulfides, and dissolves into the electrolyte, resulting in severe self-discharge. The polysulfide diffusion that occurs during cell storage results in a "static" decrease in cell capacity.[27, 33]

To address these scientific issues, current lithium-sulfur technology has focused on improving the electrical conductivity of the "composite" sulfur cathode and localizing the active material within the cathode region of the cell. These promising approaches include sulfur-porous carbon composites,[55, 56, 72, 82, 86, 226, 233-237] sulfur-conductive polymer composites,[91-96] binder/electrolyte additives,[149, 200, 207, 238, 239] cell configuration modifications,[18, 135, 138, 169, 176, 209, 240-243] and biomimetic architectures.[28, 185, 208] These approaches function as various kinds of quick cures and have shown (i) higher discharge capacity through a decrease in cathode resistance with the addition of conductive species,[11, 13, 23] (ii) improved cyclability through the confinement of the migrating polysulfides by porous agents and chemical characteristics,[11, 13, 23, 185] or (iii) suppressed polysulfide diffusion by localizing the electrolyte containing dissolved polysulfides within the cathode regions.[13, 28, 208] However, quick cures often cause some side effects while they address the major issues. For example, the composite cathodes often involve complex/unpractical multistep processes and modified cell configurations usually require a unique "free-standing component." In addition, the reduced sulfur content in the composite cathodes and the added weight of the applied free-standing component in cell modifications may lead to new concerns of a decrease in overall energy density, which may cancel off the gains in cell performance, *e.g.*, cycle life.

Here, we present various custom separators with light-weight carbon coatings for use with pure sulfur cathodes, which are facile and practical solutions. In order to

comprehensively understand the fabrication-architecture-electrochemistry-performance relationships, four functionalized separators are presented (Figure 6.1):

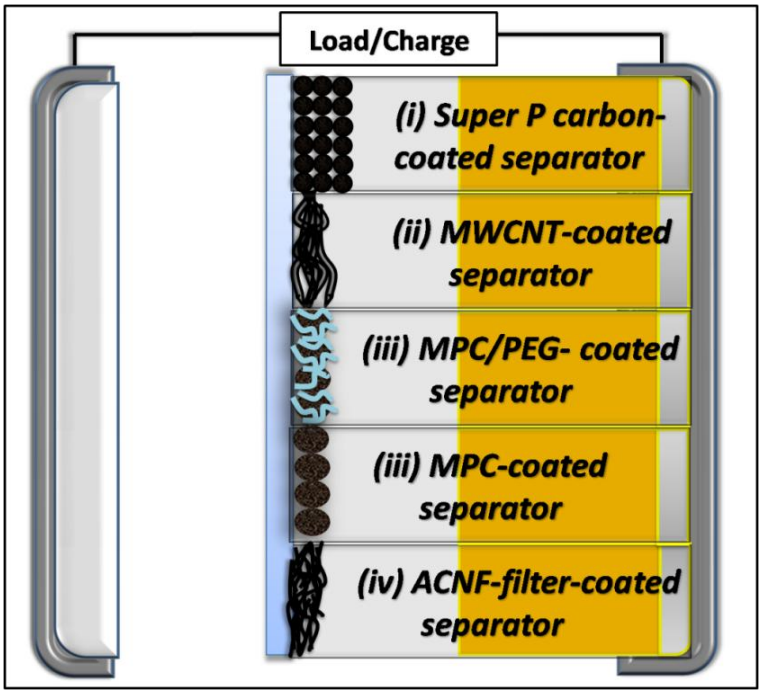

Figure 6.1: Schematic model of functionalized separators: (i) Super P carbon-coated separator, (ii) MWCNT-coated separator, (iii) MPC-coated separator and MPC/PEG-coated separator, and (iv) ACNF-filter-coated separator.

(i) A Super P carbon-coated separator demonstrates that a high-performance battery can be prepared with a new cell configuration by utilizing commonly used lab supplies and a low-cost manufacturing process;[38] (ii) a MWCNT-coated separator introduces a suitable preparation process for carbon-coated separators with enhanced polysulfide-trapping capability and with tough MWCNT coatings;[209] (iii) surface-coated separators with a MPC coating, with and without PEG, investigate the chemical and physical polysulfide-trapping capability of coated separators;[99] and (iv) an ACNF-filter-coated separator provides evidence for key parameters for improving the polysulfide-trapping/reutilizing capability. In order to develop the functionalized

separators for use in lithium-sulfur technology, these studies on the physical and chemical characteristics as well as the mechanical strength and flexibility of the carbon coatings are needed for enhancing the polysulfide-trapping capability of the ultra-tough carbon-coated separators.

6.2 EXPERIMENTAL

6.2.1 Super P carbon-coated separator preparation

The Super P carbon-coated separator was fabricated by surface coating commercial conductive carbon black (Super P; TIMCAL) on one side of a commercial polypropylene separator (CELGARD). The carbon slurry was prepared by mixing Super P carbon with isopropyl alcohol (IPA) overnight. The carbon slurry was coated onto the Celgard separator by the tape casting method and then dried for 24 h at 50 ℃ in an air oven, followed by cutting into circular disks. The application of the tape casting method, which is commonly used in cathode preparation, for the Super P carbon-coated separator fabrication makes the processing facile and easily adaptable for large-scale applications.

6.2.2 MWCNT-coated Separator Preparation

To fabricate the bifunctional MWCNT-coated separator, 0.025 g of MWCNTs (PD30L520 with a hollow structure: outer diameter = 15 – 45 nm, length = 5 – 20 μm, purity > 95 %, Nanolab Inc.) were dispersed in 500 mL of isopropyl alcohol (IPA) by high-power ultrasonication for 10 min without any additional additives. Then, the MWCNT suspension was filtered through a commercial Celgard 2500 polypropylene separator by vacuum filtration. After drying at 50 ℃ for 24 h in an air-oven, the MWCNT coating readily formed a flexible bundled nanotube layer intimately attached to the Celgard separator. The MWCNT-coating layer weighed only 0.17 mg cm^{-2}. The resultant bifunctional separators were cut into circular disks. The vacuum filtration process of the functionalized separator allows the application of fibrous material to form a bundled/porous filter that is tightly adhered onto the polypropylene membrane.

6.2.3 Functionalized MPC/PEG-coated separator and MPC-coated separator fabrication

The functionalized separator was fabricated by thin-film coating of the MPC/PEG slurry on one side of a Celgard 2500 monolayer polypropylene (PP) membrane (CELGARD) by a tape casting method. The tape casting method uses an automatic film applicator (1132N, Sheen) with a standard number 1 blade at a traverse speed of 50 mm s^{-1}. The MPC/PEG slurry was prepared by mixing 80 wt. % conductive carbon black with micropores and high surface area (Black Pearls 2000, CABOT) and 20 wt. % polyethylene glycol (PEG, average molecular weight = 300, Aldrich) in 3000 μL isopropyl alcohol (IPA) overnight. After drying at 50 ℃ for 24 h in an air-oven, the resultant MPC/PEG coating (0.15 mg cm^{-2}) formed a thin-film polysulfide trap with a thickness of 8 μm attached to the Celgard separator. On the other side of the MPC/PEG-coated separator, the Celgard separator serves as the electrically insulating membrane. As a result, all cells with the composite separator were operated normally during electrochemical analyses, even during long-term cycling, without shorting. The MPC-coated separator was fabricated by the same process but without using PEG.

The size of the MPC/PEG-coated separator is scalable, which can be enlarged or reduced by changing the cutting die of the precision disc cutter (MSK-T-06, MTI). The thickness of the MPC/PEG coating can also be easily adjusted by using different standard blades (from number 0.5 (the thinnest sample) to number 6 (the thickest sample)). The fabrication process of the functionalized separator is similar to conventional cathode preparation and the raw materials are common laboratory supplies that are available in many Li-ion battery research laboratories, demonstrating the feasibility of the MPC/PEG-coated separator.

6.2.4 Microporous ACNF-filter-coated separator fabrication

The activated carbon nanofibers (ACNFs) were prepared by Professor Kalra's group at Drexel University and provided to us. The ACNFs were coated onto one side of a commercial monolayer polypropylene membrane (Celgard 2500, thickness: 25 μm,

porosity: high) with a vacuum filtration process. The ACNFs (50 mg) were first mixed with equal weight polyethylene glycol (PEG, Aldrich) in 5 mL of isopropyl alcohol (IPA) overnight. The ACNF/PEG mixtures were then dispersed in IPA (500 mL) by high-power ultrasonication for 10 min. The uniform ACNF suspension was then vacuum-filtered onto one side of a polypropylene membrane. The resulting ACNF-coated separator was dried at 50 ℃ for 24 h in an air-oven and cut into circular disks for cell assembly. The thickness of the coating layer is highly adjustable by controlling the amount of ACNFs added to the mixture. The diameter of the ACNF-coated separators can be increased or reduced by changing the size of vacuum filters and polypropylene membranes. The adhesion between the ACNF filter and the polypropylene membrane is ultra-tough based on (i) adjusting the ratio of carbon to PEG binder and (ii) modifying the preparation process. This modified carbon-coated separator process improved the flexibility and mechanical strength of both the coating layer and the resulting functionalized separator.

6.2.5 Pure Sulfur Cathode Preparation

The active material slurry was prepared by mixing 60 wt. % precipitated sulfur, 20 wt. % Super P, and 20 wt. % polyvinylidene fluoride (PVDF, Kureha) and by mixing 70 wt. % precipitated sulfur, 15 wt% Super P, and 15 wt% PVDF in *N*-methyl- 2-pyrolidone (NMP; Aldrich) for 2 days. The active material slurry was tape casted onto an Al foil current collector and dried for 24 h at 50 ℃ in an air oven, followed by roll-pressing and cutting into circular disks. In this work, the pure sulfur cathode refers to the basic cathode material containing only the necessary components: sulfur, conductive carbon additive, and binder.[47] The sulfur loadings in the regular cathode disk are, respectively, 1.1 – 1.3 mg cm^{-2} in 60 wt. % sulfur-cathode samples that were used in the Super P carbon-coating work and 2.0 – 2.3 mg cm^{-2} in 70 wt. % sulfur-cathode samples that were used in other carbon-coating work.

6.2.6 Sulfur-MPC composite cathode preparation

The sulfur-MPC nanocomposite was synthesized by an *in situ* deposition route

and was controlled to produce ~ 80 wt. % sulfur in a sulfur-MPC core-shell structure. Therefore, cells used in the configuration comparison have a similar sulfur content of ~ 65 wt. % and cathode active material loading of 2.0 mg cm^{-2}, which is used in the comparative analysis in section 6.3.3 to evidence that the functionalized-separator configuration may possess better polysulfide-trapping capability than the composite cathode configuration. In addition, the reason that MPC is selected as the carbon substrate in the composite cathode for the control cell in the comparative analysis is its enhanced cycle stability as compared to many other carbon substrates, which makes our comparative analysis reliable.

6.2.7 Cell assembly

The CR2032-type coin cells were assembled with the pure sulfur cathode, carbon-coated separator, lithium anode (Aldrich), and nickel-foam spacer in an argon-filled glove box. The separators and cathodes were dried in a vacuum oven for one hour at 50 ℃ prior to cell assembly. The carbon-coated separator was inserted between the sulfur cathode and the Li-metal anode. The functionalized-separator configuration has the carbon-coating side facing the sulfur cathode while the polypropylene-membrane side facing the Li-metal anode. The custom-cell configuration is illustrated in Figure 6.1. The electrolyte contained 1.85 M $LiCF_3SO_3$ salt (Acros Organics) and 0.1 M $LiNO_3$ co-salt (Acros Organics) in a 1:1 volume ratio of 1, 2-dimethoxyethane (DME; Acros Organics) and 1,3-dioxolane (DOL; Acros Organics).

6.3 RESULTS AND DISCUSSION

6.3.1 Functionalized separator: a light-weight Super P carbon coating for dynamic and static stability

Sulfur is appealing as a high-capacity cathode for rechargeable lithium batteries as it offers a high theoretical capacity of 1672 mA h g^{-1} and is abundant. However, the commercialization of lithium-sulfur batteries is hampered by fast capacity fade during both dynamic cell cycling and static cell resting. The poor electrochemical stability is due

to polysulfide diffusion, leading to a short cycle life and severe self-discharge. Here, we present the novel design of a bifunctional separator with a light-weight carbon coating that integrates the two necessary components already inside the cell: the conductive carbon and the separator. With no extra additives, this bifunctional carbon-coated separator allows the use of pure sulfur cathodes involving no complex composite synthesis process, provides a high initial discharge capacity of 1389 mA h g^{-1} with excellent dynamic stability, and facilitates a high reversible capacity of 828 mA h g^{-1} after 200 cycles. In addition, the static stability is evidenced by low self-discharge and excellent capacity retention after a 3 month rest period.

6.3.1.1 Functionalized separator design

We first present a bifunctional separator with a light-weight carbon coating for use with pure sulfur cathodes, which is a facile and practical solution. The carbon-coated separator integrates two necessary, cost-effective, and commonly used components that are already present inside the cell: the conductive carbon black (Super P carbon) and the polymeric separator (Celgard separator).[47] The architecture of the carbon-coated separator consists of a layer of Super P thin film coated onto one side of the Celgard separator. The bifunctional carbon coating functions as a conductive upper-current collector and a polysulfide-diffusion barrier region while the Celgard separator serves as the electrically insulating membrane. Moreover, the light-weight carbon-coating layer is only 0.2 mg cm^{-2} (the weight of the Celgard separator is 1.0 mg cm^{-2}), which overcomes the drawbacks of the low sulfur content issue of the composite cathodes and the added weight of the free-standing components employed in cell modifications.

The commercialization feasibility of lithium-sulfur cells greatly depends on overcoming the severe cell stability challenges with practical solutions that can be easily translated into industrial processes. Here, we demonstrate such a solution by introducing a functionalized carbon-coated separator, which greatly enhances the dynamic and static performance of lithium-sulfur cells, while utilizing low-cost materials and simple processing techniques.

6.3.1.2 Configuration and characterization of the Super P carbon-coated separator

Figure 6.2a presents the Super P carbon-coated separator that consists of a lightweight conductive carbon coating on one side of a polypropylene separator. The carbon-coated side of the separator faces the pure sulfur cathode and acts as a barrier region (with the thickness of ~ 20 μm). In Figure 6.2b, the carbon-coating barriers aim at impeding the free migration of the polysulfides and preventing them from smoothly diffusing through the Celgard separator.[209, 240] Moreover, this conductive carbon coating offers additional electron pathways for the insulating sulfur cathode and functions as the "upper" current collector to accelerate fast electron transport.[174, 209] During long-term cycling, this upper-current collector easily transports electrons into the intercepted active material to reactivate them. Therefore, high sulfur utilization and effective active material reutilization are accomplished.[174, 209] On the other side, the insulating Celgard remains highly electronically resistive. For a comparison, Figure 6.2c shows the schematic cell configuration of the conventional lithium-sulfur cell, suffering from the issues described above, especially the severe polysulfide diffusion issue (Figure 6.2d).

It is worth emphasizing that the weight of the carbon coating is only 0.2 mg cm^{-2}, much lighter than the weight of the Celgard separator. Therefore, even as we include the weight of the carbon coating, the cell with the carbon-coated separator allows a high sulfur content of above 55 wt. % in the whole cathode region, higher than that in most high-performance lithium-sulfur cells.[127] Moreover, the carbon-coated separator has good flexibility and mechanical strength, as shown in Figure 6.2e, allowing it to retain its normal function during cell cycling.

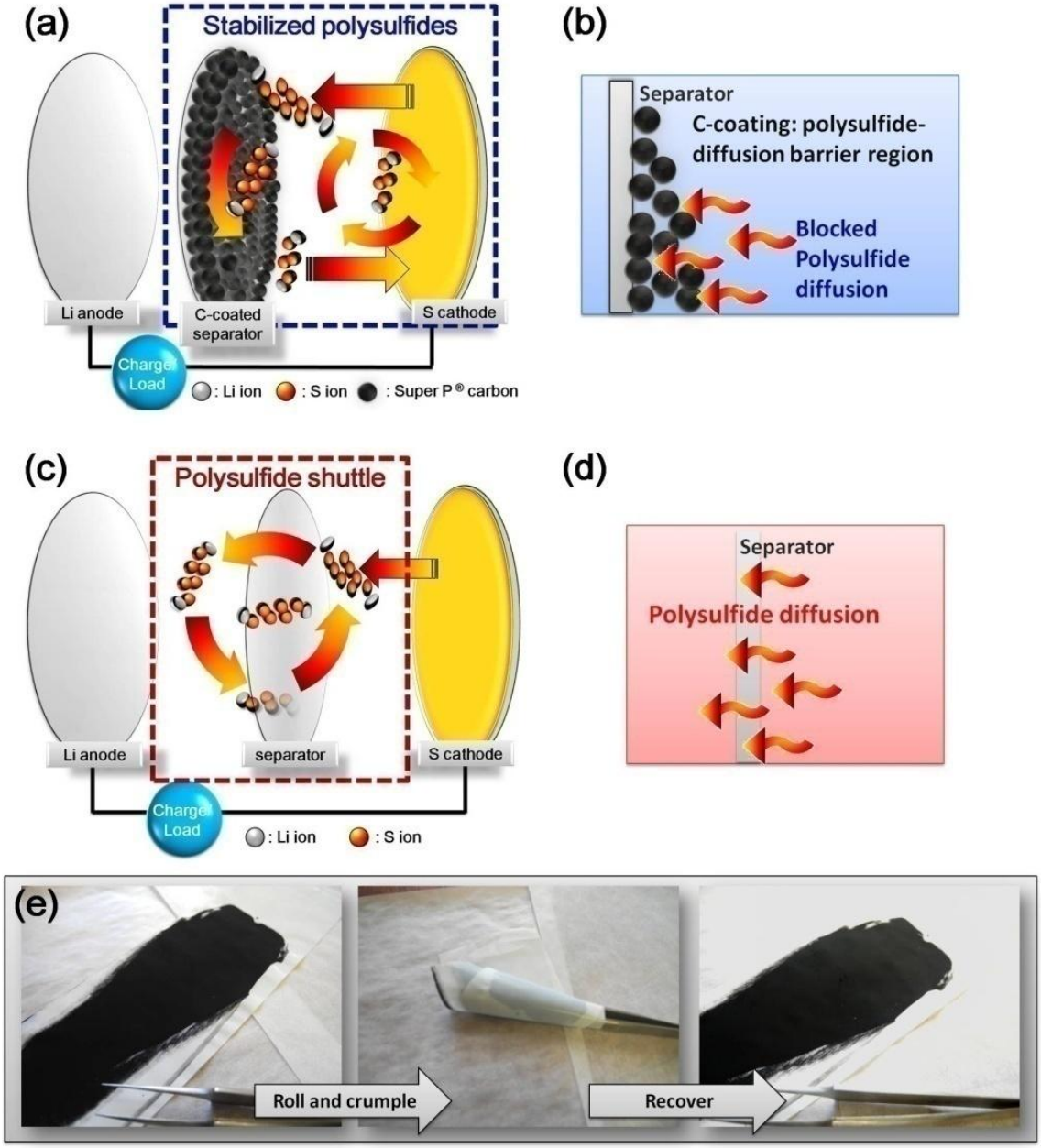

Figure 6.2: Schematic cell configuration modification of lithium-sulfur cells. (a) Schematic configuration of a lithium-sulfur cell with the carbon-coated separator and (b) the polysulfide-diffusion barrier region. (c) Schematic configuration of a lithium-sulfur cell with the Celgard separator and (d) the typical severe polysulfide diffusion. (e) Demonstration of the flexibility and mechanical strength of the carbon-coated separator.

6.3.1.3 Morphological and elemental mapping analyses of the cycled carbon-coated separator

To demonstrate the efficacy of the carbon-coated separator, the morphological changes before and after cycling were analyzed by scanning electron microscopy (SEM) and elemental mapping was performed with energy-dispersive X-ray spectroscopy (EDX), as summarized in Figure 6.3 . Figure 6.3a shows that the surface of the fresh carbon-coated separator consists of a layer of porous nanoparticle clusters uniformly attached to the polypropylene separator. The porous structure of the carbon coating allows the liquid electrolyte to freely penetrate through the coating layer, ensuring that the electrochemical reaction proceeds in the cathode.[174, 209] However, the carbon coating can (i) work as barriers for suppressing the free diffusion of polysulfides and (ii) function as absorption agent for localizing the electrolyte containing the dissolved polysulfides within the cathode region of the cell.[169, 173, 177, 209, 240, 241] To support this statement, low-magnification SEM and elemental mapping of the carbon-coated separator after 200 cycles are shown in Figure 6.3b. The overlays of the sulfur EDX signal (marked as red) and the carbon EDX signal (marked as green) on the SEM image show that the sulfur-containing species are uniformly distributed on the carbon matrix. This demonstrates that the carbon coating effectively intercepts the dissolved polysulfides within its barrier region. As a further evidence, in the high-magnification SEM image (Figure 6.3c), the obstructed active material (marked in white) is observed on the surface of the carbon coating.

The fact that there are no large agglomerates on the carbon coating in both Figure 6.3b and 6.3c suggests that the obstructed active material is continuously reutilized and that there is no formation of large insulating precipitates during long-term cycling. Both of these are vital to solving the severe capacity fade in lithium-sulfur cells.[32, 171] These enhancements may result from (i) the high conductivity of the Super P network, which supplies electrons to reactivate the trapped species[174] and (ii) the nanoscale Super P clusters of the carbon coating that limits the formation of large precipitates.[55] As

evidenced, the elemental sulfur signals (Figure 6.3b and 6.3c) show no obvious dense spots and the elemental carbon signals are still strong.

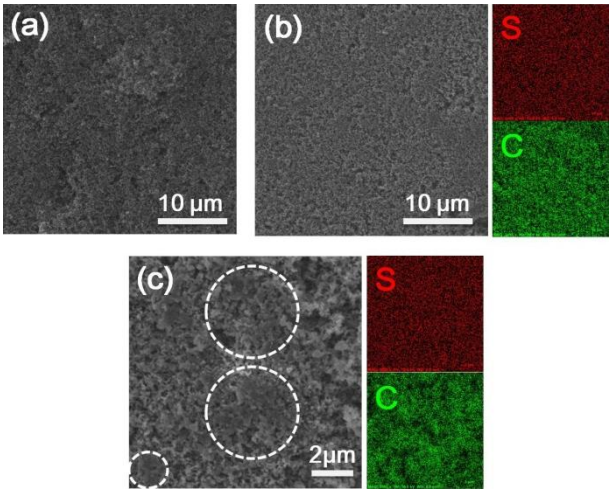

Figure 6.3: Morphology and elemental analyses of the carbon-coated separator. (a) SEM observation of the carbon-coated separator before cycling. SEM observation and elemental mapping of the carbon-coated separator after cycling: (b) wide-range morphological observation and (c) local microstructural observation.

The cross-sectional SEM and elemental mapping conducted on cells after 200 cycles demonstrate how the carbon-coated separator suppresses the severe polysulfide diffusion (Figure 6.2b and 6.2d). Figure 6.4 a shows a cross-section of the cell, with (from left to right) the Super P carbon coating (~ 20 μm), pure sulfur cathode (~ 40 μm), and aluminum foil current collector. The Celgard separator was carefully removed to avoid the electron beam charging. Evidence of the polysulfide interception mechanism can be found in the results of the elemental sulfur mapping (Figure 6.4b), which shows obvious sulfur concentration changes: (i) lack of sulfur at the interface of the carbon coating and sulfur cathode[28, 208] and (ii) decrease in sulfur concentration within the carbon coating.[28, 208, 209] The sulfur concentration gap demonstrates that most of the polysulfides were obstructed on the surface of the carbon coating.

Then, in the carbon coating, there is a sulfur concentration gradient, with stronger sulfur signals pointing towards the cathode and weaker signals towards the separator. This further demonstrates that the nanoparticle cluster network serves as the barrier region to obstruct and immobilize the migrating polysulfides before they are able to penetrate through the carbon coating. This conclusion is well supported by the SEM inspection on the Celgard side of the cycled carbon coating that was peeled off from the cycled carbon-coated separator, as shown in Figure 6.5. On this side, the carbon coating retains its porous structure and no obvious trapped active material can be found. The corresponding elemental mapping results in Figure 6.5b also exhibit weak sulfur signals and strong carbon signals, reconfirming that the intercepted active materials cannot reach the Celgard separator. In addition, the elemental carbon signals in Figure 6.4b are also discernible, suggesting that the intercepted active materials do not grow into insulating agglomerates and block the porous electrolyte channels but rather are continuously reactivated and thus contribute to the capacity.[28, 174, 208]

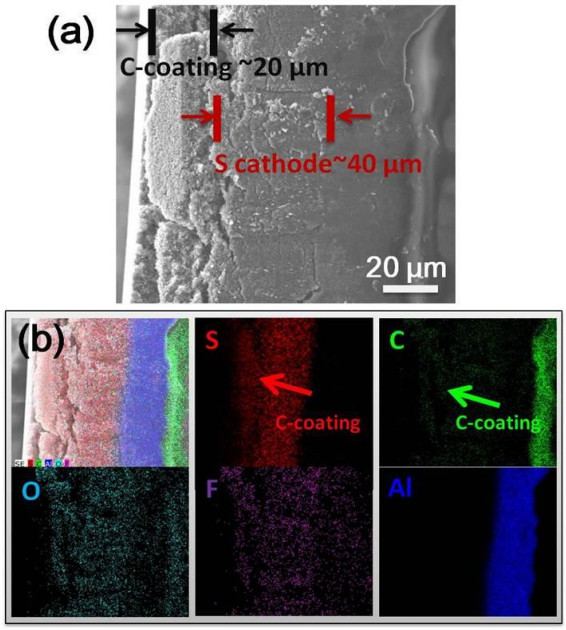

Figure 6.4: Microstructural analysis of a cell with the carbon-coated separator. (a) Cross-sectional SEM observation and (b) elemental mapping of the carbon coating and cathode configuration.

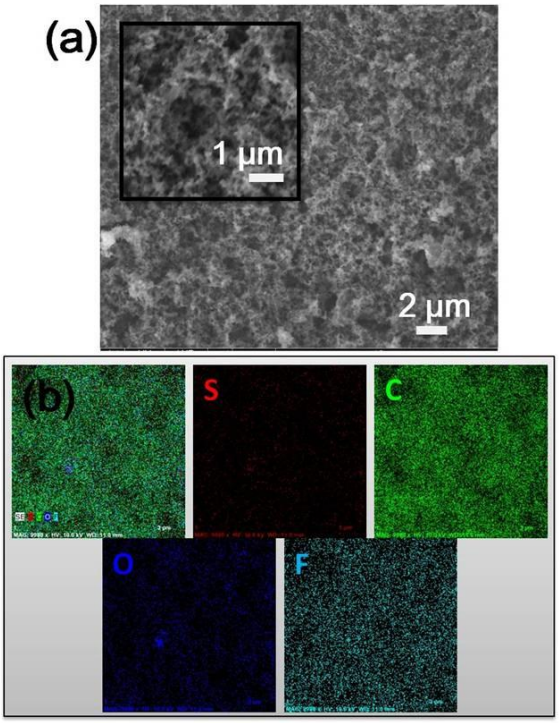

Figure 6.5: SEM images and elemental mapping of the Celgard side of the cycled carbon coating that is separated from the cycled carbon-coated separator. (a) Surface SEM observation (inset is the high-magnification SEM) and (b) elemental mapping.

6.3.1.4 Electrochemical analyses of the pure sulfur cathode utilizing the carbon-coated separator

Based on the visual inspection of the morphological changes of the carbon coating presented in Figure 6.3 and 6.4, it is reasonable to expect that the conductive carbon coating can facilitate smooth electron transport between the insulating active material and the electrical conductor. This may facilitate (i) a low resistance and (ii) excellent reutilization of the trapped active material. To identify these enhancements, electrochemical impedance analysis was used to compare the impedance/resistance of the cell with the carbon-coated separator to that of a cell with a standard Celgard separator. The electrochemical impedance spectroscopy (EIS) data of the cells with different separators indicate that the charge transfer resistance (R_{ct}, in the high-frequency region)

decreases by over 75 % after replacing the Celgard separator by the carbon-coated separator, as shown in Figure 6.6. This demonstrates a significant decrease in the cathode resistance. After cycling, the impedance semicircles of the carbon-coated separator are much smaller than those of the Celgard separator. This is because the carbon coating functions as the conductive network to reactivate the intercepted active material, so it limits the formation of insulating active material agglomerates. The EIS data thus demonstrate low cathode resistance and reutilization the trapped active material.

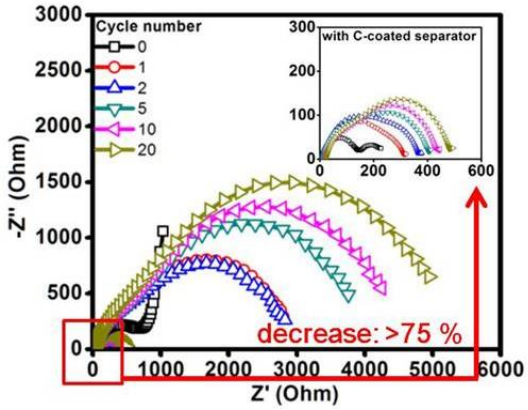

Figure 6.6: Electrochemical impedance spectroscopy of cells with different separators. (Inset is the EIS of the cell with the carbon-coated separator).

It is well known in the literature that a low cathode resistance and successive reutilization of the active material are vital to, respectively, increasing the active material utilization and extending the cycle life.[18, 27, 55] These improvements are identified by a comparison of the discharge/charge voltage profiles during the initial 20 cycles at a C/5 rate of cells with different separators, as presented in Figure 6.7a and 6.7b. Figure 6.7a shows the discharge/charge curves of the cell utilizing the carbon-coated separator. During discharge, the two separate plateaus indicate the occurrence of the two complete reduction reactions.[17, 181] The upper discharge plateau at ~ 2.35 V corresponds to the first reduction from elemental sulfur (S_8) to long-chain polysulfide (Li_2S_x, x = 4 – 8). The corresponding discharge capacity (Q_H) is 416 mA h g^{-1}, approaching 99 % of the

theoretical value (419 mA h g^{-1}) and implying limited polysulfide diffusion.[17] The lower discharge plateau at ~ 2.05 V represents the second reduction from long-chain polysulfides to Li_2S_2/Li_2S.[17, 34] As seen in Figure 6.7a and 6.7b, the carbon coating increases the initial discharge capacity from 1051 to 1389 mA h g^{-1}, demonstrating improved sulfur utilization (from 63 % to 83 %), consistent with the EIS analysis. In the subsequent cycles, the upper discharge plateaus are well retained, which provides evidence that the carbon coating successfully intercepts the escaping polysulfides and limits the loss of the active material. Moreover, the overlapped discharge curves demonstrate that the carbon coating continuously reactivates the trapped active material, leading to stable cell cycling. During charge, the two continuous plateaus at ~ 2.25 and ~ 2.4 V are attributed to the reversible oxidation reactions of Li_2S_2/Li_2S to Li_2S_8/S_8. As the voltage approaches 2.8 V, the vertical rise in voltage indicates a complete charge reaction.[27, 32, 171] Similarly stable cycling performance is observed in cells employing the carbon-coated separator at various cycling rates (Figure 6.8).

The suppressed polysulfide diffusion is confirmed by an investigation of the upper discharge voltage plateaus and their corresponding capacities. This upper plateau region corresponds to the formation of highly soluble polysulfides.[33, 227] In Figure 6.7a, the upper discharge voltage plateaus of the cells with the carbon-coated separator remain complete and show almost no decrease in capacity. For the sake of comparison, Figure 6.7b shows that the upper discharge plateaus of the cells with the Celgard separator exhibit the typical plateau shrinkage along with severe capacity fade. The upper plateau capacities of cells with different separators are summarized in Figure 6.7c. The upper plateau capacities of the cells with the carbon-coated separator remain highly reversible at various cycling rates. However, the upper plateau capacity of the Celgard separator-only cell decreases to 45 % of its original value after 10 cycles at a C/5 rate. This enhancement demonstrates that the carbon coating effectively suppresses the diffusion of polysulfides and thus eliminates the severe loss of active material/capacity during cell cycling.

The enhanced cycle stability is further illustrated by the overlapping curves of the cyclic voltammograms (CVs), as shown in Figure 6.7d. The two cathodic peaks and the two overlapped anodic peaks are consistent with the discharge/charge curves. Notably, there are no apparent current or potential changes in these CV peaks with repeated scans, attesting to superior cell reversibility and stability.

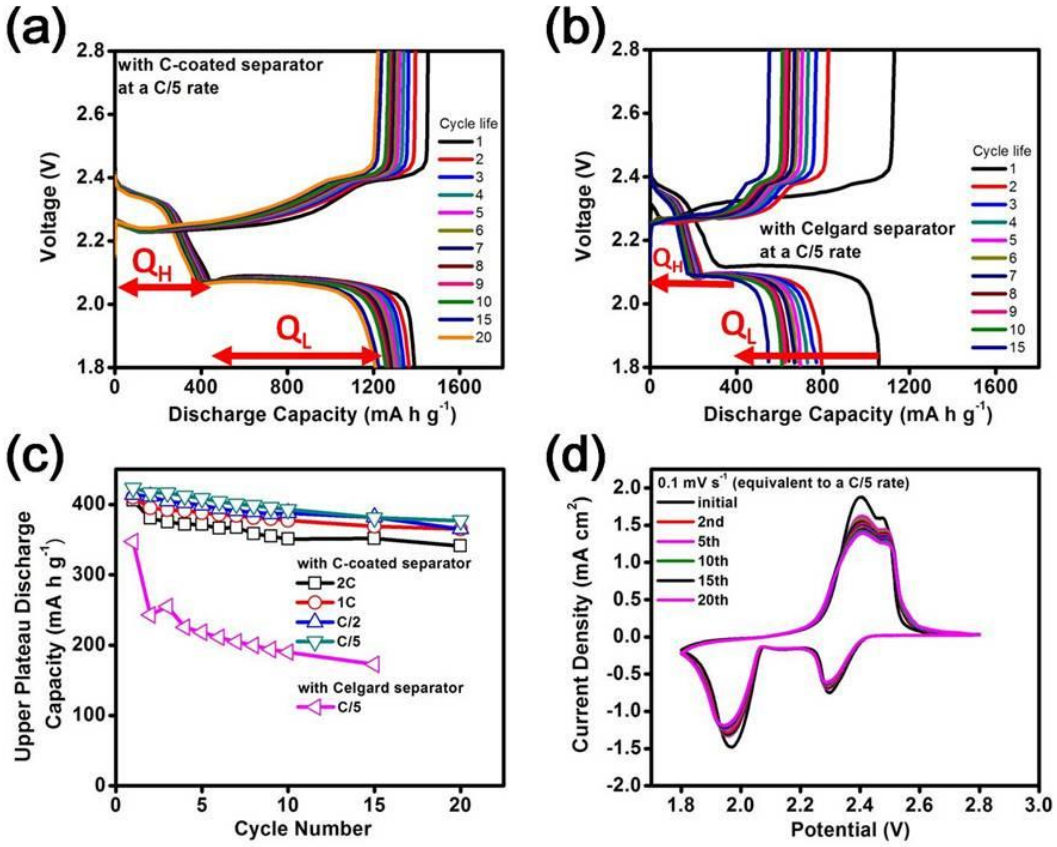

Figure 6.7: Electrochemical measurements of lithium-sulfur cells. Discharge/charge curves of cells: (a) carbon-coated separator, (b) Celgard separator, and (c) upper plateau discharge capacities of cells employing different separators at various cycling rates. (d) Cyclic voltammograms of the cell with the carbon-coated separator.

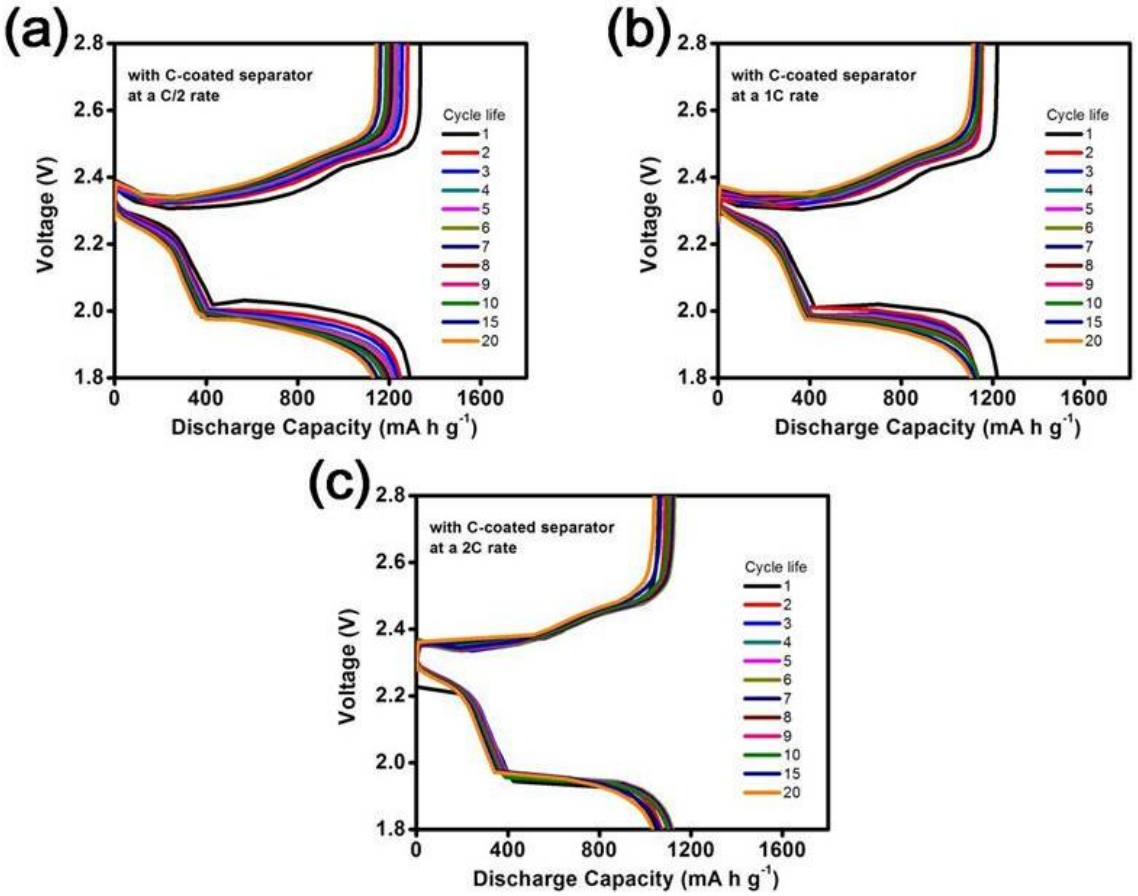

Figure 6.8: Electrochemical measurements of lithium-sulfur cells with the carbon-coated separator. Discharge/charge curves of cells at (a) C/2, (b) 1C, and (c) 2C rates.

6.3.1.5 Dynamic electrochemical stability of pure sulfur cathodes utilizing carbon-coated separators

Figure 6.9a demonstrates that the carbon-coated separator leads to significant enhancements in the dynamic electrochemical stability of the pure sulfur cathode, as evidenced by the high discharge capacity and stable cyclability. The pure sulfur cathodes achieve initial discharge capacities of 1389, 1289, 1220, and 1045 mA h g^{-1} at, respectively, C/5, C/2, 1C, and 2C rates. After 50 cycles, the reversible capacities approach 1112, 1074, 1021, and 920 mA h g^{-1} which corresponds to capacity retentions of, respectively, 80, 83, 84, and 88 %. The stable cyclability allows the cells to remain

highly reversible over a wide range of cycling rates, from C/5 to 2C. As a comparison, the pure sulfur cathode with a Celgard separator has an initial capacity of 1051 mA h g^{-1} (marked as black) at a C/5 rate, which decreases to 785 mA h g^{-1} after the second cycle. Moreover, the discharge capacity after 50 cycles is only 500 mA h g^{-1}, indicating that long-term cycling is not feasible with this type of cell.

On the other hand, the high electrochemical reversibility of the carbon-coated separator ensures the cell to accomplish long-term cyclability over 200 cycles, with the capacity fading as low as 0.20 % per cycle, as shown in the Figure 6.9b. The long-term cyclability may result from the successive interception, reactivation, and reutilization of polysulfides in the nano-sized conductive carbon coating, which concomitantly stabilizes the electrochemical reactions and the active material within the cathode region during long cycle life. The reversible capacity of the cells (with the calculated capacity fading in parentheses) cycling at C/5, C/2, 1C, and 2C rates after 200 cycle are, respectively, 828 (0.20 %), 810 (0.19 %), 771 (0.18 %), and 701 mA h g^{-1} (0.16 %). The average Coulombic efficiencies at various cycling rates are above 98.2 %. The addition of a small amount of $LiNO_3$ co-salt in the electrolyte can protect the lithium anode by forming a passivation layer on its surface, and effectively enhance the Coulombic efficiency to above 90 %.[36, 208] The application of the carbon-coated separator further improves the efficiency from 92 % to 98 %. In addition, no fast capacity fade can be found in the cells with the carbon-coated separator during long-term cycling, indicating that the carbon coating remains intact with good mechanical strength and normal function during cycling. Such good mechanical integrity of the carbon coating may result from the physical adsorption between the carbon nanoparticles and the porous Celgard separator, avoiding the peeling-off of the carbon coating from the Celgard separator.[169, 242] The superior cycling stability suggests that the carbon-coated separator provides a more stable electrochemical environment for the pure sulfur cathode than that found with the conventional cells.

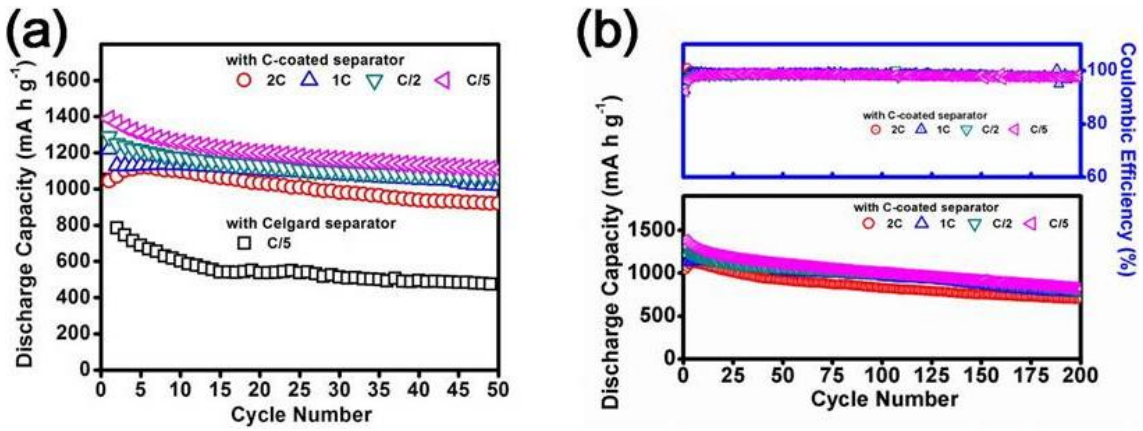

Figure 6.9: Cell performance of lithium-sulfur cells. Dynamic electrochemical stability: (a) cycle stability and (b) long-term cycle life of the cells with different separators at various cycling rates.

6.3.1.6 Static electrochemical stability of pure sulfur cathodes utilizing carbon-coated separators

Lithium-sulfur cells also suffer from self-discharge that occurs due to polysulfide diffusion during cell rest.[26, 33, 39, 40, 160, 227] The success of the carbon-coated separator in mitigating the cell instability during cycling has also been investigated for reducing the self-discharge. In Figure 6.10a, the conventional cells with the Celgard separator (marked in black) could not limit the static polysulfide diffusion and, therefore, show the typical self-discharge behavior during cell rest. After one month of resting, the initial discharge capacity decreases from 1051 to 520 mA h g^{-1}, a loss of more than half of the original capacity. After three months, the severe self-discharge causes static capacity fading as high as 0.60 % per day. On the other hand, the same pure sulfur cathode in a cell employing the carbon-coated separator (marked in red) manifests superior static capacity retention. In the first month, the cell retains 86 % of its original capacity. In the subsequent two months, the capacity fading is almost negligible and the cell maintains 81 % of its original capacity. The static capacity fading is around 0.19 % per day over a 3-month period, implying a good suppression of the self-discharge behavior. The low

self-discharge is attributed to the carbon-coated separator, which acts as a polysulfide fishnet and confines the active material within the cathode region of the cell during cell rest.

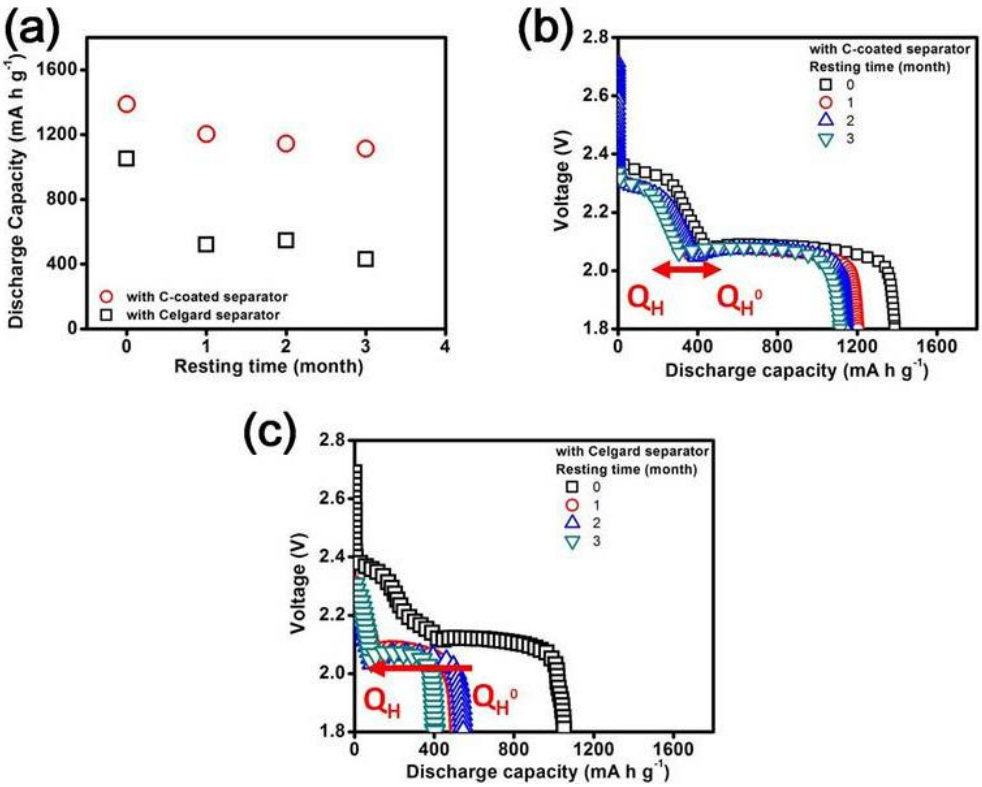

Figure 6.10: Cell performance of lithium-sulfur cells. Static electrochemical stability: (a) self-discharge behavior of the cells with different separators with various storage times. Initial discharge curves after different storage times employed with cells consisting of (b) carbon-coated separator and (c) the Celgard separator.

Detailed analysis of the self-discharge behavior is summarized in the comparison of Figures 6.10b and 6.10c. Figure 6.10b shows the discharge curves of cells with the carbon-coated separator after various rest times. After resting for a period of one month, the cell capacity shows a slight decrease from 1389 to 1204 mA h g^{-1}, then becomes mostly stable after that point. The complete shape of the upper voltage plateaus and the

overlapping of the discharge curves indicate that the active material is well retained within the cathode region of the cell. In contrast, cells with the Celgard separator exhibit obvious capacity fading and a severe reduction of the upper discharge plateau after resting for one month, as seen in Figure 6.10c. The disappearance and shrinkage of the discharge plateaus result from the dissolution of sulfur and the subsequent formation of inactive precipitates during long-term storage, corresponding to severe cathode degradation and unstoppable static capacity fading.[26, 39, 40, 160] The active material dissolution leads to the formation of pits on the cathode surface and the formation of insulating precipitates (Figure 6.11a and 6.11b). These features are not easily identified on the cathode with a carbon-coated separator (Figure 6.11c and 6.11d). Even after resting for 3 months, the carbon-coated separator cells exhibit good cycling stability (Figure 6.12).

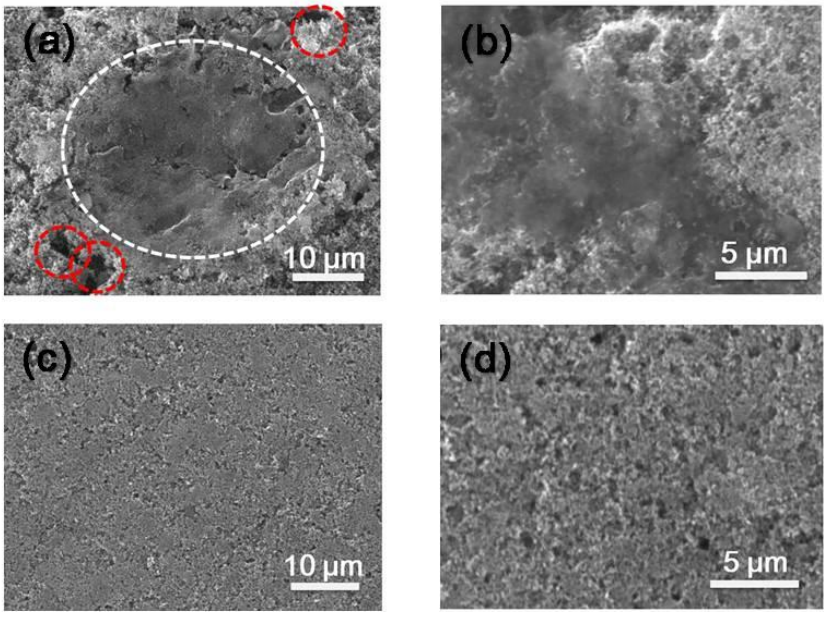

Figure 6.11: SEM images of the fresh cathode with the Celgard separator after resting for one month: (a) low-magnification observation and (b) high-magnification observation. SEM images of the fresh cathode after resting for one month with the carbon-coated separator: (c) low-magnification observation and (d) high-magnification observation.

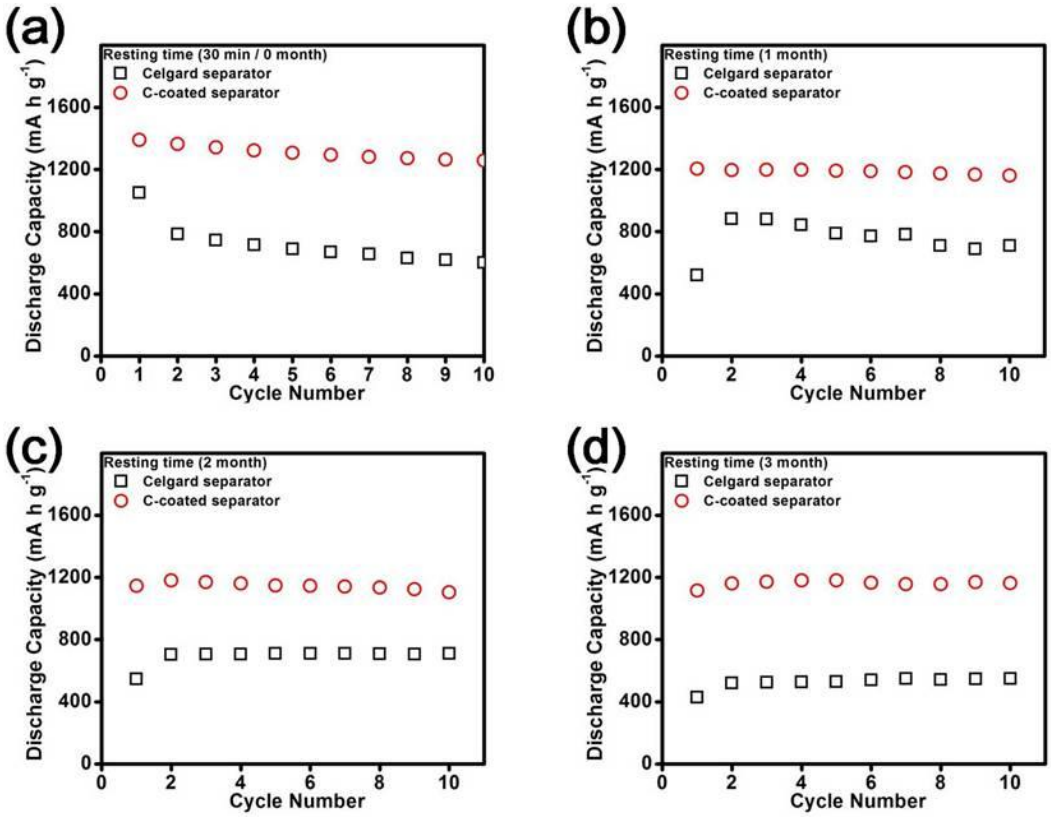

Figure 6.12: Reversible capacity after the initial cycle of the cells employing different separators with various resting times: (a) 30 min (0 month), (b) 1 month, (c) 2 months, and (d) 3 months.

Based on these electrochemical and microstructural results, it is possible to conclude that the severe self-discharge has been appreciably attenuated in cells applying the carbon-coated separator. To support this statement, it is instructive to compare the self-discharge constants of both separators by a mathematical model (Figure 6.13):[33, 135]

$$\ln\frac{(Q_H)}{(Q_H^0)} = -K_s \times T_R$$

The self-discharge constant (K_s) can be determined by comparing the upper plateau discharge capacity (Q_H) and the initial upper plateau discharge capacity (Q^0_H) with the resting time (T_R). The carbon-coated separator shows a low K_S of 0.05 per

month, which is the lowest K_S compared to other reported self-discharge data on the lithium-sulfur cells. [33, 135] In contrast, the K_S of the Celgard separator is as high as 0.44 per month. The low K_S demonstrates that the carbon coating functions as a protective layer for the pure sulfur cathode, keeping the active material from dissolving into the electrolyte during long-term storage. Therefore, this separator configuration modification eliminates the severe loss of active material and the irreversible capacity fading problem of pure sulfur electrodes during cell rest.

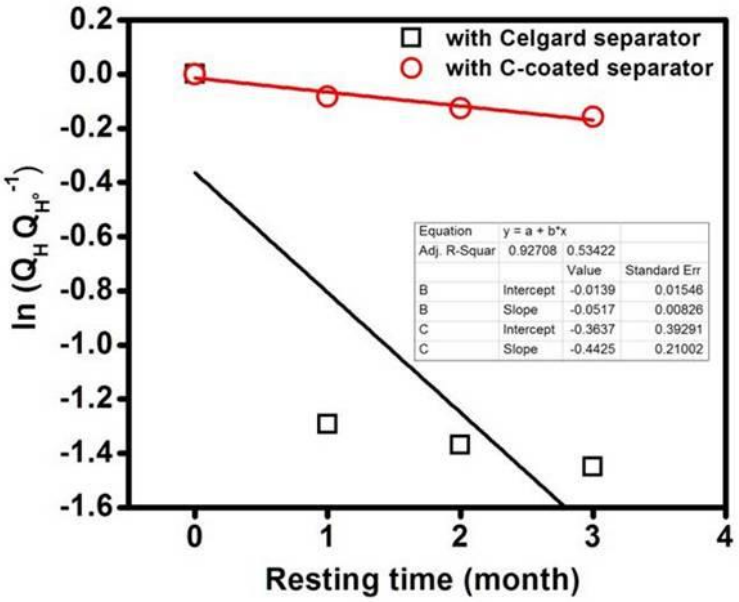

Figure 6.13: Natural logarithm of upper plateau discharge capacity (Q_H) divided by the original upper plateau discharge capacity (Q^0_H) as a function of resting time (T_R) for self-discharge constant calculation. (Inset is the self-discharge constant fitting.)

6.3.1.7 Summary

In conclusion, the carbon-coated separator that combines and rearranges two necessary components in lithium-sulfur cells, the Super P conductive carbon and the Celgard separator, is a facile, lightweight, and cost-effective separator configuration modification for improving lithium-sulfur batteries. After applying the carbon-coated

separator, cells with the pure sulfur cathode accomplish both dynamic and static cycle stability. The enhanced cycling performance was demonstrated with higher sulfur content and a simpler fabrication method than those of many composite sulfur cathodes. In addition, the electrochemical analyses of the upper discharge plateau and their corresponding capacities that are effective for determining the dynamic and static stability of the lithium-sulfur battery solidly confirm the high performance of the carbon-coated separator.

6.3.2 Functionalized separator: a lightweight MWCNT-coated separator

A bifunctional separator consisting of a layer of multiwall carbon nanotubes (MWCNTs) on the cathode-side of a Celgard polypropylene sheet has been investigated to overcome the challenges of lithium-sulfur cells. The conductive/porous MWCNT coating functions (i) as an upper current collector to facilitate electron transport and high active-material utilization and (ii) as a filter to intercept/absorb the migrating polysulfides and thereby suppress the polysulfide diffusion. Also, the access to the electrolyte through the porous network of MWCNT along with its fast electronic transport facilitates the reutilization of the trapped active material and superior long-term cyclability. The MWCNT coating is lightweight (0.17 mg cm^{-2}), yet allows the successful use of pure sulfur cathodes (high sulfur content of 70 wt. %) with high discharge capacity, excellent rate performance, and long cycle life, demonstrating that the MWCNT-coated separator is a viable solution to practical lithium-sulfur batteries.

6.3.2.1 Functionalized separator design

The MWCNT-coated separator is fabricated by ultrasonically dispersing the MWCNTs in isopropyl alcohol (IPA), followed by a simple vacuum filtration of the suspension through the commercial Celgard separator without any additional additives or treatments (Figure 6.14). The prepared MWCNT-coated separator is flexible and robust (Figure 6.15) with excellent mechanical strength for ensuring its normal function in cells.

After cycling, the coating layer of the cycled MWCNT-coated separators maintains good integrity and homogeneity (Figure 6.15d), consistent with the above statements and indicating that the robust and flexible MWCNT coating can cushion the strain generated by the volume changes of the active material conversion. Most importantly, the weight of the MWCNT coating is only 0.17 mg cm^{-2}. As a reference, the weights of the Celgard separator and the active material are, respectively, 1.0 mg cm^{-2} and ~ 2.0 mg cm^{-2}. Thus, even if the weight of the MWCNT coating is included in the calculation of the active material content, the cell utilizing the MWCNT-coated separator has a sulfur content of 65 wt. %, achieving a reasonable sulfur loading that is higher than that of many reported high-performance lithium-sulfur cells.[127]

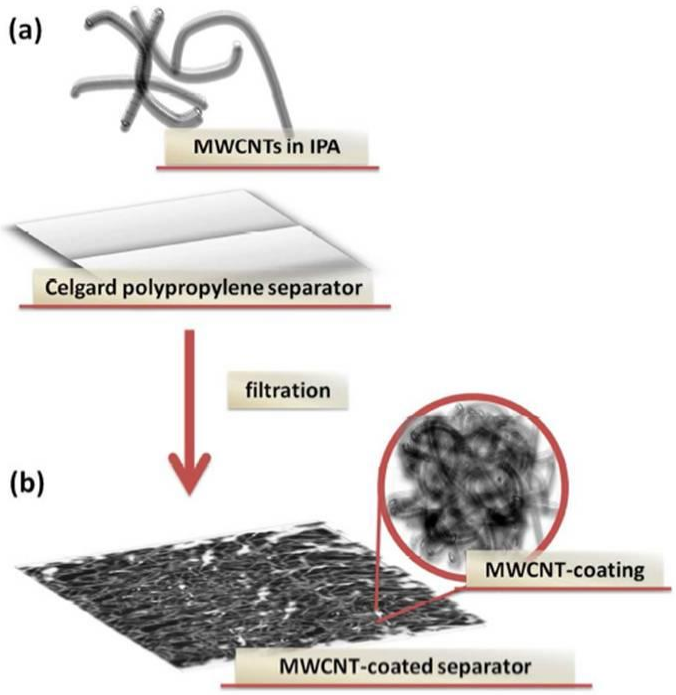

Figure 6.14: A schematic of the fabrication process of the MWCNT-coated separator: (a) vacuum filtration of the MWCNT suspension through the commercial Celgard 2500 polypropylene separator and (b) resultant MWCNT-coated separator (the inset is the schematic configuration of the MWCNT coating as the polysulfide filter).

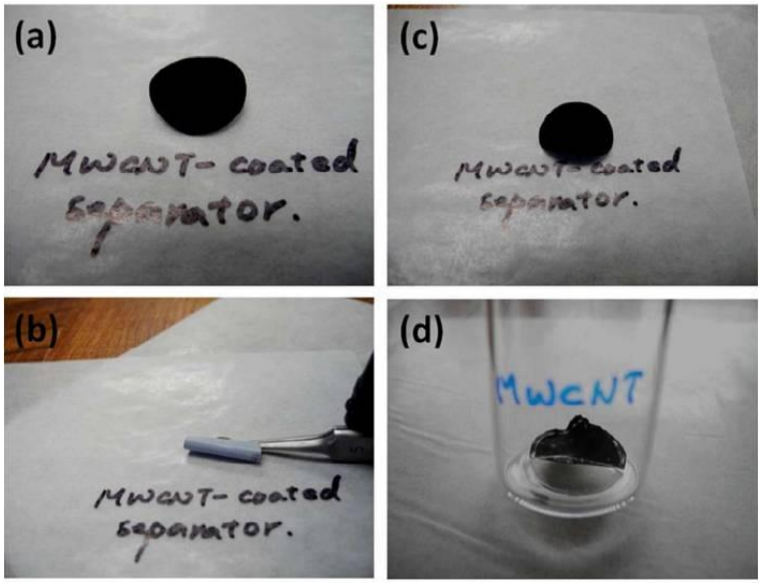

Figure 6.15: Demonstration of the flexibility and mechanical strength of the MWCNT-coated separator: (a) MWCNT-coated separator, (b) rolled and crumpled MWCNT-coated separator, (c) recovered MWCNT-coated separator, and (d) cycled MWCNT-coated separator.

6.3.2.2 Morphology and microstructure analysis

Figure 6.16a shows the schematic configuration of the cell with the MWCNT-coated separator. The MWCNT-coating side facing the pure sulfur cathode intercepts the diffusing polysulfides before they freely migrate through the polypropylene separator. As a result, the polysulfide species is stabilized within the cathode region of the cell (marked as red circulating arrows) and a stable electrochemical environment exists (marked as blue circulating arrows).

Figure 6.16b shows the SEM image and the corresponding EDX elemental mapping of the MWCNT-coated separator. The inset shows the high-magnification SEM inspection of the MWCNT coating. The MWCNT-coating layer consists of interwoven, curved MWCNTs that are deposited as a bundled/porous filter on the Celgard separator. This porous filter with uneven surface is the key architectural element for blocking the

free migration of polysulfides.[169, 174, 208] The MWCNT coating possesses a high surface area of 410.42 m^2 g^{-1} with a total pore volume of 2.76 cm^3 g^{-1} (0.18 cm^3 g^{-1} for micropore volume). Thus, the MWCNT-coated separator possesses not only abundant porous space for localizing the electrolyte containing dissolved polysulfides but also the microporous absorption sites for trapping the intercepted polysulfides. Moreover, its long-range porous network ensures charge transport and electrolyte immersion, which is necessary for reactivating the trapped active material.[174, 208]

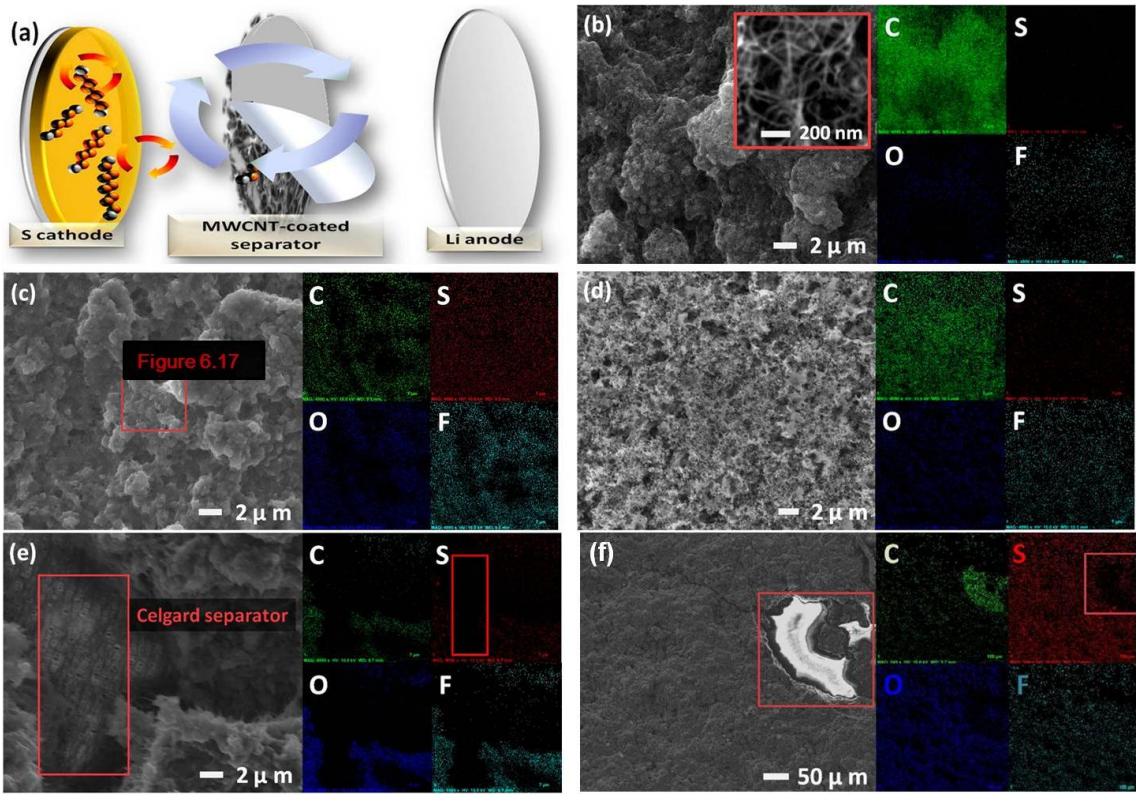

Figure 6.16: (a) A schematic cell configuration of the lithium-sulfur cell employing the MWCNT-coated separator. SEM observation and elemental mapping: (b) MWCNT-coated separator, (c) cycled MWCNT-coated separator, (d) the separator side of the cycled MWCNT coating, (e) the broken surface of the cycled MWCNT-coated separator, and (f) low-magnification observation of the broken surface of the cycled MWCNT-coated separator.

The suppressed polysulfide diffusion is evident in the cycled MWCNT-coated separator, displaying obvious morphological and elemental changes compared to the fresh one, as shown in Figures 6.16c and 6.17 (high magnification of the marked region in Figure 6.16c). The SEM inspection shows the obstructed active material, which was filtered out by the MWCNT coating, and the corresponding EDX elemental mapping shows clear elemental sulfur signal (marked as red) distributed in the carbon matrix (marked as green), evidencing the excellent interception and absorption effects of the porous MWCNT coating. As a result, the cycled MWCNT coating that was painted off from the MWCNT-coated separator by a razor blade shows low surface area of 30.58 $m^2 g^{-1}$ with a low pore volume and micropore volume of, respectively, only 0.06 $cm^3 g^{-1}$ and 0.0085 $cm^3 g^{-1}$ (Figure 6.18). The decrease in the surface area and pore volume demonstrates that the porous space and microporous absorption sites of the MWCNT coating are effectively utilized for absorbing and then trapping the migrating polysulfides. On the other hand, it is worth emphasizing that the uniform elemental sulfur signal (Figure 6.16c and Figure 6.17) shows no dense spots, and the elemental carbon signal remains strong and distinguishable. These phenomena indicate that there is no formation of severe nonconductive agglomerations on the MWCNT-coated separator. The reason for this may come from two possible mechanisms. First, the interwoven conductive MWCNTs successfully transfer electrons to reactivate the trapped active material during cycling, suppressing the formation of inactive precipitates.[28, 173, 240] Second, the uneven and porous structure of MWCNT coating is unfavorable for the formation of nonconductive agglomerations.[135, 173] It can also be seen that the elemental fluorine and oxygen signals are homogeneous with the carbon signals, implying good electrolyte immersion and penetration. Therefore, the electrochemically active materials are stabilized within the cathode region of the cell with intimate three-phase boundary involving the active material, the conductive network, and the electrolyte. Such an optimized electrochemical environment ensures efficient sulfur utilization and high reversibility.

To understand the ability of the MWCNT-coated separator to physically inhibit polysulfide diffusion, it is beneficial to look at the morphology of the "separator side" of the cycled MWCNT coating. In Figure 6.16d, the separator side of the MWCNT coating retains its porous structure and shows no obvious polysulfide agglomerations, which is confirmed by the strong carbon signal and the weak sulfur signal in the corresponding elemental mapping. The weak sulfur signal may come from the $LiCF_3SO_3$ salt in the electrolyte. Furthermore, in Figure 6.16e and Figure 6.16f (low-magnification SEM inspection), the broken surface SEM of the cycled MWCNT-coated separator were obtained by scraping the MWCNT coating from the Celgard polypropylene sheet. The scraped region shows almost no elemental sulfur signal on the surface of the Celgard separator. Therefore, we believe that the dissolved polysulfides are trapped within the MWCNT coating and are not able to penetrate the separator to cause severe capacity fading.

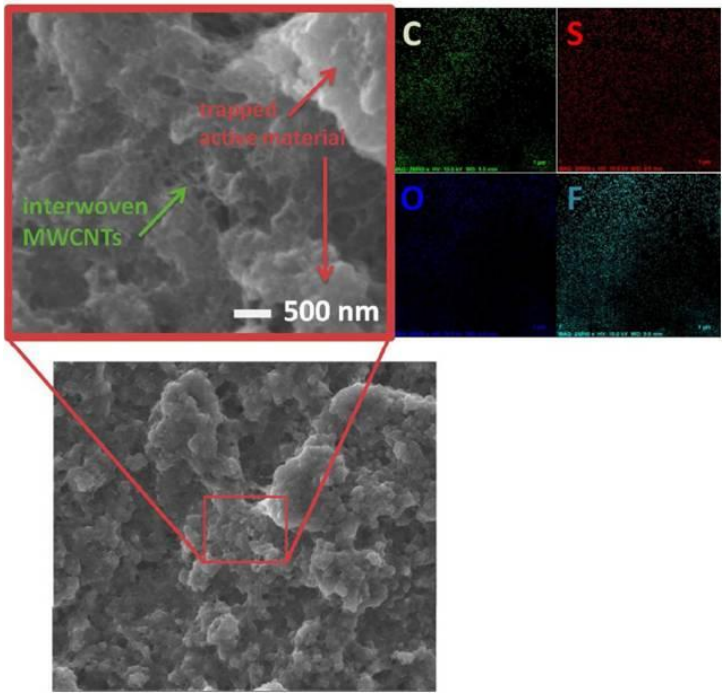

Figure 6.17: High-magnification SEM observation and elemental mapping of the cycled MWCNT-coated separator (high-magnification SEM of Figure 6.16c).

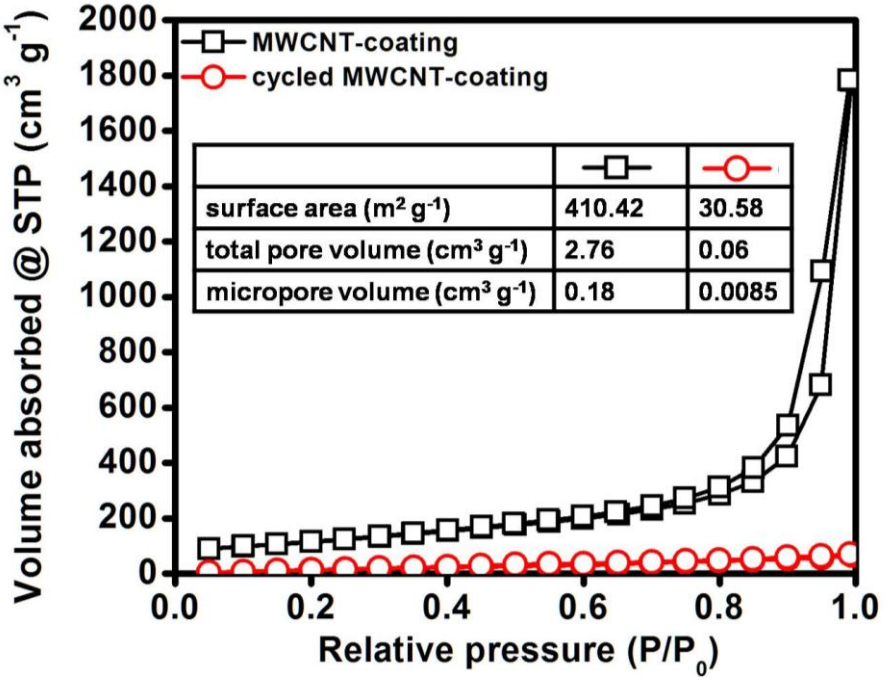

Figure 6.18: BET analyses: surface area, pore volume, and isotherms of the MWCNT coating and the cycled MWCNT coating.

6.3.2.3 Electrochemical analysis

The electrochemical analyses of the cell with the MWCNT-coated separator are summarized in Figure 6.19. Figure 6.19a shows the discharge/charge voltage profiles during the initial 20 cycles at a C/5 rate. The upper discharge plateau at 2.35 V and lower discharge plateau at 2.05 V represent, respectively, the reduction from sulfur to long-chain polysulfides and from long-chain polysulfides to Li_2S_2/Li_2S.[17, 171] The initial discharge capacity is 1324 mA h g^{-1} with the sulfur utilization approaching 80 %, facilitated by the MWCNT coating that provides additional conductive pathways and increases the cell conductivity.[208, 240]The significantly smaller semicircle in the impedance analysis, as electrochemical evidence, reconfirms that the MWCNT-coated separator increases the cell conductivity by reducing the charge-transfer resistance of the cell by about 85 % (Figure 6.20a).[18, 169] The excellent charge-transfer ability of the

conductive MWCNT coating enables a high reactivation of the trapped active material, inhibiting severe inactive agglomeration and ensuring the stable cyclability of the cell.[19, 24] Thus, in the subsequent cycles, the overlapping discharge curves show no severe shrinkage and decline in capacity.[208] The two continuous charge plateaus at 2.25 and 2.40 V represent the reversible oxidation reaction from Li_2S_2/Li_2S to Li_2S_8/S. The vertical voltage rise from 2.4 to 2.8 V at the end of charge indicates a complete charge process with limited polysulfide shuttling.[28, 32] At various cycling rates of C/2 and 1C, the cells utilizing the MWCNT-coated separator also possess overlapping discharge curves and charge curves (Figure 6.20b and 6.20c), demonstrating superior cycle stability and excellent rate performance.[171, 177, 208] Figure 6.19b shows the cyclic voltammograms (CV) of the cell with the MWCNT-coated separator during the initial 20 cycles at a scanning rate of 0.1 mV s^{-1}. The two cathodic peaks and overlapping anodic peaks are in agreement with the discharge/charge curves (Figure 6.19a), displaying the typical sulfur reduction/oxidation reactions of lithium-sulfur cells.[39,42] After the initial cycle, the disappearance of the overpotential of the cathodic peak implies that the active material rearranges itself and migrates to electrochemically favorable positions.[30,33] It can be visualized in Figure 6.19b that there is no decrease in peak intensity or a shift in potential during subsequent CV scans, confirming the high reversibility facilitated by the MWCNT-coated separator.

The suppressed polysulfide diffusion and the high electrochemical reversibility facilitated by the MWCNT-coated separator can be analyzed by investigating the changes in the upper discharge plateaus and their corresponding discharge capacity (Q_H, theoretical capacity = 419 mA h g^{-1}) during cycling because this region corresponds to the formation and existence of highly soluble polysulfides.[13, 33, 64] First, in Figures 6.19a, 6.20b, and 6.20C, the completeness of the overlapping upper discharge plateaus during cycling provides evidence that the MWCNT polysulfide filter efficiently suppresses polysulfide diffusion and that severe active material loss has not occurred.[28, 174] Second, in Figure 6.19c, the initial Q_H at a C/5 rate is 414 mA h g^{-1} approaching 99 % of the

theoretical value, implying that the severe polysulfide diffusion has been suppressed. During cycling, the Q_H of the cells with the MWCNT-coated separator remains highly reversible at various cycling rates. However, the Q_H of the cell with the Celgard separator (marked in green) decreases to 53 % of its original value after the initial cycle at a C/5 rate, exhibiting the typical capacity fade issue. The complete upper discharge plateau and stable Q_H throughout cycling demonstrate that the MWCNT coating effectively alleviates the polysulfide diffusion and eliminates the loss of active material/capacity.

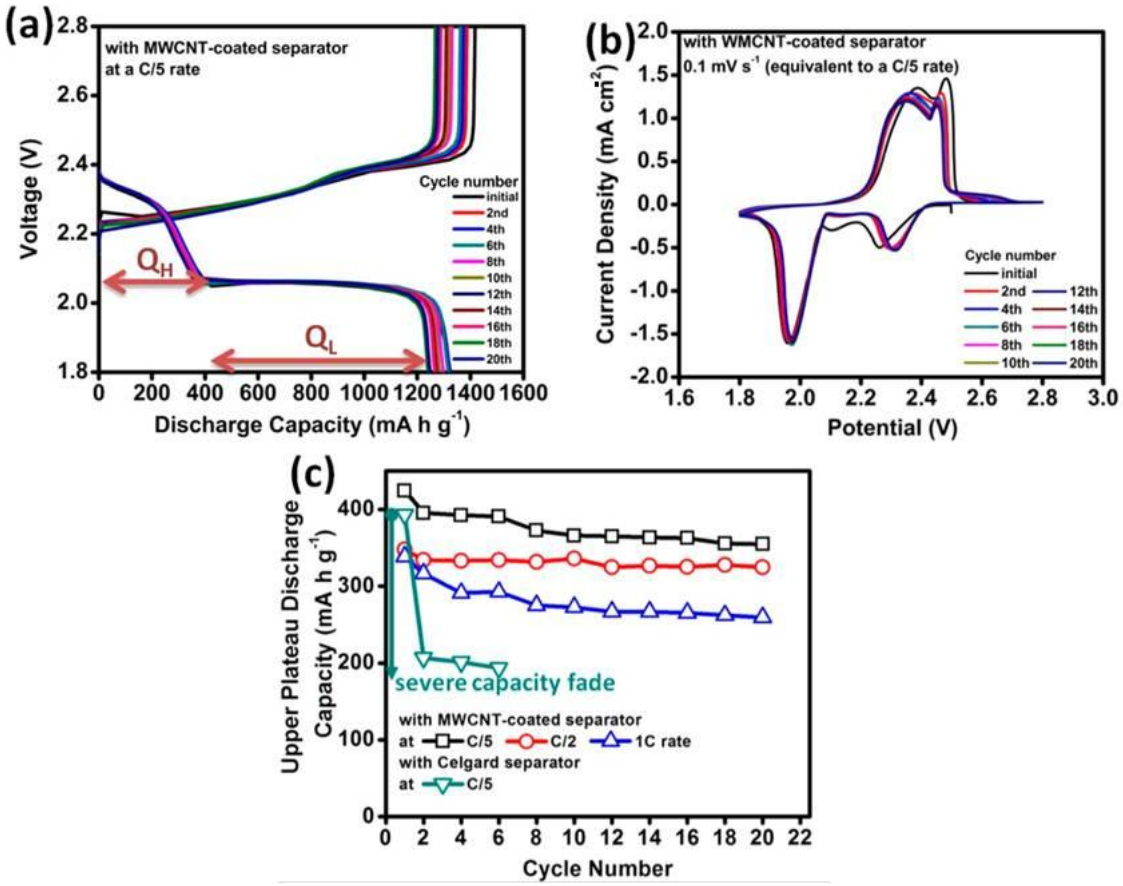

Figure 6.19: Electrochemical measurements of lithium-sulfur cells employing the MWCNT-coated separator: (a) discharge/charge curves at a C/5 rate, (b) cyclic voltammograms at a 0.1 mV s^{-1} scanning rate, and (c) upper-plateau discharge capacities at various cycling rates.

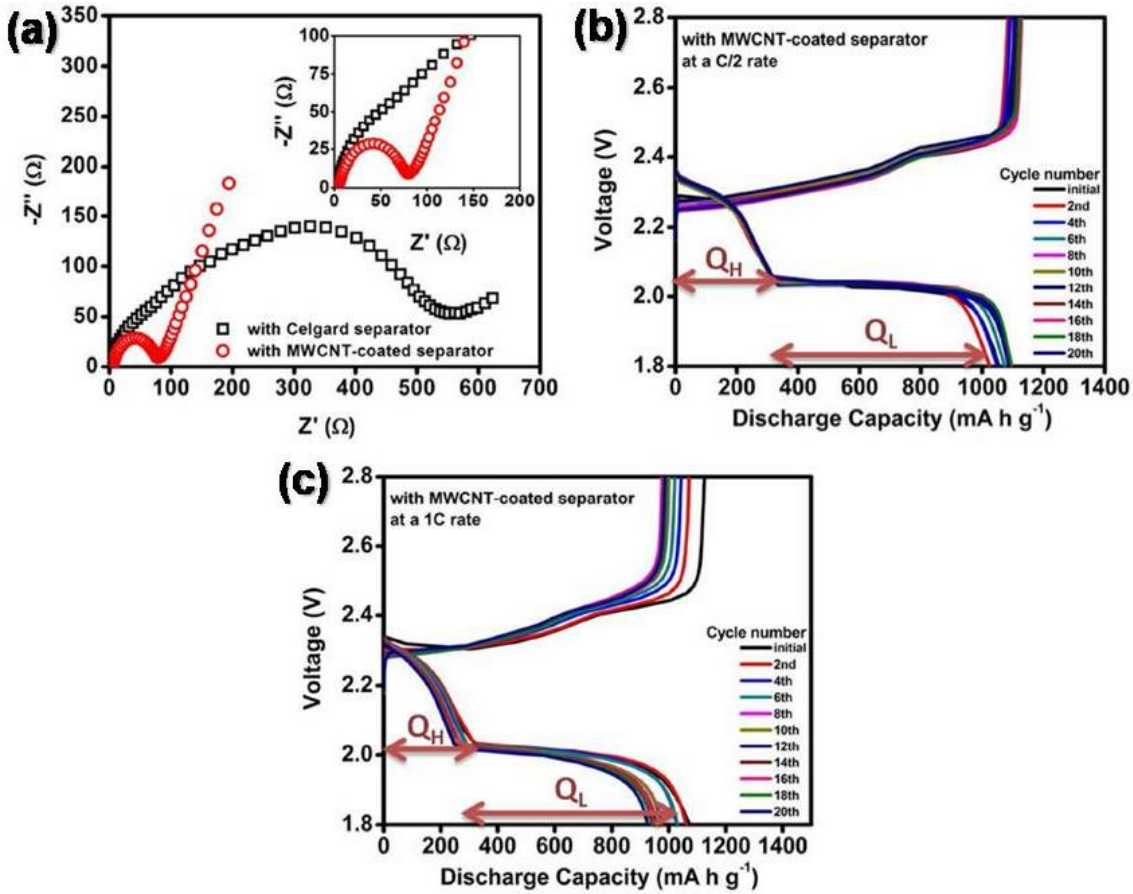

Figure 6.20: Electrochemical analysis of lithium-sulfur cells: (a) impedance analysis of cells with the Celgard separator and the MWCNT-coated separator, (b) discharge/charge curves at a C/2 rate, and (c) discharge/charge curves at a 1C rate.

6.3.2.4 Electrochemical performance

The properties of the bifunctional MWCNT-coated separator allows successful implementation of a pure sulfur cathode containing 70 wt. % sulfur and leads to high discharge capacities (sulfur utilization in parentheses) of 1324 (79 %), 1107 (66 %), and 1073 mA h g^{-1} (64 %) at, respectively, C/5, C/2, and 1C rates, as shown in Figure 6.21a. The excellent rate capability allows the cells to remain stable under a range of cycling

rates from C/5 to 1C. After 150 cycles, the reversible discharge capacities of the cells with the MWCNT-coated separator are 881, 809, and 798 mA h g^{-1} at, respectively, C/5, C/2, and 1C rates. The corresponding capacity fading rates at various cycling rates are only 0.19 ± 0.03% per cycle. For a comparison, the same pure sulfur cathode with the Celgard separator suffers from low capacity, severe capacity fade, and short cycle life. The excellent cycle stability achieved by the application of the MWCNT-coated separator arises from two mechanisms: (i) the soluble polysulfides are stabilized within the cathode region by the porous MWCNT coating and (ii) the conductive MWCNT coating facilitates the successive reutilization of the trapped active materials within the conductive bundled filter during subsequent cycles.[28, 169] These effects ensure no severe loss of active material and suppression of inactive agglomerations covering on the cycled pure sulfur cathode.[169, 208]

With a high reversibility, the cell with the MWCNT-coated separator achieves long cycle life over 300 cycles with a reasonable capacity retention and high discharge/charge efficiency of > 96 % at a 1 C rate, as shown in Figure 6.21b. The capacity after 300 cycles is 621 mA h g^{-1} with a corresponding capacity fade rate of as low as 0.14 % per cycle. Such long-term cycle stability results from an alleviation of the severe polysulfide diffusion and the reutilization of the trapped polysulfides within the conductive MWNCT coating.[173, 174]

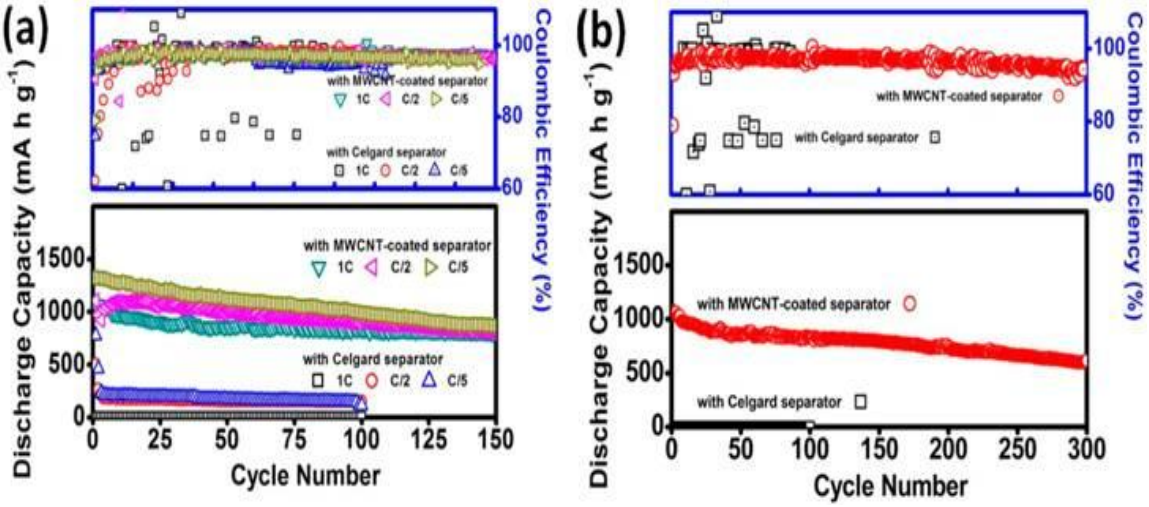

Figure 6.21: Cell performance of the lithium-sulfur cells employing the MWCNT-coated separator: (a) cycle stability and rate performance and (b) long-term cycle life.

6.3.2.5 Summary

In summary, the MWCNT-coated separator successfully integrates a lightweight bundled polysulfide filter with the polypropylene separator component in the cell and offers several enhancements. The bifunctional separator possesses the conductive/porous MWCNT coating for obstructing the free polysulfide diffusion, reactivating the trapped active material, and stabilizing the electrochemical material within the cathode region of the cell. As a result, the sulfur cathode employing the MWCNT-coated separator displays a high initial discharge capacity of 1324 mA h g^{-1}, excellent rate performance from C/5 to 1C rates, and superior long-term cycle stability over 300 cycles. In addition, the successful use of the pure sulfur cathode with a high sulfur content of 70 wt. % narrows the gap between scientific research and commercial feasibility.

6.3.3 Functionalized separator: a polyethylene glycol-supported microporous carbon coating for investigating the chemical and physical polysulfide-trapping capability

A composite separator with a thin-film polysulfide trap that is attached to one side of a Celgard polypropylene (PP) separator has been developed for lithium-sulfur batteries. The polysulfide trap consists of a polyethylene glycol-supported microporous carbon coating (MPC/PEG coating) and hence suppresses polysulfide diffusion by the physical and chemical polysulfide-trapping capabilities. In this configuration, the conductive/porous MPC/PEG coating on the separator faces the pure sulfur cathode and functions as (i) an upper-current collector for facilitating enhanced sulfur utilization and (ii) a polysulfide trap for suppressing polysulfide diffusion.[18, 28, 242] The other side of the Celgard PP separator in contact with the lithium-metal anode serves as an electrically insulating membrane. This flexible and robust PP membrane cooperates with the PEG binder to minimize the weight and thickness of the MPC/PEG coating and enhance its mechanical strength. Therefore, cells utilizing the MPC/PEG-coated separator achieve high discharge capacity and outstanding cyclability. In addition to the improved electrochemical performance, the MPC/PEG-coated separator solves the problems of low sulfur content and added device weights from additional components by utilizing common laboratory supplies and simple processing techniques, allowing it to be easily translated into industrial processes.

6.3.3.1 Functionalized separator development

Compared with our previous carbon-coated separators that use only the carbon materials (MWCNT[154] and Super P conductive carbon[38]) as the lightweight functionalized coating, the MPC/PEG-coated separator has PEG-modified microporous substrates. The use of MPC substrates aims to physically trap the migrating polysulfide by their micropores.[18] The use of PEG binder can chemically improve the polysulfide-trapping capability and enhance the mechanical strength of the MPC/PEG coating.[55, 223] Therefore, the MPC/PEG-coated separator not only improves the

electrochemical performance (extend the cycle life with decreased capacity fading) but also decreases the weight/thickness of the coating layer.

6.3.3.2 Morphology and microstructure analysis

Figure 6.22a illustrates the cell configuration with the MPC/PEG-coated separator. The MPC/PEG coating side of the composite separator faces the sulfur cathode as the "polysulfide trap" for intercepting the migrating polysulfides before they diffuse to the Celgard PP. It also works as an upper current collector to facilitate electron transport for enhancing the electrochemical utilization of sulfur and for reactivating the trapped active material.[28, 174] The thin-film MPC/PEG coating with a thickness of 8 μm weighs only 0.15 mg cm^{-2}. Therefore, even when its weight is included, the cell utilizing the MPC/PEG-coated separator has a sulfur content of 65 wt. %, overcoming the persistent drawback of low sulfur content encountered in many high-performance lithium-sulfur cells.[127] On the other side, the insulating Celgard membrane functions as a flexible support for the MPC/PEG coating while facilitating Li^+-ion transport. Thus, the MPC/PEG-coated separator possesses excellent mechanical strength, ensuring its normal functions during cell assembly and cycling (Figure 6.23).

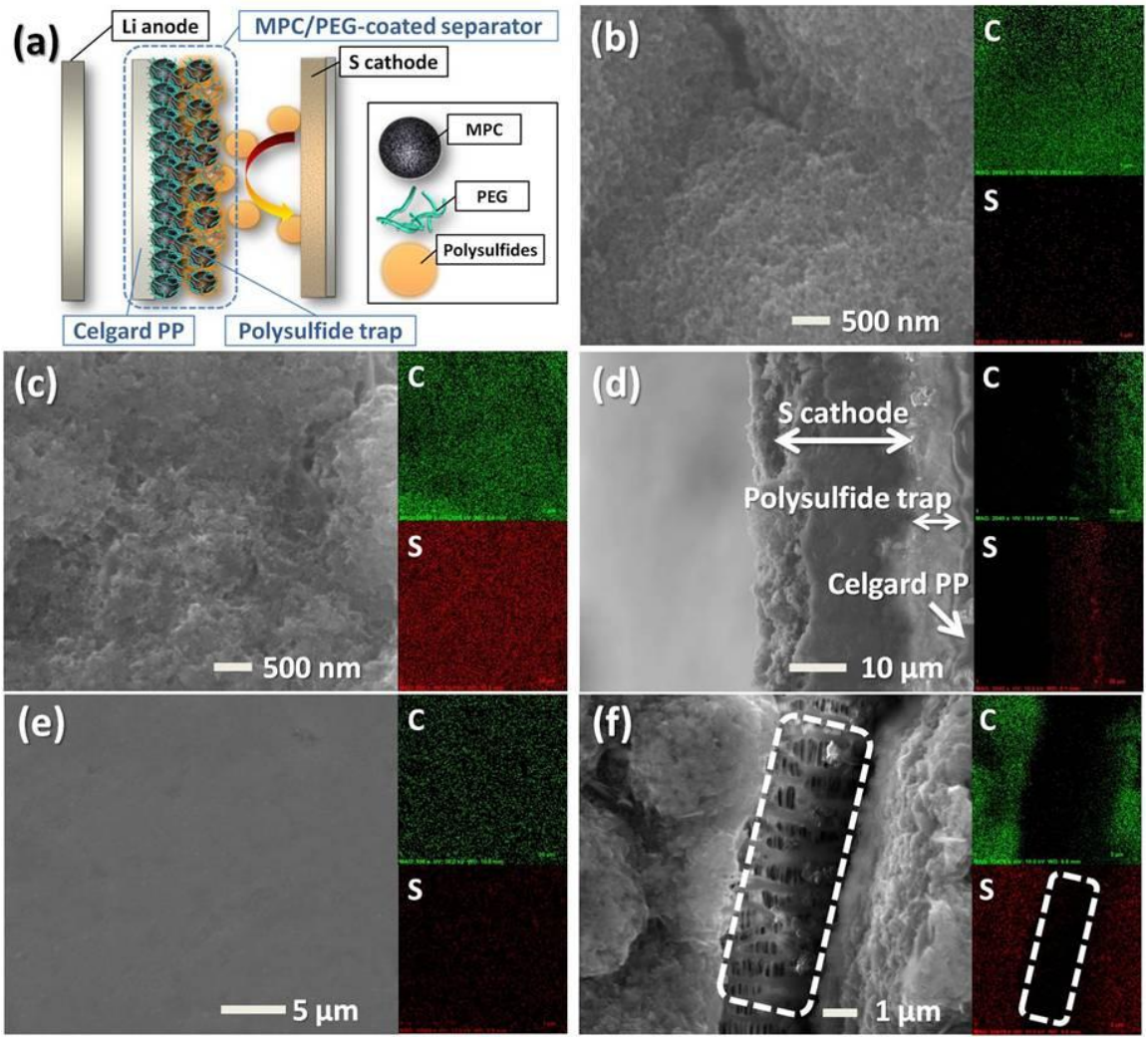

Figure 6.22: (a) The schematic of a lithium-sulfur cell configuration with a MPC/PEG-coated separator. (b) SEM observation and elemental mapping of the MPC/PEG-coated separator. SEM observation and elemental mapping of the cycled MPC/PEG-coated separator: (c) surface SEM, (d) cross-sectional SEM, (e) SEM of the separator side, and (f) SEM of the scraped surface.

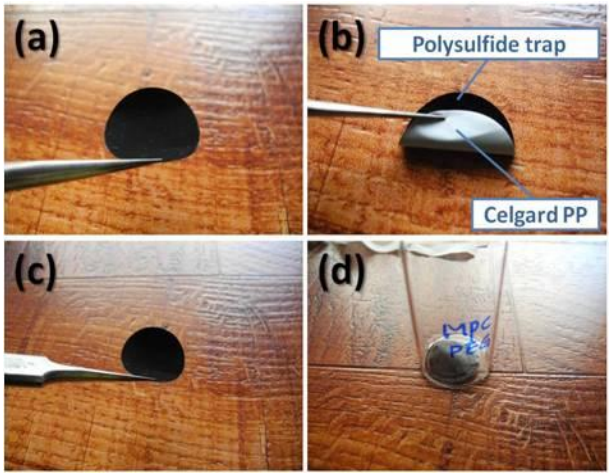

Figure 6.23: Digital images of the composite separators: (a) MPC/PEG-coated separator, (b) folded/crumpled MPC/PEG-coated separator, (c) recovered MPC/PEG-coated separator, and (d) cycled MPC/PEG-coated separator.

Figure 6.22b show the morphology of the MPC/PEG-coated separator examined with SEM. The MPCs form porous micron-sized clusters attached to the Celgard separator. The interconnected conductive MPC clusters work as an electron pathway for improving active material utilization.[28, 37, 207] The MPC nanoparticles (Figure 6.24) possess a high surface area of 1321 $m^2\ g^{-1}$, a large pore volume of 3.62 $cm^3\ g^{-1}$, and many micropores (0.5 nm and 1.2 nm) (Figure 6.25). Considering the length of Li-S and S-S bonds to be approximately 2 Å, the estimated chain lengths of polysulfides are in the range of 1.0 to 1.8 nm for Li_2S_x with $4 < x \leq 8$.[244, 245] It is reasonable to expect that polysulfides could be effectively intercepted by the microporous trapping sites of the MPC/PEG coating.[174] After the electrochemical cycling, the surface area of the MPC/PEG coating is decreased to 49 $m^2\ g^{-1}$ and the pore volume is lowered to 0.09 $cm^3\ g^{-1}$. The BET analyses suggest that the porous MPC/PEG coating works as the polysulfide trap by (i) absorbing the electrolyte containing the dissolved polysulfides into its porous spaces,[28, 208] (ii) physically filtering/localizing the migrating polysulfides by its microporous trapping sites,[28, 207] and (iii) chemically anchoring the trapped active material by the PEG.[87, 205, 223]

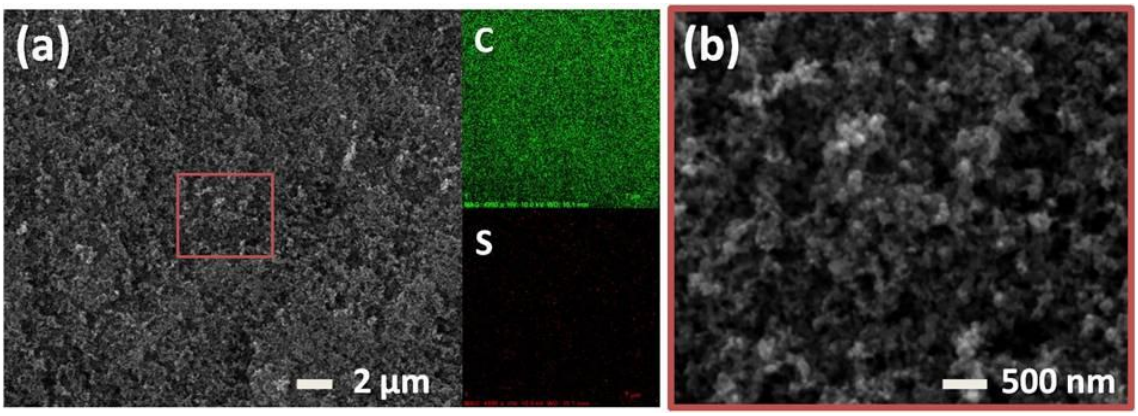

Figure 6.24: (a) Low- and (b) high-magnification SEM observation and elemental mapping of the MPC nanoparticles.

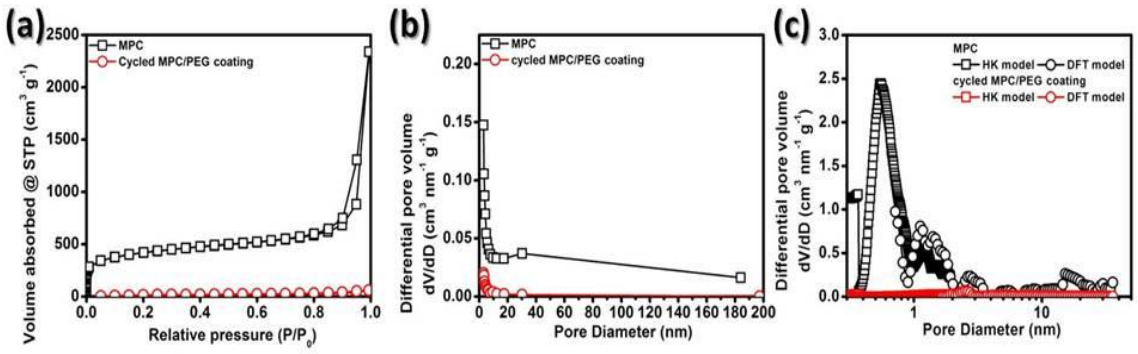

BET analyses	Surface area [$m^2 g^{-1}$]	Total Pore Volume [$cm^3 g^{-1}$]	Micropore Volume [$cm^3 g^{-1}$]
MPC	1320.952	3.618	0.6485
Cycled MPC/PEG coating	49.497	0.08779	0.0114

Figure 6.25: Surface area analyses of the MPC and the cycled MPC/PEG coating: (a) isotherms, (b) pore size distributions with the Barrett-Joyner-Halenda (BJH) method, and (c) pore size distributions with the Horvath-Kawazoe (HK) and the density functional theory (DFT) methods.

Figure 6.22c demonstrates that after 200 cycles, the cycled MPC/PEG-coated separator displays obvious morphological and elemental changes as observed via SEM and EDX elemental mapping. SEM inspection shows that the trapped active material (the elemental sulfur signals) is uniformly distributed on the MPC/PEG coating (the elemental carbon matrix), evidencing the physical interception and absorption properties of the porous MPC clusters. On the other hand, the elemental carbon mapping signals are distinguishable and the elemental sulfur signals show no dense spots. These observations demonstrate that the conductive polysulfide traps can transfer electrons to reactivate the trapped active material, avoiding the formation of non-conductive agglomerations on the cathode.[28, 57, 169, 208] In addition to the physical absorption, the PEG chains further chemically improve the polysulfide-trapping capability. During cell cycling, polysulfides easily dissolve into the ether-based solvents due to the low viscosity of and solvation by the ether-based electrolyte. The addition of PEG can introduce a highly hydrophilic surface chemical gradient for trapping the polysulfides, as demonstrated by various PEG modified composite cathodes. The reported mechanism is that the migrating polysulfides will be solubilized by the added ether groups and trapped by the PEG chains but not dissolved in the bulk electrolyte.[55, 87, 205, 223] Thus, the MPC/PEG-coated separator can physically and chemically trap the polysulfide within the cathode region.[205, 223] The PEG also works as a flexible cushion to accommodate the volume change that arises from the trapped active material.[47] Moreover, the PEG binder improves the connection between MPCs (Figure 6.22b) and thereby enhances the electrical conductivity of the MPC/PEG coating.

To understand how the MPC/PEG-coated separator suppresses the polysulfide diffusion, it is necessary to look at the cross-sectional SEM of the cycled cell. Figure 6.22d shows, from left to right, the pure sulfur cathode (*ca.* 25 μm), the MPC/PEG coating (*ca.* 8 μm), and the Celgard separator. In the pure sulfur cathode, the uniform sulfur signals indicate that there are no active material agglomerations and no active material loss, which is reconfirmed by the SEM images of the cycled pure sulfur cathode

(Figure 6.26). Evidence of the outstanding polysulfide-trapping capability is found at the interface between the cathode and the MPC/PEG coating, showing strong sulfur signals in the elemental mapping result. This demonstrates that most of the migrating polysulfides are intercepted by the polysulfide trap before they diffuse into the MPC/PEG coating. As a further evidence, the decreasing concentration gradient of sulfur signals from the cathode side to the separator side depicts that the escaping polysulfides are trapped within the MPC/PEG coating. As a result, very weak sulfur signals are detected in the Celgard region, which is reconfirmed by SEM on the separator side of the MPC/PEG coating (Figure 6.22e). Notably, in Figure 6.22f, the scraped surface of the cycled MPC/PEG-coated separator shows no elemental sulfur signals on the exposed Celgard separator, demonstrating that the dissolved polysulfides are not able to penetrate through the polysulfide trap. This phenomenon illustrates the excellent polysulfide-trapping capability of the MPC/PEG coating.

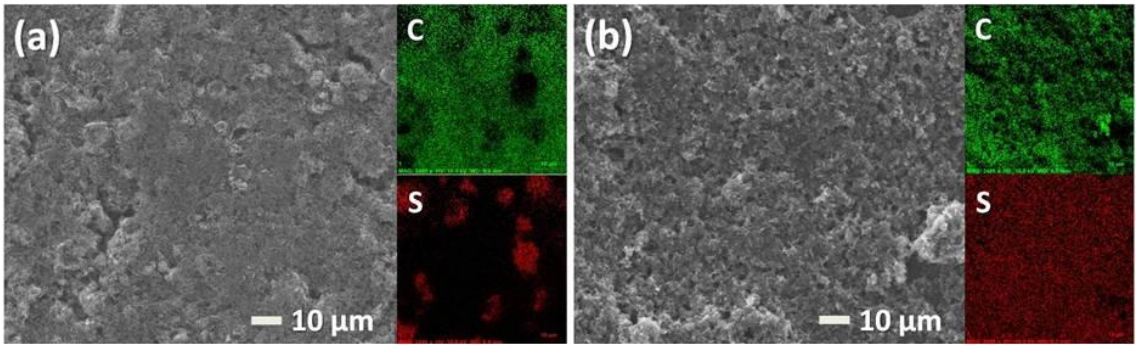

Figure 6.26: SEM observation and elemental mapping of the pure sulfur cathode utilizing a MPC/PEG-coated separator (a) before and (b) after cycling.

6.3.3.3 Electrochemical analysis and performance

Figure 6.27a shows the discharge/charge curves of the cells utilizing the MPC/PEG-coated separator at a C/5 rate. During cell discharge, the upper discharge plateau at 2.3 V indicates the reduction reaction from sulfur to long-chain polysulfides

(Li_2S_x, $x = 4 – 8$).[17, 52] The lower discharge plateau at 2.1 V represents the transformation of long-chain polysulfides to Li_2S_2/Li_2S.[18, 52] During cell charge, the two continuous charge plateaus at 2.2 and 2.4 V correspond to the oxidation reactions of Li_2S_2/Li_2S to Li_2S_8/S.[13, 52] The overlapping upper discharge plateaus are well-retained, indicating limited polysulfide diffusion and almost no active material loss.[154, 208] The overlapping discharge curves, on the other hand, demonstrate that the MPC/PEG coating continuously reactivates the trapped active material, attesting to the high electrochemical reversibility and stability of the cell. The cyclic voltammograms (CVs) of the cell (Figure 6.27b) display the typical two-step reduction reactions (cathodic peak I and II) in the cathodic sweep and two overlapping oxidation reactions (anodic peaks III) in the anodic sweep, consistent with the discharge/charge curves. Those cathodic and anodic peaks maintain almost the same magnitude and show no severe potential shifts, confirming the excellent reversibility and stability.[28, 169]

Figure 6.27c demonstrates that the MPC/PEG-coated separator allows the successful implementation of a pure sulfur cathode containing 70 wt. % sulfur and leads to high discharge capacities, stable cyclability, and good rate performance. After upgrading the Celgard separator to the MPC/PEG-coated separator, the initial discharge capacities (with sulfur utilization in parentheses) increase from 843 (50 %) to 1307 mA h g^{-1} (78 %) and from 543 (32 %) to 1018 mA h g^{-1} (61 %) at, respectively, C/5 and C/2 rates. At a 1C rate, the MPC/PEG-coated separator allows the pure sulfur cathode to function normally by offering efficient electron conduction and fast ion transport through the conductive and porous MPC/PEG coating. A capacity increase is observed during the initial 10 cycles at various C rates, due to the rearrangement of the active material as it conditions itself to occupy the more electrochemically favorable positions.[18] The rearranged active material may be surrounded by conductive carbon and stabilized in the cathode (Figure 6.26b) or immobilized in the conductive polysulfide trap (Figure 6.22). In the sequent cycles, the conductive/porous MPC/PEG coating easily transfers electrons, charges, and liquid electrolyte to reactivate the trapped cycled products, [18, 28]

accomplishing efficient reutilization of the trapped active material and high reversibility. Therefore, after 200 cycles, the discharge capacities of the cells employing the MPC/PEG-coated separator are 839, 795, and 782 mA h g^{-1} at, respectively, C/5, C/2, and 1C rates. The composite separator greatly lowers the capacity fading to 0.18 % (at a C/5 rate), 0.11 % (at a C/2 rate), and 0.08 % (at a 1C rate) per cycle.

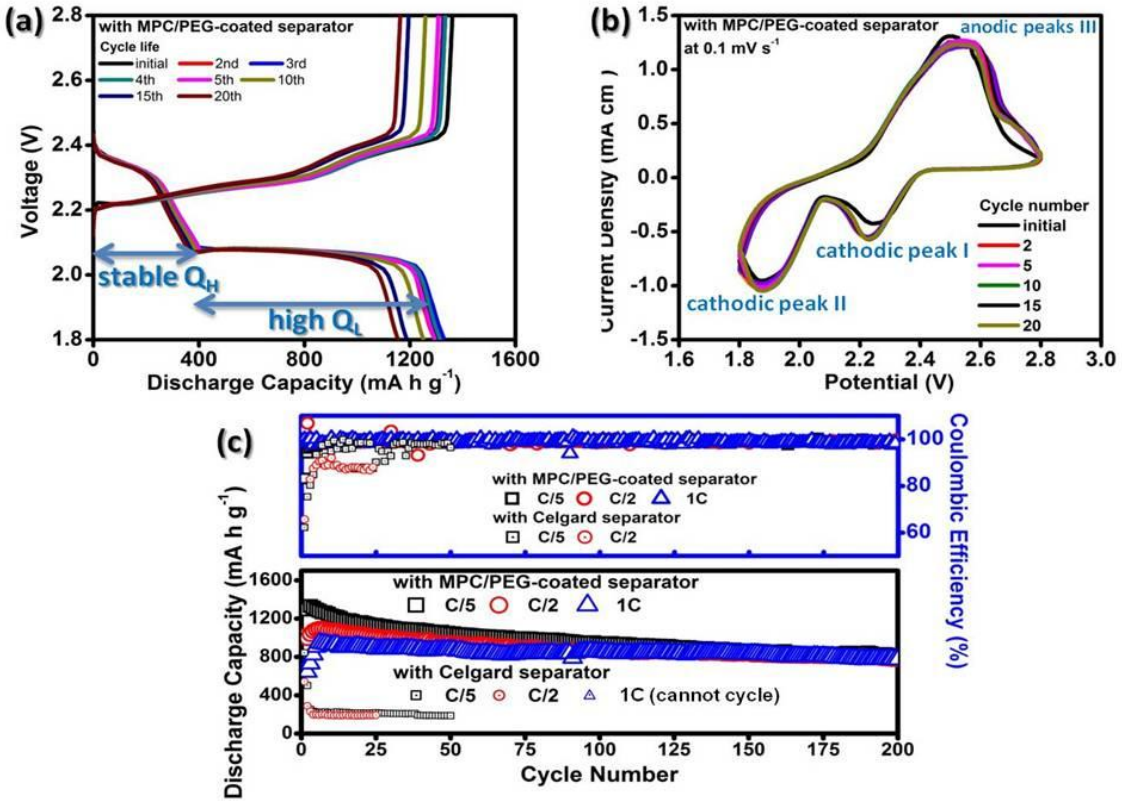

Figure 6.27: Electrochemical analyses of the lithium-sulfur cells with the MPC/PEG-coated separator: (a) discharge/charge curves, (b) CVs, and (c) cycle stability at various cycling rates.

6.3.3.4 Comparative analysis: cell configurations

To validate the potential of introducing the MPC/PEG-coated separator as an advanced cell configuration in lithium-sulfur cells, it is instructive to make a comparison with different cell configurations: (i) pure sulfur cathodes with the MPC-coated separator and (ii) sulfur-MPC composite cathodes with the Celgard separator.

Figures 6.26 and 6.28 show the SEM inspections of, respectively, cycled pure sulfur cathodes with the MPC-coated separator and cycled sulfur-MPC composite with the Celgard separator. The comparison between the cycled cathodes emphasizes the main advantage of the MPC/PEG-coated separator: the improved polysulfide-trapping capability. In Figure 6.29a, the surface of the cycled composite cathode is covered by aggregates (marked in white), which may result from the redeposition of the escaping polysulfide.[55, 176] This phenomenon implies that the polysulfides cannot be immobilized within the sulfur-MPC nanocomposite. As a result, the polysulfide diffusion causes an irreversible and rapid 260 mA h g^{-1} decrease in capacity during the initial cycles (Figure 6.30), which is commonly found in other composite cathodes. The MPC/PEG-coated separator that solves this rapid capacity fading may act as a better "containment building" for suppressing the "polysulfide leak."

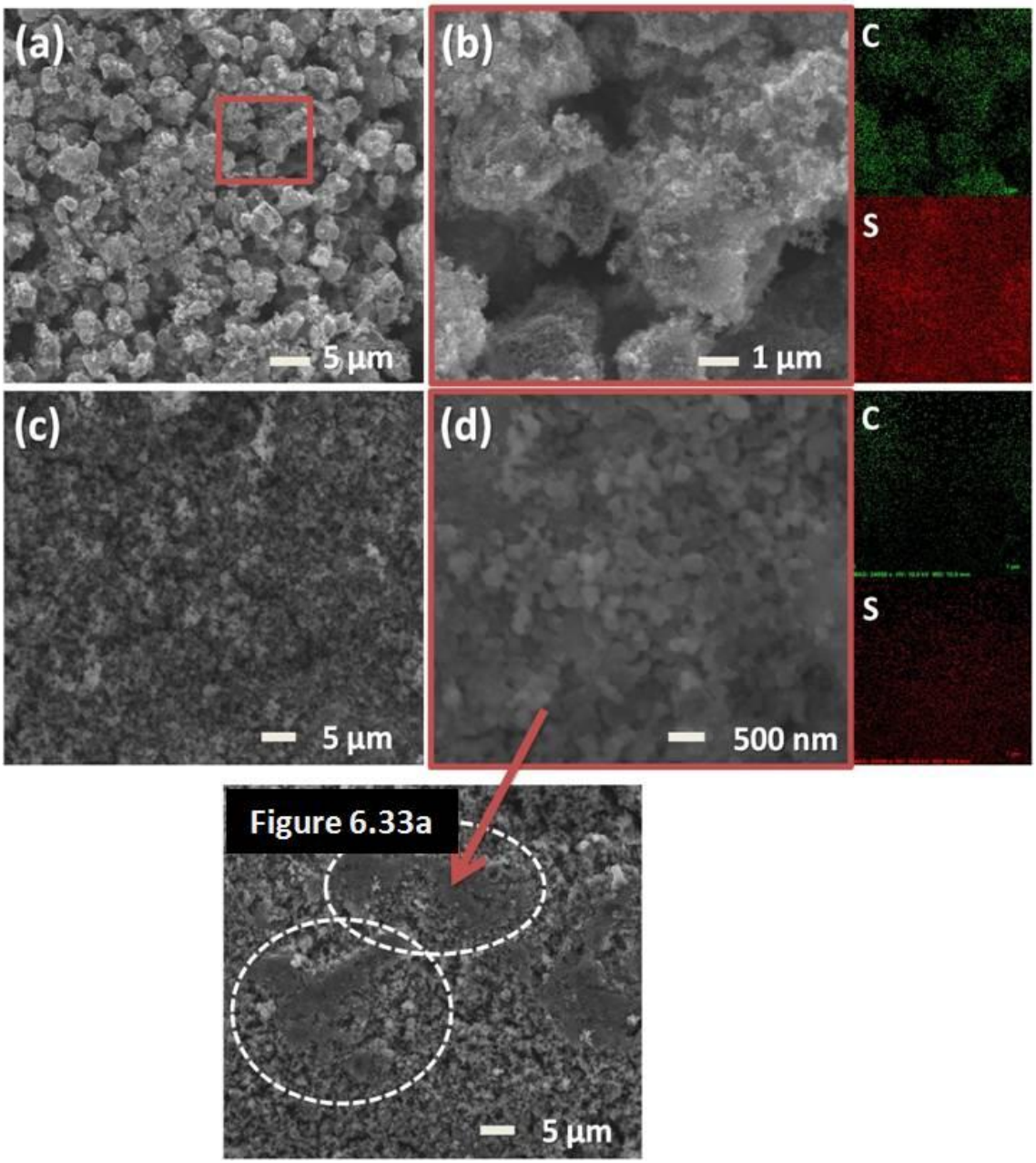

Figure 6.28: Low- and high-magnification SEM observation and elemental mapping of the sulfur-MPC nanocomposites. (a) Low magnification and (b) high magnification. SEM observation and elemental mapping of the sulfur-MPC composite cathode (c) before and (d) after cycling.

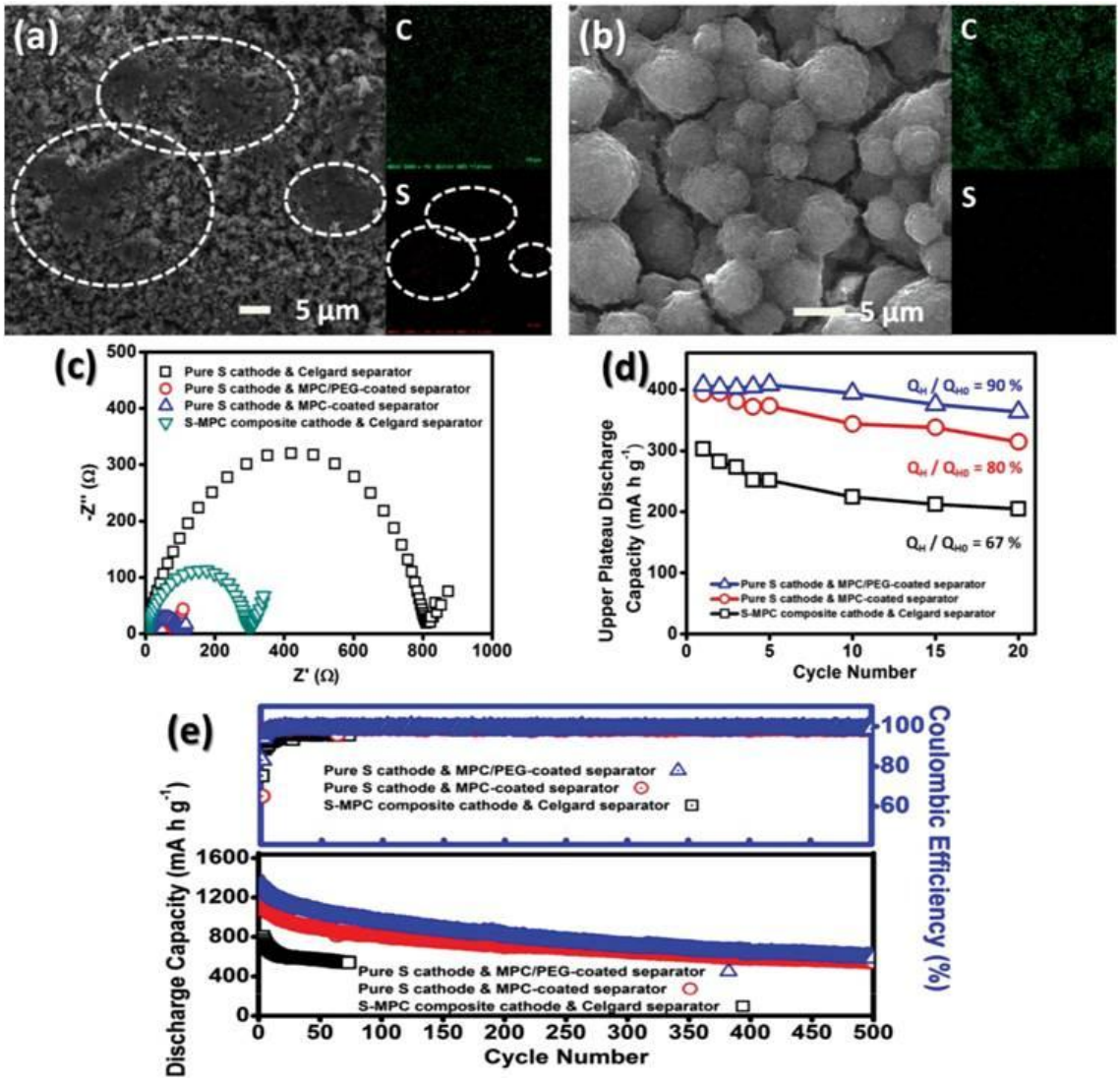

Figure 6.29: Comparison of the lithium-sulfur cell configurations utilizing a composite cathode, a MPC-coated separator, and a MPC/PEG-coated separator. SEM observation and elemental mapping: (a) cycled composite cathode and (b) the MPC-coated separator. Electrochemical analyses: (c) EIS data of the fresh cathode, (d) upper-plateau discharge capacities (Q_H), and (e) long-term cycle life at a C/5 rate.

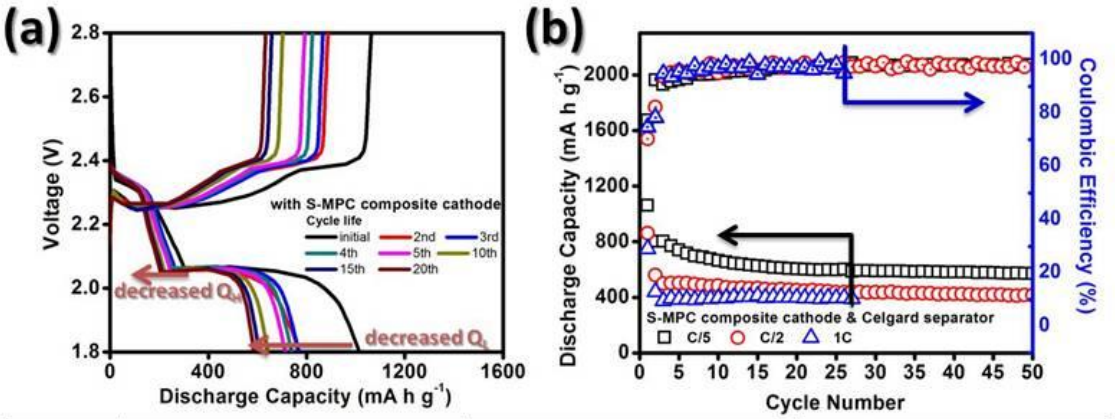

C-rates	Initial discharge capacity (sulfur utilization)	Reversible capacity (cycle number)	Capacity retention (Capacity fade rate)
C/5	1060 mA h g^{-1} (63 %)	570 mA h g^{-1} (50 cycles)	54 % (0.92 % per cycle)
C/2	861 mA h g^{-1} (51 %)	414 mA h g^{-1} (50 cycles)	48 % (1.04 % per cycle)
1C	749 mA h g^{-1} (45 %)	388 mA h g^{-1} (28 cycles)	52% (1.72 % per cycle)

Figure 6.30: Electrochemical analyses of lithium-sulfur cells with the sulfur-MPC composite cathode and the Celgard separator. (a) discharge/charge curves and (b) cycle stability at various cycling rates.

The functions of the PEG in the composite separator are two-fold. First, its physical functions are to improve the adhesion between the MPC/PEG coating and the Celgard separator and to bind the MPC clusters. Second, its chemical function is to anchor the migrating polysulfides within the cathode region.[13, 223, 246] Without PEG, the SEM of the MPC-coated separator demonstrates the presence of cracks that isolate MPC clusters (Figure 6.29b). The separator side of the MPC coating shows pores and cracks (Figure 6.31). These may decrease the physical absorption ability of the MPC clusters toward migrating polysulfides and, especially, the reactivation capability of the MPC coating toward the trapped active material. Furthermore, the MPC coating has no chemical trapping agents. Thus, although the cell with a MPC-coated separator exhibits good performance, its long-term cyclability is poor as compared with the cell with a MPC/PEG-coated separator, as summarized in Figure 6.32.

A comprehensive comparison of the electrochemical behaviors of these cell configurations explains how the MPC/PEG-coated separator facilitates the use of pure sulfur cathode. First, the electrochemical impedance spectroscopy (EIS) data of the cells with various configurations indicate that the MPC/PEG-coated separator decreases the charge transfer resistance (R_{ct}) of the cell from 810 to 79 Ω,[28, 174, 235] which is also lower than that of the sulfur-MPC composite cathodes (300 Ω) (Figure 6.29c). This demonstrates a significant decrease in the cathode resistance and implies excellent utilization of the active material. Second, in Figure 6.29d, the initial utilization of the upper plateau discharge capacity (Q_H = 419 mA h g^{-1}) increases from 72 % to 97 % after upgrading the cell configuration from the composite cathode to the MPC/PEG-coated separator. The Q_H analysis is a simple pre-assessment for the polysulfide diffusion because this upper plateau region corresponds to the formation of soluble polysulfides.[17, 154, 208] After 20 cycles, the cell with the MPC/PEG-coated separator retains 90% of its original value (Q^0_H: 416 mA h g^{-1}), which is the highest value compared with those of the other cell configurations. This Q_H analysis indicates that the MPC/PEG coating possesses an outstanding polysulfide-trapping capability and facilitates excellent reactivation of the trapped species. Finally, the cycling performance of the various cell configurations is summarized in Figure 6.29e and Table 6.1. The MPC/PEG-coated separator achieves a high initial discharge capacity of 1307 mA h g^{-1} and the highest reversible capacity, approaching 600 mA h g^{-1} after 500 cycles. The corresponding capacity fading is only 0.11 % per cycle. Such long lifespan and low capacity fading conclude that the MPC/PEG-coated separator facilitates high electrochemical reversibility with a pure sulfur cathode.

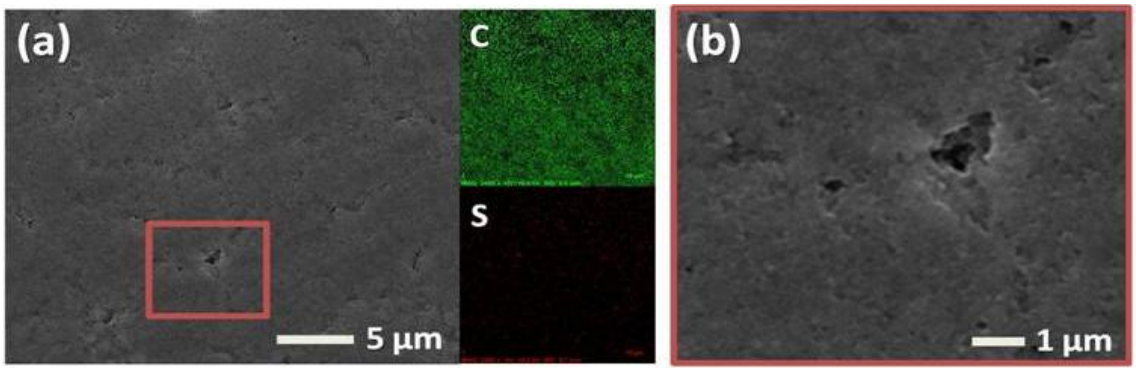

Figure 6.31: Low- and high-magnification SEM observation and elemental mapping of the separator side of the cycled MPC coating separator. (a) Low magnification and (b) high magnification.

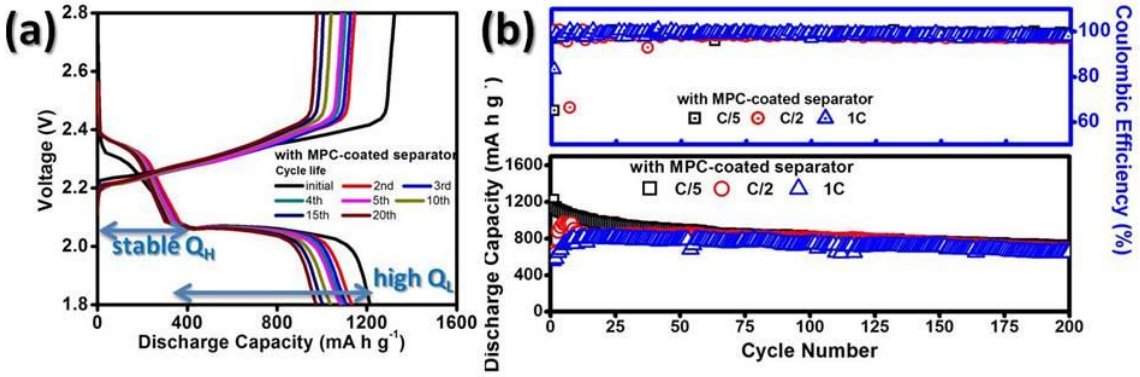

C-rates	Initial discharge capacity (sulfur utilization)	Reversible capacity (cycle number)	Capacity retention (Capacity fade rate)
C/5	1214 mA h g^{-1} (73 %)	707mA h g^{-1} (200 cycles)	58% (0.21 % per cycle)
C/2	641 mA h g^{-1} (38 %)	681 mA h g^{-1} (200 cycles)	70% (0.16 % per cycle)
1C	558 mA h g^{-1} (33 %)	646 mA h g^{-1} (200 cycles)	80% (0.10 % per cycle)

Figure 6.32: Electrochemical analyses of lithium-sulfur cells with a pure sulfur cathode and the MPC-coated separator. (a) Discharge/charge curves and (b) cycle stability at various cycling rates.

Table 6.1: Summarized battery parameters of the cells at a C/5 rate with different cell configurations.

Cell configuration	**Pure sulfur cathode Celgard separator**	**Pure sulfur cathode with MPC/PEG-coated separator**	**Pure sulfur cathode with MPC-coated separator**	**Sulfur-MPC composite cathode with Celgard separator**
Initial discharge capacity (sulfur utilization)	843 mA h g^{-1} (50 %)	1307 mA h g^{-1} (78 %)	1214 mA h g^{-1} (73 %)	1060mA h g^{-1} (63 %)
Cycle number	50 cycles	500 cycles	500 cycles	75 cycles
Reversible capacity	189 mA h g^{-1}	596 mA h g^{-1}	503 mA h g^{-1}	541 mA h g^{-1}
Capacity fade rate	1.5516 % per cycle	0.1088 % per cycle	0.1171 % per cycle	0.6528 % per cycle
R_{ct} of the cell	810.48 Ohms	79.09 Ohms	103.04 Ohms	300.11 Ohms

6.3.3.5 Carbon materials for the Comparative Analysis of Cell Configurations

A reliable comparison of the various high-performance cell configurations (the composite cathode and the composite separator) is a key factor to demonstrate that the functional separator could be a suitable method to suppress polysulfide diffusion. Thus, the comparative analysis in section 6.3.3.4 should use the same raw materials. Moreover, the selected materials in both cell configurations should have enhanced cell performance as compared to the pure sulfur cathodes. We use MPC as the carbon substrate because the S-MPC composite shows the most stable cyclability compared to other composite cathodes, as shown in Figure 6.33. We did not select other carbon substrates because of their limited improvement on the cycling performance for the composite cathodes, including the S-Super P (black) and S-MWCNT (dark cyan) nanocomposites. As a reference, Super P carbon and MWCNT were used in our previous carbon-coated separators. The previous work aimed at introducing a novel separator configuration and extending the functionalized separator preparation processes for various materials with different morphologies.

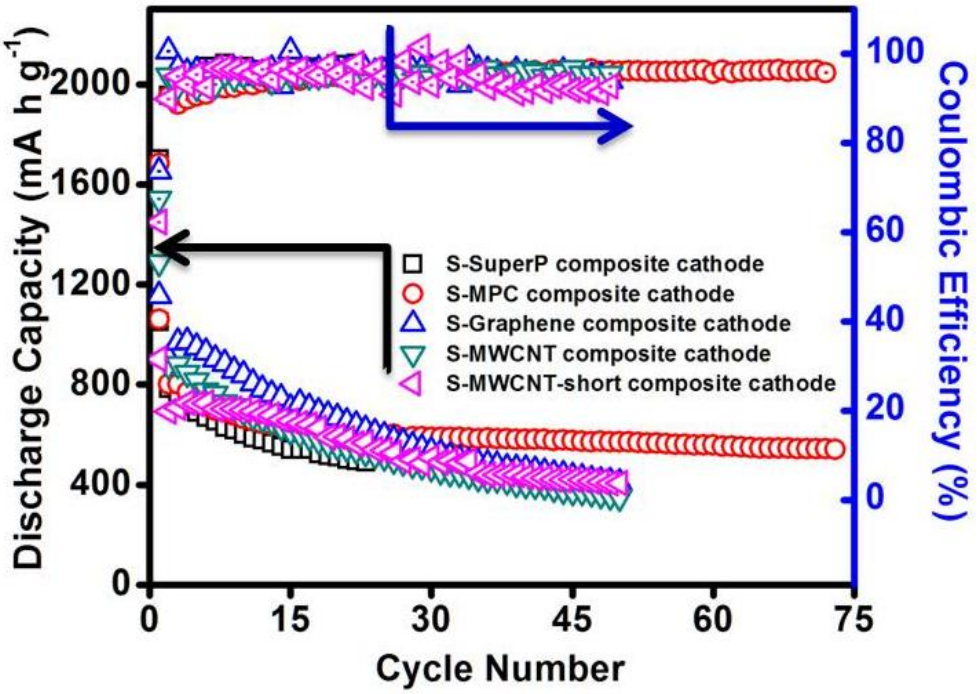

Figure 6.33: Cycling performance of various sulfur-based composite cathodes at a C/5 rate.

3.3.3.6 Summary

In summary, the MPC/PEG-coated separator is a practical solution for utilizing pure sulfur cathodes in lithium-sulfur cells that exhibit a high discharge capacity (1307 mA h g^{-1}), a long lifespan (500 cycles), and high reversibility (0.11 % capacity fade per cycle). The excellent cycle stability arises from two major factors: (i) the MPC/PEG coating physically and chemically traps the migrating polysulfides and (ii) the conductive polysulfide trap reactivates and reutilizes the immobilized active material. Moreover, the cells with the lightweight MPC/PEG-coated separator can utilize the readily-prepared pure sulfur cathodes, making this composite separator an advanced material for narrowing the gap between scientific research and commercial feasibility.

6.3.4 Functionalized separator: microporous ACNF-filter-coated separator for optimizing microstructure and materials characteristics

As a primary component in lithium-sulfur batteries, the separator may require a custom design in order to facilitate electrochemical stability and reversibility. Here, we present a custom separator with an activated carbon nanofiber (ACNF) filter coated on a polypropylene membrane. The entire configuration is comprised of the ACNF filter arranged adjacent to the sulfur cathode so that it can suppress the severe polysulfide diffusion during cell discharge. Four differently optimized ACNF-filter-coated separators have been developed with tunable micropores as an investigation into the electrochemical and engineering design parameters of functionalized separators. The optimized parameters that are verified by electrochemical and microstructural analyses require the coated ACNF filter to possess (i) a porous architecture with abundant micropores, (ii) small micropore sizes of 0.4 – 1.2 nm, and (iii) high electrical conductivity and effective electrolyte immersion. We found that the ACNF20-filter-coated separator demonstrates an overall superior boost in the electrochemical utilization (discharge capacity: 1270 mA h g^{-1}) and the polysulfide retention (capacity fading rate: 0.13 % per cycle after 200 cycles). These results show that using a modified thin-film-coating technique is a viable approach in designing ultra-tough ACNF-filter-coated separators with outstanding mechanical strength and flexibility as an advanced component in lithium-sulfur cells.

6.3.4.1 Functionalized separator optimization

In this work, we present a series of activated-carbon nanofiber-filter-coated separator (ACNF-filter-coated separator) as the electrochemical testing platform. We first explored the impact of the surface area, porosity, and pore size that the carbon-filter coatings have on polysulfide-trapping capability. Then, we investigated the effective electrical conductivity of the filter coatings toward polysulfide reutilization. It is found that ACNF-filter coatings with a higher microporosity and small micropore sizes of 0.4 – 1.2 nm effectively filter out the migrating polysulfides. More importantly, we improved the mechanical strength of the carbon-coated separator by strengthening the adhesion

between the coating layer and the polypropylene membrane. These developments are necessary in order to promote the functionalized separator as an advanced energy material towards a better lithium-sulfur cell.

6.3.4.2 Morphology of the ACNF-filter-coated separators

In Figure 6.34a and 6.34b, ACNF-filter-coated separators demonstrate a uniform ACNF filter coated onto the surface of a polypropylene membrane. In Figures 6.34c and 6.34d, after being either folded or fully crumpled, the ACNF-filter-coated separators are able to retain their original shapes. The coated ACNF filter did not flake or peel under stress and remained strongly adhered onto the polypropylene membrane. This demonstrates that the ACNF filter and the ACNF-filter-coated separator have excellent flexibility and outstanding mechanical strength. The applied ACNFs were fabricated by an electrospinning process (by Drexel University) and then activated with varying concentrations of potassium hydroxide (KOH) in order to adjust their surface area and porosity by permeating the conductive carbon hosts with tunable nanopores (from micropores to mesopores). Thus, ACNFs with different levels of activation were denoted as ACNF01 (before activation), ACNF20 (20 wt. % KOH activation), ACNF40 (40 wt. % KOH activation), and ACNF60 (60 wt. % KOH activation).

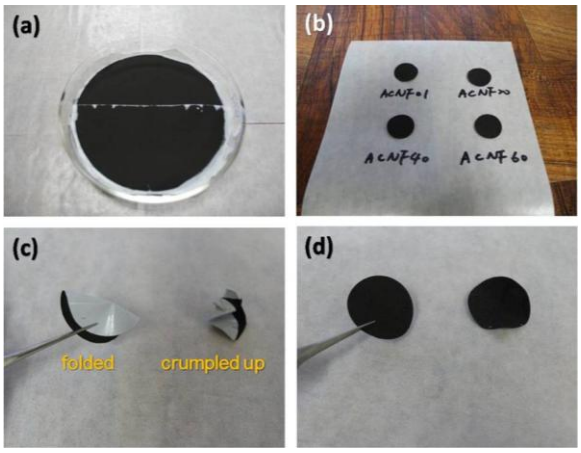

Figure 6.34: Digital images of ACNF-filter-coated separators: (a, b) ACNF-filter-coated separators, (c) folded/crumpled ACNF-filter-coated separators, and (d) recovered ACNF-filter-coated separators.

6.3.4.3 Microstructure and porosity analyses

The SEM images of ACNF01s and its corresponding EDX analysis indicate that ACNF01s have a non-woven nanofibrous network consisting of long carbon nanofibers, as shown in Figure 6.35. After alkali activation, ACNF20s, ACNF40s, and ACNF60s attain the same porous carbon nanofiber network, as shown in Figure 6.36. Fourier transform infrared spectroscopy (FTIR) shows similar spectra among the compared ACNFs (Figure 6.37), indicating that the chemical characteristics of various ACNF filters are similar. Hence, the physical characteristics of the ACNF filters are the predominant factors responsible for improvements in the polysulfide-trapping capability.

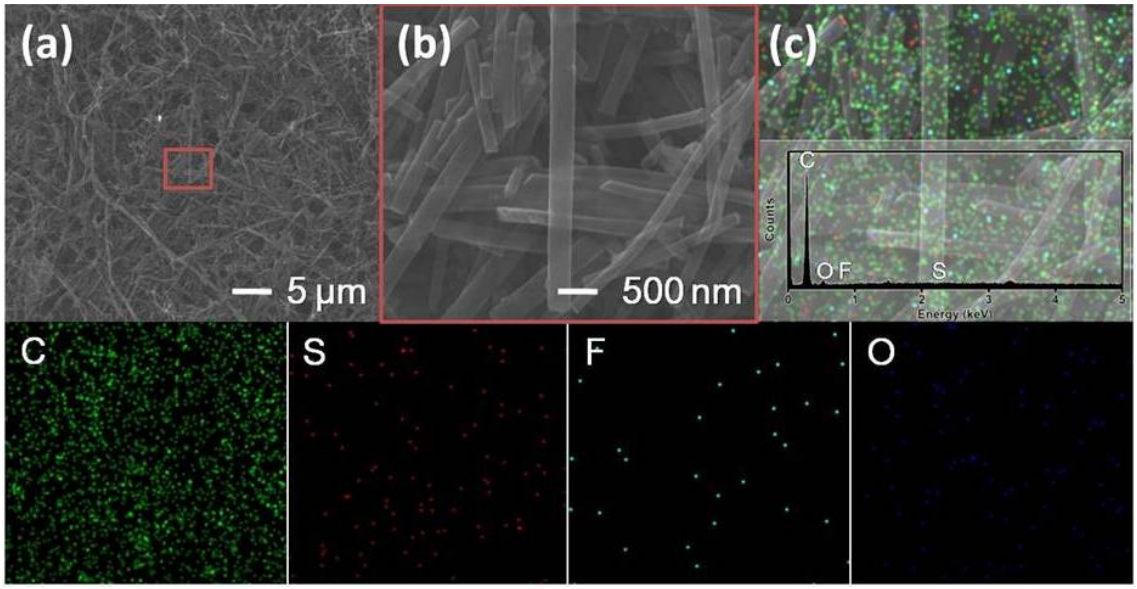

Figure 6.35: Microstructural analysis of ACNF01s: (a) low magnification inspection, (b) high magnification inspection of (a), and (c) corresponding EDX analyses and elemental mapping of (b).

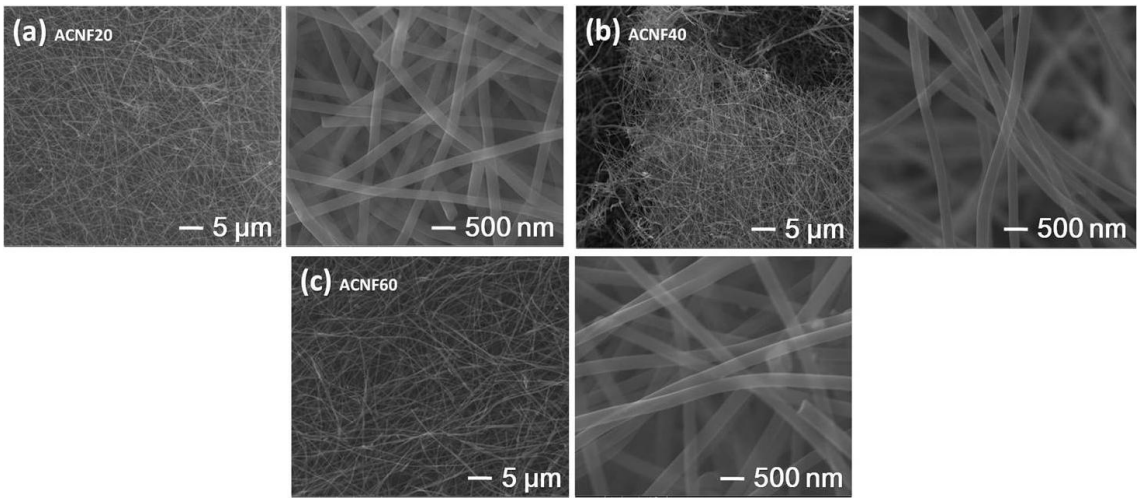

Figure 6.36: Microstructural analysis of ACNFs: (a) ACNF20, (b) ACNF40, and (c) ACNF60.

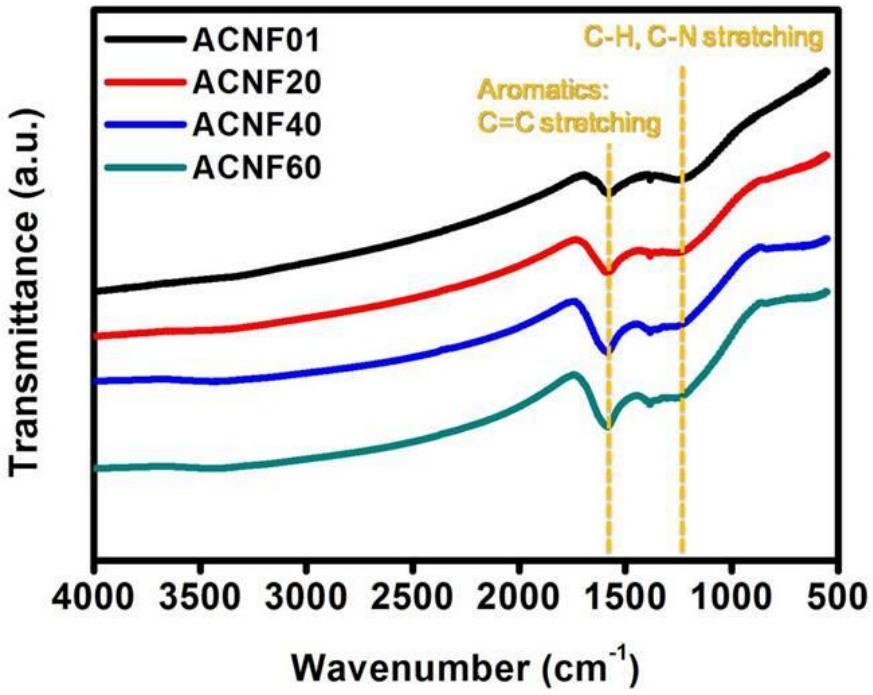

Figure 6.37: Fourier transform infrared spectra of various ACNFs.

The Brunauer-Emmett-Teller (BET) method measures the high surface area of ACNFs. The surface area (with the micropore surface area and the micropore size in parentheses) of ACNF01s, ACNF20s, ACNF40s, and ACNF60s are, respectively, 313 $m^2 g^{-1}$ (163 $m^2 g^{-1}$; 1.18 nm), 641 $m^2 g^{-1}$ (436 $m^2 g^{-1}$; 1.17 nm), 744 $m^2 g^{-1}$ (384 $m^2 g^{-1}$; 1.46 nm), and 1079 $m^2 g^{-1}$ (292 $m^2 g^{-1}$; 1.64 nm). The surface area increases in trend with the increase of the alkali-activated level from ACNF01s to ACNF60s. The increase in the micropore surface area from ACNF01s to ACNF20s reveals that the base solution corrodes ACNF01s and decorates the carbon host with an abundant amount of micropores. As the alkali-activation level increases, the higher concentrations of KOH may corrode the newly formed micropores into larger micropores and mesopores. As a result, the surface areas of ACNF40s and ACNF60s keep increasing while the detected micropore surface areas start to decrease. The tendency of the surface-area changes is summarized in Figure 6.38.

Figure 6.38 summarizes the microstructural analyses of ACNFs. Figure 6.39a displays the nitrogen adsorption-desorption isotherms. The IUPAC type I isotherm at $P/P_0 < 0.1$ shows that the microporosity increases significantly after initial KOH activation (as shown in ACNF20s) and then eases as the concentration of KOH further increases (as observed in ACNF40s and ACNF60s).[182] These analyses are in accordance with the micropore surface area measurement as shown in Figure 6.38. The tail at P/P_0 around 1.0 shows that ACNF01s possess a long-range porous network (macropores) and also indicates that the same continuous porous architecture exists in ACNF20s, ACNF40s, and ACNF60s. [182] In Figure 6.39b, broad pore-size distributions evaluated by the Barrett-Joyner-Halenda (BJH) method shows no newly added large mesopores (pore size > tens of nanometers) or macropores (pore size > 50 nm).

The micro-/meso-pore-size distribution was analyzed with density functional theory (DFT, Figure 6.39c) and the Horvath-Kawazoe model (HK, Figure 6.39d). In Figure 6.39c, the comparison between ACNF01s and ACNF20s demonstrate that micropore peaks in the regions below 0.8 nm and between 1.0 – 1.1 nm appear to

increase after initial alkali activation. With increasing KOH concentrations, ACNF40s and ACNF60s show an increase of micropores sizes with the pore size larger than 1.4 nm. Additionally, there is the appearance of new micropore peaks at 1.8 nm and new mesopores between 2.4 nm (ACNF40s) and 2.7 nm (ACNF60s). In Figure 6.39d, the HK micropore analyses show high microporosity in ACNF20s. In the HK model micropore distribution analyses, the detected micropore sizes enlarge with the increase in KOH concentration. Also, the pore size distribution analyses in Table 6.2 and the ratio of the micropores surface area to the total pore surface area in Figure 6.38 are consistent with this trend. Furthermore, the pore sizes of the ACNFs seem to be perfectly controlled in the range from micropores to small mesopores (less than 5 nm). Therefore, the ACNFs are suitable for investigating the influence of the micro-/meso-porous structure toward polysulfide-trapping capacity and battery performance.

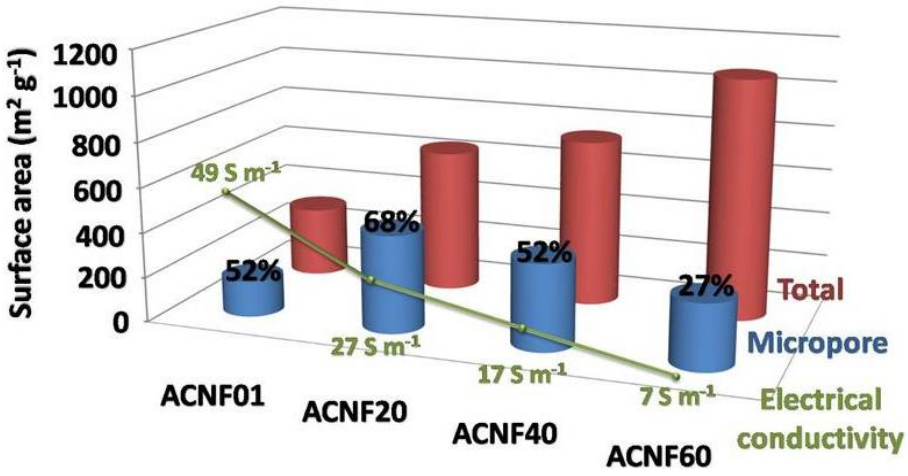

Figure 6.38: Physical characteristics of ACNFs: (red) total pore surface area (red), micropore surface area (blue), and electrical conductivity (green).

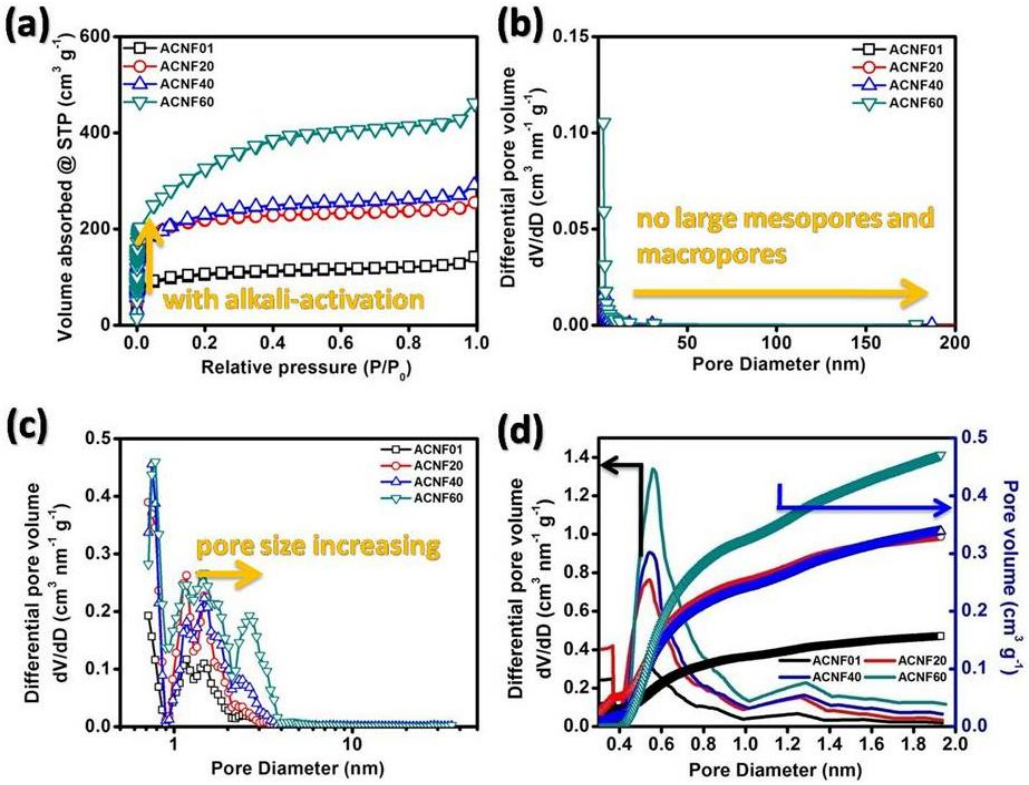

Figure 6.39: Porosity analyses of ACNFs: (a) isotherms, (b) pore-size distributions using the Barrett-Joyner-Halenda (BJH) method, (c) micro-/meso-pore-size distributions using the density functional theory (DFT) methods, and (d) micropore-size distributions using the Horvath-Kawazoe (HK) model.

Table 6.2: Properties of the ACNFs

	ACNF01	ACNF20	ACNF40	ACNF60
Electrical conductivity (S m^{-1})	49.03	26.75	16.72	6.69
Surface area ($m^2 g^{-1}$)	312.81	640.76	744.49	1069.60
Total pore volume ($cm^3 g^{-1}$)	0.22	0.39	0.45	0.82
Average pore size (nm)	2.49	2.46	2.67	3.08
Micropore surface area ($m^2 g^{-1}$)	162.51	435.64	384.22	291.96
Micropore volume ($cm^3 g^{-1}$)	0.13	0.30	0.28	0.28
Micropore size (nm)	1.18	1.17	1.46	1.64

6.3.4.4 Morphology and microstructure of the ACNF-filter coating

Figure 6.40 (in-plane SEM inspection) shows the microstructural inspection of ACNF filters of various ACNF-filter-coated separators. The low (left) and high (right) magnification SEM observation depicts that long and curved ACNFs were uniformly deposited as a bundled/porous filter on the Celgard separator to form ACNF filters. The coalescing ACNFs have a diameter of 200 ± 20 nm with a length of several micrometers. The alkali-treated ACNFs have a more porous surface than untreated ACNF01s.

In a corresponding cross-section SEM inspection (Figure 6.41), ACNF filters have similar thicknesses (~ 25 μm) and attain a good interfacial adhesion with the polypropylene membrane. This amount of desired adhesion guarantees outstanding flexibility and durability of the ACNF-filter-coated separator. Furthermore, the ACNF filter that is coated on the functionalized separator is pointed toward the sulfur cathode. Because of this, during cell discharge, the ACNF filter is able to intercept the dissolved polysulfides that are driven from the cathode side toward the anode side due to the chemical potential and concentration difference (Figure 6.40e).[11, 12] In addition, the porous ACNF filter possesses enough channels for effective electrolyte immersion (Figure 6.42) while its fibrous carbon network yields high electrical conductivity for fast electron transfer, which effectively reactivates the immobilized active material during cycling.[18, 154, 173, 208]

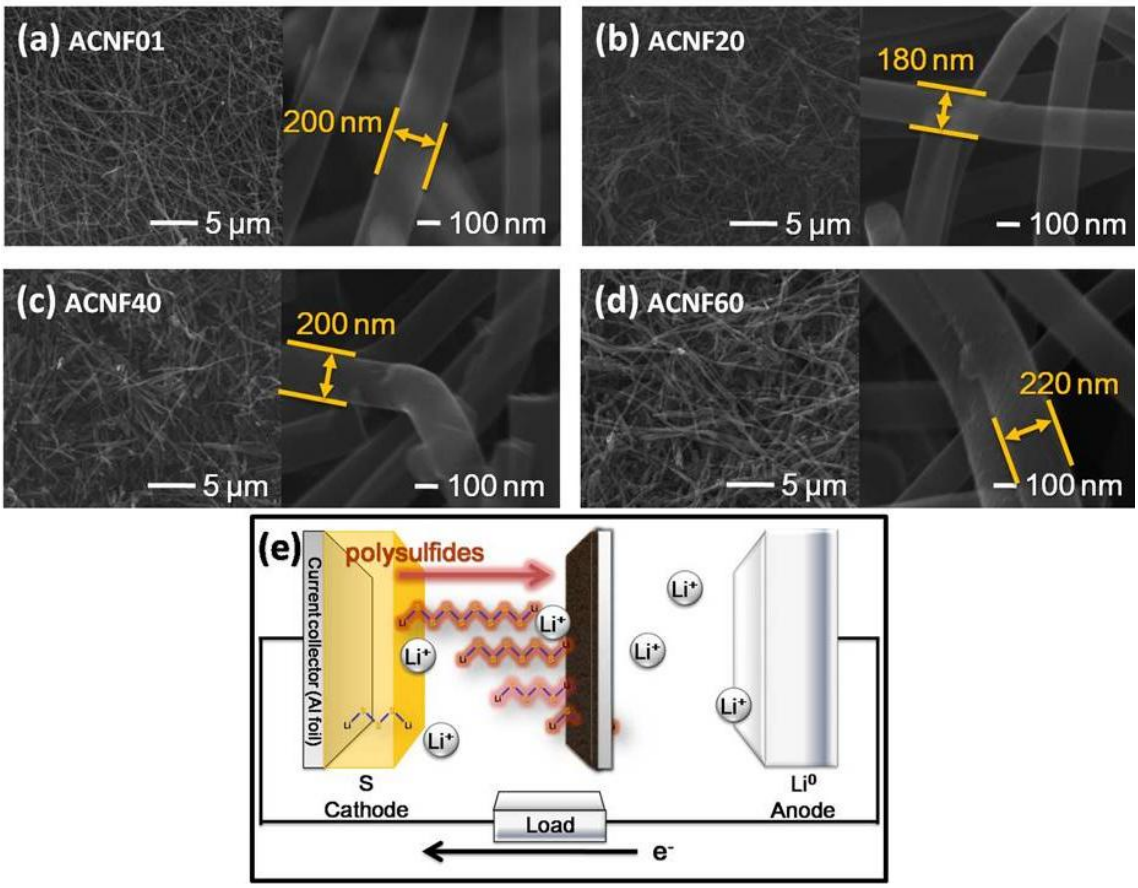

Figure 6.40: Microstructural analysis of various ACNF-filter-coated separators: (a) ACNF01, (b) ACNF20, (c) ACNF40, and (d) ACNF60. (e) Schematic configuration of a lithium-sulfur cell with the ACNF-filter-coated separator for filtering out the polysulfides during cell discharge.

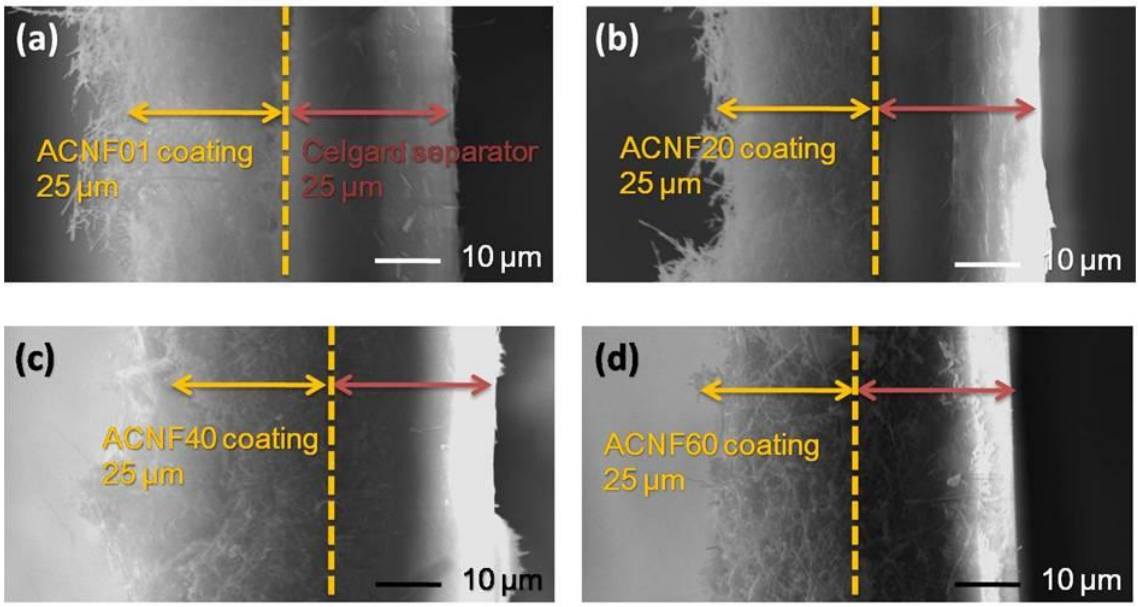

Figure 6.41: Cross-section SEM inspection of ACNF-filter-coated separators: (a) ACNF01, (b) ACNF20, (c) ACNF40, and (d) ACNF60.

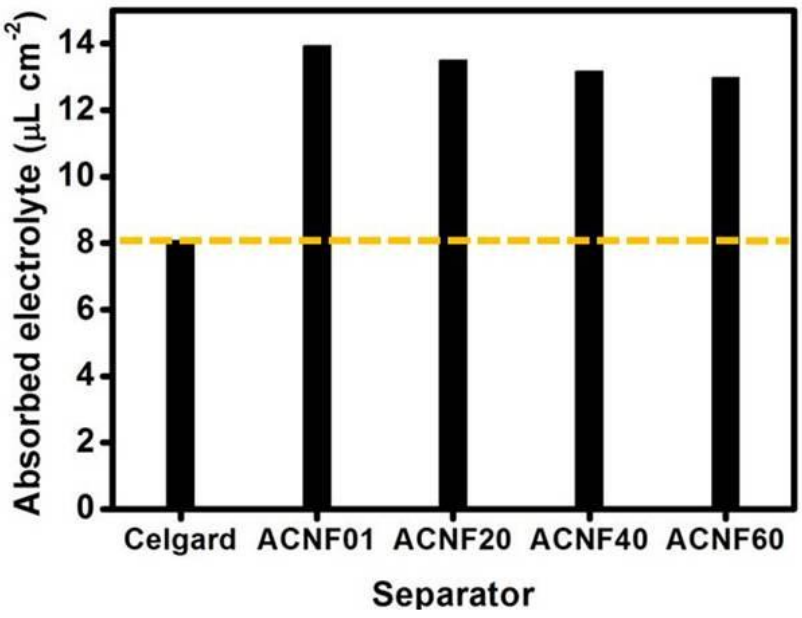

Figure 6.42: Electrolyte absorption tests of various separators.

It is well known that a porous carbon substrate with high surface area and large pore volume is important for composite cathodes.[61, 70, 80-83, 138, 189, 200, 234, 247] The high porosity of the carbon substrate provides the composite cathode with an abundant amount of sulfur-encapsulation space and a high reaction surface area. In contrast, the key factor for a polysulfide filter is having many decorated nanopores on the carbon filter to inhibit the diffusion of polysulfides. The polysulfide-trapping mechanism is primarily dependent on congruent molecular sizes between the polysulfides (1.0 – 1.8 nm) and the micropores (less than 2.0 nm).[99, 174, 244, 248] Because of this, ACNF20s, which have the greatest microporosity and smallest size micropores (less than 1.1 nm), are found to be the most functional polysulfide filter among the compared ACNFs. Along with inhibiting the polysulfide migration, there also needs to be an effective reutilization of the trapped active material. Table 6.2 and Figure 6.38 demonstrate the high electrical conductivity of ACNF20s, which facilitates electron transport to reactivate and convert the trapped redox intermediates.[60, 142, 176, 210, 228] However, further increase in the alkali concentration spawns defects throughout the conductive fibrous network, which causes a slight decrease in the electrical conductivity of ACNF40s and ACNF60s.

6.3.4.5 Electrochemical analyses

Figure 6.43 shows the improved electrochemical activity due to the application of ACNF-filter-coated separators in cells. Figure 6.43a displays the electrochemical impedance spectroscopy (EIS) of cathodes before cycling with a conventional separator and with ACNF-filter-coated separators. It is evident that the charge-transfer resistance decreases among cells that employ ACNF-filter-coated separators. The improved electronic and ionic conductivity mainly results from the conductive and porous ACNF filter that provides additional electron/Li^+-ion pathways and continuous electrolyte channels for insulating pure sulfur cathodes.[15, 53] Therefore, pure sulfur cathodes achieve improved electrochemical kinetics with the application of ACNF-filter-coated separators.[99, 169, 208]

To provide support to this statement, the initial discharge-charge curves of ACNF-filter-coated separators are compared in Figure 6.43b. The initial redox process involves the activation of bulk-sized sulfur particles and the subsequent rearrangement of the redox intermediates.[10, 17, 30, 249] The upper-discharge plateau at 2.35 V represents the reduction of sulfur to long-chain polysulfides, which has a theoretical upper-plateau discharge capacity (Q_H) of 419 mA h g^{-1}.[11, 17, 23, 53, 193] The experimental values of Q_H show that the ACNF20 filter (with the Q_H utilization in parentheses, 99 %) and the ACNF40 filter (95 %) have higher utilization than that of the ACNF01 filter (91 %) and the ACNF60 filter (90 %). The high Q_H utilization is indicative of the suppressed polysulfide migration and the effective electrochemical conversion.[17, 208] The lower discharge plateau at 2.05 V represents the reduction from long-chain polysulfides to Li_2S_2/Li_2S.[17] The ACNF20-filter coating attains the highest Q_L utilization due to two possible reasons. First, the ACNF20 filter has the best polysulfide-trapping capability due to its high microporosity and hence stabilizes more polysulfides in the cathode region of the cell as compared with the other ACNF filters.[28, 72, 99] Second, the high electrical conductivity of the ACNF20 filter efficiently utilize the localized redox intermediates for the subsequent electrochemical conversion reaction.[173, 174, 208] The two continuous charge plateaus at 2.30 and 2.40 V represent the reversible oxidation reaction from Li_2S_2/Li_2S to Li_2S_8/S.[11, 23, 53] The sharp voltage increase from 2.50 to 2.80V is indicative that the cells are charged completely.[33]

The electrochemical cyclability of cells applying ACNF-filter-coated separators is shown in Figure 6.43c. The initial discharge capacities (with the sulfur utilization in parentheses) of cells employing ACNF01, ACNF20, ACNF40, and ACNF60 filters are, respectively, 993 mA h g^{-1} (59 %), 1270 mA h g^{-1} (76 %), 1179 mA h g^{-1} (71 %), and 1047 mA h g^{-1} (63 %). After 50 cycles, the capacity retention rates are 67 %, 81 %, 81 %, and 80%. The increase in capacity retention can, therefore, be attributed to the introduction of micropores into the ACNF filter. The EIS of the cycled cells demonstrates that the cell with ACNF20 filters has the lowest cell impedance, as shown in Figure 6.43d

The low cell resistance contributed by the ACNF20-filter coating leads to fast and reversible conversion reaction as well as the highest reversible discharge capacity of 1024 mA h g^{-1} as compared with that provided by other ACNFs-filter coatings. Therefore, the high electrochemical utilization and capacity retention of the ACNF20-filter-coated separator reaffirms that the high microporosity, small micropores, and good electrical conductivity of the ACNF20 filter are important for high reversibility.[99, 174, 244, 248]

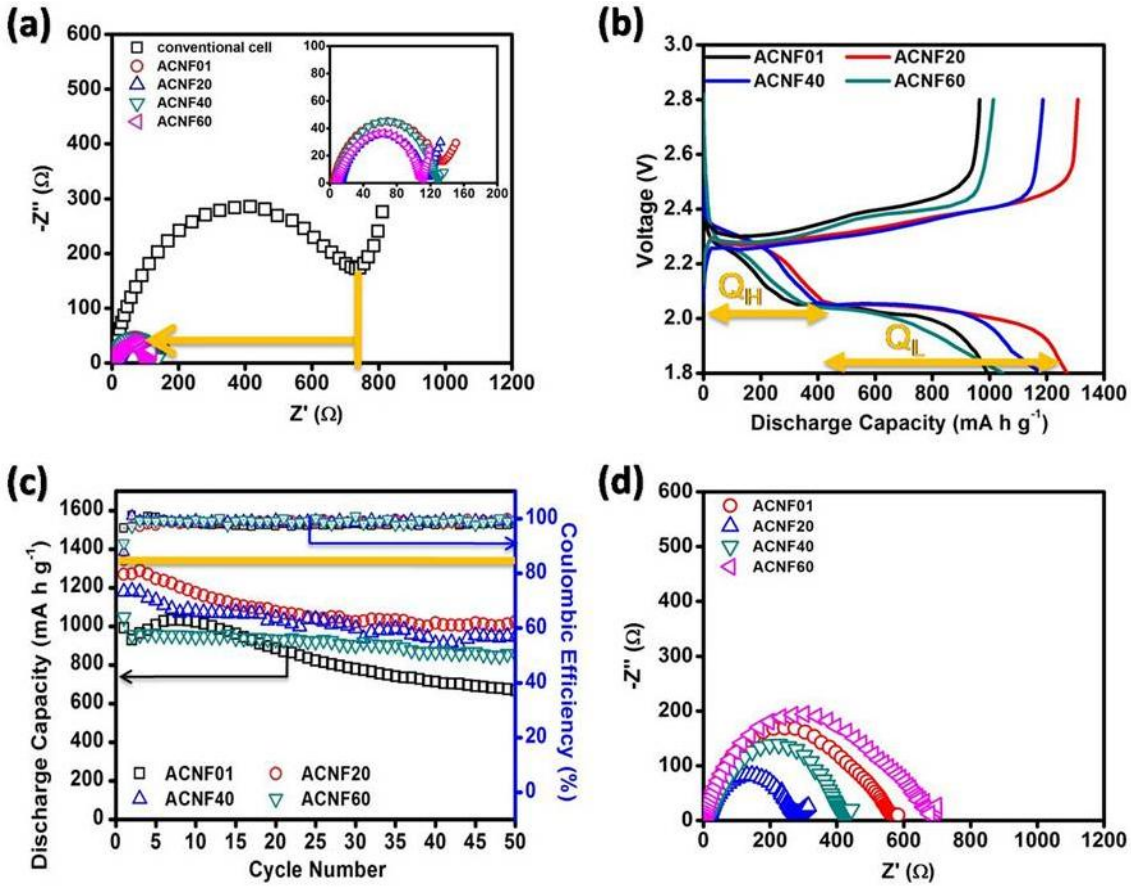

Figure 6.43: Electrochemical measurements of lithium-sulfur cells employing various ACNF-filter-coated separators: (a) EIS of fresh cells, (b) initial discharge-charge curves, (c) cyclability, and (d) EIS of cycled cells.

6.3.4.6 Discharge-charge stability analysis

Figure 6.44 shows the discharge-charge profiles of cells employing various ACNF-filter-coated separators. The cell configured with the ACNF01-filter-coated separator shows shrinkage of both the upper and lower discharge plateaus and an increase in polarization (ΔE) from 0.33 to 0.49 V after 50 cycles. This is attributed to the loss of active material and the formation of nonconductive Li_2S_2/Li_2S agglomerates on the surface of the electrodes.[17, 33, 152] Thus, this demonstrates the need for micropores decorated on the coated ACNF filter in order to effectively curb the free migration of polysulfides.[15, 99, 174] Accordingly, cells configured with microporous ACNF20- and ACNF40-filter-coated separators display low ΔE values of 0.24 and 0.26 V as well as overlapping discharge-charge curves after 50 cycles as expected. The high electrochemical reversibility indicates that the rearranged active material gravitates towards the electrochemically favorable sites and is stabilized in the cathode by the ACNF-filter configuration. The cell using the ACNF60-filter-coated separator displays overlapping discharge-charge curves with a ΔE of 0.32 V. The slight increase in ΔE as compared to that of ACNF20 and ACNF40 mainly results from the relatively lower conductivity of ACNF60s, leading to slower kinetics during the redox reaction. The incomplete reactivation of the trapped active material builds up gradually, eventually becoming a detrimental barrier that blocks electrolyte and electron pathways in the ACNF60 filter.[154, 169, 208]

In Figure 6.44e, the Q_H analysis is a pre-assessment for evaluating the polysulfide-trapping capability in new cathode designs.[99, 154, 208] A comparison among the initial Q_H and reversible Q_H values in the initial several cycles gives an idea of the successfulness of polysulfide retention. The upper plateau region corresponds to the formation and the subsequent diffusion of soluble polysulfides.[17, 250] The analytical results demonstrate that the cell employing the ACNF20-filter-coated separator attains high cycle reversibility due to their high microporosity, abundant amount of small micropores, and good electrical conductivity, as evidenced in the previous two sections.

To support these results, we look at the battery performance of these conductive, porous ACNF filters.

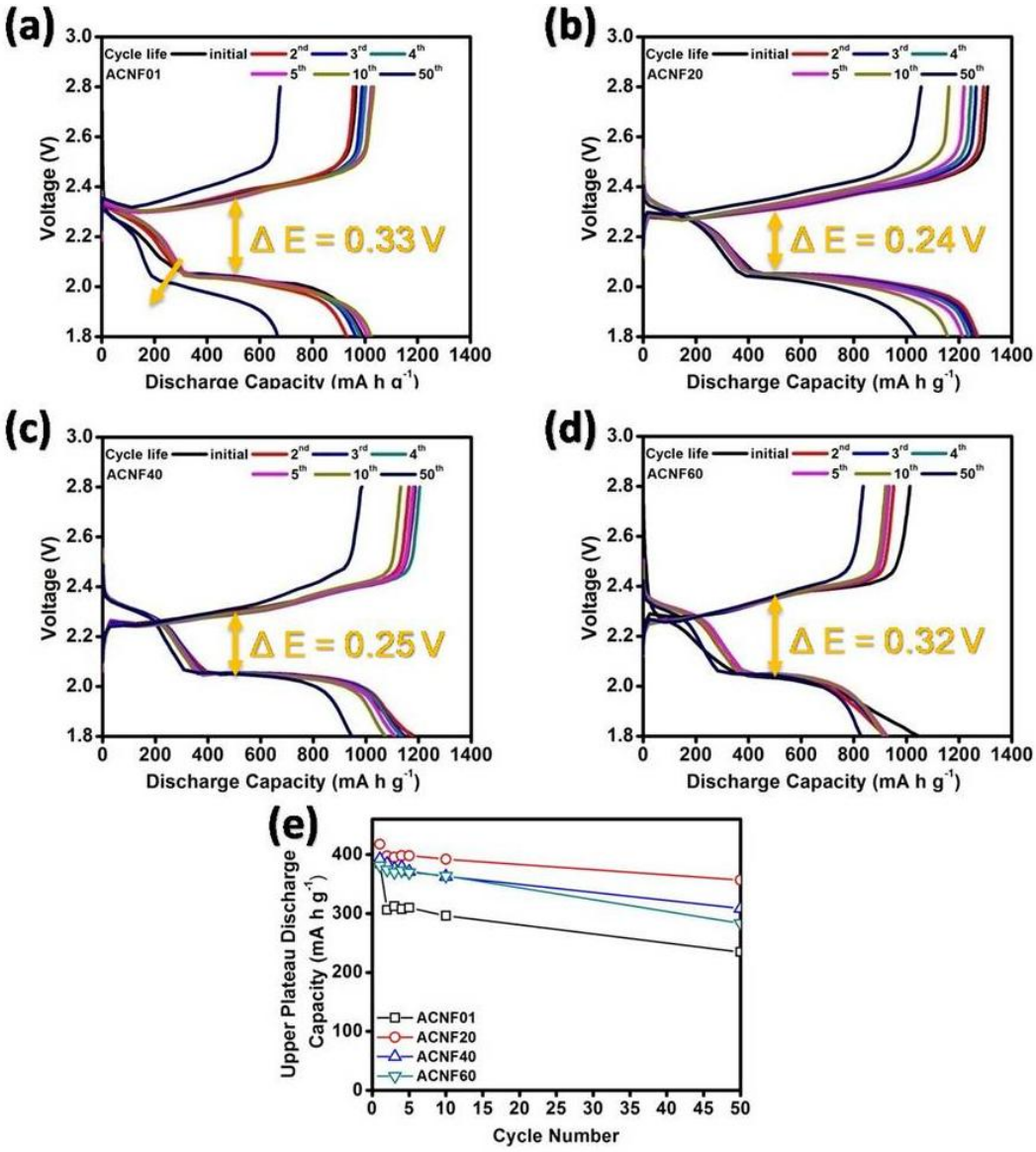

Figure 6.44: Discharge-charge of lithium-sulfur cells employing various ACNF-filter-coated separators at a C/5 rate: (a) ACNF01, (b) ACNF20, (c) ACNF40, and (d) ACNF60. (e) Upper plateau discharge capacities of cells employing different separators.

6.3.4.7 Battery performance

Figure 6.45a and 6.45b compares the cycling performance of cells configured with various ACNF-filter-coated separators at a C/5 rate. The cell fabricated with the ACNF01-filter-coated separator has a reversible discharge capacity of 422 mA h g^{-1} with a corresponding capacity fading rate of 0.17 % per cycle after 200 cycles. This performance is better than that of the cell with a conventional cell configuration.

The application of the ACNF20-filter-coated separator in cells increases the reversible capacity to 819 mA h g^{-1} with an improvement in the capacity fading rate of 0.13 % per cycle after 200 cycles. The reversible discharge capacities for ACNF40- and ACNF60-filter-coated separators are, respectively, 721 and 552 mA h g^{-1} after 200 cycles. The ACNF40- and ACNF60-filter-coated separators fail to demonstrate further improvement in the capacity retention due to their enlarged micropores and added mesopores. During longer cycling times, these factors tend to allow polysulfides to gradually diffuse out from the sulfur cathodes and thus inhibit good capacity retention. The electrochemical utilization slightly decreases from ACNF40s to ACNF60s, which may be caused by the decrease of their electrical conductivity. Figures 6.45c and 6.45d show battery performances of the same cell configurations but cycled at a C/2 rate. Capacity fading rates with the ACNF01-, ACNF20-, ACNF40-, and ACNF60-filter-coated separators are, respectively, 0.16 %, 0.08 %, 0.11 %, and 0.11 % per cycle after 200 cycles. The overall cycle stability improves at a high cycling rate due to the fact that dissolved polysulfides have less time to either form or diffuse out from the cathode and escape from the ACNF filter through the separator.

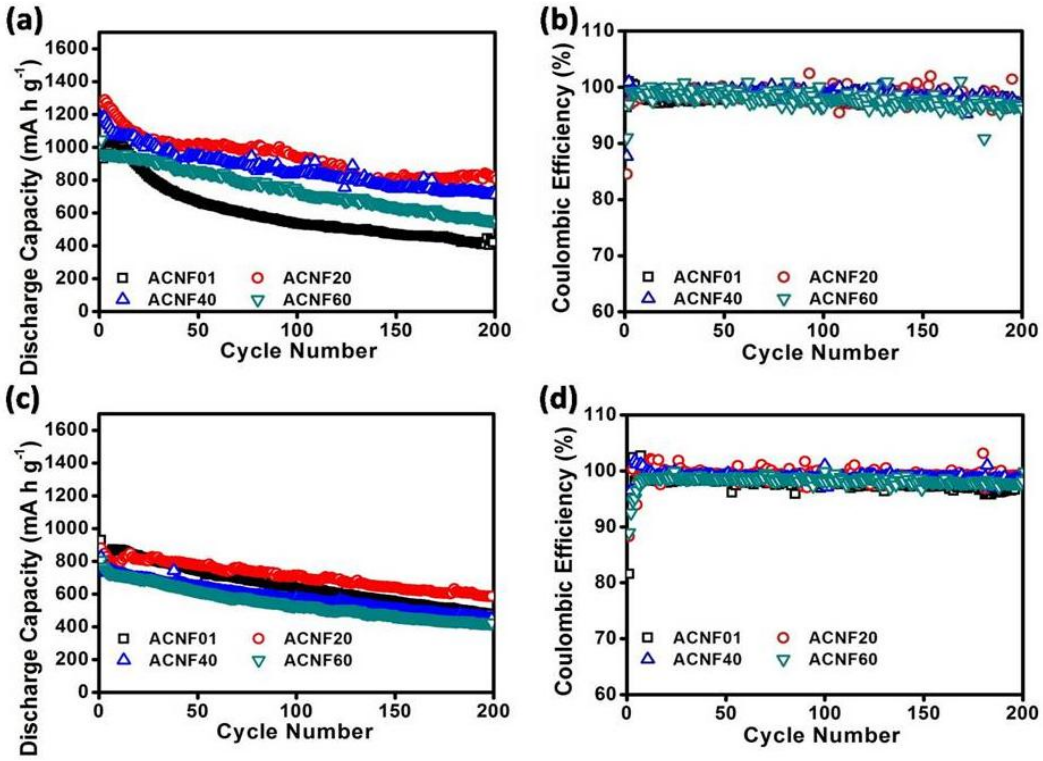

Figure 6.45: Performances of lithium-sulfur cells employing various ACNF-filter-coated separators at (a, b) C/5 and (c, d) C/2 rates.

It was found that the ACNF20 and ACNF40 filters displayed an improved electrochemical performance at a C/5 rate. At a C/2 rate, the cell employing ACNF20-filter-coated separators demonstrated better performance than the cell with the ACNF40-filter-coated separator. The limited enhancement of the highly porous ACNF40 filter is possibly attributed to its relatively low electrical conductivity, leading to a greater increase in polarization ($\Delta E = 0.45V$) and a decrease in sulfur reutilization at a C/2 rate. This indicates that the fast charge-transport ability of the ACNF filter is important for higher cycling rates.[28, 99, 107, 169, 251] The corresponding discharge-charge profiles and Q_H analyses of the cells agree with these statements, as summarized in Figure 6.46. Thus, the electrochemical characteristics of cells and their corresponding cell performances allow us to draw the following conclusions: (i) A high-performance functionalized separator

requires a highly microporous substrate; (ii) the small micropore sizes of 0.4 – 1.2 nm; and (iii) the porous filter coating should have good electrical conductivity in order to maintain high reutilization of the trapped active material and good rate performance.

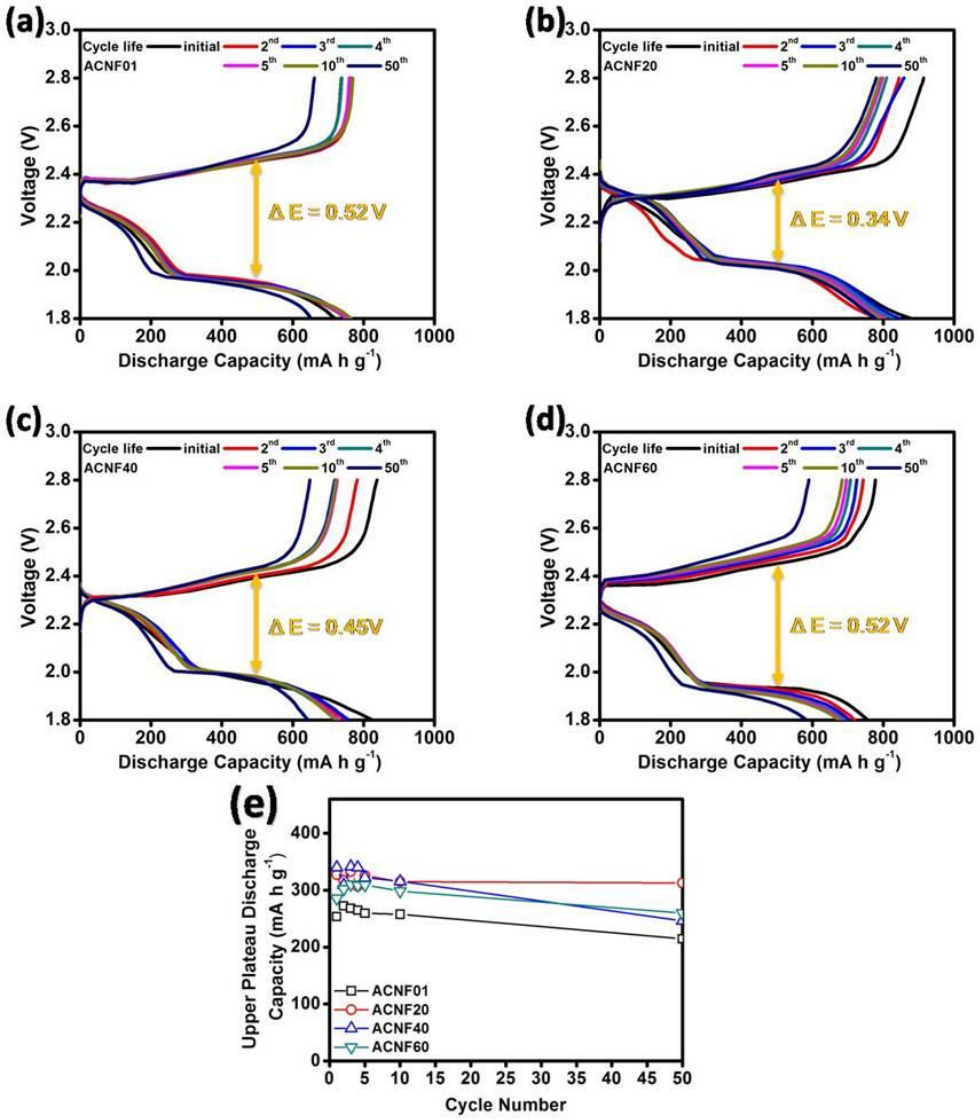

Figure 6.46: Discharge-charge of lithium-sulfur cells employing various ACNF-filter-coated separators at a C/2 rate: (a) ACNF01, (b) ACNF20, (c) ACNF40, and (d) ACNF60. (e) Upper plateau discharge capacities of cells employing different separators.

6.3.4.8 Polysulfide-trapping capacity of optimized microporous ACNF filters

Figure 6.47a (in-plane SEM inspection) and Figure 6.47b (cross-section SEM inspection) display the morphological changes and the polysulfide absorption of the ACNF20 filter after 200 cycles. A comparison of these SEM images with the images gathered before cycling (Figure 6.40b) shows that the microstructure and morphology of the ACNF20 coating appear to remain the same. The lack of nonconductive agglomerates on the surface indicates that there is fast electron transport, smooth Li^+-ion penetration, and good electrolyte wetting for facilitating the electrochemical conversion.[174, 251] The elemental mapping results display the sulfur signals as uniformly distributed over the surface of the cycled ACNF20 filter. This evidences that most migrating polysulfides are intercepted and trapped by the microporous ACNF20 filter from diffusing through to the separator. Looking at the cross-section of the ACNF20-filter-coated separator under SEM (Figure 6.47b), it is evident that the migrating polysulfides neither penetrate the ACNF20 filter nor reach the polypropylene membrane, successfully preventing the loss of active material. In elemental mapping (Figure 6.47a and 6.47b), the sulfur signals show no dense spots of clustering while the elemental carbon mapping signals remain distinguishable. Additionally, the oxygen and fluoride mapping signals, indicative of the electrolyte immersion, are in accordance with the evenly distributed carbon signals.[174] These images show that the conductive, porous ACNF20 filter is able to transfer electrons and electrolyte successfully for reactivating the trapped active material without materializing any non-conductive aggregates on the sulfur cathode or on the filter coating. Therefore, the electrochemically active materials in the cathode region of the cell are stabilized within an intricate three-phase architecture made up of the active material, the porous carbon network, and the electrolyte.

To investigate the polysulfide-trapping capability of the ACNF20 filter, it is beneficial to also look at the morphology of the reverse side of the ACNF20 filter. The ACNF20 filter was carefully peeled off from the cycled ACNF20-filter-coated separator and the previously adhered side was analyzed with EDX mapping (Figure 6.47c). The mapping shows weak sulfur signals while the carbon, oxygen, and fluoride signals are

still evenly distributed, confirming that dissolved polysulfides were unable to penetrate through the fibrous filter to the separator while cycling. Therefore, this proves both the ability of the ACNF20-filter coating to physically intercept polysulfides and the excellent capability of microporous ACNF20s to absorb polysulfides during cell discharging. These two integrated polysulfide-immobilization steps are illustrated in Figure 6.47d. In addition, the ACNF20 filter proved to be difficult to peel off the polypropylene membrane after cycling, indicating a strong adhesion of the ACNF20 with the separator.

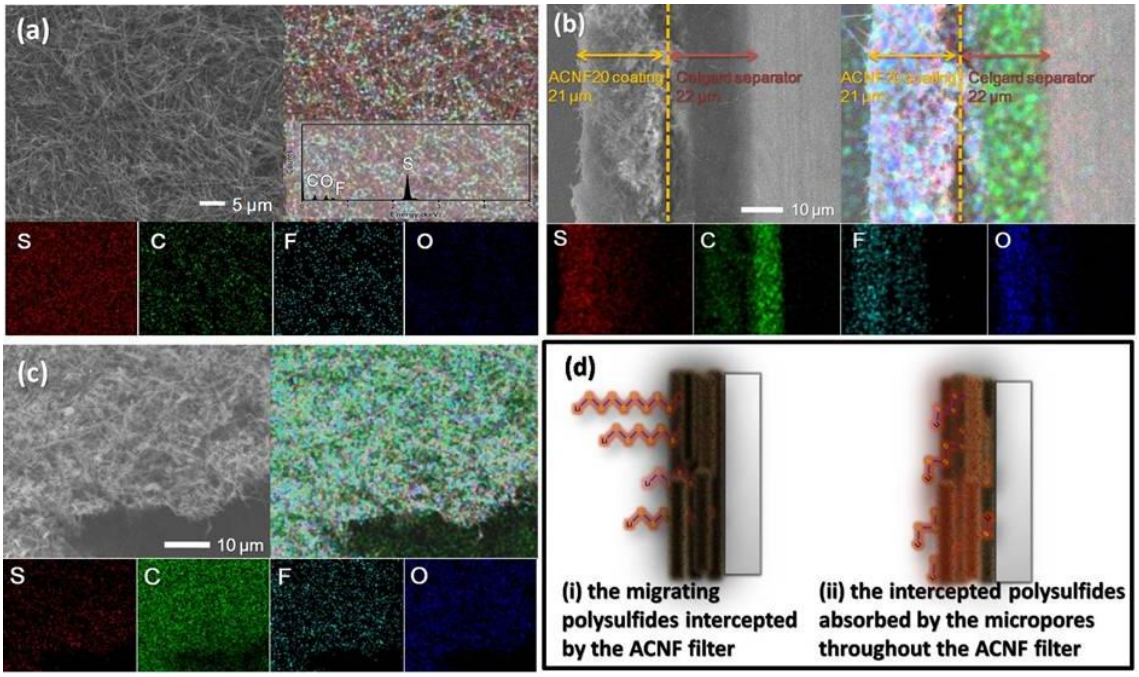

Figure 6.47: Morphology and elemental analyses of the cycled ACNF20-filter-coated separator: (a) in-plane SEM inspection, (b) cross-section SEM inspection, and (c) in-plane SEM inspection on the side previously adhered to the separator of the ACNF20 filter. (d) Schematic illustration of the polysulfide-trapping mechanism of the microporous ACNF20 filter.

3.3.4.9 Summary

In summary, flexible and robust ACNF-filter-coated separators with tunable carbon micropores effectively improve the cycle stability of lithium-sulfur batteries that use pure sulfur as the active material. The microporous ACNF filter, which is coated onto a single side of the polypropylene separator and configured to face the cathode, is successful in filtering and stabilizing the dissolved polysulfides during cell cycling. The porous, conductive ACNF network gives electrons and Li^+-ions access to reactivate the immobilized active material during cycling for subsequent reutilization. The tunable pore sizes of ACNFs allow us to adjust critical electrochemical and engineering parameters in order to optimize functionalized separator development and production. To enhance polysulfide-trapping capability, we suggest that the coated layer on the functionalized separator have an abundance of small micropores with small micropore sizes of 0.4 – 1.2 nm in order to intercept and trap any migrating polysulfides. In order to guarantee the stable cyclability of cells employing this custom-separator design, high electrical conductivity and proper electrolyte-absorption ability of the microporous ACNF filter are needed. These factors help in increasing the kinetics of the redox reactions in the trapped active material. In conclusion, the analytical results of the flexible and robust ACNF-filter-coated separator provide substantial support in aiding the development of advanced functionalized separators. The optimal design will overcome the current technical limitations of lithium-sulfur batteries and facilitate commercialization of lithium-sulfur batteries with facile, cost-effective manufacturing process.

6.4 CONCLUSIONS

In general, the functionalized separator with a carbon coating exhibits the advantages as an outstanding “containment building” to suppress the “polysulfide leak.” In addition, the lightweight coating excludes weight and thickness concerns of the other novel cell components and the low sulfur content problems of sulfur-based nanocomposites. In light of these achievements, our functionalized carbon-coated separator design opens up a new direction for scientific research. The key factor for

creating a custom separator is to integrate a conductive and porous polysulfide blocking region tightly onto the commercial separator. The functional coating with physical or chemical polysulfide-trapping agents aims to intercept, absorb, and then trap the dissolved polysulfide species. The coating substrate also has high electrical conductivity and porous channels to introduce electrons, lithium ions, and electrolyte for reactivating the trapped active material. As a result, an outstanding reutilization of the active material leads to improved long-term cycle stability.

The findings with a series of carbon-coated separators are summarized below:

- *Super P carbon-coated separator:* This prototypical carbon-coated separator demonstrated a facile and practical method to realize high-performance lithium-sulfur batteries.
- *MWCNT-coated separator:* A modified manufacturing process was presented for integrating a fibrous-filter coating onto the functionalized separator and for further enhancing the cell performance. The preparation processes presented in our two initial carbon-coated separator studies could be applied to all kinds of carbon materials, and the study introduced fundamental polysulfide-trapping capability of different carbon coatings.
- *MPC(/PEG)-coated separator:* The MPC-coated separator proved that a carbon-coated separator possesses better physical polysulfide-trapping capability than the MPC/S composites. We further investigated the chemical polysulfide-trapping capability by utilizing PEG binder for not only bonding the MPC particles but also to aim at chemically immobilizing the migrating polysulfides.
- *Microporous ACNF-filter-coated separator:* First, we improved the flexibility and mechanical strength of both the coating layer and the resulting functionalized separator. We then demonstrated the key factors for developing functionalized separator for lithium-sulfur batteries: (a) high microporosity with small micropores of size less than 1.1 nm and (b) good electrical conductivity and a long-range porous architecture.

Chapter 7: Summary

As a conversion-reaction cathode, the high-capacity sulfur cathode may need novel cathode or cell configurations to overcome the persistent problems and realize its full potential with long shelf-life and cycling stability at high sulfur loadings while keeping the processing cost low. Accordingly, my dissertation focused on improving the performance of lithium-sulfur batteries by developing custom-cell components. The approaches developed in this dissertation are beneficial to purse facile and practical solutions for the commercialization of lithium-sulfur batteries. The major findings of this dissertation are briefly summarized below:

- Conventional cell components that are borrowed from current lithium-ion technology may need new architectures or chemical/physical characteristics to be adapted to sulfur cathodes.
- Porous current collectors allow pure sulfur cathodes to attain high electrochemical reversibility. The high porosity of the substrates is the key factor to achieve high areal cathode capacity.
- Polysulfide traps (*e.g.*, interlayers or functionalized separators) have tremendous potential in solving the polysulfide diffusion and migration.
- High-performance carbon interlayers between the sulfur cathode and the polymer separator depend mainly on their thickness and surface morphology to suppress the polysulfide diffusion, so requires a lightweight design.
- Carbon-coated separators fulfill the criteria of achieving high electrochemical reversibility and satisfying the lightweight design. Key parameters for the follow-up development require the carbon coatings to have high microporosity and small micropores.

The commercialization feasibility of lithium-sulfur cells greatly depends on achieving excellent electrochemical stability and reversibility, while utilizing low-cost materials and simple processing techniques. This dissertation presented various practical solutions, which utilize pure sulfur as cathodes without involving expensive, complicated processes; they can

be easily translated into industrial processes. The findings in this dissertation could offer ways to facilitate the commercialization of lithium-sulfur batteries.

Appendix: List of publications

1. R. Singhal, **S.-H. Chung**, A. Manthiram, and V. Kalra, “Free-standing Carbon Nanofiber Interlayer for High-performance Lithium-Sulfur Batteries,” *Journal of Materials Chemistry A* 3, 4530-4538 (2015).

2. A. Manthiram, **S.-H. Chung**, and C. Zu, “Lithium-sulfur Batteries: Progress and Prospective,” *Advanced Materials* 27, 1980-2006 (2015).

3. C.-L. Wang, J.-Y. Liao, **S.-H. Chung**, and A. Manthiram, "Carbonized Eggshell Membranes as a Natural and Abundant Counter Electrode for Efficient Dye-sensitized Solar Cells," *Advanced Energy Materials* DOI:10.1002/aenm.201401524 (2015).

4. **S.-H. Chung** and A. Manthiram, "Eggshell-membrane-derived Polysulfide Absorbents for Highly Stable and Reversible Lithium-Sulfur Cells," *ACS Sustainable Chemistry & Engineering* 2, 2248-2252 (2014).

5. **S.-H. Chung** and A. Manthiram, "A Polyethylene Glycol-Wrapped Microporous Carbon Coating as a Polysulfide Trap for Utilizing Pure Sulfur Cathodes in Lithium-Sulfur Batteries," *Advanced Materials* 26, 7352-7357 (2014).

6. A. Manthiram, Y.-Z. Fu, **S.-H. Chung**, C. Zu, and Y.-S. Su, “Rechargeable Lithium-Sulfur Batteries,” *Chemical Reviews* 114, 11751-11787 (2014).

7. **S.-H. Chung** and A. Manthiram, "High-performance Li-S Batteries with an Ultra-lightweight MWCNT-coated Separator," *Journal of Physical Chemistry Letters* 5, 1978-1983 (2014).

8. **S.-H. Chung** and A. Manthiram, "Bifunctional Separator with a Light-weight Carbon-coating for Dynamically and Statically Stable Lithium-Sulfur Batteries," *Advanced Functional Materials* 24, 5299-5306 (2014).

9. **S.-H. Chung** and A. Manthiram, "A Hierarchical Carbonized Paper with Controllable Thickness as a Modulable Interlayer System for High Performance Li-S Batteries," *Chemical Communications* 50, 4184-4187 (2014).

10. **S.-H. Chung** and A. Manthiram, "A Natural Carbonized Leaf as a Polysulfide Inhibitor for High-performance Lithium-Sulfur Cells," *ChemSusChem* 7, 1665-1661 (2014).

11. **S.-H. Chung** and A. Manthiram, “Low-Cost, Porous Carbon Current Collector with High Sulfur Loading for Lithium-sulfur Batteries,” *Electrochemistry Communications* 38, 91-95 (2014).

12. **S.-H. Chung** and A. Manthiram, "Carbonized Eggshell Membrane as a Natural Polysulfide Reservoir for Highly Reversible Li-S Batteries," *Advanced Materials* 26, 1360-1365 (2014)**.**

13. **S.-H. Chung** and A. Manthiram, “Nano-cellular Carbon Current Collectors with Stable Cyclability for Li-S Batteries,” *Journal of Materials Chemistry A* 1, 9590-9596 (2013).

14. **S.-H. Chung** and A. Manthiram, “Lithium-sulfur Batteries with Superior Cycle Stability by Employing Porous Current Collectors,” *Electrochimica Acta* 107, 569-576 (2013).

15. **S.-H. Chung**, P. Han, R. Singhal, V. Kalra, and A. Manthiram, “Microporous Carbon Nanofiber Filter for Polysulfide towards Electrochemically Stable Rechargeable Lithium-Sulfur Batteries,” (2015).

16. **S.-H. Chung,** R. Singhal, V. Kalra, and A. Manthiram, “A Micro-/meso-porous Carbon Mat as an Electrochemical Testing Platform for Investigating the Performance of Various Cathode Configurations in Li-S Cells,” (2015).

17. C.-H. Chang, **S.-H. Chung**, and A. Manthiram, “Ultra-lightweight PANiNF/MWCNT-functionalized Separators with Synergistic Protections for Li-S Batteries of Pure Sulfur Cathode,” (2015).

References

1. M. S. Whittingham, *Chemical Reviews*, 2004, **104**, 4271-4302.
2. M. Winter and R. J. Brodd, *Chemical Reviews*, 2004, **104**, 4245-4270.
3. J. Cabana, L. Monconduit, D. Larcher and M. R. Palacín, *Advanced Materials*, 2010, **22**, E170-E192.
4. M. Armand and J. M. Tarascon, *Nature*, 2008, **451**, 652-657.
5. Y.-K. Sun, S.-T. Myung, B.-C. Park, J. Prakash, I. Belharouak and K. Amine, *Nat Mater*, 2009, **8**, 320-324.
6. J. B. Goodenough and A. Manthiram, *MRS Communications*, 2014, **4**, 135-142.
7. N. Nitta and G. Yushin, *Particle & Particle Systems Characterization*, 2014, **31**, 317-336.
8. J. B. Goodenough, *Accounts of Chemical Research*, 2012, **46**, 1053-1061.
9. J. B. Goodenough and Y. Kim, *Chemistry of Materials*, 2009, **22**, 587-603.
10. P. G. Bruce, S. A. Freunberger, L. J. Hardwick and J. M. Tarascon, *Nat Mater*, 2012, **11**, 172-172.
11. A. Manthiram, S.-H. Chung and C. Zu, *Advanced Materials*, 2015.
12. L. Chen and L. L. Shaw, *Journal of Power Sources*, 2014, **267**, 770-783.
13. Y.-X. Yin, S. Xin, Y.-G. Guo and L.-J. Wan, *Angewandte Chemie International Edition*, 2013, **52**, 13186-13200.
14. X. Fang and H. Peng, *Small*, 2014, DOI: 10.1002/smll.201402354.
15. D.-W. Wang, Q. Zeng, G. Zhou, L. Yin, F. Li, H.-M. Cheng, I. R. Gentle and G. Q. M. Lu, *Journal of Materials Chemistry A*, 2013, **1**, 9382-9394.
16. J. B. Goodenough and K.-S. Park, *Journal of the American Chemical Society*, 2013, **135**, 1167-1176.
17. C. Barchasz, F. Molton, C. Duboc, J.-C. Leprêtre, S. Patoux and F. Alloin, *Analytical Chemistry*, 2012, **84**, 3973-3980.
18. Y.-S. Su, Y. Fu, T. Cochell and A. Manthiram, *Nat Commun*, 2013, **4**.
19. L. Yuan, X. Qiu, L. Chen and W. Zhu, *Journal of Power Sources*, 2009, **189**, 127-132.
20. J. Nelson, S. Misra, Y. Yang, A. Jackson, Y. Liu, H. Wang, H. Dai, J. C. Andrews, Y. Cui and M. F. Toney, *Journal of the American Chemical Society*, 2012, **134**, 6337-6343.
21. D. Bresser, S. Passerini and B. Scrosati, *Chemical Communications*, 2013, **49**, 10545-10562.
22. G. Xu, B. Ding, J. Pan, P. Nie, L. Shen and X. Zhang, *Journal of Materials Chemistry A*, 2014, **2**, 12662-12676.
23. A. Manthiram, Y. Fu, S.-H. Chung, C. Zu and Y.-S. Su, *Chemical Reviews*, 2014, **114**, 11751-11787.

24. A. Manthiram, Y. Fu and Y.-S. Su, *Accounts of Chemical Research*, 2012, **46**, 1125-1134.
25. R. D. Rauh, F. S. Shuker, J. M. Marston and S. B. Brummer, *Journal of Inorganic and Nuclear Chemistry*, 1977, **39**, 1761-1766.
26. R. D. Rauh, K. M. Abraham, G. F. Pearson, J. K. Surprenant and S. B. Brummer, *Journal of The Electrochemical Society*, 1979, **126**, 523-527.
27. S. S. Zhang, *Journal of Power Sources*, 2013, **231**, 153-162.
28. S.-H. Chung and A. Manthiram, *Advanced Materials*, 2014, **26**, 1360-1365.
29. Y. Fu, Y.-S. Su and A. Manthiram, *Angewandte Chemie International Edition*, 2013, **52**, 6930-6935.
30. R. Chen, T. Zhao and F. Wu, *Chemical Communications*, 2015, **51**, 18-33.
31. J. Lim, J. Pyun and K. Char, *Angewandte Chemie International Edition*, 2015, **54**, 3249-3258.
32. S.-E. Cheon, K.-S. Ko, J.-H. Cho, S.-W. Kim, E.-Y. Chin and H.-T. Kim, *Journal of The Electrochemical Society*, 2003, **150**, A796-A799.
33. Y. V. Mikhaylik and J. R. Akridge, *Journal of The Electrochemical Society*, 2004, **151**, A1969-A1976.
34. Y. Diao, K. Xie, S. Xiong and X. Hong, *Journal of Power Sources*, 2013, **235**, 181-186.
35. D. Aurbach, E. Pollak, R. Elazari, G. Salitra, C. S. Kelley and J. Affinito, *Journal of The Electrochemical Society*, 2009, **156**, A694-A702.
36. S. S. Zhang, *Electrochimica Acta*, 2012, **70**, 344-348.
37. S. S. Zhang, *Journal of The Electrochemical Society*, 2012, **159**, A920-A923.
38. S.-H. Chung and A. Manthiram, *Advanced Functional Materials*, 2014, **24**, 5299-5306.
39. H. S. Ryu, H. J. Ahn, K. W. Kim, J. H. Ahn, K. K. Cho and T. H. Nam, *Electrochimica Acta*, 2006, **52**, 1563-1566.
40. H. S. Ryu, H. J. Ahn, K. W. Kim, J. H. Ahn, J. Y. Lee and E. J. Cairns, *Journal of Power Sources*, 2005, **140**, 365-369.
41. B. H. Jeon, J. H. Yeon, K. M. Kim and I. J. Chung, *Journal of Power Sources*, 2002, **109**, 89-97.
42. S.-E. Cheon, S.-S. Choi, J.-S. Han, Y.-S. Choi, B.-H. Jung and H. S. Lim, *Journal of The Electrochemical Society*, 2004, **151**, A2067-A2073.
43. J. A. Dean, *Lange's handbook of chemistry*, New York : McGraw-Hill, ed. , 15th ed edn., 1999.
44. X. He, J. Ren, L. Wang, W. Pu, C. Jiang and C. Wan, *Journal of Power Sources*, 2009, **190**, 154-156.
45. Y. Wang, Y. Huang, W. Wang, C. Huang, Z. Yu, H. Zhang, J. Sun, A. Wang and K. Yuan, *Electrochimica Acta*, 2009, **54**, 4062-4066.

46. S.-E. Cheon, J.-H. Cho, K.-S. Ko, C.-W. Kwon, D.-R. Chang, H.-T. Kim and S.-W. Kim, *Journal of The Electrochemical Society*, 2002, **149**, A1437-A1441.
47. J. Shim, K. A. Striebel and E. J. Cairns, *Journal of The Electrochemical Society*, 2002, **149**, A1321-A1325.
48. S.-C. Han, M.-S. Song, H. Lee, H.-S. Kim, H.-J. Ahn and J.-Y. Lee, *Journal of The Electrochemical Society*, 2003, **150**, A889-A893.
49. J. L. Wang, J. Yang, J. Y. Xie, N. X. Xu and Y. Li, *Electrochemistry Communications*, 2002, **4**, 499-502.
50. J. Wang, L. Liu, Z. Ling, J. Yang, C. Wan and C. Jiang, *Electrochimica Acta*, 2003, **48**, 1861-1867.
51. W. Zheng, Y. W. Liu, X. G. Hu and C. F. Zhang, *Electrochimica Acta*, 2006, **51**, 1330-1335.
52. X. Ji and L. F. Nazar, *Journal of Materials Chemistry*, 2010, **20**, 9821-9826.
53. M.-K. Song, E. J. Cairns and Y. Zhang, *Nanoscale*, 2013, **5**, 2186-2204.
54. S. Evers and L. F. Nazar, *Accounts of Chemical Research*, 2012, **46**, 1135-1143.
55. X. Ji, K. T. Lee and L. F. Nazar, *Nat Mater*, 2009, **8**, 500-506.
56. N. Jayaprakash, J. Shen, S. S. Moganty, A. Corona and L. A. Archer, *Angewandte Chemie International Edition*, 2011, **50**, 5904-5908.
57. B. Zhang, X. Qin, G. R. Li and X. P. Gao, *Energy & Environmental Science*, 2010, **3**, 1531-1537.
58. X. Tao, X. Chen, Y. Xia, H. Huang, Y. Gan, R. Wu, F. Chen and W. zhang, *Journal of Materials Chemistry A*, 2013, **1**, 3295-3301.
59. B. Zhang, C. Lai, Z. Zhou and X. P. Gao, *Electrochimica Acta*, 2009, **54**, 3708-3713.
60. L. Ji, M. Rao, S. Aloni, L. Wang, E. J. Cairns and Y. Zhang, *Energy & Environmental Science*, 2011, **4**, 5053-5059.
61. X. Li, Y. Cao, W. Qi, L. V. Saraf, J. Xiao, Z. Nie, J. Mietek, J.-G. Zhang, B. Schwenzer and J. Liu, *Journal of Materials Chemistry*, 2011, **21**, 16603-16610.
62. H. Ye, Y.-X. Yin, S. Xin and Y.-G. Guo, *Journal of Materials Chemistry A*, 2013, **1**, 6602-6608.
63. S. Xin, L. Gu, N.-H. Zhao, Y.-X. Yin, L.-J. Zhou, Y.-G. Guo and L.-J. Wan, *Journal of the American Chemical Society*, 2012, **134**, 18510-18513.
64. S. Moon, Y. H. Jung, W. K. Jung, D. S. Jung, J. W. Choi and D. K. Kim, *Advanced Materials*, 2013, **25**, 6547-6553.
65. S. Xin, Y.-X. Yin, L.-J. Wan and Y.-G. Guo, *Particle & Particle Systems Characterization*, 2013, **30**, 321-325.
66. S.-R. Chen, Y.-P. Zhai, G.-L. Xu, Y.-X. Jiang, D.-Y. Zhao, J.-T. Li, L. Huang and S.-G. Sun, *Electrochimica Acta*, 2011, **56**, 9549-9555.
67. G. He, X. Ji and L. Nazar, *Energy & Environmental Science*, 2011, **4**, 2878-2883.

68. B. Ding, C. Yuan, L. Shen, G. Xu, P. Nie and X. Zhang, *Chemistry – A European Journal*, 2013, **19**, 1013-1019.
69. C. Zhang, H. B. Wu, C. Yuan, Z. Guo and X. W. Lou, *Angewandte Chemie International Edition*, 2012, **51**, 9592-9595.
70. X. Yang, L. Zhang, F. Zhang, Y. Huang and Y. Chen, *ACS Nano*, 2014, **8**, 5208-5215.
71. L. Ji, M. Rao, H. Zheng, L. Zhang, Y. Li, W. Duan, J. Guo, E. J. Cairns and Y. Zhang, *Journal of the American Chemical Society*, 2011, **133**, 18522-18525.
72. C. Liang, N. J. Dudney and J. Y. Howe, *Chemistry of Materials*, 2009, **21**, 4724-4730.
73. J. Guo, Y. Xu and C. Wang, *Nano Letters*, 2011, **11**, 4288-4294.
74. M. Rao, X. Song and E. J. Cairns, *Journal of Power Sources*, 2012, **205**, 474-478.
75. Y.-S. Su and A. Manthiram, *Electrochimica Acta*, 2012, **77**, 272-278.
76. C. Wang, J.-j. Chen, Y.-n. Shi, M.-s. Zheng and Q.-f. Dong, *Electrochimica Acta*, 2010, **55**, 7010-7015.
77. W. Ahn, K.-B. Kim, K.-N. Jung, K.-H. Shin and C.-S. Jin, *Journal of Power Sources*, 2012, **202**, 394-399.
78. P. Skytt, P. Glans, D. C. Mancini, J. H. Guo, N. Wassdahl, J. Nordgren and Y. Ma, *Physical Review B*, 1994, **50**, 10457-10461.
79. G. He, S. Evers, X. Liang, M. Cuisinier, A. Garsuch and L. F. Nazar, *ACS Nano*, 2013, **7**, 10920-10930.
80. C. Tang, Q. Zhang, M.-Q. Zhao, J.-Q. Huang, X.-B. Cheng, G.-L. Tian, H.-J. Peng and F. Wei, *Advanced Materials*, 2014, **26**, 6100-6105.
81. Y.-S. Su, Y. Fu and A. Manthiram, *Physical Chemistry Chemical Physics*, 2012, **14**, 14495-14499.
82. H.-J. Peng, J.-Q. Huang, M.-Q. Zhao, Q. Zhang, X.-B. Cheng, X.-Y. Liu, W.-Z. Qian and F. Wei, *Advanced Functional Materials*, 2014, **24**, 2772-2781.
83. Y. Zhao, W. Wu, J. Li, Z. Xu and L. Guan, *Advanced Materials*, 2014, **26**, 5113-5118.
84. T. Xu, J. Song, M. L. Gordin, H. Sohn, Z. Yu, S. Chen and D. Wang, *ACS Applied Materials & Interfaces*, 2013, **5**, 11355-11362.
85. Y. You, W. Zeng, Y.-X. Yin, J. Zhang, C.-P. Yang, Y. Zhu and Y.-G. Guo, *Journal of Materials Chemistry A*, 2015.
86. J. Song, T. Xu, M. L. Gordin, P. Zhu, D. Lv, Y.-B. Jiang, Y. Chen, Y. Duan and D. Wang, *Advanced Functional Materials*, 2014, **24**, 1243-1250.
87. F. Sun, J. Wang, H. Chen, W. Li, W. Qiao, D. Long and L. Ling, *ACS Applied Materials & Interfaces*, 2013, **5**, 5630-5638.
88. H.-J. Peng, T.-Z. Hou, Q. Zhang, J.-Q. Huang, X.-B. Cheng, M.-Q. Guo, Z. Yuan, L.-Y. He and F. Wei, *Advanced Materials Interfaces*, 2014, **1**, DOI: 10.1002/admi.201400227.
89. C. Wang, K. Su, W. Wan, H. Guo, H. Zhou, J. Chen, X. Zhang and Y. Huang, *Journal of Materials Chemistry A*, 2014, **2**, 5018-5023.

90. P. Zhu, J. Song, D. Lv, D. Wang, C. Jaye, D. A. Fischer, T. Wu and Y. Chen, *The Journal of Physical Chemistry C*, 2014, **118**, 7765-7771.
91. J. Wang, J. Yang, J. Xie and N. Xu, *Advanced Materials*, 2002, **14**, 963-965.
92. Y. Fu and A. Manthiram, *The Journal of Physical Chemistry C*, 2012, **116**, 8910-8915.
93. Y. Fu and A. Manthiram, *RSC Advances*, 2012, **2**, 5927-5929.
94. Y. Fu, Y.-S. Su and A. Manthiram, *Journal of The Electrochemical Society*, 2012, **159**, A1420-A1424.
95. L. Xiao, Y. Cao, J. Xiao, B. Schwenzer, M. H. Engelhard, L. V. Saraf, Z. Nie, G. J. Exarhos and J. Liu, *Advanced Materials*, 2012, **24**, 1176-1181.
96. Y. Fu and A. Manthiram, *Chemistry of Materials*, 2012, **24**, 3081-3087.
97. H. Wang, Y. Yang, Y. Liang, J. T. Robinson, Y. Li, A. Jackson, Y. Cui and H. Dai, *Nano Letters*, 2011, **11**, 2644-2647.
98. F. Wu, J. Chen, L. Li, T. Zhao and R. Chen, *The Journal of Physical Chemistry C*, 2011, **115**, 24411-24417.
99. S.-H. Chung and A. Manthiram, *Advanced Materials*, 2014, **26**, 7352-7357.
100. Y. Fu, Y.-S. Su and A. Manthiram, *ACS Applied Materials & Interfaces*, 2012, **4**, 6046-6052.
101. S. Lim, R. Lilly Thankamony, T. Yim, H. Chu, Y.-J. Kim, J. Mun and T.-H. Kim, *ACS Applied Materials & Interfaces*, 2015, **7**, 1401-1405.
102. W. Zhou, H. Chen, Y. Yu, D. Wang, Z. Cui, F. J. DiSalvo and H. D. Abruña, *ACS Nano*, 2013, **7**, 8801-8808.
103. J. Wang, Y.-S. He and J. Yang, *Advanced Materials*, 2015, **27**, 569-575.
104. G.-C. Li, G.-R. Li, S.-H. Ye and X.-P. Gao, *Advanced Energy Materials*, 2012, **2**, 1238-1245.
105. T. Takeuchi, H. Kageyama, K. Nakanishi, M. Tabuchi, H. Sakaebe, T. Ohta, H. Senoh, T. Sakai and K. Tatsumi, *Journal of The Electrochemical Society*, 2010, **157**, A1196-A1201.
106. J. Hassoun and B. Scrosati, *Angewandte Chemie International Edition*, 2010, **49**, 2371-2374.
107. Y. Fu, Y.-S. Su and A. Manthiram, *Advanced Energy Materials*, 2014, **4**, DOI: 10.1002/aenm.201300655.
108. Y. Fu, C. Zu and A. Manthiram, *Journal of the American Chemical Society*, 2013, **135**, 18044-18047.
109. J. Hassoun, Y.-K. Sun and B. Scrosati, *Journal of Power Sources*, 2011, **196**, 343-348.
110. J. Hassoun, J. Kim, D.-J. Lee, H.-G. Jung, S.-M. Lee, Y.-K. Sun and B. Scrosati, *Journal of Power Sources*, 2012, **202**, 308-313.
111. S. Meini, R. Elazari, A. Rosenman, A. Garsuch and D. Aurbach, *The Journal of Physical Chemistry Letters*, 2014, **5**, 915-918.
112. K. Cai, M.-K. Song, E. J. Cairns and Y. Zhang, *Nano Letters*, 2012, **12**, 6474-6479.

113. S. Zheng, Y. Chen, Y. Xu, F. Yi, Y. Zhu, Y. Liu, J. Yang and C. Wang, *ACS Nano*, 2013, **7**, 10995-11003.
114. F. Wu, A. Magasinski and G. Yushin, *Journal of Materials Chemistry A*, 2014, **2**, 6064-6070.
115. S. Jeong, D. Bresser, D. Buchholz, M. Winter and S. Passerini, *Journal of Power Sources*, 2013, **235**, 220-225.
116. J. Guo, Z. Yang, Y. Yu, H. D. Abruña and L. A. Archer, *Journal of the American Chemical Society*, 2012, **135**, 763-767.
117. F. Wu, J. T. Lee, A. Magasinski, H. Kim and G. Yushin, *Particle & Particle Systems Characterization*, 2014, **31**, 639-644.
118. Z. Lin, Z. Liu, N. J. Dudney and C. Liang, *ACS Nano*, 2013, **7**, 2829-2833.
119. F. Wu, J. T. Lee, N. Nitta, H. Kim, O. Borodin and G. Yushin, *Advanced Materials*, 2015, **27**, 101-108.
120. C.-P. Yang, Y.-X. Yin and Y.-G. Guo, *The Journal of Physical Chemistry Letters*, 2014, **6**, 256-266.
121. A. Abouimrane, D. Dambournet, K. W. Chapman, P. J. Chupas, W. Weng and K. Amine, *Journal of the American Chemical Society*, 2012, **134**, 4505-4508.
122. C.-P. Yang, S. Xin, Y.-X. Yin, H. Ye, J. Zhang and Y.-G. Guo, *Angewandte Chemie International Edition*, 2013, **52**, 8363-8367.
123. Y. Liu, L. Si, X. Zhou, X. Liu, Y. Xu, J. Bao and Z. Dai, *Journal of Materials Chemistry A*, 2014, **2**, 17735-17739.
124. Z. Zhang, X. Yang, Z. Guo, Y. Qu, J. Li and Y. Lai, *Journal of Power Sources*, 2015, **279**, 88-93.
125. Y. Jiang, X. Ma, J. Feng and S. Xiong, *Journal of Materials Chemistry A*, 2015, **3**, 4539-4546.
126. L. Liu, Y. Wei, C. Zhang, C. Zhang, X. Li, J. Wang, L. Ling, W. Qiao and D. Long, *Electrochimica Acta*, 2015, **153**, 140-148.
127. S. S. Zhang and J. A. Read, *Journal of Power Sources*, 2012, **200**, 77-82.
128. R. Xu, I. Belharouak, J. C. M. Li, X. Zhang, I. Bloom and J. Bareño, *Advanced Energy Materials*, 2013, **3**, 833-838.
129. H. Chen, Q. Zou, Z. Liang, H. Liu, Q. Li and Y.-C. Lu, *Nat Commun*, 2015, **6**.
130. J. W. Braithwaite, A. Gonzales, G. Nagasubramanian, S. J. Lucero, D. E. Peebles, J. A. Ohlhausen and W. R. Cieslak, *Journal of The Electrochemical Society*, 1999, **146**, 448-456.
131. M. Yao, K. Okuno, T. Iwaki, M. Kato, K. Harada, J.-J. Park, S. Tanase and T. Sakai, *Journal of The Electrochemical Society*, 2007, **154**, A709-A714.
132. M. Yao, K. Okuno, T. Iwaki, M. Kato, S. Tanase, K. Emura and T. Sakai, *Journal of Power Sources*, 2007, **173**, 545-549.

133. M. Yao, K. Okuno, T. Iwaki, T. Awazu and T. Sakai, *Journal of Power Sources*, 2010, **195**, 2077-2081.
134. Y.-H. Lee, J.-S. Kim, J. Noh, I. Lee, H. J. Kim, S. Choi, J. Seo, S. Jeon, T.-S. Kim, J.-Y. Lee and J. W. Choi, *Nano Letters*, 2013, **13**, 5753-5761.
135. S.-H. Chung and A. Manthiram, *Electrochimica Acta*, 2013, **107**, 569-576.
136. S. Risse, S. D. Angioletti-Uberti, J. and M. Ballauff, *Journal of Power Sources*, 2014, **267**, 648-654.
137. J. A. Rodriguez and J. Hrbek, *Accounts of Chemical Research*, 1999, **32**, 719-728.
138. R. Elazari, G. Salitra, A. Garsuch, A. Panchenko and D. Aurbach, *Advanced Materials*, 2011, **23**, 5641-5644.
139. S. Dorfler, M. Hagen, H. Althues, J. Tubke, S. Kaskel and M. J. Hoffmann, *Chemical Communications*, 2012, **48**, 4097-4099.
140. M. Hagen, S. Dörfler, H. Althues, J. Tübke, M. J. Hoffmann, S. Kaskel and K. Pinkwart, *Journal of Power Sources*, 2012, **213**, 239-248.
141. Z. Yuan, H.-J. Peng, J.-Q. Huang, X.-Y. Liu, D.-W. Wang, X.-B. Cheng and Q. Zhang, *Advanced Functional Materials*, 2014, **24**, 6105-6112.
142. L. Zeng, F. Pan, W. Li, Y. Jiang, X. Zhong and Y. Yu, *Nanoscale*, 2014, **6**, 9579-9587.
143. G. Zhou, D.-W. Wang, F. Li, P.-X. Hou, L. Yin, C. Liu, G. Q. Lu, I. R. Gentle and H.-M. Cheng, *Energy & Environmental Science*, 2012, **5**, 8901-8906.
144. J.-Q. Huang, H.-J. Peng, X.-Y. Liu, J.-Q. Nie, X.-B. Cheng, Q. Zhang and F. Wei, *Journal of Materials Chemistry A*, 2014, **2**, 10869-10875.
145. S. S. Zhang, *Journal of The Electrochemical Society*, 2012, **159**, A1226-A1229.
146. J. Sun, Y. Huang, W. Wang, Z. Yu, A. Wang and K. Yuan, *Electrochimica Acta*, 2008, **53**, 7084-7088.
147. M. He, L.-X. Yuan, W.-X. Zhang, X.-L. Hu and Y.-H. Huang, *The Journal of Physical Chemistry C*, 2011, **115**, 15703-15709.
148. H. Schneider, A. Garsuch, A. Panchenko, O. Gronwald, N. Janssen and P. Novák, *Journal of Power Sources*, 2012, **205**, 420-425.
149. J. Wang, Z. Yao, C. W. Monroe, J. Yang and Y. Nuli, *Advanced Functional Materials*, 2013, **23**, 1194-1201.
150. Z. Jin, K. Xie, X. Hong, Z. Hu and X. Liu, *Journal of Power Sources*, 2012, **218**, 163-167.
151. I. Bauer, S. Thieme, J. Brückner, H. Althues and S. Kaskel, *Journal of Power Sources*, 2014, **251**, 417-422.
152. J.-Q. Huang, Q. Zhang, H.-J. Peng, X.-Y. Liu, W.-Z. Qian and F. Wei, *Energy & Environmental Science*, 2014, **7**, 347-353.
153. M. Gu, J. Lee, Y. Kim, J. S. Kim, B. Y. Jang, K. T. Lee and B.-S. Kim, *RSC Advances*, 2014, **4**, 46940-46946.

154. S.-H. Chung and A. Manthiram, *The Journal of Physical Chemistry Letters*, 2014, **5**, 1978-1983.
155. A. Manuel Stephan, *European Polymer Journal*, 2006, **42**, 21-42.
156. S. Kim, Y. Jung and S.-J. Park, *Journal of Power Sources*, 2005, **152**, 272-277.
157. X. Liang, Z. Wen, Y. Liu, M. Wu, J. Jin, H. Zhang and X. Wu, *Journal of Power Sources*, 2011, **196**, 9839-9843.
158. L. Suo, Y.-S. Hu, H. Li, M. Armand and L. Chen, *Nat Commun*, 2013, **4**, 1481.
159. D.-R. Chang, S.-H. Lee, S.-W. Kim and H.-T. Kim, *Journal of Power Sources*, 2002, **112**, 452-460.
160. J.-W. Choi, J.-K. Kim, G. Cheruvally, J.-H. Ahn, H.-J. Ahn and K.-W. Kim, *Electrochimica Acta*, 2007, **52**, 2075-2082.
161. Q. Wang, J. Jin, X. Wu, G. Ma, J. Yang and Z. Wen, *Physical Chemistry Chemical Physics*, 2014, **16**, 21225-21229.
162. K. Jeddi, M. Ghaznavi and P. Chen, *Journal of Materials Chemistry A*, 2013, **1**, 2769-2772.
163. L. Wang, X. Li and W. Yang, *Electrochimica Acta*, 2010, **55**, 1895-1899.
164. D. Aurbach, *Journal of Power Sources*, 2000, **89**, 206-218.
165. H. Kim, G. Jeong, Y.-U. Kim, J.-H. Kim, C.-M. Park and H.-J. Sohn, *Chemical Society Reviews*, 2013, **42**, 9011-9034.
166. A. Zhamu, G. Chen, C. Liu, D. Neff, Q. Fang, Z. Yu, W. Xiong, Y. Wang, X. Wang and B. Z. Jang, *Energy & Environmental Science*, 2012, **5**, 5701-5707.
167. Y. M. Lee, N.-S. Choi, J. H. Park and J.-K. Park, *Journal of Power Sources*, 2003, **119–121**, 964-972.
168. Y. Yan, Y.-X. Yin, S. Xin, J. Su, Y.-G. Guo and L.-J. Wan, *Electrochimica Acta*, 2013, **91**, 58-61.
169. G. Zhou, S. Pei, L. Li, D.-W. Wang, S. Wang, K. Huang, L.-C. Yin, F. Li and H.-M. Cheng, *Advanced Materials*, 2014, **26**, 625-631.
170. J. A. Dean, *Lange's Handbook of Chemistry,*, McGraw-Hill, New York, 3rd edn., 1985.
171. S.-E. Cheon, K.-S. Ko, J.-H. Cho, S.-W. Kim, E.-Y. Chin and H.-T. Kim, *Journal of The Electrochemical Society*, 2003, **150**, A800-A805.
172. H. S. Ryu, J. W. Park, J. Park, J.-P. Ahn, K.-W. Kim, J.-H. Ahn, T.-H. Nam, G. Wang and H.-J. Ahn, *Journal of Materials Chemistry A*, 2013, **1**, 1573-1578.
173. Y.-S. Su and A. Manthiram, *Chemical Communications*, 2012, **48**, 8817-8819.
174. Y.-S. Su and A. Manthiram, *Nat Commun*, 2012, **3**, 1166.
175. C. Barchasz, F. Mesguich, J. Dijon, J.-C. Leprêtre, S. Patoux and F. Alloin, *Journal of Power Sources*, 2012, **211**, 19-26.
176. S.-H. Chung and A. Manthiram, *Journal of Materials Chemistry A*, 2013, **1**, 9590-9596.

177. S.-H. Chung and A. Manthiram, *Electrochemistry Communications*, 2014, **38**, 91-95.
178. S.-H. Chung and A. Manthiram, *ACS Sustainable Chemistry & Engineering*, 2014, **2**, 2248-2252.
179. M. Yao, K. Okuno, T. Iwaki, M. Kato, K. Harada, J.-J. Park, S. Tanase and T. Sakai, *Electrochemical and Solid-State Letters*, 2007, **10**, A56-A59.
180. H. Yamin, J. Penciner, A. Gorenshtain, M. Elam and E. Peled, *Journal of Power Sources*, 1985, **14**, 129-134.
181. H. Yamin, A. Gorenshtein, J. Penciner, Y. Sternberg and E. Peled, *Journal of The Electrochemical Society*, 1988, **135**, 1045-1048.
182. K. S. W. Sing, D. H. Everett, R. A. W. Haul, L. Moscou, R. A. Pierotti, J. Rouquero and T. Siemieniewska, *Pure and Applied Chemistry*, 1985, **57**, 603-619.
183. Y.-S. Su, Y. Fu, B. Guo, S. Dai and A. Manthiram, *Chemistry – A European Journal*, 2013, **19**, 8621-8626.
184. J. Sun, Y. Huang, W. Wang, Z. Yu, A. Wang and K. Yuan, *Electrochemistry Communications*, 2008, **10**, 930-933.
185. S. Wei, H. Zhang, Y. Huang, W. Wang, Y. Xia and Z. Yu, *Energy & Environmental Science*, 2011, **4**, 736-740.
186. X. Ji, S. Evers, R. Black and L. F. Nazar, *Nat Commun*, 2011, **2**, 325.
187. S. Evers, T. Yim and L. F. Nazar, *The Journal of Physical Chemistry C*, 2012, **116**, 19653-19658.
188. Z. Li, Z. Xu, X. Tan, H. Wang, C. M. B. Holt, T. Stephenson, B. C. Olsen and D. Mitlin, *Energy & Environmental Science*, 2013, **6**, 871-878.
189. J. T. Lee, Y. Zhao, S. Thieme, H. Kim, M. Oschatz, L. Borchardt, A. Magasinski, W.-I. Cho, S. Kaskel and G. Yushin, *Advanced Materials*, 2013, **25**, 4573-4579.
190. D. S. Jung, T. H. Hwang, J. H. Lee, H. Y. Koo, R. A. Shakoor, R. Kahraman, Y. N. Jo, M.-S. Park and J. W. Choi, *Nano Letters*, 2014, **14**, 4418-4425.
191. Y. Zhang, Y. Zhao, A. Yermukhambetova, Z. Bakenov and P. Chen, *Journal of Materials Chemistry A*, 2013, **1**, 295-301.
192. M.-S. Song, S.-C. Han, H.-S. Kim, J.-H. Kim, K.-T. Kim, Y.-M. Kang, H.-J. Ahn, S. X. Dou and J.-Y. Lee, *Journal of The Electrochemical Society*, 2004, **151**, A791-A795.
193. 2001.
194. Y. J. Choi, B. S. Jung, D. J. Lee, J. H. Jeong, K. W. Kim, H. J. Ahn, K. K. Cho and H. B. Gu, *Physica Scripta*, 2007, **2007**, 62.
195. B. Scrosati, J. Hassoun and Y.-K. Sun, *Energy & Environmental Science*, 2011, **4**, 3287-3295.
196. J. Wang, L. Yin, H. Jia, H. Yu, Y. He, J. Yang and C. W. Monroe, *ChemSusChem*, 2014, **7**, 563-569.
197. X.-G. Sun, X. Wang, R. T. Mayes and S. Dai, *ChemSusChem*, 2012, **5**, 2079-2085.

198. T. Lin, Y. Tang, Y. Wang, H. Bi, Z. Liu, F. Huang, X. Xie and M. Jiang, *Energy & Environmental Science*, 2013, **6**, 1283-1290.
199. C. S. Kim, A. Guerfi, P. Hovington, J. Trottier, C. Gagnon, F. Barray, A. Vijh, M. Armand and K. Zaghib, *Journal of Power Sources*, 2013, **241**, 554-559.
200. J. Kim, D.-J. Lee, H.-G. Jung, Y.-K. Sun, J. Hassoun and B. Scrosati, *Advanced Functional Materials*, 2013, **23**, 1076-1080.
201. G. Xu, B. Ding, P. Nie, L. Shen, H. Dou and X. Zhang, *ACS Applied Materials & Interfaces*, 2013, **6**, 194-199.
202. B. Zhang, M. Xiao, S. Wang, D. Han, S. Song, G. Chen and Y. Meng, *ACS Applied Materials & Interfaces*, 2014, **6**, 13174-13182.
203. J. Xu, J. Shui, J. Wang, M. Wang, H.-K. Liu, S. X. Dou, I.-Y. Jeon, J.-M. Seo, J.-B. Baek and L. Dai, *ACS Nano*, 2014, **8**, 10920-10930.
204. G.-L. Xu, Q. Wang, J.-C. Fang, Y.-F. Xu, J.-T. Li, L. Huang and S.-G. Sun, *Journal of Materials Chemistry A*, 2014, **2**, 19941-19962.
205. F. Wu, J. Chen, L. Li, T. Zhao, Z. Liu and R. Chen, *ChemSusChem*, 2013, **6**, 1438-1444.
206. Y. Yang, G. Yu, J. J. Cha, H. Wu, M. Vosgueritchian, Y. Yao, Z. Bao and Y. Cui, *ACS Nano*, 2011, **5**, 9187-9193.
207. W. Weng, V. G. Pol and K. Amine, *Advanced Materials*, 2013, **25**, 1608-1615.
208. S.-H. Chung and A. Manthiram, *ChemSusChem*, 2014, **7**, 1655-1661.
209. S.-H. Chung and A. Manthiram, *Chemical Communications*, 2014, **50**, 4184-4187.
210. R. Singhal, S.-H. Chung, A. Manthiram and V. Kalra, *Journal of Materials Chemistry A*, 2015.
211. Z. Li, L. Zhang, B. S. Amirkhiz, X. Tan, Z. Xu, H. Wang, B. C. Olsen, C. M. B. Holt and D. Mitlin, *Advanced Energy Materials*, 2012, **2**, 431-437.
212. J. W. Galusha, M. R. Jorgensen and M. H. Bartl, *Advanced Materials*, 2010, **22**, 107-110.
213. D. Losic, J. G. Mitchell and N. H. Voelcker, *Advanced Materials*, 2009, **21**, 2947-2958.
214. C. Tran and V. Kalra, *Journal of Power Sources*, 2013, **235**, 289-296.
215. C. O. Ania and T. J. Bandosz, *Langmuir*, 2005, **21**, 7752-7759.
216. L. Li, G. Ruan, Z. Peng, Y. Yang, H. Fei, A.-R. O. Raji, E. L. G. Samuel and J. M. Tour, *ACS Applied Materials & Interfaces*, 2014, **6**, 15033-15039.
217. D. Li, F. Han, S. Wang, F. Cheng, Q. Sun and W.-C. Li, *ACS Applied Materials & Interfaces*, 2013, **5**, 2208-2213.
218. T.-G. Jeong, Y. H. Moon, H.-H. Chun, H. S. Kim, B. W. Cho and Y.-T. Kim, *Chemical Communications*, 2013, **49**, 11107-11109.
219. H. Sohn, M. L. Gordin, T. Xu, S. Chen, D. Lv, J. Song, A. Manivannan and D. Wang, *ACS Applied Materials & Interfaces*, 2014, **6**, 7596-7606.

220. B. Ding, E. Kimura, T. Sato, S. Fujita and S. Shiratori, *Polymer*, 2004, **45**, 1895-1902.
221. A. Tsimpliaraki, S. Svinterikos, I. Zuburtikudis, S. I. Marras and C. Panayiotou, *Industrial & Engineering Chemistry Research*, 2009, **48**, 4365-4374.
222. S. Chen, S. He and H. Hou, *Current Organic Chemistry*, 2013, **17**, 1402-1410.
223. S.-M. Zhang, Q. Zhang, J.-Q. Huang, X.-F. Liu, W. Zhu, M.-Q. Zhao, W.-Z. Qian and F. Wei, *Particle & Particle Systems Characterization*, 2013, **30**, 158-165.
224. D. Tasis, N. Tagmatarchis, A. Bianco and M. Prato, *Chemical Reviews*, 2006, **106**, 1105-1136.
225. C. Tran and V. Kalra, *Soft Matter*, 2013, **9**, 846-852.
226. J. Schuster, G. He, B. Mandlmeier, T. Yim, K. T. Lee, T. Bein and L. F. Nazar, *Angewandte Chemie International Edition*, 2012, **51**, 3591-3595.
227. J. R. Akridge, Y. V. Mikhaylik and N. White, *Solid State Ionics*, 2004, **175**, 243-245.
228. W. Chen, Z. Zhang, Q. Li, Y. Lai and J. Li, *ChemElectroChem*, 2015, **2**, 246-252.
229. R. Demir-Cakan, M. Morcrette, Gangulibabu, A. Gueguen, R. Dedryvere and J.-M. Tarascon, *Energy & Environmental Science*, 2013, **6**, 176-182.
230. S. Huilan, H. Jie, W. Na, D. Qun, Z. Di and Z. Chunfu, *Smart Materials and Structures*, 2008, **17**, 015045.
231. D. Yang, L. Qi and J. Ma, *Advanced Materials*, 2002, **14**, 1543-1546.
232. M. Deka and A. Kumar, *Journal of Power Sources*, 2011, **196**, 1358-1364.
233. J. Liu, T. Yang, D.-W. Wang, G. Q. Lu, D. Zhao and S. Z. Qiao, *Nat Commun*, 2013, **4**.
234. L. Wang, Y. Zhao, M. L. Thomas and H. R. Byon, *Advanced Functional Materials*, 2014, **24**, 2248-2252.
235. Z. Zhang, Z. Li, F. Hao, X. Wang, Q. Li, Y. Qi, R. Fan and L. Yin, *Advanced Functional Materials*, 2014, **24**, 2500-2509.
236. G. Ma, Z. Wen, J. Jin, Y. Lu, X. Wu, C. Liu and C. Chen, *RSC Advances*, 2014, **4**, 21612-21618.
237. G. Ma, Z. Wen, J. Jin, Y. Lu, X. Wu, M. Wu and C. Chen, *Journal of Materials Chemistry A*, 2014, **2**, 10350-10354.
238. Z. Lin, Z. Liu, W. Fu, N. J. Dudney and C. Liang, *Advanced Functional Materials*, 2013, **23**, 1064-1069.
239. G. Ma, Z. Wen, M. Wu, C. Shen, Q. Wang, J. Jin and X. Wu, *Chemical Communications*, 2014, **50**, 14209-14212.
240. K. Zhang, F. Qin, J. Fang, Q. Li, M. Jia, Y. Lai, Z. Zhang and J. Li, *Journal of Solid State Electrochemistry*, 2014, **18**, 1025-1029.
241. J. Song, Z. Yu, T. Xu, S. Chen, H. Sohn, M. Regula and D. Wang, *Journal of Materials Chemistry A*, 2014, **2**, 8623-8627.
242. X. Wang, Z. Wang and L. Chen, *Journal of Power Sources*, 2013, **242**, 65-69.

243. G. Ma, Z. Wen, Q. Wang, C. Shen, J. Jin and X. Wu, *Journal of Materials Chemistry A*, 2014, **2**, 19355-19359.
244. O. Knop, R. J. Boyd and S. C. Choi, *Journal of the American Chemical Society*, 1988, **110**, 7299-7301.
245. S. Li, R. Zheng, S.-J. Chen and Q.-C. Fan, *Molecular Physics*, 2015, 1-9.
246. J. Wang, L. Lu, D. Shi, R. Tandiono, Z. Wang, K. Konstantinov and H. Liu, *ChemPlusChem*, 2013, **78**, 318-324.
247. M.-Q. Zhao, H.-J. Peng, G.-L. Tian, Q. Zhang, J.-Q. Huang, X.-B. Cheng, C. Tang and F. Wei, *Advanced Materials*, 2014, **26**, 7051-7058.
248. A. I. Boldyrev, J. Simons and P. v. R. Schleyer, *The Journal of Chemical Physics*, 1993, **99**, 8793-8804.
249. Y. Jung and S. Kim, *Electrochemistry Communications*, 2007, **9**, 249-254.
250. X. Liang, C. Hart, Q. Pang, A. Garsuch, T. Weiss and L. F. Nazar, *Nat Commun*, 2015, **6**.
251. L. Qie and A. Manthiram, *Advanced Materials*, 2015, **27**, 1694-1700.

Vita

Sheng-Heng Chung was born in 1984, in Kaohsiung, Taiwan. He was an intern in the electrical, magnetic, and optical ceramic laboratory. He received his B.S. degrees in Resource Engineering with minor in Materials Science and Engineering from National Cheng Kung University in Tainan, Taiwan, in 2006. He was an intern at Industrial Technology Research Institute for the solid-state fuel cell project during 2007 – 2008. He received his M.S. degree in Materials Science and Engineering from National Tsing Hua University in Hsinchu, Taiwan, in 2008. After one year military service, he worked at Safety and Health Technology Center for chemical and nanomaterial managements. In August 2011, he joined the Materials Science and Engineering Graduate Program at the University of Texas at Austin and carried out research work in the area of lithium-sulfur batteries.

Email Address: SHChung@utexas.edu

This dissertation was typed by the author.